

SEED-MEDIATED CONTROLLED GROWTH of RARE EARTH NANOCRYSTALS

By

Shihui Wen

School of Mathematical and Physical Sciences,
Faculty of Science

Supervisors:

Prof. Dayong Jin

Dr. Fan Wang



This thesis is presented for the degree of Doctor of Philosophy
September 2018

CERTIFICATE OF ORIGINAL AUTHORSHIP

I, Shihui Wen, declare that this thesis, submitted in fulfilment of the requirements for the award of Doctor of Philosophy, in the School of Mathematical and Physical Sciences, Faculty of Science at the University of Technology Sydney.

This thesis is wholly my own work unless otherwise reference or acknowledged. In addition, I certify that all information sources and literature used are indicated in the thesis.

This document has not been submitted for qualifications at any other academic institution.

Production Note:

Signature: Signature removed prior to publication.

Date: 03/09/2018

© Shihui Wen, 2018.

ACKNOWLEDGEMENTS

Firstly, I would like to extend my gratitude to my principal supervisor Prof. Dayong Jin who has always been motivating and supportive to me. What I learned and he trained is not only academic research skills but more important the Philosophy during my 3.5-year Ph.D candidature period. I enjoy these principles of success and employ them as the tool to explore the new knowledge and change my life. Definitely, they will benefit me all my life. Prof. Jin is not only the soul of our research team, but also the soul of many international collaborative research teams. I learnt a lot from his self-motivated and optimistic attitude to life, and aspiring, energetic and collaborative research style. His passion on the science research always impacts me to firmly believe what we do and will win at the end. I really appreciate his sincere help and thoughtful suggestions on my PhD program and my research career development. I also thank Jin for patiently teaching me on academic writing in a way that make my writings easily understandable by general audience.

I also would like to thank my co-supervisor Dr. Fan Wang for helping me in terms of the optical characterization and his professional advice on my research project. He gave me a lot of thoughtful comments on my publications.

Next, I would like to thank my colleagues, in particular, Dr. Deming Liu, Dr. Jiajia Zhou, Dr. Xiaoxue Xu, Dr. Gungun Lin, for significant contributions to my research projects and publications. I also thank Zhiguang Zhou, Chaohao Chen, Yongtao Liu, Chenshuo Ma, Hao He, Wei Ren, Chao Mi, Ming Guan, Yulong Sun, Yinghui Chen, Jiayan Liao, and other peers within our research group. I had a wonderful teamwork experience with them. Many colleagues at UTS, including Dr. Hien Dong, Dr. Olga Shimoni, Huan Wu, Yuan Liu, Baoming Wang, and others, gave me many valuable advices through my research projects. I also want to thank our international collaborators, Prof. Xiangyang Shi, Prof. Xiaogang Liu, Dr. Yi Du, and other members in their respective labs. Their expertise and contributions added great values to my research projects. I sincerely appreciate the generous help from all these nice people. Moreover, I want to thank Dr. Tom Lawson, who help me a lot during my joint research project at Macquarie University.

I acknowledge the financial support I received from University of Technology Sydney and Vice-Chancellor's Outstanding Achievement Scholarship to offer me many opportunities to expand my research experiences.

Finally, I would like to thank my lover, Du, who has been sacrificing so much to support me. She teaches me a lot about cooking, although I can only play some of her skills by myself now. For my beloved family, I thank my parents, JiuJun Wen and Chuanling Li, and my brother Jingke Wen, and other relatives, who have been economically and spiritually backing me up both over years.

Table of Contents

CERTIFICATE OF ORIGINAL AUTHORSHIP	I
ACKNOWLEDGEMENTS	III
List of Publications	X
ABSTRACT	XIII
List of Acronyms (in alphabetic order).....	XVI
CHAPTER 1 Introduction.....	1
1.1 Nanoparticles and Nanotechnology	1
1.1.1 Size-dependent properties.....	3
1.1.2 Shape-dependent properties.....	4
1.2 Rare-Earth Nanoparticles	8
1.2.1 Size-dependent properties.....	11
1.2.2 Shape-dependent properties.....	12
1.3 One-Pot Wet Chemical Synthesis	14
1.3.1 Formation mechanism of nanocrystals	14
1.3.2 One-pot wet-chemical synthesis of UCNPs	18
1.3.3 One-pot size control of UCNPs	22
1.3.4 One-pot shape control of UCNPs	24
1.3.5 Brief conclusion.....	25
1.4 Seed-Mediated Growth	27
1.4.1 Isotropic growth.....	28
1.4.2 Anisotropic growth.....	35
1.5 Aim and Outline	40
1.5.1 Thesis aim.....	40
1.5.2 Thesis outline.....	40

1.6 References	43
CHAPTER 2 Materials and Methods	59
2.1 General Chemicals and Reagents	59
2.2 Instruments and Equipment.....	61
2.3 Home-made Instruments	62
2.3.1 Confocal microscope for single nanoparticles.....	62
2.3.2 Dual-laser confocal/super-resolution microscope	63
2.3.3 Multi-photon near-infrared emission saturation nanoscopy.....	65
2.4 General NaREF ₄ Nanocrystals Synthesis.....	66
2.4.1 One-pot synthesis	66
2.4.2 Core@shell nanostructure synthesis.....	67
2.5 Synthesis Protocol.....	70
2.5.1 Stock solution preparation	70
2.5.2 Reaction set up.....	71
2.5.3 One-pot NaREF ₄ synthesis	71
2.5.4 Core@shell synthesis.	72
2.6 Characterization	74
2.7 General Surface Modification.....	75
2.7.1 Silica coating	75
2.7.2 POEGA-b-PMAEP polymer modified UCNPs.....	75
2.7.3 3,4-dihydroxyhydrocinnamic acid modified UCNPs.....	75
2.7.4 Dopamine modified UCNPs.....	76
2.7.5 Biotin modified UCNPs.....	76
2.8 References	76
CHAPTER 3 One-Nanometer-Scale Size-Controlled Synthesis of UCNPs by Seed-Mediated Growth	79

3.1 Introduction	79
3.2 Experimental Section	81
3.2.1. Synthesis of NaYF ₄ :20%Yb,2%Er core nanocrystals	81
3.2.2. Seed-mediated growth of nanocrystals.....	81
3.3. Results and Discussion.....	82
3.4 Applications in Joint Projects.....	87
3.4.1 STED-based super-resolution imaging.....	88
3.4.2 NIRES-based super-resolution imaging	91
3.4.3 Single nanoparticle tracking	92
3.5 Conclusion.....	94
3.6 References	95
CHAPTER 4 Fabrication of Bright and Ultra-small Core@shell UCNP's by Seed-mediated <i>in-situ</i> Growth	99
4.1 Preamble.....	99
4.2 Introduction	100
4.3 Experimental Section	102
4.3.1 Synthesis of NaYF ₄ :20%Yb,2%Er nanocrystals	102
4.3.2 Core@shell nanocrystals synthesis.....	103
4.3.3 Small core@shell nanocrystals synthesis	103
4.3.4 Characterization techniques.....	104
4.4 Results and Discussion.....	104
4.5 Conclusion.....	111
4.6 References	111
CHAPTER 5 Optimal Sensitizer-Activator Doping Concentration in Single Upconversion Nanocrystals via Seeded Growth Approach	115
5.1 Preamble.....	115

5.2 Introduction	116
5.3 Experimental Section	117
5.3.1 Synthesis of NaYF ₄ core nanocrystals.....	117
5.3.2 Core@shell@shell nanocrystals synthesis	117
5.3.3 Small core@shell nanocrystals synthesis	118
5.3.4 Characterization techniques.....	118
5.4 Results and Discussion.....	119
5.5 Conclusion.....	129
5.6 References	130
CHAPTER 6 Single-axis Epitaxial Growth of Barcoded Heterogeneous Nanorods	133
6.1 Preamble.....	133
6.2 Introduction	134
6.3 Experimental Section	134
6.3.1 Synthesis of NaYF ₄ :Yb,Er core nanocrystals.....	134
6.3.2 Longitudinal growth of NaREF ₄ onto the core of NaYF ₄ :Yb,Er nanocrystals.....	135
6.3.3 Programmable growth of versatile nanoring-coated nanodumbbell.....	135
6.3.4 Characterization techniques.....	136
6.3.5 Cytotoxicity assay.....	137
6.3.6 In vivo multimode imaging of SKOV-3 xenograft tumor model.....	137
6.4 Results and Discussion.....	138
6.5 Conclusion.....	146
6.6 References	146
CHAPTER 7 Conclusion and Future Scope	151
7.1 Conclusion.....	151
7.2 Future Scope.....	153

7.2.1 Developing highly doped UCNPs	153
7.2.2 Development of hybrid system.....	154
7.2.3 Exploring new applications	155
7.3 References	157
8. Appendix---Review.....	161
8.1 Introduction	161
8.2 Concentration Quenching.....	163
8.2.1 Emerging strategies to overcome concentration quenching.....	165
8.2.2 Recent advances in breaking the limit of concentration quenching	168
8.3 Emerging Applications Enabled by Cross-Relaxation Effect in Highly-Doped Nanoparticles ...	175
8.4 Perspective	178
8.5 References	180

List of Publications

Published papers:

- [1] **Shihui Wen**, Jiajia Zhou, Kezhi Zheng, Artur Bednarkiewicz, Xiaogang Liu, Dayong Jin, Advances in highly doped upconversion nanoparticles, *Nature Communications* (2018), **9**, 2415.
- [2] Jiajia Zhou, **Shihui Wen**, Jiayan Liao, Christian Clarke, Sherif Abbas, Wei Ren, Chao Mi, Fan Wang, Dayong Jin, Activation of surface dark-layer to enhance upconversion in a thermal field, *Nature Photonics* (2018), **12**, 154-158.
- [3] Fan Wang, **Shihui Wen**, Hao He, Baoming Wang, Zhiguang Zhou, Olga Shimoni, Dayong Jin, Microscopic inspection and tracking of single upconversion nanoparticles in living cells, *Light: Science & Applications* (2018), **7**, 18007.
- [4] Wei Ren, **Shihui Wen**, Sherif Abdulkader Tawfik, Qian P Su, Gungun Lin, Lining A Ju, Michael J Ford, Harshad Ghodke, Antoine M van Oijen, Dayong Jin, Anisotropic functionalization of upconversion nanoparticles, *Chemical Science* (2018), **9**, 4352-4358.
- [5] Chaohao Chen, Fan Wang, **Shihui Wen**, Qian Peter Su, Mike CL Wu, Yongtao Liu, Baoming Wang, Du Li, Xuchen Shan, Mehran Kianinia, Igor Aharonovich, Milos Toth, Shaun P Jackson, Peng Xi, Dayong Jin, Multi-photon near-infrared emission saturation nanoscopy using upconversion nanoparticles, *Nature Communications* (2018), **9**, 3290.
- [6] Wei Ren, Yingzhu Zhou, **Shihui Wen**, Hao He, Gungun Lin, Deming Liu, Dayong Jin, DNA-mediated Anisotropic Silica Coating of Upconversion Nanoparticles, *Chemical Communications* (2018), **54**, 7183-7186.
- [7] Yinghui Chen, Hien T. T. Duong, **Shihui Wen**, Chao Mi, Yingzhu Zhou, Olga Shimoni, Stella M. Valenzuela, Dayong Jin, Exonuclease III-Assisted Upconversion Resonance Energy Transfer in a Wash-Free Suspension DNA Assay, *Analytical Chemistry* (2018) **90**, 663-668.
- [8] Yujia Liu, Yiqing Lu, Xusan Yang, Xianlin Zheng, **Shihui Wen**, Fan Wang, Xavier Vidal, Jiangbo Zhao, Deming Liu, Zhiguang Zhou, Chenshuo Ma, Jiajia Zhou, James A. Piper, Peng Xi, Dayong Jin, Amplified stimulated emission in upconversion nanoparticles for super-resolution nanoscopy, *Nature* (2017) **543**, 229-233.
- [9] Hao He, Christopher B Howard, Yinghui Chen, **Shihui Wen**, Gungun Lin, Jiajia Zhou, Kristofer J Thurecht, Dayong Jin, Bispecific antibody-functionalized upconversion nanoprobe, *Analytical Chemistry* (2018) **90**, 3024-3029.

- [10] Deming Liu, Xiaoxue Xu, Yi Du, Xian Qin, Yuhai Zhang, Chenshuo Ma, **Shihui Wen**, Wei Ren, Ewa M. Goldys, James A. Piper, Shixue Dou, Xiaogang Liu, Dayong Jin, Three-dimensional controlled growth of monodisperse sub-50 nm heterogeneous nanocrystals, *Nature Communications* (2016) **7**, 10254.
- [11] Du Li, **Shihui Wen**, Wenjie Sun, Jiulong Zhang, Dayong Jin, Chen Peng, Mingwu Shen, and Xiangyang Shi, One-Step Loading of Gold and Gd₂O₃ Nanoparticles within PEGylated Polyethylenimine for Dual Mode Computed Tomography/Magnetic Resonance Imaging of Tumors, *ACS Applied Bio Materials* (2018) **1**, 221-225.
- [12] Chenshuo Ma, Xiaoxue Xu, Fan Wang, Zhiguang Zhou, **Shihui Wen**, Deming Liu, Jinghua Fang, Candace I. Lang, Dayong Jin, Probing the Interior Crystal Quality in the Development of More Efficient and Smaller Upconversion Nanoparticles, *The Journal of Physical Chemistry Letters* (2016) **7**, 3252-3258.
- [13] Liang Wang, Long Ren, D Mitchell, G Casillas-Garcia, Wei Ren, C Ma, XX Xu, **Shihui Wen**, F Wang, J Zhou, Xun Xu, Weichang Hao, Shi Xue Dou, Yi Du, Enhanced energy transfer in heterogeneous nanocrystals for near infrared upconversion photocurrent generation, *Nanoscale* (2017) **9**, 18661-18667.
- [14] Hien Duong, Yinghui Chen, Sherif Abdulkader Tawfik, **Shihui Wen**, Maryam Parviz, Mike J Ford, Olga Shimoni, Dayong Jin, Systematic Investigation of Functional Ligands for Colloidal Stable Upconversion Nanoparticles, *RSC Advances* (2018) **8**, 4842-4849.
- [15] Yue Cong, Bingyang Shi, Yiqing Lu, **Shihui Wen**, Roger Chung, Dayong Jin, One-step conjugation of glycyrrhetic acid to cationic polymers for high-performance gene delivery to cultured liver cell, *Scientific reports* (2016) **6**, 21891.

([1] - [10] are closely related to my PhD program)

Conferences:

- [1] **Shihui Wen**, Deming Liu, Wei Ren, Chenshuo Ma, Bingyang Shi, Xiaoxue Xu, Dayong Jin, Developing multifunctional heterogeneous upconversion nanocrystals for multimodality bioimaging and biomedicine, 6th International Nanomedicine Conference, July 6-8, 2015.
- [2] **Shihui Wen**, Deming Liu, Wei Ren, Chenshuo Ma, Xiaoxue Xu, Dayong Jin, Seed Mediated One-pot Growth of Multifunctional Heterogeneous Upconversion Nanocrystals, ICONN 2016, February 7-11, 2016.
- [3] **Shihui Wen**, Du Li, Deming Liu, Xiaoxue Xu, Yi Du, David R. G. Mitchell, Bingyang Shi, Xiangyang Shi, Dayong Jin, Seed mediated one-pot growth of versatile heterogeneous upconversion nanocrystals for multimodal bioimaging, SPIE BioPhotonics Australasia, October 17-20, 2016, pp. 1001315-1001315-7.
- [4] **Shihui Wen**, Du Li, Deming Liu, Dayong Jin, Seed Mediated One-pot Growth of Multifunctional Heterogeneous Upconversion Nanocrystals, Phosphor Safari 2016, 28 Nov - 1 Dec, 2016.
- [5] **Shihui Wen**, Du Li, Deming Liu, Dayong Jin, Develop Multi-Functional Contrast Agent for Deep Tissue In Vivo Bioimaging, 2017 MRS Spring Meeting & Exhibit, April 17-21, 2017.

ABSTRACT

With relatively large surface areas and tunable composition and morphology, nanoparticles possess unexpected properties comparing with their bulk counterparts. Controlled synthesis and fine-tuning of their composition, morphology, and surface properties are the fundamental cornerstones in nanoscience and nanotechnology towards optimized overall performance of a variety of nanoparticles discovered today.

Upconversion nanoparticles (UCNPs) are a new family of luminescent nanomaterials attracting a large amount of research interests, because these materials are capable of converting two or more lower-energy photons into one high energy photon. To date, a wide range of applications have been developed, including fluorescent microscopy, nanoscale thermometry, photodynamic therapy, optogenetics, security inks, photovoltaic converters, and 3-dimensional volumetric displays.

This thesis focuses on exploring materials science to establish new methods for fine-tuning the size, shape and composition of lanthanide doped UCNPs, and study their optical properties, in particular to integrate multiple functionalities. I demonstrate the seed-mediated controlled growth approach is very promising for on-demand production of a library of multifunctional nanocrystals. This wet-chemical approach offers high precision in controlled synthesis of homogeneous and heterogeneous nanocrystals with desirable size, shape and deposition of dopants. The outcomes of this thesis not only include a series of knowledge discovered for controlled growth of lanthanide doped nanomaterials, but also lead to a range of new applications demonstrated, such as super-resolution nanoscopy imaging, single-particle tracking, and multimodal bioimaging.

This thesis begins with a comprehensive review of the size-/shape-dependent properties and the controlled wet-chemical synthesis of nanomaterials, especially for the recently developed UCNPs, forming the introduction Chapter 1. This chapter has been further enhanced by a review article surveying the role of controlled growth and their new advances in producing highly doped UCNPs enabling new applications (published in *Nature Communications* 2018). In Chapter 2, I provide the full details of materials and methods employed in this thesis. And the following four chapters summarize the core results from 666 synthesis experiments to produce a range of homogeneous (Chapter 3), heterogeneous (Chapter 5) and single directional grown barcoded nanocrystals at arbitrary sizes (Chapter 6), as well as

a comprehensive characterization and investigation of crystal growth mechanisms (Chapter 4) that underpins these synthesis techniques.

In Chapter 3, I demonstrate the seed-mediated growth method for fabricating homogeneous nanocrystals doped with different concentrations of activator ions. While typically due to the large synthesis-to-synthesis variation, conventional methods only result in different sizes of UCNPs during different synthesis, my facile seed-mediated method achieves precise control in size (one nanometer resolution) to yield a series of monodisperse UCNPs at the same size, which enables the quantitative optical characterizations. This forms the foundation for a range of single nanocrystal measurements and evaluations of their optical properties towards a series of novel applications in nanoscopy. This work has resulted in three co-authored publications, the low-power stimulated emission depletion (STED) nanoscopy (published in *Nature* 2017), the near-infrared emission saturation (NIREs) super-resolution nanoscopy (published in *Nature Communications* 2018), and microscopic inspection and tracking of single nanocrystals in living cells (published in *Light: Science & Applications* 2018).

In Chapter 4, I systematically investigate the mechanisms and a range of potential determining factors to identify the key to the controlled growth. I discover that the reaction mix, after the core being synthesized, plays an important role in reducing the time for the successive epitaxial growth of shells in the seed-mediated growth method. I successfully fabricate the integrated heterogeneous core@shell nanocrystals with high performance in luminescence intensity. While typically due to the low stability of sub-10-nm nanocrystals in the reaction mix, it is hard to use sub-10-nm nanocrystals as the seed using conventional methods. Here using my method, I demonstrate the sub-10-nm nanocrystals as the seeds for epitaxial growth of the inert shells to yield the ultra-small core@shell nanocrystals. These bright and ultra-small core@shell UCNPs will pave the way for nanomedicine applications. This work has resulted in one first-authored research paper under submission.

In Chapter 5, I employ the heterogeneous seed-mediated growth approach to fabricate the core@shell@shell sandwich nanostructure with various sensitizer and activator doping concentrations but at the same size. These highly controlled samples enable the systematic characterizations to identify the optimum doping concentrations of both sensitizers and activators from a large dynamic range, which guarantees the same amount of active photon conversion layer between an inert core template and an inert layer of shell that isolates the surface quenchers. This allows us to directly compare and identify the

optimum combination of sensitizers (Yb^{3+}) and emitters (Tm^{3+}) as a new guideline to synthesize a range of bright and small single UCNPs, particularly optimized for different excitation conditions. With the optimized doping concentration, I have also fabricated the small and bright core@shell nanocrystals with the size comparable to that of antibodies (~ 15 nm). This work has resulted in my second first-author research work under submission.

In Chapter 6, I challenge to control the growth direction using the seed-mediated growth method. I first systematically investigate the roles of the surfactant molecule oleic acid and oleate on different facets. Through fine-tuning of the amount of surfactant molecules and the concentration of the shell precursor, I have achieved the absolute one-direction growth of UCNPs nanorods by the layer-by-layer deposition of precursor on the desired crystal facet. On-demand deposition of arbitrary kind of precursors along the longitudinal direction has resulted in a series of nanorods in the length range from 24 nm to 242 nm. Combining the heterogeneous growth approach, I demonstrate multifunctional contrast agents for multimodal bioimaging, with each functionalization being maximized and logically assembled within a single barcoded nanorod. This suggests future heterogeneous nanocrystals with integrated functions can be realized by the programmable growth of multifunctional barcode crystals with tunable size, composition, and properties. This work has resulted in a co-authored paper (published in *Nature Communications* 2016) and my third first-author research work under submission.

The conclusion and future scope part, Chapter 7, summarizes the key achievements presented in this thesis, which is around the new facile approach of the seed-mediated growth for fine-tuning the size, shape and composition of UCNPs. I have also included discussions on the potentials of using this method and knowledge developed here for UCNPs doped with other ions, and the fabrication of high-quality on-demand hybrid nanocrystals to unlock a new horizon of nanomaterials science. This, in turn, will promise a huge potential in enabling new nanotechnologies, such as super-resolution imaging, multimodal bioimaging, optogenetics, nanothermometry, photovoltaics, and laser refrigeration.

Key Words: upconversion nanocrystals, seed-mediated growth, epitaxial growth, heterogeneous structure, rare earth, lanthanides, multimode bioimaging, barcode.

List of Acronyms (in alphabetic order)

CT	Computed Tomography
EDS	Energy-Dispersive X-ray Spectroscopy
FWHM	Full-Width at Half-Maximum
MR	Magnetic Resonance
NIR	Near Infrared
NIRES	Near-Infrared Emission Saturation
OA	Oleic acid
OA ⁻	Oleate anions
OAH	Oleic acid molecular
ODE	1-octadecene
OM	Oleylamine
PDT	Photodynamic Therapy
PET	Positron Emission Tomographic
PTT	Photothermal Therapy
QDs	Quantum dots
RE	Rare Earth elements
SPECT	Single Photon Emission Computed Tomography
SPR	Surface Plasmon Resonance
STED	Stimulated Emission Depletion
STEM	Scanning Transition Electron Microscopy
TEM	Transition Electron Microscopy
TFA	Trifluoroacetate
THF	Tetrahydrofuran
UCNPs	Upconversion Nanoparticles
UV	Ultraviolet
XPS	X-ray Photoelectron Spectroscopy
XRD	X-ray Powder Diffraction

CHAPTER 1 Introduction

1.1 Nanoparticles and Nanotechnology

Nanotechnology is the “design, characterization, production and application of structures, devices, and systems by controlling the shape and size of materials at the nanoscale”. [1] Richard Feynman in his famous presentation “There’s Plenty of Room at the Bottom”, [2] described nanotechnology’s goal as the manipulation of our world at the atomic and molecular scale. This ability would allow one to tailor nanostructures with unprecedented accuracy and to tune their physico-chemical properties to precisely match the parameters required. The field of nanoscience and nanotechnology has produced various types of nanoparticles with the size normally smaller than 100 nm at least in one dimension. These functional nanoparticles have created a broad range of revolutionary impacts in the fields of electronics and photonics, [3, 4] sensing, [4-8] catalysis, [9-11] imaging, [12-14] biomedicine, [15-18] fuel cells, [19] and solar cells. [20, 21]

The size effect is the primary characteristic of nanoparticles. Since the free path of electrons in metals is around 10-100 nm at room temperature, many unique and novel properties can be observed when the size of metallic particles becomes smaller in nanoscale, compared with their bulk counterparts. [22-25] For example, gold nanoparticles (Au NPs) appear purple to red (instead of gold color) when being suspended in solution. Similarly, when the size of semiconductor materials is getting smaller down to only a few nanometers (smaller than the Bohr exciton radius), semiconductor nanoparticles exhibit a strong quantum size effect, known as quantum dots (QDs). [26-29] Because the mobile charges, either negative electrons or positive electron holes, were tightly and spatially confined in small nanocrystals, this confinement makes the crystal has discontinuous band structure. The bandgaps of these QDs can be fine-tuned simply by adjusting their size without any changes of their chemical compositions. [30, 31] Also, the huge surface (area)-to-volume ratio makes the interactions between the nanocrystal surfaces and their surrounding environments increase exponentially, which largely affect the physical and chemical properties of the nanoparticles (**Fig. 1.1**). It has been demonstrated that small Au NPs (<3 nm) are no longer unreactive but show excellent catalytic performance in various chemical reactions. [32-34]

Apart from the size effect, shape is another characteristic of nanoparticles introducing new properties and functions. [35-37] Shape control includes tailoring the proportion of various facets and atoms on a

nanocrystal's surface, and thus offers greater versatility in tuning the performance and properties of a nanocrystal. This shape-dependent effect introduces many advantages to some nanocrystals. For example, the absorbance spectrum of Au NPs is a function of its shape.[17, 38] Changing its shape can change its absorption from visible to near-infrared (NIR) region.

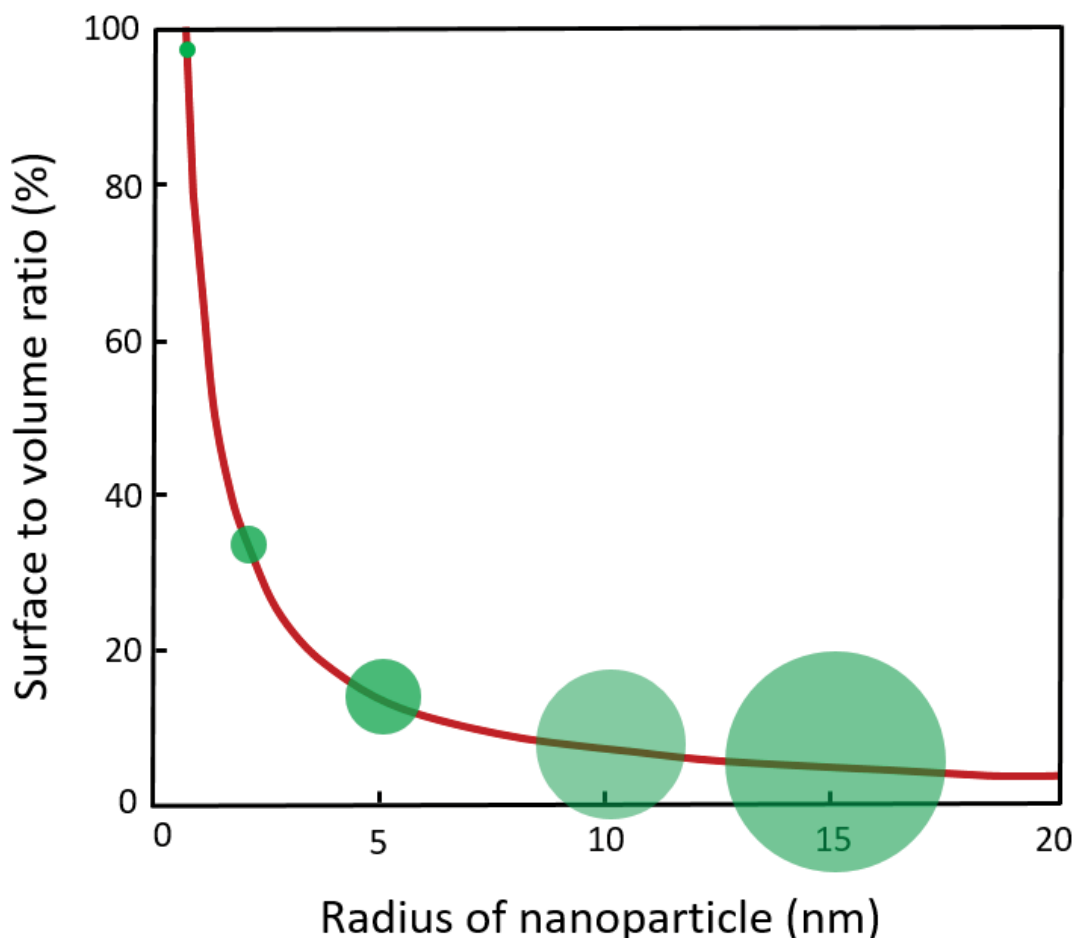


Figure 1.1 Surface to volume ratio of the nanoparticles dramatically increases when decreasing their size (radius).

Over the past three decades, nanoparticles have gained considerable attentions and emerged as a promising platform to resolve the impasses incurred in various branches of science.[5, 14, 16, 17] Numerous research works well reveal the correlation between the properties of nanocrystals with respect to their size and shape. In this section, we will briefly summarize the important role of the size and shape of nanocrystals in tuning to optimize their properties and performance.

1.1.1 Size-dependent properties.

A size-dependent effect was first reported for the optical properties of some nanomaterials. QDs serves as a good example of this. It is possible to continuously tune its fluorescent emission across the visible spectrum. It is reported that changes to a particle's emission resulted from changes to its band structure as its size changed.[26, 27, 29] Tunable QDs are employed to analyze multiple biomolecules and color displays. The color of noble metal-based colloids is fine-tuned by adjusting their size, as their absorption and light scattering properties are size-dependent.[13] As shown in **Fig. 1.2a**, Au NPs synthesized with different sizes produce different colors (from pink to brown) when suspended in a solution.[39] This feature makes them valuable for colorimetric detection. The color of a modified Au NPs indicates the concentration of an ion of interest. This reporting ability is highly selective and sensitive.[40-42]

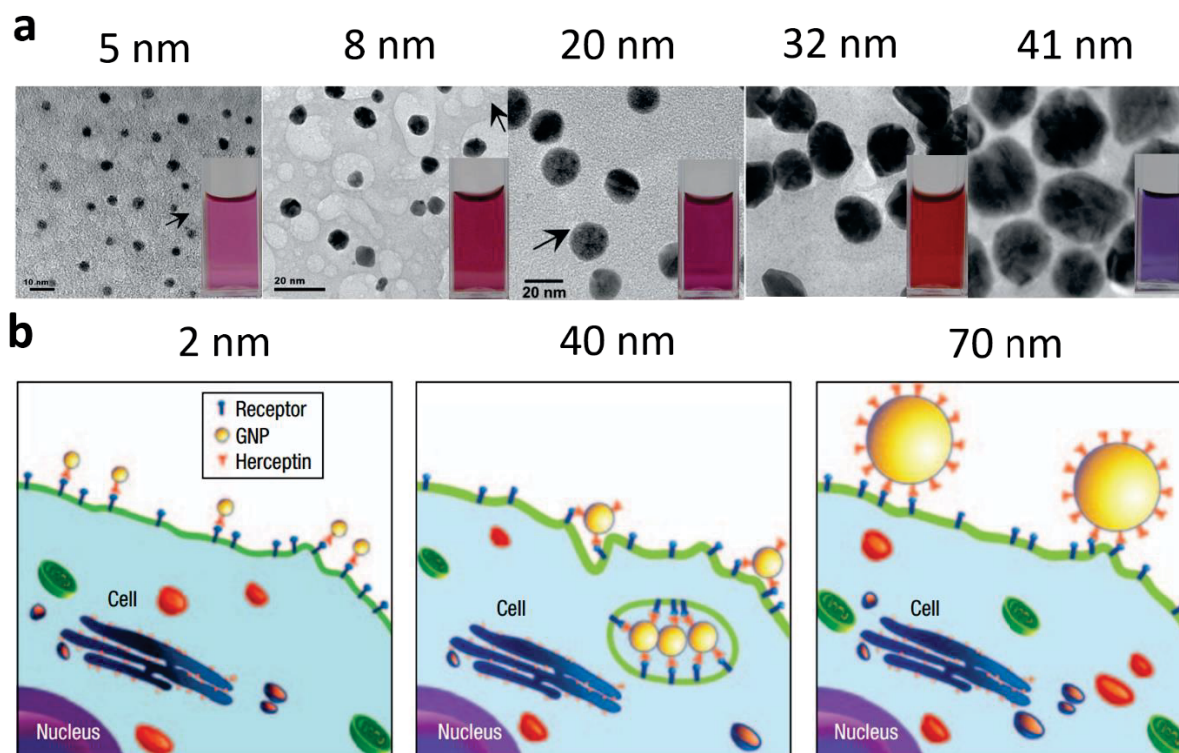


Figure 1.2 (a) Color images and corresponding transmission electron microscope (TEM) images of the Au NPs synthesized with different sizes. Adapted with permission from Ref.[39] Copyright (2012) Royal Society of Chemistry. (b) Illustrations of ErbB2 receptor localization after treatment with different-sized Herceptin-AuNPs. Reproduced with permission from Ref.[43] Copyright (2008) Macmillan Publishers Limited.

Magnetic and catalytic properties of nanoparticles are also dependent on their size. Superparamagnetism in ferromagnetic nanoparticles, for example, is seen when their diameter is less than 20

nm.[44, 45] At this size and at certain temperatures, the average zero magnetization is achieved by a random flipping direction in the particle.[45] Chen et al. showed that saturation magnetization drops significantly as particle size becomes smaller.[45] MnFe_2O_4 nanoparticles had reduced magnetism at smaller sizes due to the increased surface area of the nanocrystals. In terms of catalytic properties, it is well known that the rate of heterogeneous catalysis is strongly depends on the quantity of catalytic active sites presenting on a crystal's surface.[36, 46] Therefore, the size of the particles determines their catalytic properties, and smaller sizes lead to an increase in catalytic performance. Sau et al. reported Au NPs catalyzing the reduction of eosin in the presence of NaBH_4 . [46] The kinetics of catalytic reduction demonstrated that the catalytic rate increased with a decrease in the size of the crystals from 46 to 10 nm. This occurred even when the surface area of the different particles tested remained unchanged. Zhou et al. investigated the catalytic activity and dynamics of Au NPs in solution with single-molecule fluorescence microscopy.[47] Clear size-dependent catalytic activities were seen across many reactions. The catalysis of single Au NP at three different sizes were observed at a resolution of a single-turnover.

The size of a nanocrystal not only affects its properties, but also changes how it interacts with its surroundings. This is especially true when particles are applied in biomedicine. Nanoparticles coated with antibodies can be employed for regulating the process of membrane receptor internalization. Their binding and activation of membrane receptors and subsequent protein expression strongly depend on the size of the nanoparticles (**Fig. 1.2b**). [43] Although all Au NPs with different sizes (2 to 100 nm) changed signaling processes essential for the cell functions, 40 to 50 nm diameter nanoparticles caused the largest change. Shan et al. tested the force of endocytosing single Au NPs by HeLa cells, and they showed that both the uptake and unbinding force values were found to be size-dependent. Also, the size of Au NPs was found to affect their distribution in living cells.[48] Au NPs smaller than 10 nm in diameter were able to enter the nucleus, while larger particles (10 to 16 nm) could only access the cytoplasm. This suggests that the performance of nanocarriers is a function of their size.

1.1.2 Shape-dependent properties

While size determines the surface-to-volume ratio of a particle, shape controls the fraction of various facets and atoms on its surface. Sometimes, the shape of the nanocrystals offers greater tailorability than their size, especially when these facets and atoms on the surface possess different activities. In the same time, the relationship between the shapes of nanocrystals with respect to their performance provides a tool

to reveal their working mechanism, and in turn guides the design of more effective nanostructures. Thus, shape control has received the considerable attention in the exploration of various nanocrystals, which have already shown the dramatic impacts on their properties.

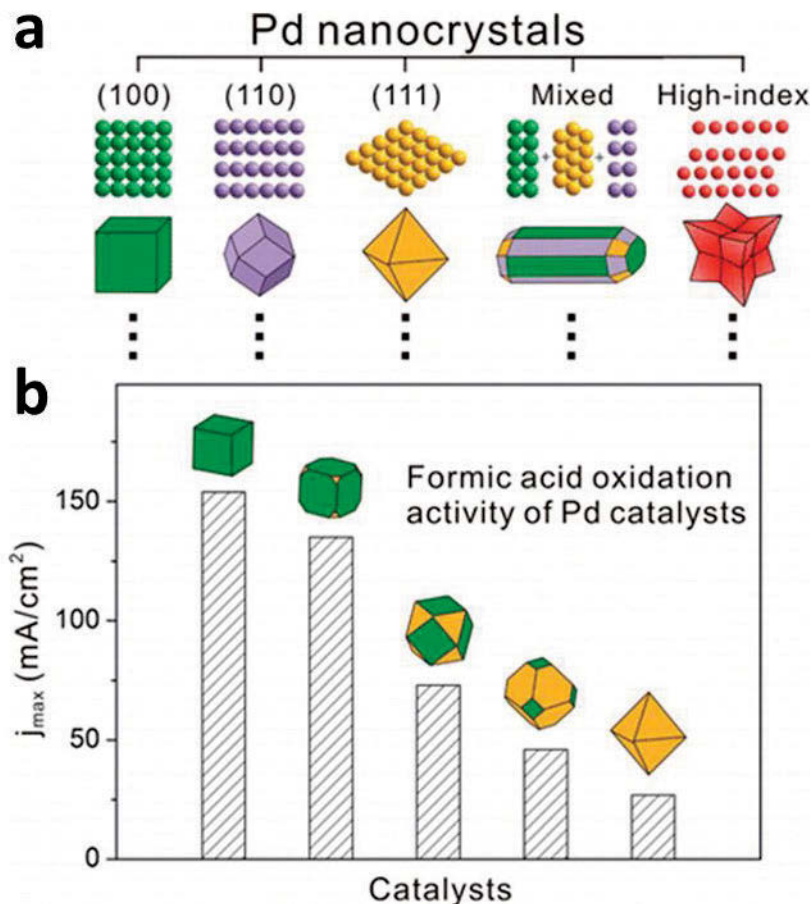


Figure 1.3 (a) Pd nanocrystals with different shapes in rich variety types of facets exposed on the surface, (b) Maximum current densities of formic acid oxidation over Pd cubes, truncated cubes, cuboctahedrons, truncated octahedrons, and octahedrons enclosed by (111) and (100) facets in different proportions. Reproduced with permission from Ref.[49] Copyright (2013) American Chemical Society.

Metal nanoparticles (such as Au and Ag) have shape-dependent tunable spectrum through the visible and NIR region.[23] This is because the shape of these nanomaterials largely affects the collective oscillation of free electrons in the nano-sized crystal, known as localized surface plasmon resonance (SPR).[24] An intense local electric field is generated at the surface of these crystals and accelerates the formation of energetic electrons. These energetic electrons, such as hot electrons and electron hole pairs, can active lattice vibrations for the heat generation. Remote light-induced nanoparticle-based heating is

applied in cancer photothermal therapy (PTT). For example, Au nanorods, as developed by Murphy and El-Sayed, are promising candidates in phototherapeutic. El-Sayed et al. first showed that Au nanorods based PTT could inhibit tumor growth after a single NIR laser exposure for 10 min.[51] Followed, Au nanorods was employed to ablate tumors in mouse colon cancer as well as squamous cell carcinoma.[52]

The catalytic activity of nanocrystals is also correlated with its facets.[49] The spatial arrangement and coordination number of atoms on its surface have a big influence. In terms of the Pd nanocrystals, their shapes can be divided into five groups according to its facet type as shown in **Fig. 1.3a**. [49] Jin et al. at 2012 described Pd nanocrystals with various shapes displaying different proportions of Pd(100) to Pd(111) facets on the surface.[50] These nanocrystals enable systematically evaluate and optimize the facet-dependent catalytic properties. As shown in **Fig. 1.3b**, five different Pd-based catalysts with various shapes display the different catalytic properties toward formic acid oxidation.[50] Current density decreases in the order of cubes, truncated cubes, cuboctahedrons, truncated octahedrons, and octahedrons. This reveals that the Pd(100) facets have a higher catalytic activity than Pd(111) facets for the oxidation of formic acid. Yet, the ideal catalyst for formic acid oxidation should also have the lowest potential, while cubes have the highest potentials among all five polyhedrons. Taken together, Pd nanocrystals with truncated cubes shape were the optimal catalyst for formic acid oxidation. [50]

The shape is also play an important role in the magnetic performance of the nanocrystals. For instance, Song et al. demonstrated that CoFe_2O_4 in a cubic form had a lower coercivity than those in a spherical form with the same volume.[53] This is because the surface anisotropy is much smaller in cubic CoFe_2O_4 than in spheres. The flat surfaces of cubic crystals have surface metal cations that are symmetrically coordinated. This is greater than that seen in the curved topology of sphere-shape CoFe_2O_4 . Therefore, the surface-shape is a dominant factor in determining the coercivity of a crystal. Also, the octapod Fe_3O_4 exhibited relatively ultrahigh r_2 relaxivity ($679.3 \pm 30 \text{ mM}^{-1}\text{s}^{-1}$) when compared to spherical crystals (around $100 \text{ mM}^{-1}\text{s}^{-1}$). This is because octapod's had a unique surface structure and a highly effective boundary radius.[54] This excellent r_2 relaxivity enables the octapod Fe_3O_4 nanocrystals to be employed for *in vivo* magnetic resonance (MR) imaging and early tumor detection. More recently, Liu et al. made Fe_3O_4 nanocrystals into spherical, triangular and cubic shapes and systematically studied the shape-dependent magnetic properties of the crystals.[55] Magnetic measurements revealed that triangular Fe_3O_4 had a blocking behavior at a high temperature, while the spherical nanocrystals only had a blocking temperature much lower than room temperature. Also, the triangular Fe_3O_4 had a higher permittivity and permeability than spheres or cube-shaped crystals.

These results demonstrate the function of crystal size and shape (the type of facets or surface structure) to their optical, catalytic, or magnetic properties. Hence, it is necessary to tune a particle's size and shape during its fabrication to tailor its properties.

1.2 Rare-Earth Nanoparticles

Rare-earth (RE) elements are composed of 15 lanthanides (from La to Lu), plus Sc and Y.[56, 57] Among them, lanthanide ions (Ln^{3+}) have unique and fascinating optical properties due to the abundant energy levels of 4f configurations.[58-60] Tunable emissions could be obtained *via* various energy transfer between different intermediate energy levels of the Ln^{3+} . The major energy levels of different lanthanides, which endow various energy transfer and emission potentials of Ln^{3+} -based luminescent materials, are shown in Fig. 1.4a.[58]

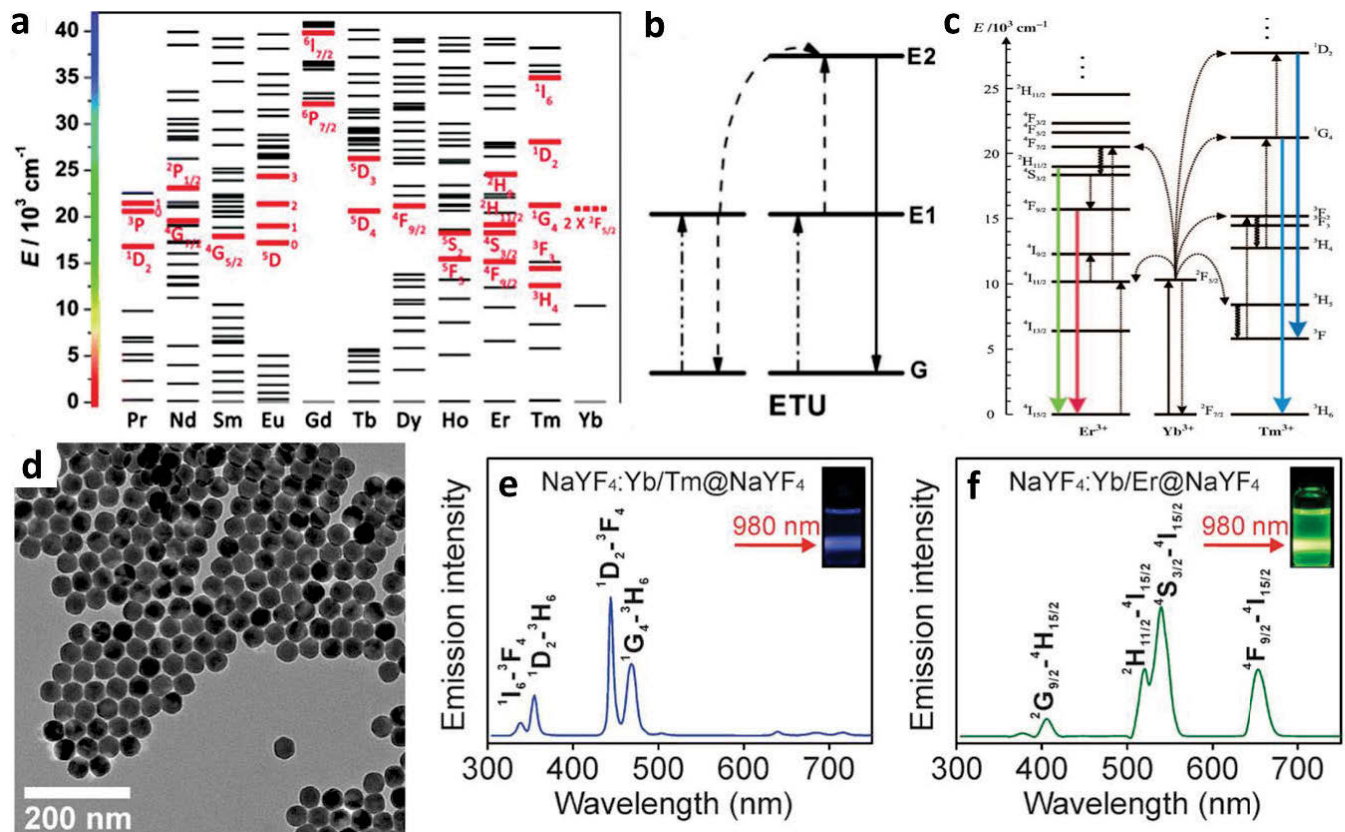


Figure 1.4 (a) Partial energy level diagrams of Ln^{3+} . Corresponding typical UC emissive excited levels are highlighted with red bold lines. Reproduced with permission from Ref.[58] Copyright (2015) Royal Society of Chemistry. (b) Schematic illustrating energy transfer upconversion modes of Ln^{3+} . Upward and downward full arrows stand for photon excitation and emission processes, respectively. (c) Energy-level diagram of photon upconversion in the typical Yb^{3+} -sensitized Er^{3+} and Tm^{3+} UCNPs. Reproduced with permission from Ref.[61] Copyright (2004) John Wiley and Sons. (d) Typical TEM image of lanthanide doped NaYF_4 nanocrystals. **e,f** Emission spectra ($\lambda_{\text{exc}} = 980 \text{ nm}$, 33.8 W cm^{-2}) of $\text{NaYF}_4:\text{Yb}/\text{Tm}@\text{NaYF}_4$ and $\text{NaYF}_4:\text{Yb}/\text{Er}@\text{NaYF}_4$ UCNPs. Insets in **(e,f)** are photographs of

UCNPs upon a 980 nm laser exposure. Reproduced with permission from Ref.[62] Copyright (2016) John Wiley and Sons.

RE-based materials display down conversion (Stokes type) and upconverting luminescence (anti-Stokes type) due to their native intra-configurational transitions.[58, 63, 64] Upconversion, known since the 1960s, refers to a non-linear optical process. It occurs by converting two or more lower-energy photons into one higher energy photon (**Fig. 1.4b**).[61] The successful integration of RE-based nanoparticles with biological analytes and for medical applications have created ongoing research interest (**Fig. 1.4c-f**).[58, 62, 65]

Upconversion nanoparticles (UCNPs) as optical imaging contrast agents can perform better than conventional organic dyes.[58, 63, 66]. (1) They minimize auto-fluorescence background emission for the improved signal-to-noise ratio (**Fig. 1.5a**).[67] (2) They can perform *in vivo* deep-tissue optical imaging due to the excitation located at NIR region which is within the optical transparency window (**Fig. 1.5b**).[62] (3) They resist photo-bleaching after illumination (**Fig. 1.5c**).[68] And (4) their emissions are narrow in the wavelength, which allows the ease of multiplexed imaging (**Fig. 1.5d**).[58] In addition, heavy Tm³⁺ doping creates a wide dynamic range of lifetimes from 25.6 μ s to 662.4 μ s in the blue emission band to produce a library of lifetime-tunable τ -dots (**Fig. 1.5e**).[69] These provided another dimension in optical multiplexing methods apart from the color tuning. These excellent properties make the UCNPs an ideal luminescent platform in biology and medicine.[18, 70]

Apart from these excellent optical imaging applications, UCNPs can also be applied as contrast agents for computed tomography (CT) and MR imaging, due to the high attenuation and magnetic properties of some lanthanide ions. For example, NaGdF₄-based T_1 MR contrast agents[71-73] and NaDyF₄- or NaHoF₄-based T_2 MR contrast agents [74, 75] were used for MR imaging. Lanthanide elements have a higher X-ray attenuation in CT imaging than the clinical used Iodine-based CT contrast agents.[76] Also, the ¹⁵³Sm emits a gamma photon with a long half-life (46.3 h) and is applied as a single photon emission computed tomography (SPECT) imaging contrast agent in clinical settings.[77, 78] Because of similar ionic radius and valence values, lanthanide cations are easily doped to a single host. Multifunctional UCNPs have hierarchically built nanostructures so that upconversion luminescence imaging can be combined with other imaging modalities such as MR,[71, 75] CT,[74, 76] SPECT,[77, 78] and positron emission tomographic (PET),[79, 80]. These can be applied to multimode imaging to get the

complementary *in vivo* information from different imaging modalities after a single administration.[74, 75, 80, 81]

Multifunctional UCNP are a promising theranostic nanoplatform for multi-modality diagnostics and targeted drug delivery.

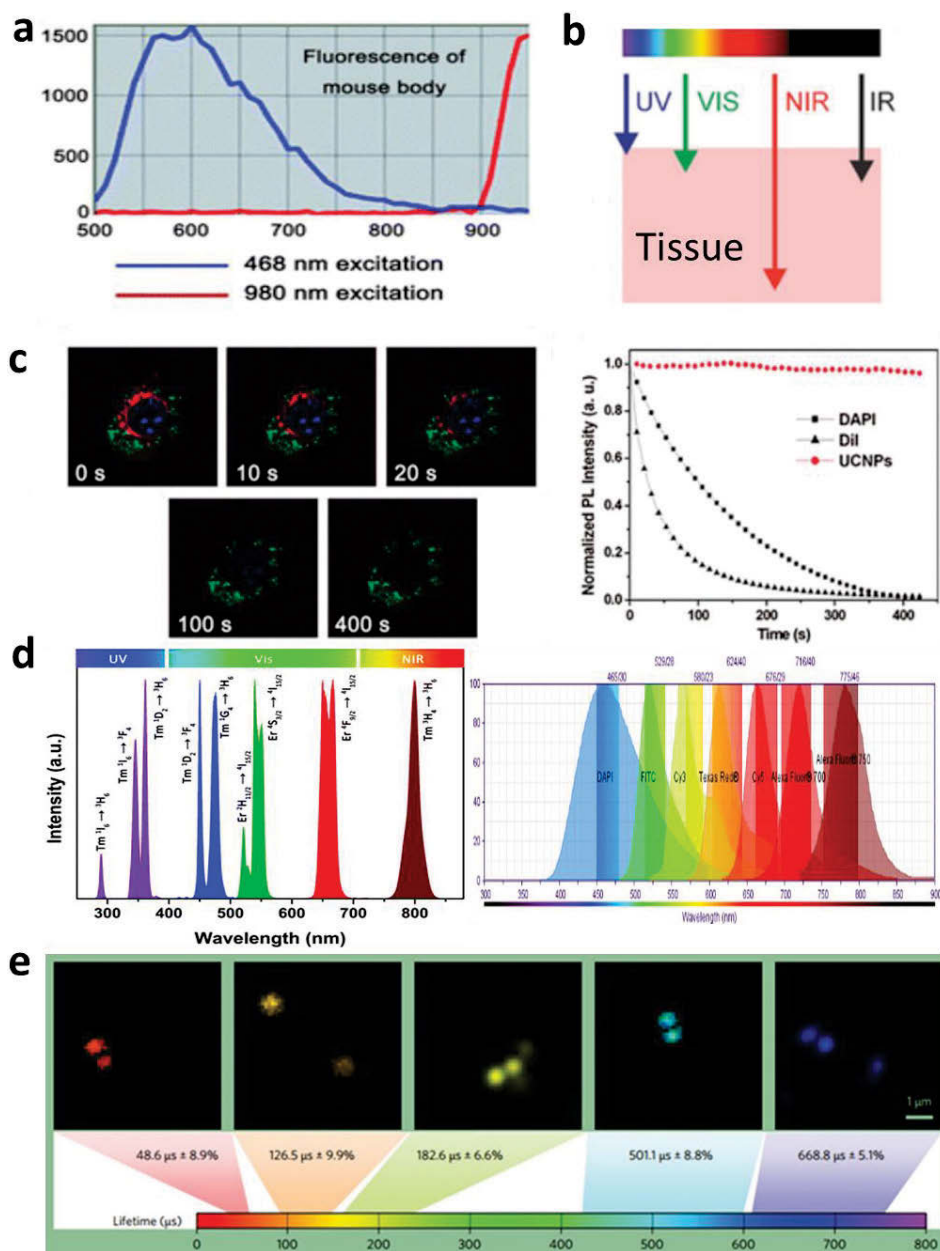


Figure 1.5 The advantages of the UCNP as the luminescent probes compared with organic dyes. (a) Under different excitation wavelength of organic dye (468 nm) and UCNP (980 nm), the auto-fluorescence back ground of the mouse body at different wavelength. Reproduced with permission from Ref.[67] Copyright (2009) Royal

Society of Chemistry. This shows the UCNP have the advantages of minimized zero the auto-fluorescence background. (b), The tissue penetration of lights with different wavelength from UV to IR. Reproduced with permission from Ref.[62] Copyright (2016) John Wiley and Sons. This shows the NIR with in the optical for transparency window have the deepest tissue penetration. Therefore, UCNP excited by NIR could be used for in vivo imaging. (c) Comparison of photobleaching of DAPI, DiL, and UCNP in conversional confocal microscopy imaging (left) and Quantitative analysis of the changes in fluorescence intensities of DAPI, DiL, and UCNP (right). The luminescence signals of DAPI, DiL, and UCNP are shown in blue, red, and green respectively. Simultaneous excitations were provided by lasers at 405, 543, and 980 nm with powers of approximately 1.6, 0.13, and 19 mW in the focal plane, respectively. Reproduced with permission from Ref.[68] Copyright (2009) American Chemical Society. From this result, compared with organic dye DAPI and DiL, Ln-UCNP have higher resistance to photo-bleaching, which is the key for long-term repetitive imaging. (d) The narrow emission bandwidths of UCNP (left) and the relatively broad emission bandwidths of organic dyes (right). Reproduced with permission from Ref.[58] Copyright (2015) Royal Society of Chemistry. The narrow emission bandwidths of UCNP allows the ease of multiplexed imaging. (e) Lifetime tuning and time-resolved confocal images of $\text{NaYF}_4:\text{Yb}^{3+},\text{Tm}^{3+}$ UCNP with increasing doping concentration of Tm^{3+} (from left to right 4%, 2%, 1%, 0.5%, and 0.2% respectively). Reproduced with permission from Ref.[69] Copyright (2014) Macmillan Publishers Limited.

1.2.1 Size-dependent properties

Different from the QDs or metal nanocrystals, the size of the UCNP does not determine its emission positions and absorption properties. But the size of the nanocrystal affects its surface to volume ratio and emission intensity.[82] Smaller UCNP have increased surface phonon activity, which quenches the luminescence emissions. In the same time, the luminescence lifetime of UCNP reduces as its size decreases, which allows lifetime-tailoring for multiplexed applications.[83]

It is notable the size of Gd^{3+} doped UCNP show significantly influences on their T_1 -relaxation performance. For example, for T_1 -enhanced MR imaging, only the outside NaGdF_4 contributed more to their achievement.[84] Nearly complete loss of relaxivity of Gd^{3+} ions occurs if they are buried within the NaGdF_4 crystal lattices (> 4 nm),[84] which indicating that Gd^{3+} should be added to the outside layer for better T_1 -enhanced MR imaging. Therefore, the smaller size of NaGdF_4 with larger surface area shows improved MRI performance by shortening T_1 relaxation time. Gd^{3+} containing nanostructures at various sizes can help work out the relationship between particle size and relaxivity. Van Veggel et al. synthesized NaGdF_4 at four sizes (2.5, 4.0, 6.5, and 8.0 nm) and analyzed their ability to affect T_1 relaxivity at 1.5

T.[85] Relaxivity values increased from 3.0 to 7.2 mM⁻¹ s⁻¹ as the particle size decreased. The relaxivity of the 2.5-nm particle was twice that of Magnevist (**Fig. 1.6a**). Similarly, Lee et al. reported the synthesis of ~1 nm Gd₂O₃ NPs with a large r_1 of 9.9 mM⁻¹ s⁻¹. [86] These results suggested that surface rather than inner Gd³⁺ ions accelerated the longitudinal relaxation of water protons. The optimal diameter of particles was about 1 to 2.5 nm for T_1 -enhanced MR imaging.

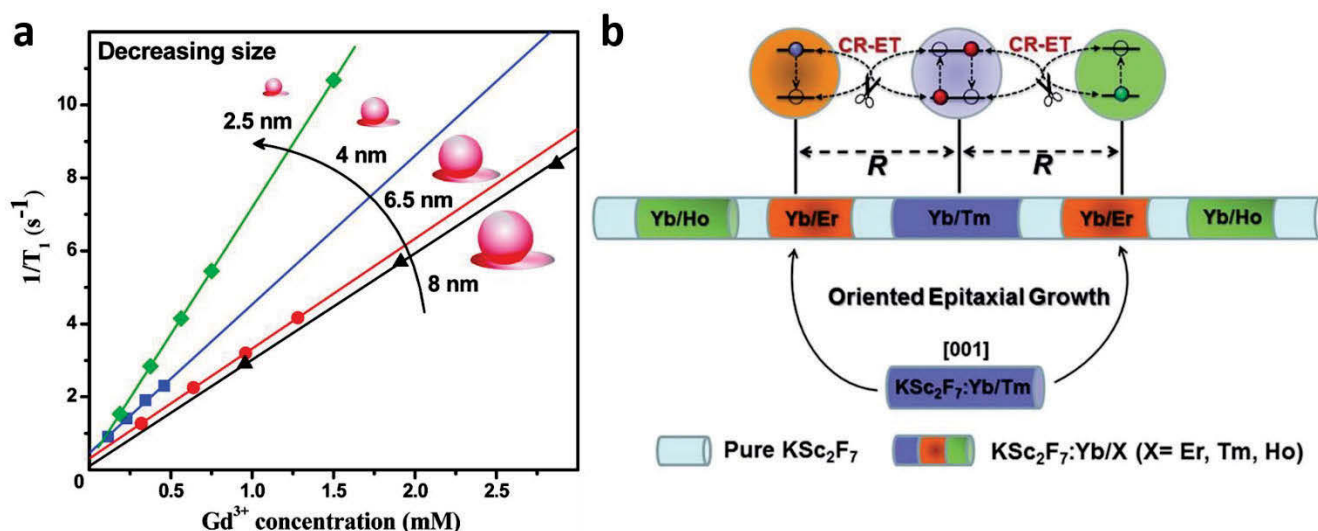


Figure 1.6 (a) T_1 relaxivity plot for NaGdF₄ nanoparticles with different sizes (2.5, 4.0, 6.5, and 8.0 nm) at 1.5 T. Reproduced with permission from Ref.[85] Copyright (2011) American Chemical Society. (b) Schematic design of a multilayer-structured KSc₂F₇ nanorod comprising different Yb/X pairs separately incorporated in layers and thickness-tunable pure KSc₂F₇ interlayers to manipulate cross-relaxation in single nanorod for highly enhanced upconversion luminescence. Reproduced from Ref.[87].

1.2.2 Shape-dependent properties

Recently reports indicated that UCNPs with different shapes have already shown their excellent properties in various scientific fields.[87-89] **Fig. 1.6b** shows an example of this illustration, in which KSc₂F₇ nanorods with multilayer-structure have been demonstrated as an ideal platform to remarkably enhance their upconversion luminescence.[87] The structures manipulate deleterious cross-relaxation among diverse emitters. This enables UCNPs to emit 70 times higher than normal ones. They exhibit a wide range of tunable upconversion emission and lifetime outputs with the flexibility of the nanostructures. This makes it possible to apply UCNPs as single-nanorod-based barcodes for multiplexing and anti-counterfeiting applications. Ding et al. reported the fabrication of NaYF₄:Yb/Er@NaGdF₄

nanoparticles with different shapes (quasi-sphere, nano-dumbbells, and nano-cubes).[88] Their results demonstrated that the anisotropy core@shell shapes have significant influence in the upconversion luminescence. More recently, Xu et al. reported the formation of Nd³⁺ sensitized NaYF₄:Yb/Er@NaNdF₄:Yb nanodumbbells for photodynamic therapy (PDT) application.[90] It is notable that the nanodumbbells could realize a more efficient PDT compared to isotropic coating multilayer UCNPs.

1.3 One-Pot Wet Chemical Synthesis

Since the size and shape are two typical parameters for tailoring the performances and properties of nanocrystals, the controlled synthesis of high-quality monodispersed nanoparticles at specific sizes and with specific shapes is essential for extended applications.[91] Their uniformity is also important and nanocrystals should have an extremely narrow size distribution ($\sigma_r \leq 5\%$). Their behavior becomes inconsistent if their sizes vary widely.

For the nanocrystal synthesis, there are two different approaches: the “top-down” method using a physical procedure, and the “bottom-up” method using wet-chemical synthesis. The “top-down” method has the advantage of the large-quantity nanocrystals synthesis, but it is difficult to achieve the high-quality nanocrystals with uniform size.[91] The “bottom-up” method produces uniform nanocrystals with controlled size and shape, and the gram quantities are produced recently with the advanced wet-chemical synthetic approaches.[56, 92] More importantly, high-quality shape controlled nanocrystals could also be achieved by simply varying the reaction conditions through the “bottom-up” method.[91]

The pioneering work of the wet-chemical synthesis was done by Faraday at 1857,[93] in which phosphorus was used as the reducing agent for gold chloride in an aqueous solution to yield the solution of colored Au NPs. Attributed to the general applicability of this synthetic approach, wet-chemical synthesis has persisted as the unparalleled method for producing uniform known nanocrystals and evaluating unexplored colloidal systems.[94, 95] Therefore, it has been the most commonly used approach for the fabrication of various kinds of nanocrystals in the literature to date.

1.3.1 Formation mechanism of nanocrystals

Understanding the mechanism by which nanocrystals are formed can provide insight into controlling their morphology.[91, 92, 96] For long history, “burst nucleation” and seed growth was considered an accurate model of crystal formation as shown in a LaMer plot (**Fig. 1.7a**).[97] As is depicted, the formation process primarily proceeds through three different stages. In stage I, the monomer concentration continually increases as precursors in the reaction mix thermally decompose. It should be noted that nucleation does not occur at this stage, even the monomer concentration is above the saturated concentration. For spontaneous self-nucleation, there is a high energy barrier. In stage II, with the further rise of the monomer concentration, the degree of super-saturation is high enough for nucleation, and in

turn resulting in the generation of stable nuclei. With the quick consumption by the nucleation and growth processes, the concentration of the monomer drops quickly until it down to the level at which nucleation is stopped. Then, the system arrives the next growth stage (stage III) without nucleation process and the existing nuclei form nanocrystals with increasingly larger size, as long as the monomer concentration is higher than the solution's supersaturation. This concentration is the reaction's equilibrium concentration, C_{∞}^{eq} .

Crystal growth can be observed by *in-situ* and *ex-situ* measurement.[98-103] Burst nucleation and crystal growth are linked, especially in stage II. But for clarity, these processes are reviewed separately.

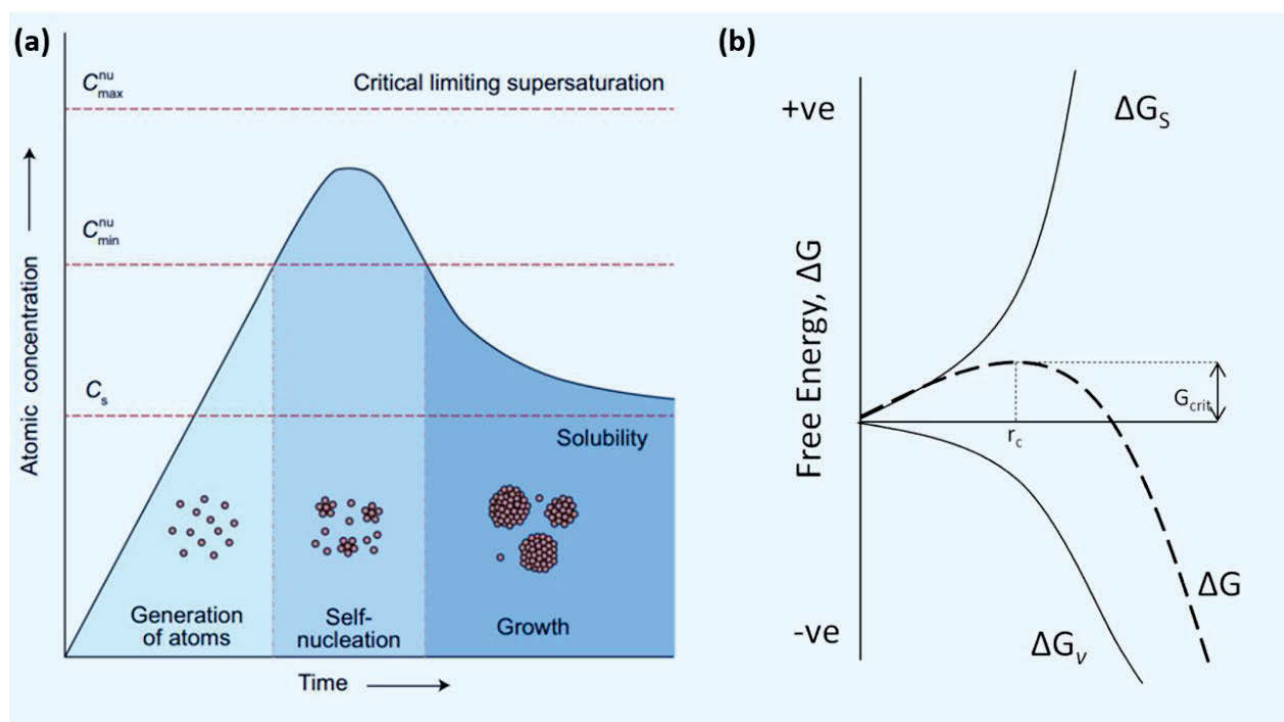


Figure 1.7 (a) LaMer model describing nucleation and growth of nanocrystals as a function of reaction time and concentration of precursor atoms. C_s represents the saturated concentration of precursor atoms in the reaction solution at the reaction conditions. C_{\min}^{nu} and C_{\max}^{nu} indicate the bottom limit (minimum) and the top limit (maximum) concentrations, respectively, that determine the range of super-saturation of precursor atoms. Reproduced with permission from Ref.[104] Copyright (2015) Oxford University Press. (b) Classical nucleation model showing the free energy diagram for nucleation. Adapted with permission from Ref.[96] Copyright (2014) American Chemical Society.

Uniform nanocrystals are prepared by inducing a single nucleation event. After initial nucleation, it is important to stop further nucleation.[96] During initial ‘burst nucleation’, many nuclei are made simultaneously when the concentration of the precursor increase above their saturation concentration for a concise period. After that, the formed nuclei start to grow without additional nucleation. Simultaneous nucleation is, in fact, very important to make sure the nearly same growth histories and obtain uniform nanoparticles. Otherwise, if nucleation process was to continue throughout the synthesis, the growth process of the nanocrystals would vary largely from one another and thus result in nanocrystals with broad size distribution.

The widely accepted theory for nucleation process is the classical nucleation theory, which was initially derived for modeling the condensation of a vapor into a liquid.[96] It was then applied to crystal formation in supersaturated solution. In 19th century, Gibbs developed a thermodynamic theory. He found that the total free energy change needed for the crystal formation can be calculated. It is the sum of the free energy change required for the phase transformation of a solution to a unit volume of the crystal and the free energy change required for the crystal’s surface formation. Spherical particles, at a particular radius and surface energy, have a total free energy calculated by **Eq. 1.1**.[91] The resulting free energy diagram for nucleation is shown in **Fig. 1.7b**. As a crystal’s radius increases, its free energy becomes negative. The thermodynamic stability of its solid-state material increases. At the same time, the formation of the solid/liquid interface increases the free energy significantly by an amount proportional to the surface of the crystal. Since the positive surface free energy dominates at relatively small radii, the total free energy change increases. Yet, as the crystal size increases, the total energy rises to a maximum at a critical size. Above this size, the total free energy drops continuously. The growth of the nucleus becomes energetically unfavorable and the crystal stops growing.[91]

$$\Delta G = 4\pi r^2 \gamma + \frac{4}{3} \pi r^3 \Delta G_v \quad 1.1$$

As ΔG_v equals to $(-RT \ln S)/V_m$, ΔG_v is negative when the solution is super-saturated. The surface term enforces an additional free energy requisite for the generation of nuclei. Nuclei smaller than the critical radius will dissolve again to reduce their total free energy ΔG . The critical radius for nuclei is its minimum size where it resists dissolution and instead becomes larger. Setting $d\Delta G/dr$ equal to zero allows the calculation of the minimum critical radius for a stable nucleus (**Eq. 1.2**). [91]

$$r_c = \frac{-2\gamma}{\Delta G_v} = \frac{2\gamma V_m}{RT \ln S} \quad 1.2$$

According to the classical growth model, the growth rate of a particle is determined by two factors. (1) The numbers of monomers reacting at the particle surface per unit time by diffusion. (2) The rates of their reaction with the particle surface. If the diffusion of monomers on the surface of the crystal limits the growth rate of a particle, the reaction is called diffusion-controlled growth. If the reaction of the monomers with the particle is slower than their transport to the surface, the reaction is called kinetically controlled growth. In 1961, Wagner et al developed an equation for calculating the growth rate of a particle (**Eq. 1.3**).[105]

$$\frac{dr}{dt} = \frac{2\gamma C_\infty^{eq} V_m^2}{RT} \frac{k_\infty D}{k_\infty r + D} \left(\frac{1}{r_{cr}} - \frac{1}{r} \right) \quad 1.3$$

However, this growth theory is only useable for large crystals. This is because the developed model is only considering the linear term of the Gibbs-Thomson equation. This approximation fails when particles are very small, such as 3 nm or less at radii.

Followed, Talapin et al. developed the modified expression for the crystals growth rate (**Eq. 1.4**).[106] It can be applied to particles of any size. The modified growth law describes the temporal evolution of the size distribution of the particles. It should be noted that particles with a radius that is too small have a negative growth rate. They dissolve and release their monomers back into the reaction solution. The value of this critical radius corresponds to the point when the growing rate is equal to zero. It can be calculated by setting **Eq. 1.4** equal to zero. The result is same with the **Eq. 1.2**, which shows that a high super-saturation results in a very small critical radius for particle dissolution. If this number is smaller than the smallest nuclei initially formed, none of them dissolve and all will over time increase in size.

$$\frac{dr}{dt} = V_m D C_\infty^{eq} \left\{ \frac{\frac{C}{C_\infty^{eq}} - \exp\left[\frac{2\gamma V_m}{rRT}\right]}{r + \frac{D}{k_\infty} \exp\left[\frac{2\gamma V_m}{rRT}\right]} \right\} \quad 1.4$$

1.3.2 One-pot wet-chemical synthesis of UCNPs

Wet chemical synthetic methods to prepare various UCNPs are well documented.[58, 65, 107, 108] The size and morphology of the nanoparticles can be well controlled through adjusting different synthetic parameters, such as temperature, reaction time, the concentration of precursors and the type of surfactants. Wet approaches include thermal decomposition, hydrothermal method, co-precipitation, microwave and microemulsion-assisted synthesis.[56] Thermal decomposition, co-precipitation, and hydrothermal methods are the most frequently reported for the preparation of high-quality tailored nanoparticles. These approaches for making UCNPs will be discussed next.

1.3.2.1 Thermal decomposition

Thermal decomposition method refers to the UCNPs synthesis through oxygen-free decomposition of the organometallic precursors at high temperature.[56, 109] RE³⁺-based trifluoroacetates are frequently used as the organometallic precursors, while octadecene (ODE) is employed as the high-boiling-point solvent. Oleic acid (OA) and oleylamine (OM) with polar groups can selectively adsorb to specific facets of the nanocrystals. Therefore, they are usually employed as polar capping reagents to control the size and shape of the formed nanocrystals. Nucleation and growth are precisely controlled by adjusting the heating rate, temperature of the reaction, or concentration of precursors in the reaction mix. Also, the nanoparticles made with this approach are monodispersed and they are uniform in their morphology and size.[109]

Yan et al. reported the first LaF₃ triangular nanoplates synthesis in 2005 through thermal decomposition of La(CF₃COO)₃ in the solvents of OA and ODE (**Fig. 1.8a**).[110] Various solvent systems were systematically assessed in their study. The application of OA or ODE alone as the solvent resulted in less uniform nanoparticles, while the use of their mixture as the solvent formed uniform LaF₃ nanoplates with triangular shape. Monodispersed lanthanide oxyfluoride nanoparticles can also be obtained *via* the thermolysis of Ln(CF₃COO)₃ in the solvent of OA and OM (**Fig. 1.8b**).[111] EuOF nanowires could also be synthesized by the decomposition of Eu(CF₃COO)₃ in OA and OM solvents.[112] Using La(CCl₃COO)₃ as organometallic precursor, high-quality LaOCl nanoplates could be made in the solvents of OM and ODE (**Fig. 1.8c**).[113]

In 2006, Yan et al. developed a universal method to synthesize NaREF₄ and Yb/Er/Tm doped NaYF₄ nanoparticles with different phases and varied shapes by the co-thermolysis of Na(CF₃COO) and RE(CF₃COO)₃ (**Fig. 1.8d-f**).[109] Monodispersed cubic KLaF₄ and KCeF₄ worm-like nanowires, KREF₄ nanopolyhedra, LiREF₄ nanoplates could be formed by the co-thermolysis of RE(CF₃COO)₃ with

$K(CF_3COO)$ or $Li(CF_3COO)$. Murray et al. also synthesized high-quality LnF_3 nanoplates [114] and $NaLnF_4$ nanoparticles [115] using the similar method. These uniform LnF_3 nanoplates exhibited subtle self-assembly behavior at the liquid-air interface (**Fig. 1.8g,h**). The shape of the $NaLnF_4$ nanocrystals could be well controlled, including plates, rods, spheres, and hexagonal prisms.

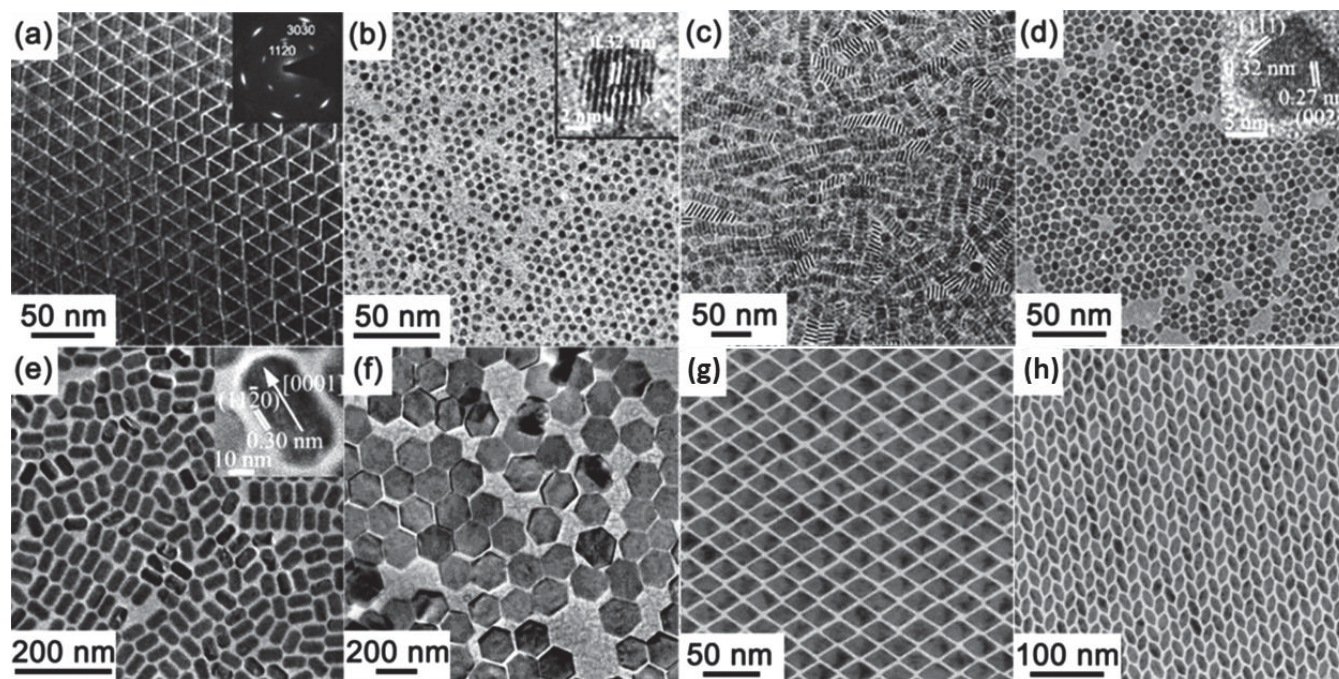


Figure 1.8 TEM images of LaF_3 (a), $LaOF:Eu$ (b), $LaOCl$ (c), cubic phased $NaYF_4$ (d), hexagonal phased $NaYF_4$ (e), hexagonal phased $NaYF_4:Yb,Er$ (f), DyF_3 (g), and TbF_3 (h) nanoparticles synthesized from thermal decomposition. Adapted with permission from Ref.[59] Copyright (2015) American Chemical Society.

A limitation of using trifluoroacetate precursors is their toxicity. Toxic fluorinated and oxyfluorinated carbon species that are formed from their decomposition include carbonyl difluoride, trifluoroacetic, tetrafluoroethylene, and trifluoroacetyl fluoride.[109, 115] Trifluoroacetate derivatives are thus not environmentally-friendly. The identification of less toxic precursors is a desirable goal.

1.3.2.2 Hydrothermal synthesis

Hydrothermal synthesis is where nanoparticles are made with superheated solvents in high-pressure autoclaves. Reactants have enhanced solubility and reactivity under high temperature and pressure. Particles made this way have high crystallinity. $RECl_3$, $RE(NO_3)_3$, and $RE(Ac)_3$ are frequently employed as the precursors for hydrothermal reactions.

Li et al. reported a liquid-solid solution-based hydrothermal synthesis approach toward inorganic nanoparticles.[116] This method is based on a phase transfer and separation mechanism at the liquid/solid/solution interfaces. Wang et al. successfully synthesized high-quality lanthanide-doped NaYF₄ nanorods, nanoplates, and nanospheres using this approach.[117] They found that the size and shape of the nanocrystals could be well controlled by modulating the reaction temperature, duration time, and the molar ratio of different precursors. For example, a high NaF/Ln(NO₃)₃ ratio and relatively long reaction time favored the formation of nanocrystals with sphere-like shape. Also the aspect ratio of lanthanides doped Na(Y_{1.5}Na_{0.5})F₆ nanorods could be controlled by adjusting the reaction temperature.[118] Liu et al. systematically studied the phase and size control of NaYF₄ nanocrystals through doping of different lanthanide ions in a hydrothermal reaction.[119] Their results reveal that the size of nanorods reduced with increases in the doping concentration of Gd³⁺ and the phase structure of the yield changed from cubic to hexagonal as its doping concentration increased. Elsewhere, Zhao et al. developed a modified hydrothermal method to synthesize nanoarrays of tubes and rods of lanthanide-doped NaYF₄. [120]

CeO₂ nanocrystals with different shapes (including nanopolyhedra, nanocubes, and nanorods) was also reported by Yan et al. through adjusting NaOH concentrations in a hydrothermal approach. Ce(NO₃)₃ was employed as the cerium source to studied the formation process.[121] The authors found that the concentration of NaOH is important for the transformation from hexagonal Ce(OH)₃ intermediates into CeO₂, and in turn controlling the morphology of the crystals produced. Kaneko et al. reported decanoic acid could be used to induce anisotropic growth of the CeO₂ nanocrystals using Ce(NO₃)₃ as the cerium source.[122] Qian et al. developed an improved hydrothermal method for CeO₂ nanoparticles. They applied CeCl₃ as the cerium source and hexadecylamine as the organic surfactant.[123] The concentration of hexadecylamine, the type of amine, and water proportion were important in determining nanoparticle morphology. Yan et al. made lanthanide-doped CeO₂ nanowires in a hydrothermal synthesis using CeCl₃ as the cerium source.[124] It is found that adding small amounts of NaCl made uniform and anisotropic Ce(OH)₃ intermediate crystals.

The hydrothermal approach has some limitations. Because sealed pressure vessels are employed, the reaction process is difficult to measure, understand and control. Typically, a small amount of product is produced. Easier access to the reaction would lead to understanding it better. Hence, other approaches can sometimes be desirable.

1.3.2.3 Co-precipitation synthesis

The simultaneous precipitation, or co-precipitation of several ions, can form nano-sized particles.[56, 125] However, differences in ion precipitation rates can lead to poor results. Coordinating surfactants and/or co-solvents added to the reaction system can reduce these differences. The co-precipitation method can take advantage of aqueous or organic solvents. The crystallinity of particles formed can be low when an aqueous solvent is used with the low reaction temperatures. As such, only co-precipitation in organic solvents will be discussed next.

For typical co-precipitation process, RECl_3 , RE(OA)_3 , or RE(Ac)_3 provide RE^{3+} cations, while NaF , NaOH , or NH_4F is applied to provide F^- anions and Na^+ cations. In 2008, Zhang et al. developed the facile co-precipitation method for the synthesis of high-quality $\beta\text{-NaYF}_4\text{:Yb,Er/Tm}$ nanoparticles in the solvent of OA and ODE (**Fig. 1.9**).[126-128] This approach is similar to a thermal decomposition method: (1) they operate in an anhydrous, oxygen-free environment, and (2) they employ OA and ODE as a solvent and a surfactant. But this co-precipitation synthesis have two steps, which is different from the one-step thermal decomposition process. The first step occurs at room temperature. Nucleation is started by slowly adding a methanol solution with NaOH and NH_4F to a homogeneous solution of RE(OA)_3 , OA, and ODE. For the second step, methanol is evaporated at 150 °C and particle growth can be initiated at elevated temperature (around 300 °C). This approach has several advantages. (1) Nucleation and growth of the nanocrystals are separated, which is favored to form monodispersed nanoparticles.[91] By adjusting the temperature, nucleation and growth can be tuned. (2) Large amounts of fluorides (NaF , NH_4F , NH_4HF_2 , CF_3COOH , and so on.) are not required. Stoichiometric amounts of NH_4F are consumed completely. The decomposition of fluoride reactants and the generation of fluorinate species such as the HF gas are minimized. (3) Reaction precursors can be simple inorganic salts. Zhang et al. and Qin et al. independently tested what affected morphology and size of the NaYF_4 nanoparticles.[125, 129] They found that reaction temperature, duration time, and the amount of OA are important to control the size and morphology of the formed nanocrystals. Different kind of sodium lanthanide fluoride nanomaterials, including NaGdF_4 , NaLuF_4 , NaDyF_4 , and NaYbF_4 nanoparticles, were successfully synthesized using this method.[130-133] Followed, Hyeon et al. synthesized $\text{NaYF}_4\text{:Yb,Er}$, and $\text{NaYF}_4\text{:Yb,Er@NaGdF}_4$ nanoparticles using RE(OA)_3 instead of RECl_3 as the precursor.[134, 135] Liu and van Veggel groups also tested RE(Ac)_3 as the RE precursor.[136-141] They ascertained that RE(OA)_3 was firstly formed by the reaction of RE(Ac)_3 and OA after heating $\text{RE(Ac)}_3\text{-OA-ODE}$ solution to 140 °C under vacuum. The *in situ* formed RE(OA)_3 acted as an intermediate for making monodisperse UCNPs.

Chen et al. applied Ln^{3+} -based oleates and NaF in OA and ODE solvent to make NaGdF_4 nanoparticles.[142] Running the reaction at a high temperature made hexagonal phased NaGdF_4 nanoparticles, while reacting at a low temperature and using OM as a solvent favored cubic phase nanoparticles. NaYF_4 nanoparticles could be synthesized the same way.[143] The morphology of the nanoparticles depended upon the lanthanide ions used in the reaction. For example, hexagonal LnF_3 nanoplates could be formed if the lanthanide ions are La-Pr. For Sm-Er and Tm-Lu, hexagonal NaLnF_4 and cubic $\text{Na}_5\text{Ln}_9\text{F}_{32}$ particles are favored, respectively.[144] Also, it is shown that the morphology of the LaF_3 could be changed from nanorods to polyhedron particles by adjusting the reaction mix.[145] Huang et al. made lanthanide-doped $\text{Na}_x\text{ScF}_{3+x}$ -based nanoparticles using various RECl_3 , NaOH, and NH_4F in the solvent of OA and ODE.[146] They revealed that the phase, morphology and the composition of $\text{Na}_x\text{ScF}_{3+x}$ can be well controlled by the molar ratio of the OA/ODE in the reaction mix. Zhu et al. synthesized orthorhombic $\text{KSc}_2\text{F}_7:\text{Yb,Er}$ nanorods using KOH instead of NaOH.[147] They found the size of the nanorods can be adjusted by the F^- concentration and reaction temperature. Larger sized $\text{KSc}_2\text{F}_7:\text{Yb,Er}$ nanorods is favored at high concentration of F^- and high reaction temperature.

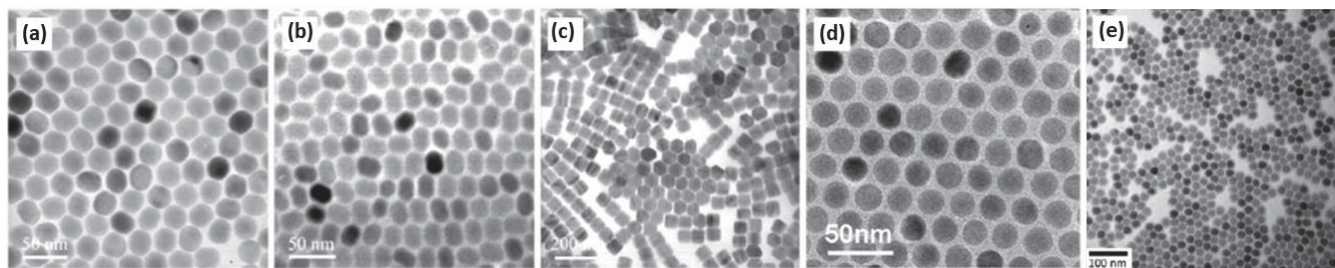


Figure 1.9 (a-c) TEM images of $\text{NaYF}_4:\text{Yb,Er}$ nanospheres, nanoellipses, and nanoplates. (d) TEM image of monodisperse $\text{NaYF}_4:\text{Yb,Tm}$ nanocrystals. (e) TEM image of $\text{NaYF}_4:\text{Yb,Tm}$ nanocrystals. Adapted with permission from Ref.[56] Copyright (2014) American Chemical Society.

1.3.3 One-pot size control of UCNPs

The size of the nanoparticles made depends upon two factors: the number of nuclei formed and their rate of growth into crystals. These factors are influenced by the reaction temperature, the precursor concentration, and the amount and types of surfactants employed. Next, techniques for controlling the size and shape of UCNPs using thermal decomposition and co-precipitation are described.

Temperature is an important determinate of nuclei formation and crystal growth. Yan's group investigated nucleation and growth of $\beta\text{-NaYF}_4$ nanocrystals using thermal decomposition.[148]

NaYF₄:Yb,Er nanocrystals at various sizes (20 to 300 nm) were controlled by adjusting the reaction temperature between 300 and 330 °C. Adjustments to the temperature can affect the Ostwald-ripening of the crystals. But this approach could not precisely control nanocrystal size and generate a highly monodispersity nanoparticles due to the largely increased reaction rate at relatively high temperature. Song's group tested the relationship between reaction temperature and NaLuF₄ crystal size. Nanocrystals from 17 to 246 nm were made at temperatures of 300 to 320 °C.[149] Huang et al. changed the size of NaYF₄ NPs by changing the initial and final temperature of the reaction.[150] An initial temperature of 25, 40, 50, and 60 °C made 25×35 nm rods, 40 nm nanospheres, 66×48 nm nanoplates, and 90×72 nm nanoplate crystals, respectively.

Gao's group adjusted the concentration of F⁻ and Na⁺ source while the concentration of RE³⁺ was kept the same.[151] The size of the NaGdF₄:Yb,Er nanocrystals increased from 14.6 to 24.6 and 36.7 nm when the F⁻/Ln³⁺ ratio decreased from 4:1 (the stoichiometric ratio) to 3.2:1 and 2.4:1, respectively. Unfortunately, a high concentration of F⁻ (F⁻/Ln³⁺ ratio of 8:1) led to polydispersed NaGdF₄:Yb,Er nanoparticles with diameters ranged from 8 to 25 nm. This indicated that repeated nucleation appears to have taken place as the prepared F⁻/Ln³⁺ ratio is increased. Increasing the Na⁺/Ln³⁺ ratio favors the formation of monodispersed NaGdF₄:Yb,Er nanospheres. Decreasing the Na⁺/Ln³⁺ ratio led to bigger sized NaGdF₄:Yb,Er particles. It also changed their shape from spheres to sheets.[151]

Apart from regulating nanocrystal growth, surfactants can tailor crystal size.[152, 153] Liu et al. fine-tuned NaYF₄ nanocrystals from 50 to 30 nm diameter by adjusting the amount of OA surfactant added.[154] A high concentration of OA led to a high concentration absorbed onto the surface of growing nanocrystals, as RE³⁺ ions were coordinated with the carboxylic groups. Its effect was to delay the rate of crystal growth, and in turn reduce the size of the nanocrystals. The surfactant type also plays an important role. Cohen's group tested OM with OA. They made monodispersed sub-10 nm NaREF₄ nanocrystals.[155, 156] By adjusting the ratio of these two surfactants, their size could be adjusted from 4.5 to 15 nm.

Even one-pot synthesis could be used to change the size of the UCNPs by adjusting the reaction conditions, it is impossible to fine-tuning the size of the formed nanocrystals to get the desired products. Also, the repeatability is big issue for the size-controlling.

1.3.4 One-pot shape control of UCNPs

While nucleation rate could be used to control the size of nanocrystals, the growth rate for each facet on a particle could be employed to adjust the shape of the nanocrystals. Next, techniques for controlling facet shape of UCNPs *via* hydrothermal treatment is introduced.

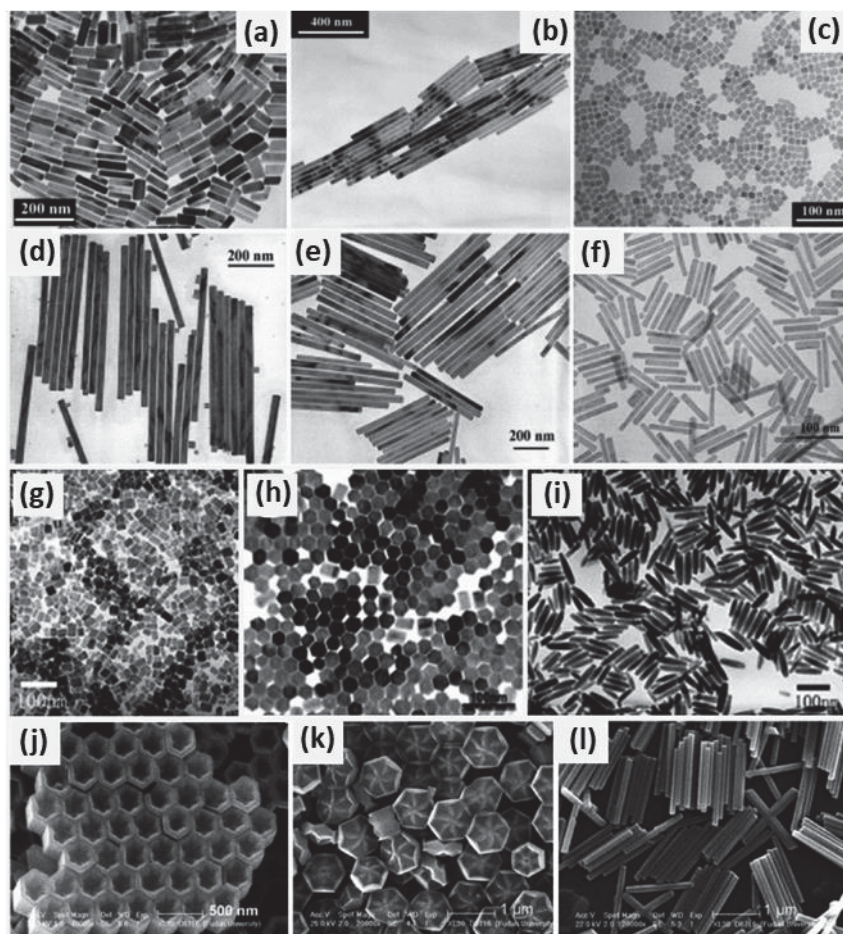


Figure 1.10. (a-c) Effect of reaction temperature and time on the shape of NaYF₄:Yb,Er nanocrystals: (a) 210 °C, 20 h; (b) 180 °C, 20 h; and (c) 180 °C, 8 h. (d-f) TEM images of NaYF₄:Eu nanocrystals used to investigate the effect of doped Eu³⁺ concentrations: (d) 5 mol %, (e) 28.6 mol %, and (f) 71.4 mol %. (g-i) TEM images of YPO₄·xH₂O nanocrystals obtained by altering the reactant concentrations: (j) PO₄³⁻/Y³⁺ = 1; (h) PO₄³⁻/Y³⁺ = 1, doubled OA and NaOH; and (i) PO₄³⁻/Y³⁺ = 1.5, doubled OA and NaOH. (j-l) SEM images of arrays of hexagonal nanotubes (j), flower-patterned hexagonal disks (k), and hexagonal nanorods (l) of β-NaYF₄ samples. Adapted with permission from Ref.[56] Copyright (2014) American Chemical Society.

Li et al. synthesized a series of UCNPs with different shapes and crystal structures using a hydrothermal method. These included NaREF₄, REF₃, LnPO₄, Eu doped YBO₃, LaVO₄, NaLa(MoO₄)₂, and Yb/Er doped BaY₂F₈. [116-118, 157-165]. The effect of the different reaction on morphology and crystal phase purity of the nanocrystals was systematically studied. A lower temperature increased the length-to-diameter ratio of NaYF₄:Yb,Er nanorods, while a short reaction time made nanospheres (**Fig. 1.10a-c**). Also, REPO₄·xH₂O nanoparticles with different shapes (including rod, rectangle, and hexagon-like shape) could be synthesized through a modified hydrothermal route using NaH₂PO₄ as the precursor. [157, 166, 167] For example, YPO₄·xH₂O crystals with a cube, plate or rod-like shape are shown in **Fig. 1.10g-i**. Detailed studies shown that these shape could be well controlled by adjusting the concentration of OA and NaOH or modulating the PO₄³⁻/Y³⁺ ions ratio in the reaction mix. OA with polar capping groups can selectively adsorb to specific facets of the YPO₄·xH₂O crystals. Therefore, the increase in OA will induce the different crystallographic growth and change the growth direction of the nanocrystals. Also, relatively higher concentration of PO₄³⁻ will increased the monomer concentration and reaction rate, which will benefit the formation of one-dimensional nanocrystals. Liu et al. reported the formation of a series of NaYF₄ nanoparticles doped with different lanthanide ions. They found that the doping concentrations of Ln³⁺ ions could be used to well control the sizes, the phases, and the upconversion emission colors (green to blue) of the particles produced. [119] Zhao et al. also extended the hydrothermal method to synthesize both α-NaREF₄ nanoparticles and β-NaREF₄ nanoarrays with different shapes, including hexagonal nanotubes (**Fig. 1.10j**), flower-patterned hexagonal disks (**Fig. 1.10k**), and hexagonal nanorods (**Fig. 1.10l**). [120, 168]

Even the hydrothermal method could be used to change the shape of the UCNPs, it is impossible to fine-tuning the shape of the formed nanocrystals. Also, only large particles with a broad distribution of size (several hundred nanometers) are formed in a hydrothermal reaction, which largely limits their further applications.

1.3.5 Brief conclusion

Colloidal nanocrystals are frequently made by applying a one-pot method. In these reactions, homogeneous nucleation and growth occur simultaneously, which is not favored to get the uniform nanocrystals with tailored size and shape. For example, selected surfactant could be used to adjust the growth rate of different facets to form the nanocrystals with various shapes, but the added surfactant could affect the nucleation process in the same time. Nanocrystals have polydispersed size could be formed with

this selected surfactant. Therefore, the optimization of nucleation and growth may substantially differ. A diversity of crystallinity and various internal structure can occur when changing the reaction conditions.

These limitations can be overcome if the crystal's nucleation and growth processes are separated. Seed-mediated growth can circumvent heterogeneous nucleation. It works by depositing atoms directly onto preformed homogenous seeds that have well-defined structures.[169, 170]

1.4 Seed-Mediated Growth

The one-pot synthesis approach has the disadvantage of nucleation and growth occurring simultaneously. It creates crystals that are polydispersed in size and shape.[91, 96] In contrast, a seed-mediated growth method separates the process of nucleation and growth. Premade nanocrystals are added as seed nuclei to the reaction mix.[169, 170] These act as templates for crystal growth and suppress the formation of additional nuclei. Monomers added to the reaction mix precipitate to seed surfaces. Their concentration is kept low to suppress further nucleation. For each step, conditions can be optimized to control over facile size and shape of the crystals. Tailored homogeneous nanocrystals can be made. A combination of capping agents and reduction kinetics can also be added to the reaction mix. Many new particles can become feasible to make, which extends their further applications.

A seed-mediated method for making nanocrystals is illustrated in **Fig. 1.11a**. In the growth process, a seed acts as a template for the atom deposition. They can be applied with their original reaction solvent or in a new solvent. Reaction conditions could be adjusted to transform the seeds into crystals that have finely-tuned compositions, sizes, shapes, and structures. A multitude of nanocrystals can be made from a single seed type. The approach offers a system for modeling the mechanisms involved in the atomistic deposition of monomers on the surface of the seeds. “Seed-mediated growth” is often mentioned in the literature and frequently applied in colloidal chemistry. Murphy et al. made Au nanorods using seeds based on Au colloidal particles.[171, 172]. They demonstrated that this approach was practical to well control the size of the nanoparticles from 4 to 50 nm.[173] Since their reports, seed-mediated growth techniques have advanced. Control over the placement of single molecules onto crystals is now practical.[174]

The seed-mediated technique can be applied two ways (**Fig. 1.11b**). Firstly, it can be used for the isotropic growth of particles. In this approach, epitaxial growth occurs in 3-dimensions (forming nanospheres or nanocubes). Secondly, it can be used for the anisotropic growth of particles. In this approach, epitaxial growth occurs in 2-dimensions (forming nanoplates) or in 1-dimension (forming nanowires, nanorods, or nanodumbbells). Both approaches can make homogeneous and heterogeneous nanostructures. The use of seed-mediated growth to precisely control nanocrystal formation was reported extensively elsewhere.

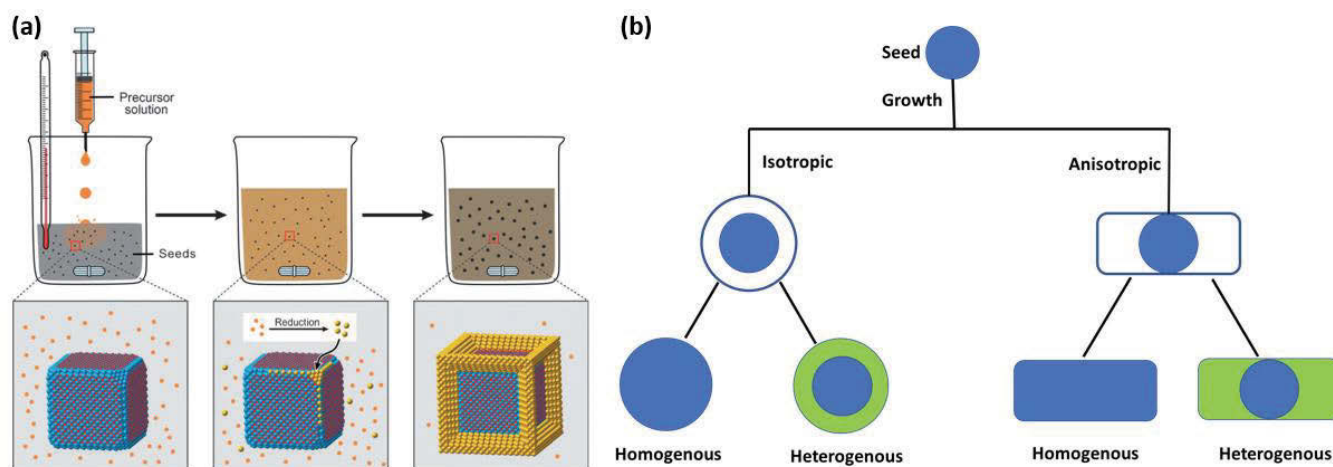


Figure 1.11 (a) General strategy used for the seed-mediated growth of nanocrystals. A precursor solution is injected into the mixture of seeds, reductant, capping agent, and colloidal stabilizer. The precursor heterogeneously nucleates on the surface of the seeds. Continued growth of the seeds, through one of the many possible pathways, results in the formation of well-defined nanocrystals. Reproduced with permission from Ref.[169] Copyright (2017) John Wiley and Sons. (b) Seed-mediated growth divided into two categories: isotropic growth and anisotropic growth, in anisotropic growth we only chose nanorods as an example to represent nanowires or nanodumbbells. Both isotropic and anisotropic growth could be used for the synthesis of homogenous or heterogeneous particles.

1.4.1 Isotropic growth

Isotropic growth is a 3-dimensional process when a particle expands epitaxially without directional control. In this case, spherical crystals can be obtained with two types of different nanostructures: homogenous structure or heterogeneous core@shell structure. With homogenous growth, the size of the seed nanocrystal become bigger. With heterogeneous growth, the seed is covered by various multifunctional shell materials as coatings.

1.4.1.1 Homogenous structure

Nanocrystal size could be well controlled with seed-mediated growth approach, as various ratios of precursor to seed materials can be applied. Also, the growth process could be further adjusted using different types of the precursors, selected surfactant, duration time, and the reaction temperature. The growth reaction can occur thermodynamically or kinetically.[175] This approach will be helpful to obtain nanocrystals with different sizes to study the size-dependent properties.

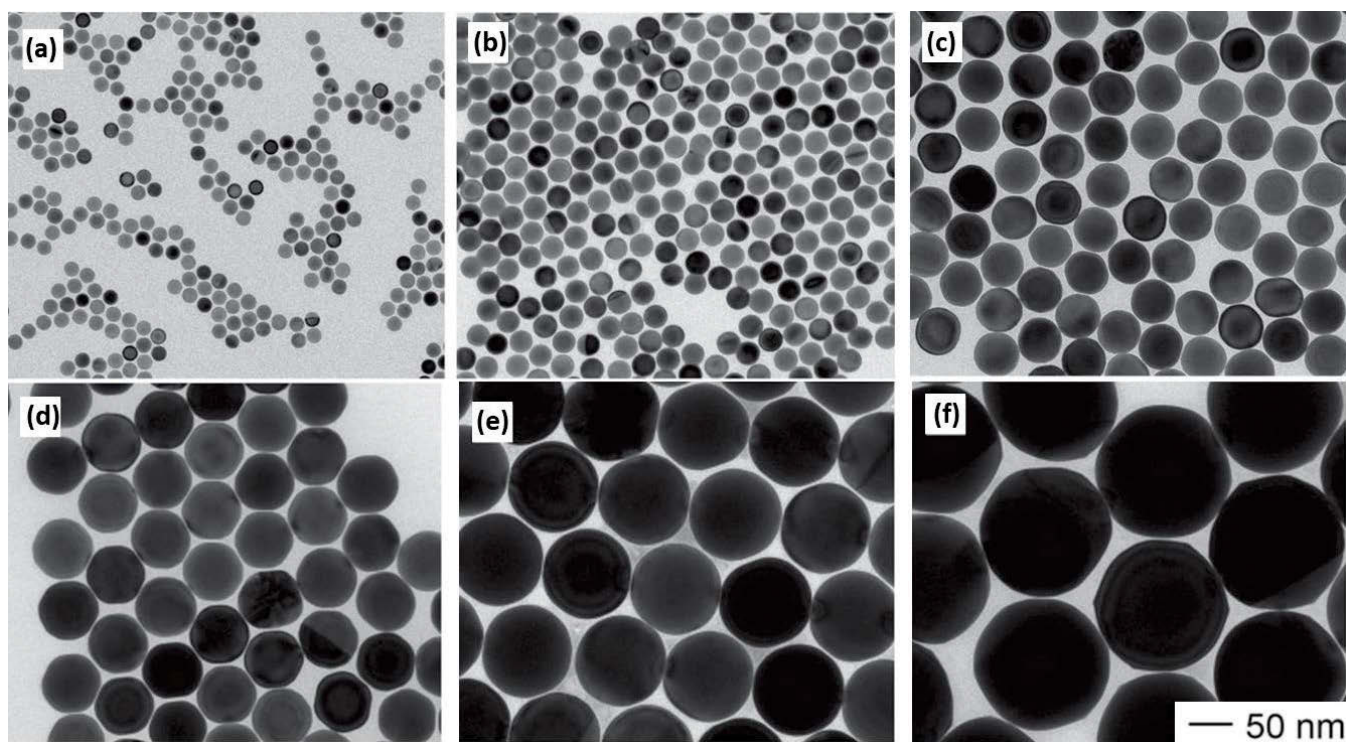


Figure 1.12 (a-c) TEM images of single-crystal Au nanospheres with controlled diameters in the range of 15–46 nm: **(a)** 15 nm; **(b)** 23 nm; and **(c)** 46 nm. They were obtained using the standard dropwise injection procedure, except that the volumes of the 10-nm seed solution were: **(a)** 300 μL ; **(b)** 100 μL ; and **(d)** 10 μL , respectively. **(d-f)** TEM images of single-crystal Au nanospheres with controlled diameters in the range of 70–150 nm: **(d)** 70 nm; **(e)** 100 nm; and **(f)** 150 nm. They were obtained using the standard dropwise injection procedure, except that the volumes of the 46-nm seed solution were: **(a)** 1500 μL ; **(b)** 500 μL ; and **(d)** 50 μL , respectively. Reproduced with permission from Ref.[176] Copyright (2014) John Wiley and Sons.

The usefulness of Au nanocrystals is their size dependent properties. Crystals need to be small enough to cross through biological systems to their target. Their properties also need to match their application. In one report, seed-mediated growth made uniform Au nanospheres with a diameter of 5 to 150 nm.[176] Small Au nanospheres were firstly made at room temperature as the seeds. Then, these Au seeds were mixed with an aqueous solution of HAuCl_4 , cetyltrimethylammonium chloride, and ascorbic acid for the further growth. **Fig. 1.12 a-c** shows these nanospheres with a 15, 23, and 46 nm diameters. These different sizes were made by adjusting the number of smaller-sized seeds (10 nm) added. When larger Au nanospheres were added as seeds, as bigger as 150 nm spheres were made (**Fig. 1.12d-f**). Various sizes can then be used to test the relationship between a particle's diameter and its performance in biomedical field.[177, 178] Unlike polycrystalline quasi-spherical particles reported elsewhere, these nanoparticles

with single-crystal structure was truly spherical in shape. Reaction surface diffusion was a factor in making highly spherical particles from seeds. A slow deposition rate for the atoms via dropwise adding of Au precursor was used for the formation of the highly uniform nanoparticles. A reductant at a low concentration was also employed. Atoms added to the seeds could diffuse across their surface uniformly, which led to the formation of a spherical shaped nanoparticles. [176]

Spherical single-crystal Ag seeds were also used to make larger Ag nanocubes with the edge lengths of 30 to 200 nm.[179] The size of the particle was adjusted by changing the amount of AgNO_3 in the reaction system. It was important to have polyvinylpyrrolidone at a sufficient concentration to passivate the Ag(100) facets. This is how the cubic shape was maintained during its growth. With adequate reductant, the number of newly deposited Ag atoms and the growth rate of the nanocubes depended upon the amount of AgNO_3 precursors. Varying the number of seeds to a fixed amount of metal precursors determined the final size of the formed nanocrystals.

Sun et al. used a high-temperature (265 °C) reaction to make monodisperse magnetite nanoparticles. $\text{Fe}(\text{acac})_3$ in phenyl ether with alcohol, OA, and OM was used in the reaction mix. Small magnetite nanoparticles were added as seeds. Up to 20 nm in diameter monodisperse magnetite nanoparticles were made without size-selection procedure, which makes its mass production straightforward.[180] Using seed-mediated growth, Park et al. made monodisperse iron oxide nanocrystals with a continuous size spectrum of 6 to 13 nm in diameter. These nanocrystals were employed for size-dependent magnetic measurements.[170]

1.4.1.2 Heterogenous core@shell structure

Nanoparticles can be made from single or multiple materials to form a homogeneous or heterogeneous core@shell structure. Homogeneous nanoparticles are prepared from a single material. Composite and core@shell nanoparticles comprise of two or more types of materials in different positions: core (inner material) and a shell (outer layer material). Many combinations were reported and the choice of material depends on its end use. Heterogeneous core@shell structured particles are frequently applied to biomedicine.[181-183] Their useful properties can be changed by adjusting the materials employed or the core/shell ratio of the materials.[184] Particle surface functionality can also be manipulated for their intended use. It is possible to program desired properties with core@multi-shell design, especially for inorganic/inorganic core@shell nanoparticles. These tailored or programmed core@shell nanoparticles

are useful in biomedical [185, 186] and pharmaceutical applications,[187] catalysis,[34, 188] electronics,[189] and enhancing photoluminescence,[66, 190] and so on.

Metal core@shell nanoparticles

Gold-based shell fabrication was extensively reported to enhance the performance of the core nanocrystals.[191-193] These include chemical stability, as gold protects the core material from oxidation and corrosion. Gold coating also exhibited the enhanced the optical properties due to the SPR effect.[191, 193] Ni, Co, Pd, Pt, and Cu coatings have also been tested. They can enhance catalysis and magnetic properties, and so on.[194] Moreover, it is found that surface-enhanced Raman scattering activity of Pd coating is lower than that of Au, Ag, or Cu coating. Yet, activity can be increased by using an Au core and decreased with the shell thickness.[195, 196]

Metal nanoshells could also be seen as a new class of nanoparticles. They have a dielectric core and can be silica-coated and can have a nanorange metallic layer. Like the size-dependent color of Au NPs, the color of the Au nanoshells changes with the size of the core particle and the thickness of the Au shell.[197] Adjusting to the relative core and shell thicknesses changes the particles optical spectrum from visible to NIR. This is beneficial for biomedical imaging, biological sensing.

Semiconductor core@shell nanoparticles

Colloidal semiconductor nanocrystals have good size-dependent optical properties. Their fluorescence quantum yield performance is limited by a significant fraction of stabilizing ligands passivated on the surface of nanocrystals. These typically display surface-related trap states. They act as fast non-radiative de-excitation channels to quench the luminescence. To improve surface passivation of the nanocrystals and in turn the emission efficiency, fabrication of a core@shell nanostructure with a shell of a second semiconductor can be performed. Also, the appropriate select of core and shell materials can adjust the emission wavelength to relatively larger spectral window than seen in its individual materials.[198-200] For example, Hines et al. over-coated 3-nm CdSe nanocrystals with 1 or 2 monolayers of ZnS to build the CdSe@ZnS core@shell nanoparticles. This made quantum yield of the nanoparticles in the order of 50% more efficient.[198] ZnS coated CdSe nanorods with 30 nm lengths was also reported.[201] In this study, hexadecylamine was used as the surfactant in the reaction system to control the ZnS shell growth kinetics. This approach made particles with a low size distribution and high quantum yields at around 60%.[202]

Small CdSe/ZnS core@shell nanocrystals were also reported by Kudera et al., which enables the blue emission accessible with this system.[203]

UCNPs core@shell structure

Similar to semiconductor nanocrystals, small nanocrystal UCNPs experience surface-related trap states that act as sinks for luminescence quenching. To avoid this effect, much effort has been made to synthesize core@shell nanostructure.[190, 204, 205] Thanks to the small lattice mismatch between different types of NaREF₄, core and shell structures sourced from various materials was easy to make. Hierarchical design of core@shell UCNPs with various functional shells have made it possible to achieve particles with desired properties. This capability has provided solutions that address the trap state problem (**Fig. 1.13**).

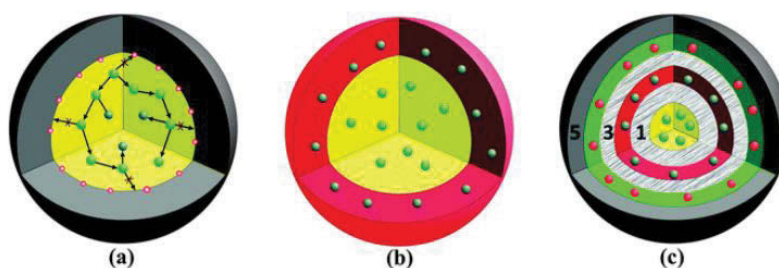


Figure 1.13 Different types of core@shell UCNPs with epitaxial layers: (a) core@shell UCNPs with an “inert” shell layer, (b) Core@shell UCNPs with an active shell layer, and (c) core@shell UCNPs with multiple shell layers. Reproduced with permission from Ref.[205] Copyright (2015) Royal Society of Chemistry.

Since the first fabrication of NaYF₄:Yb,Er@NaYF₄ and NaYF₄:Yb,Tm@NaYF₄ core@shell for luminescence enhancement in 2007 by Chow et al,[206] various types of high-quality core@shell nanocomposites were fabricated with improved luminescence efficiency. These include NaYF₄:Yb,Er(Tm)@NaGdF₄, NaYF₄:Yb,Er(Tm)@NaYF₄, NaGdF₄:Yb,Er/Tm/Ce/Tb@NaYF₄, KYF₄:Yb,Er@KYF₄, and so on.[58, 206] The excitation of UCNPs can be changed from 980 to 795 nm to minimize the overheating problem associated with the 980 nm laser through core@shell design (**Fig. 1.14a,b**). *Via* spatially confined doping of Nd³⁺ ions, various lanthanide activators (Tm³⁺, Er³⁺, or Ho³⁺) could show markedly enhanced the upconversion emission.[207] For example, Wang et al. showed light management using the core@shell@shell nanostructure design, in which various lanthanide dopants were selectively doped into different domains (**Fig. 1.14c,d**).[208] Core area was doped with Nd³⁺ to harvest

light excitation at around 800 nm, inner shell was doped with Yb³⁺ and activators to yield upconversion emission with different colors, while the outmost shell was doped with Eu³⁺, Tb³⁺, or Dy³⁺ to adjust the color of the emission. Through the Yb³⁺ sub-lattice network, the energy could be transfer from Nd³⁺ to the inner shell emitter.

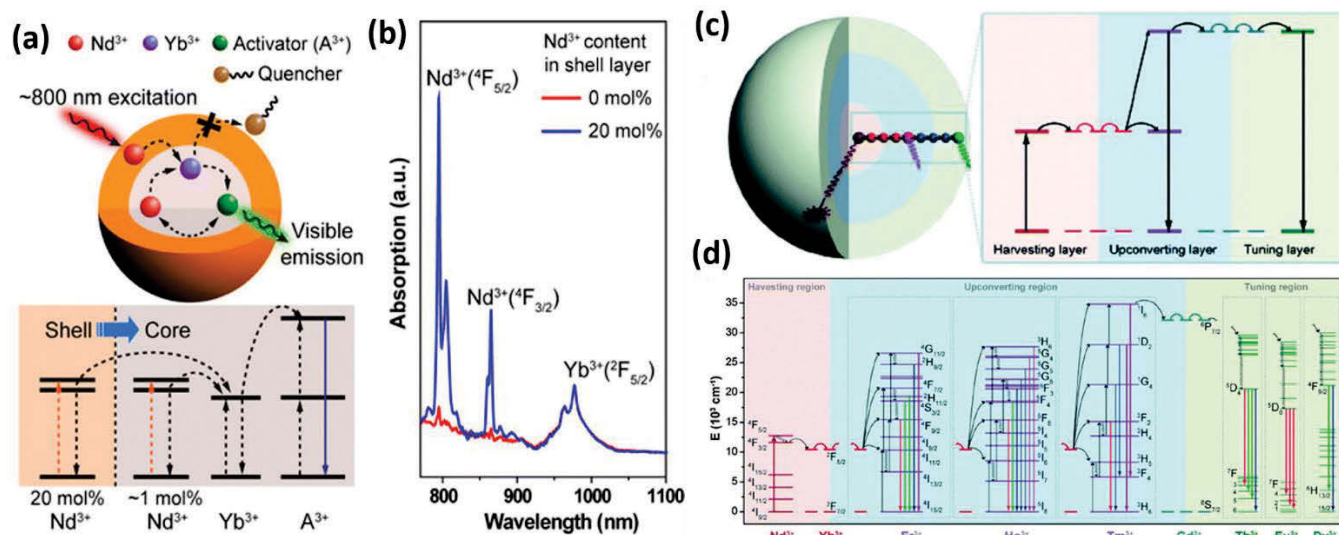


Figure 1.14 (a) Schematic design (top) and simplified energy level diagram (bottom) of a core@shell nanoparticle for photon upconversion under 800 nm excitation. (b) NIR absorption spectra of NaYF₄:Yb/Nd nanoparticles coated with an inert NaYF₄ shell or an active NaYF₄:Nd shell. Reproduced with permission from Ref.[207] Copyright (2013) American Chemical Society. (c) Schematic illustration of the principle of energy flow in a NaYbF₄@Na(Yb,Gd)F₄@NaGdF₄ core@shell@shell structure. (d) The corresponding energy levels of Nd³⁺ doped in the core domain, Yb³⁺/(Er³⁺, Ho³⁺, Tm³⁺) in the inner shell, and the Eu³⁺, Tb³⁺, or Dy³⁺ in the outmost shell. Reproduced with permission from Ref.[208] Copyright (2013) John Wiley and Sons.

Core@shell structures can be designed for multimode imaging. Sun et al. reported the fabrication of core@shell nanoparticles with a NaLuF₄:Yb,Tm core and a ¹⁵³Sm³⁺-doped NaGdF₄ shell for four-modal imaging (**Fig. 1.15**).[81] Their results showed that NaLuF₄:Yb,Tm@NaGdF₄(¹⁵³Sm) nanoparticles combined upconversion luminescence, CT, MR, SPECT imaging. These nanoparticles are beneficial for *in vivo* animal mode organ as well as tumor angiogenesis analysis. Rieffel et al. reported core@shell UCNPs-based hexamodal imaging contrast agents.[79] Porphyrin-phospholipids coated core@shell UCNPs with ⁶⁴Cu labeling were applied for multimodal imaging both *in vitro* and *in vivo*, including fluorescence, upconversion luminescence, PET, CT, Photoacoustic, and Cerenkov luminescence. However, the conventional core@shell structures showed incremental imaging modalities only. There is

still room for optimizing the performance of each modalities for biomedical applications. Recently, Almutairi et al. describe lanthanide-based core@shell@shell nanoparticles as triple-modal contrast agents. Its performance was better than when each component was run on its own for upconversion luminescence, CT, and MR imaging.[209] When the thickness of the interfacial layer was optimal, the MR r_1 relaxivity was enhanced by 5-fold at 1.5 T, while the CT Hounsfield Unit gain was 70% higher than a conventional iodine-based agent. In the same time, upconversion luminescence intensity was enhanced from completely dark state to a brightly emissive state. These results indicated that the multimodal imaging contrast agents, through carefully designed, can achieve simultaneously enhanced performance in all the integrated modalities.

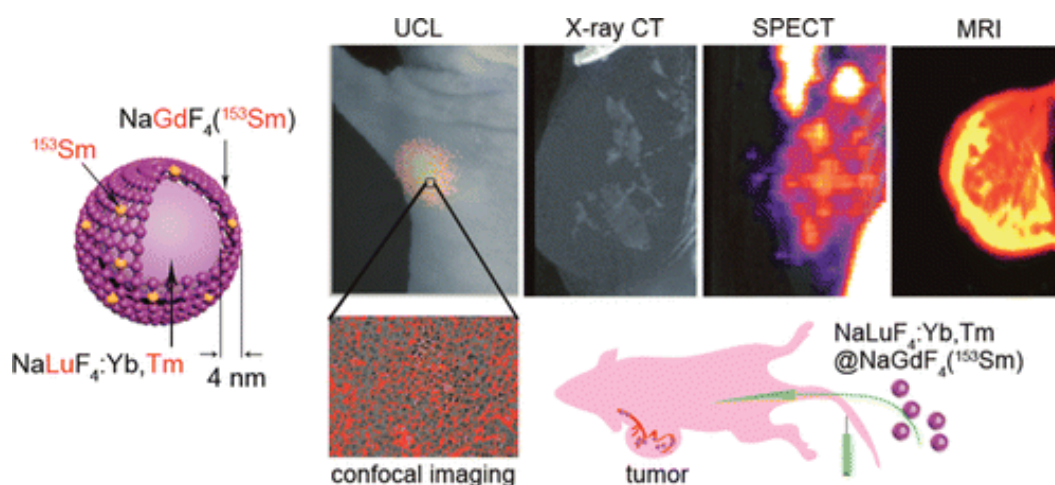


Figure 1.15. The $\text{NaLuF}_4:\text{Yb,Tm}@ \text{NaGdF}_4(^{153}\text{Sm})$ for in vivo animal mode tumor angiogenesis analysis by combining upconversion luminescence, CT, MR, and SPECT imaging. Reproduced with permission from Ref.[81] Copyright (2013) American Chemical Society.

Magnetic core@shell nanoparticles

Magnetic nanoparticles have limits when applied to some areas. (i) They are very easy to aggregate. (ii) They can suffer rapid biodegradation in the biological systems. (iii) Unstable particles may structurally change in a magnetic field. To address this, magnetic nanoparticles with various inert inorganic coatings were developed. These core@shell magnetic nanoparticles were frequently used in the field of MR imaging, magnetic separation, and magnetically targeted drug delivery.[191] More recently, dual-core and shell biomagnetic particles were employed to fabricate devices for novel nanomagnetic application. These types of particles allow precise engineering of their magnetic properties through carefully adjusting of the

core and shell sizes. Fe_3Pt and $\text{FePt}@\text{Fe}_3\text{O}_4$ nanocrystals were harnessed for high adsorption capacity and environmental remediation.[210, 211]. Fe_2O_3 coating on MgO and CaO nanocrystals show the enhanced adsorption of poisonous gases, like SO_2 and H_2S .[212]

1.4.2 Anisotropic growth

Other than the spherical nanoparticles, different shaped nanoparticles by anisotropic growth have proven essential due to their potential applications in the fields of catalysis, electronics, information storage, biomedical imaging, and biology sensors.[213-215] Generally, a suitable organic capping agent is employed to control the growth direction of the nanocrystals. Capping agent can change the free energy along different crystallographic planes, and in turn changes the growth rate of different facets to form the shape-controlled nanocrystals.

1.4.2.1 Homogeneous nanocrystals

Growth patterns of crystallographic facets can be adjusted by controlling the kinetics of a reaction. This makes nanocrystals with high-index facets or with concave surfaces. For seeded growth, atoms are added to the surface of preformed seed particles. This offers a simple and versatile route to avoid the additional nucleation and control the shape of a final particle. Growth kinetics can be well controlled through adjusting the rate at which precursors are added to seed solution. For example, Polyvinylpyrrolidone shows the strong binding abilities to Ag(100) and can selectively stabilize this facet during the growth process.[216] In this case, truncated octahedra and cube-shaped Ag nanocrystals enclosed by (100) facets could be obtained by slowing the reduction rate. Alternatively, citrate shows the strong binding abilities to Ag(111) and can selectively stabilize these facets for the generation of octahedra shaped nanocrystals covered with (111) facets.[216] Therefore, the synthesis of nanocrystals with different shapes or faceting could be well controlled by using desired capping agents.[50, 217, 218]

Researchers have reported making non-spherical shaped core@shell nanoparticles with properties that are different to those with a spherical shape.[219-222] In 2010, Sau et al. [219] reviewed nonspherical plasmon resonant nanoparticles, and showed that these nanoparticles offer favorable properties for their further applications. Hence, it is reasonable to assume that there would be similar changes in properties for core@shell nanocrystals by cause of the shape changes. For metallic nanoparticles, improvements to their catalytic properties were attributed to the exposure of many desired facets of the crystals. The introduction of a number of edges and corners leads to changes in a particle's catalytic selectivity and thus

its activity. For example, Narayan et al. [221] reported that anisotropic Pt nanocrystals exhibit enhanced catalytic activity compared with their corresponding spherical particles. Moreover, Pt nanocrystals with different shapes display various catalytic activity for the electron-transfer reaction. The activity followed an increasing in the shape's order of cubes, spheres, and tetrahedra. Optical properties of nonspherical nanocrystals also varied with changes in their physical dimensions. For example, the resonance frequency of noble metal-based particles is tunable from blue to NIR region by changing a particle's shape.[220] Also, extinction efficiency of noble metals varies as the shape of its particles changes, which proves another approach to adjust their performance for better biological applications. Through adjusting the shape, the resonance of the anisotropic Au nanocrystals can be located in the NIR region (800 to 1300 nm), known as transparent biological window.[219, 220]

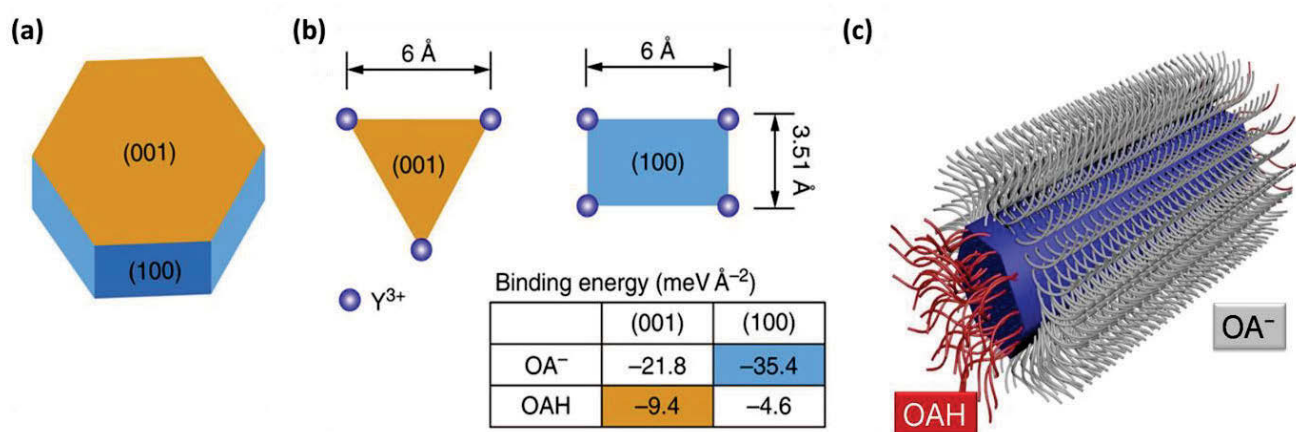


Figure 1.16 (a) The schematic shape of a hexagonal cylinder NaYF₄ nanocrystal consists of the (001) facets and identical (100) and (010) facets. (b) The Y³⁺ arrangements and binding energies of OAH and OA⁻ on the (001) and (100) facets. Reproduce from Ref.[223]. (c) The schematic structure of the OAH and OA⁻ stabilized nanocrystals.

In our previous study, we found that a typical UCNPs (NaREF₄) had anisotropy surfaces with different ligands on different crystal faces (**Fig. 1.16b,c**),[223] which was confirmed by first-principle calculations using density functional theory. This allowed us to employ a molecular approach to adjusting the shape and composition of NaREF₄ nanoparticles (**Fig. 1.17a**). The ratio of oleate anions (OA⁻) and OA in the reaction system directionally inhibited or promoted the growth of different crystallographic facets on the nanoparticles. This controlled method made the selective epitaxial anisotropy growth over nanocrystal cores possible in the longitudinal direction. It made the fabrication of a diverse library of monodisperse nanorods with different aspect ratios possible.

1.4.2.2 Heterogeneous nanorods

Heterogeneous nanostructures combine different elements into a single particle. This introduces new and enhanced properties that are multi-functional and are not seen in the parent material. Direction-controlled growth, described before, can form five or seven-section ‘bamboo-shaped’ NaYF₄/NaGdF₄ nanorods (Fig. 1.17b). Various predesigned 3-dimensional nanocrystal with different shapes can be easily engineered using this seed mediated growth approach.

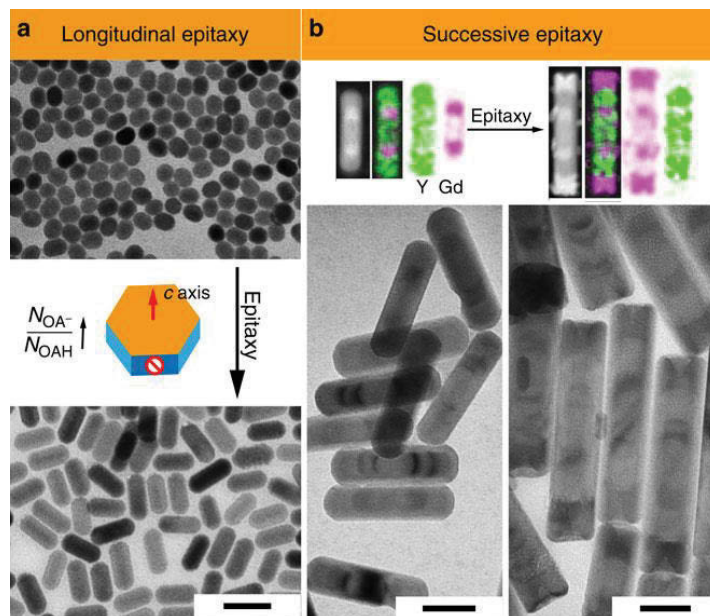


Figure 1.17 Controlled epitaxial growth of NaREF₄ nanocrystals. (a) NaYF₄ core and nanorods through longitudinal epitaxial growth with NaYF₄; (b) five-section and seven-section ‘bamboo-shaped’ NaYF₄/NaGdF₄ NRs formed through longitudinal epitaxial growth with NaGdF₄ and NaYF₄. Reproduce from Ref.[223].

Programmable design and fabrication can place different materials optimally with atomic-scale precision. NaYF₄:Yb,Er is added to the center of a particle to enhance its luminescence. NaGdF₄ was placed on the surface of the final particles, as Gd³⁺ on the particle’s surface are major contributors to its relaxivity enhancement. T2 contrast agent, NaDyF₄, should be separated with NaYF₄:Yb,Er as it will quench the luminescence. For CT imaging, Lu³⁺ has a high attenuation and so should be added to the nanostructure. It should be noted that a conventional core@shell structure would not work for this kind of heterogeneous UCNP synthesis. The service of a programmable placement of these materials is still a challenge.

Anisotropy UCNPs are beneficial for various applications.[88, 90] Ding et al. reported a seed-mediated sequential growth process to synthesize NaYF₄:Yb/Er@NaGdF₄ nanoparticles with different shapes (quasi-sphere, nanodumbbells, and nanocubes).[88] These anisotropy core@shell structures have various luminescence. Xu et al. made Nd³⁺ sensitized NaYF₄:Yb/Er@NaNdF₄:Yb nanodumbbells for PDT application (**Fig. 1.18**).[90] These nanodumbbells had a better therapy effect than the isotropic coated multilayer UCNPs.

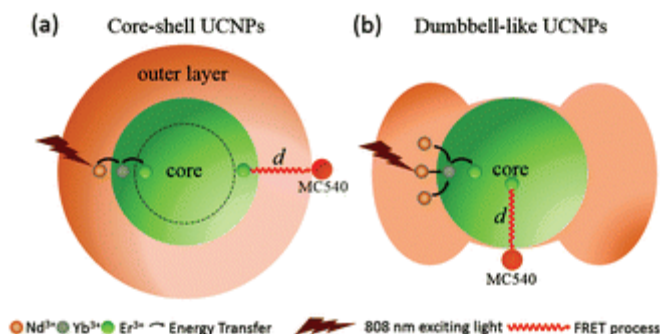


Figure 1.18. FRET process of (a) core@shell and, (b) dumbbell-like UCNPs excited by 808 nm NIR laser. Reproduced with permission from Ref.[90] Copyright (2016) Royal Society of Chemistry.

Localized SPR spectrum of a metal nanocrystal include resonance signals, their position, and their scattering/absorption efficiency. These attributes correlate with a particle's composition, size, shape, and structure.[224, 225] Accordingly, these can be tailored via seed-growth for optimal optical properties. For example, Xia et al. reported a facile approach to synthesize Au@Ag nanocubes with tunable edge lengths (13.4 to 50 nm) by the seed-mediated growth.[226] Precise shell growth control was helpful for testing the evolution of localized SPR as a function of the shell thickness (**Fig. 1.19a-d**). As shown in **Fig. 1.19e**, localized SPRs of core@shell nanocrystals gradually became dominated with the increase of the thickness of Ag shell. Also, the resonance of the Ag increases and fully screens the response from Au core at the thickness of 3 nm. Moreover, the signal position of localized SPR could be effectively adjusted through changing the aspect ratio of the formed nanocrystal. For example, Mayer et al. reported that highly anisotropic Ag shell could be achieved through its 1-dimensional controlled growth.[227] The decahedral Au seed was reported as a good candidate.[38, 228-230] Au nanorods with decahedral shapes was added as seeds for the continues Ag growth and the formed Au@Ag nanorods could be several micrometers long.[227] TEM images of Au@Ag nanorods at various sizes are shown in **Fig. 1.19 f-i**. The extinction spectra of these nanorods shows a distinct red-shift as a function of their length (**Fig. 1.19 j**).

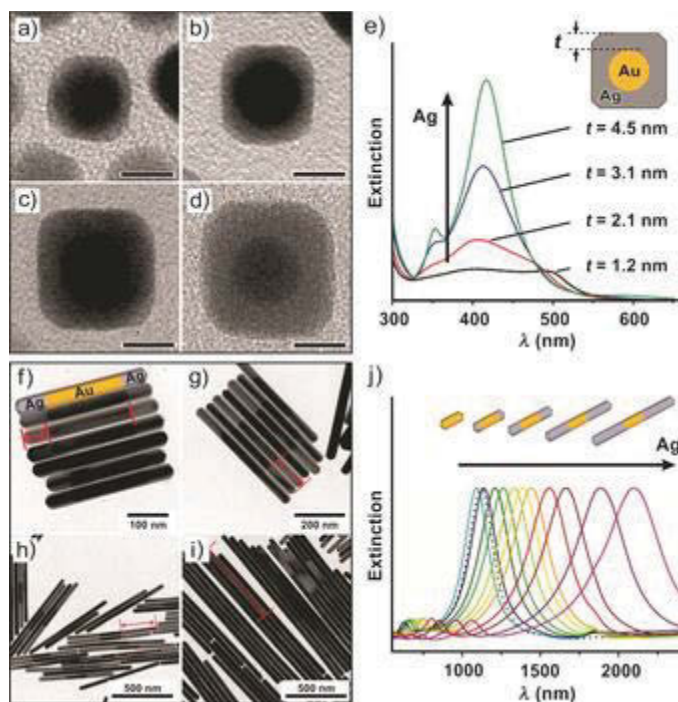


Figure 1.19 (a-d) TEM images of individual Au@Ag nanocubes obtained by injecting different volumes of AgNO₃ into growth solutions containing a fixed number of Au seeds (scale bars: 8 nm). (e) UV-Vis extinction spectra of Au@Ag nanocubes with increasing thicknesses t of the Ag shells. (f-i) TEM images of decahedral Au@Ag nanorods with lengths of (f) 61, (g) 130, (h) 280, and (i) 660 nm for one of the Ag segments (marked on the rods). (j) UV-Vis-NIR spectra of the Au@Ag nanorods. Reproduced with permission from Ref.[169] Copyright (2017) John Wiley and Sons.

1.5 Aim and Outline

1.5.1 Thesis aim

Lanthanide doped UCNPs are a new family of luminescent nanomaterials attracting a large amount of research interests, especially in bioimaging and biomedicine. The controlled synthesis of lanthanide doped UCNPs with fine-tuning the size, shape and composition becomes the next grand challenge aiming to push their real applications. Also, heterogeneous structured UCNPs have the potential to integrate many different functionalities and positively enhance each property within one nanoscale platform. Direct size/shape/composition-control in the conventional synthesis process, however does remain a challenge via the one-pot wet chemical synthesis route. This thesis thus aims to establish new methods for the fabrication of UCNPs with fine-tuning the size, shape and composition. Then, I use these well-controlled nanocrystals to study the optical property at single nanocrystal level. Further, this knowledge is leveraged to develop a robust engineering protocol for fabrication of monodisperse multifunctional luminescent nanocrystals. The outcomes of this thesis not only include a series of knowledge discovered for controlled growth of lanthanide doped nanomaterials, but also lead to a range of new applications demonstrated, such as super-resolution nanoscopy imaging, single-particle tracking, and multimodal bioimaging.

1.5.2 Thesis outline

This thesis begins with a comprehensive review of the size-/shape-dependent properties and the controlled wet-chemical synthesis of nanomaterials, especially for the recently developed UCNPs, forming the introduction Chapter 1. In Chapter 2, I provide the full details of materials and methods employed for seed-mediated growth in this thesis. And the following four chapters summarize the core results from 666 synthesis experiments to produce a range of homogeneous (Chapter 3), heterogeneous (Chapter 5) and single directional grown barcoded nanocrystals at arbitrary sizes (Chapter 6), as well as a comprehensive characterization and investigation of crystal growth mechanisms (Chapter 4) that underpins these synthesis techniques.

In Chapter 3, I demonstrate the seed-mediated growth method for fabricating homogeneous nanocrystals doped with different concentrations of activator ions. This facile seed-mediated method achieves precise control in size (one nanometer resolution) to yield a series of monodisperse UCNPs, which forms the foundation for evaluations of their optical properties at single-nanoparticle level towards a series of novel applications in nanoscopy.

In Chapter 4, I systematically investigate the mechanisms and a range of potential determining factors to identify the key to the controlled growth. I discovered that the reaction mix plays an essential role in catalyzing the epitaxial growth. This knowledge enables the fabrication of integrated heterogeneous core@shell nanocrystals with high performance in luminescence intensity.

In Chapter 5, I employ the heterogeneous seed-mediated growth approach to fabricate the core@shell@shell sandwich nanostructure with various sensitizer and activator doping concentrations to identify the optimum doping concentrations of both sensitizers and activators.

In Chapter 6, I challenge to control the growth direction using the seed-mediated growth method. Through fine-tuning of the amount of surfactant molecules and the concentration of the shell precursor, I have achieved the absolute one-direction growth of homogenous and heterogenous UCNPs nanorods by the layer-by-layer deposition of precursor on the desired crystal facet.

In Chapter 7, I summarize the key achievements presented in this thesis and discuss the potentials of using this developed approach for the fabrication of high-quality on-demand hybrid nanocrystals. Also, I discuss their potential application in new nanotechnologies, such as super-resolution imaging, multimodal bioimaging, optogenetics, nanothermometry, photovoltaics, and laser refrigeration.

Chapter 1	1. Nanoparticles and Nanotechnology	
	1.1 Size-dependent properties	
	1.2 Shape-dependent properties	
	2. Rare-Earth Nanoparticles	
	2.1 Size-dependent properties	
	2.2 Shape-dependent properties	
	3. One-Pot Wet-Chemical Synthesis	
	3.1 Formation mechanism and general synthesis method	
	3.2 Size-controlled synthesis	
	3.3 Shape-controlled synthesis	
	4. Seed-Mediated Growth	
	4.1 Isotropic growth (Homogeneous and heterogeneous)	Chapter 2
	4.2 Anisotropic growth (Homogeneous and heterogeneous)	
		1 Chemicals and instrument
		2 Methods for core synthesis
		3. Seed-Mediated Growth
		3.1 Heating up approach
		3.2 Hot-injection approach

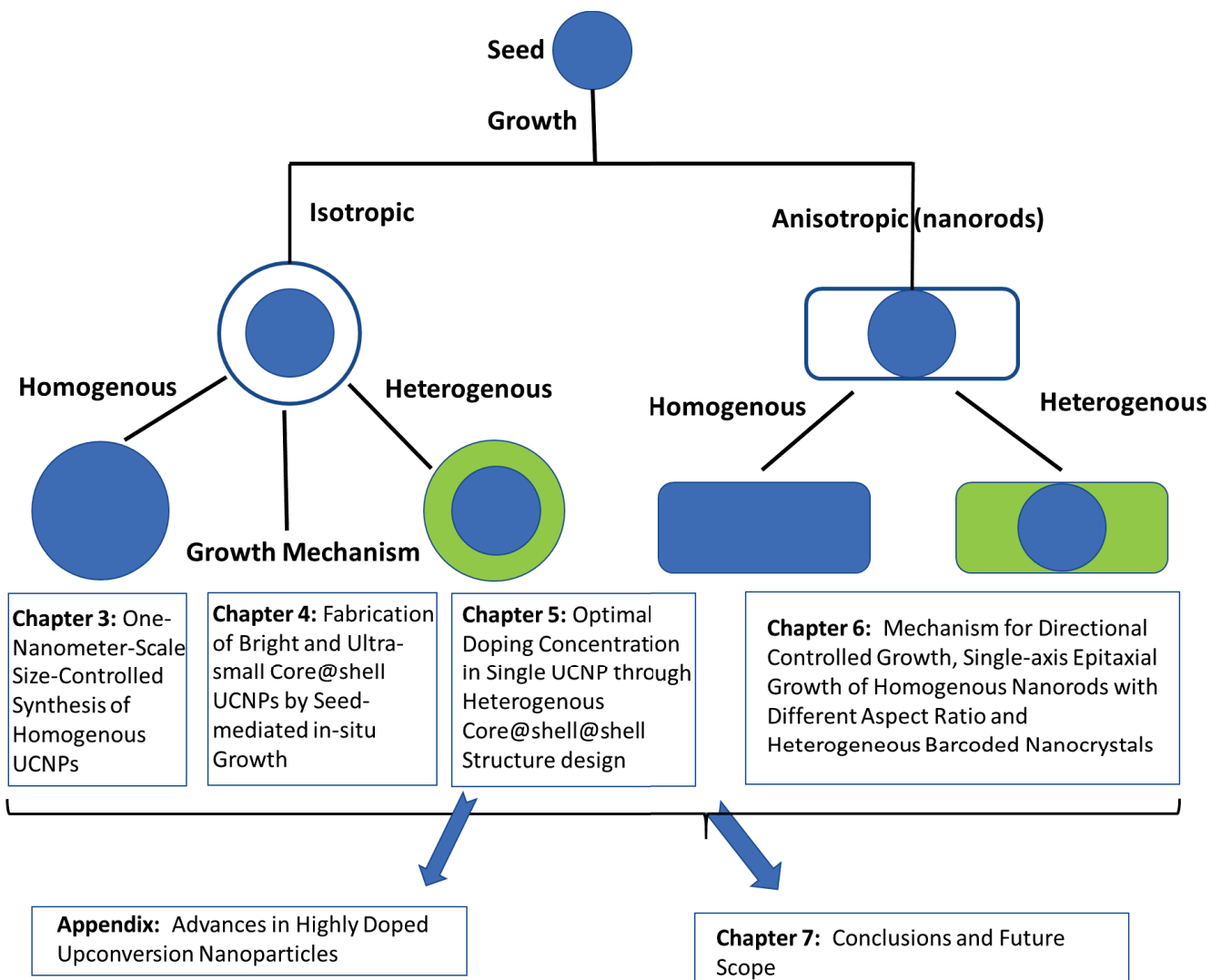


Figure 1.20 Flow chart outlines the logic structure of this thesis.

1.6 References

- [1] Nanoscience and nanotechnologies: opportunities and uncertainties, The Royal Society and The Royal Academy of Engineering (2004) Page 5. (also available at www.nanotec.org.uk).
- [2] Feynman, R.P., There's plenty of room at the bottom, *Engineering and science* 23 (5) (1960) 22-36.
- [3] West, J.L., Halas, N.J., Engineered Nanomaterials for Biophotonics Applications: Improving Sensing, Imaging, and Therapeutics, *Annual Review of Biomedical Engineering* 5 (1) (2003) 285-292.
- [4] Jariwala, D., Sangwan, V.K., Lauhon, L.J., Marks, T.J., Hersam, M.C., Carbon nanomaterials for electronics, optoelectronics, photovoltaics, and sensing, *Chemical Society Reviews* 42 (7) (2013) 2824-2860.
- [5] Zeng, S., Baillargeat, D., Ho, H.-P., Yong, K.-T., Nanomaterials enhanced surface plasmon resonance for biological and chemical sensing applications, *Chemical Society Reviews* 43 (10) (2014) 3426-3452.
- [6] Biju, V., Chemical modifications and bioconjugate reactions of nanomaterials for sensing, imaging, drug delivery and therapy, *Chemical Society Reviews* 43 (3) (2014) 744-764.
- [7] Hatchett, D.W., Josowicz, M., Composites of Intrinsically Conducting Polymers as Sensing Nanomaterials, *Chemical Reviews* 108 (2) (2008) 746-769.
- [8] Slowing, I.I., Trewyn, B.G., Giri, S., Lin, V.S.Y., Mesoporous Silica Nanoparticles for Drug Delivery and Biosensing Applications, *Advanced Functional Materials* 17 (8) (2007) 1225-1236.
- [9] Astruc, D., Lu, F., Aranzas, J.R., Nanoparticles as Recyclable Catalysts: The Frontier between Homogeneous and Heterogeneous Catalysis, *Angewandte Chemie International Edition* 44 (48) (2005) 7852-7872.
- [10] Crooks, R.M., Zhao, M., Sun, L., Chechik, V., Yeung, L.K., Dendrimer-Encapsulated Metal Nanoparticles: Synthesis, Characterization, and Applications to Catalysis, *Accounts of Chemical Research* 34 (3) (2001) 181-190.
- [11] Li, Y., Wang, H., Xie, L., Liang, Y., Hong, G., Dai, H., MoS₂ Nanoparticles Grown on Graphene: An Advanced Catalyst for the Hydrogen Evolution Reaction, *Journal of the American Chemical Society* 133 (19) (2011) 7296-7299.
- [12] Zhou, J., Liu, Z., Li, F., Upconversion nanophosphors for small-animal imaging, *Chemical Society Reviews* 41 (3) (2012) 1323-1349.
- [13] Jain, P.K., Lee, K.S., El-Sayed, I.H., El-Sayed, M.A., Calculated Absorption and Scattering Properties of Gold Nanoparticles of Different Size, Shape, and Composition: Applications in Biological Imaging and Biomedicine, *The Journal of Physical Chemistry B* 110 (14) (2006) 7238-7248.
- [14] Sun, C., Lee, J.S.H., Zhang, M., Magnetic nanoparticles in MR imaging and drug delivery, *Advanced Drug Delivery Reviews* 60 (11) (2008) 1252-1265.
- [15] Reddy, L.H., Arias, J.L., Nicolas, J., Couvreur, P., Magnetic Nanoparticles: Design and Characterization, Toxicity and Biocompatibility, Pharmaceutical and Biomedical Applications, *Chemical Reviews* 112 (11) (2012) 5818-5878.
- [16] Doane, T.L., Burda, C., The unique role of nanoparticles in nanomedicine: imaging, drug delivery and therapy, *Chemical Society Reviews* 41 (7) (2012) 2885-2911.

- [17] Boisselier, E., Astruc, D., Gold nanoparticles in nanomedicine: preparations, imaging, diagnostics, therapies and toxicity, *Chemical Society Reviews* 38 (6) (2009) 1759-1782.
- [18] Fan, W., Bu, W., Shi, J., On The Latest Three-Stage Development of Nanomedicines based on Upconversion Nanoparticles, *Advanced Materials* 28 (21) (2016) 3987-4011.
- [19] Bruce, P.G., Scrosati, B., Tarascon, J.-M., Nanomaterials for Rechargeable Lithium Batteries, *Angewandte Chemie International Edition* 47 (16) (2008) 2930-2946.
- [20] Huynh, W.U., Dittmer, J.J., Alivisatos, A.P., Hybrid Nanorod-Polymer Solar Cells, *Science* 295 (5564) (2002) 2425-2427.
- [21] Bi, D., Tress, W., Dar, M.I., Gao, P., Luo, J., Renevier, C., Schenk, K., Abate, A., Giordano, F., Correa Baena, J.-P., Decoppet, J.-D., Zakeeruddin, S.M., Nazeeruddin, M.K., Grätzel, M., Hagfeldt, A., Efficient luminescent solar cells based on tailored mixed-cation perovskites, *Science Advances* 2 (1) (2016).
- [22] Sondheimer, E.H., The mean free path of electrons in metals, *Advances in physics* 1 (1) (1952) 1-42.
- [23] El-Sayed, M.A., Some Interesting Properties of Metals Confined in Time and Nanometer Space of Different Shapes, *Accounts of Chemical Research* 34 (4) (2001) 257-264.
- [24] Murphy, C.J., Sau, T.K., Gole, A.M., Orendorff, C.J., Gao, J., Gou, L., Hunyadi, S.E., Li, T., Anisotropic Metal Nanoparticles: Synthesis, Assembly, and Optical Applications, *The Journal of Physical Chemistry B* 109 (29) (2005) 13857-13870.
- [25] Gall, D., Electron mean free path in elemental metals, *Journal of Applied Physics* 119 (8) (2016) 085101.
- [26] Bawendi, M.G., Steigerwald, M.L., Brus, L.E., The quantum mechanics of larger semiconductor clusters ("quantum dots"), *Annual Review of Physical Chemistry* 41 (1) (1990) 477-496.
- [27] Dabbousi, B.O., Rodriguez-Viejo, J., Mikulec, F.V., Heine, J.R., Mattoussi, H., Ober, R., Jensen, K.F., Bawendi, M.G., (CdSe) ZnS core-shell quantum dots: synthesis and characterization of a size series of highly luminescent nanocrystallites, *The Journal of Physical Chemistry B* 101 (46) (1997) 9463-9475.
- [28] Resch-Genger, U., Grabolle, M., Cavaliere-Jaricot, S., Nitschke, R., Nann, T., Quantum dots versus organic dyes as fluorescent labels, *Nature methods* 5 (9) (2008) 763-775.
- [29] Li, X., Wu, Y., Zhang, S., Cai, B., Gu, Y., Song, J., Zeng, H., CsPbX₃ Quantum Dots for Lighting and Displays: Room-Temperature Synthesis, Photoluminescence Superiorities, Underlying Origins and White Light-Emitting Diodes, *Advanced Functional Materials* 26 (15) (2016) 2435-2445.
- [30] Veamatahau, A., Jiang, B., Seifert, T., Makuta, S., Latham, K., Kanehara, M., Teranishi, T., Tachibana, Y., Origin of surface trap states in CdS quantum dots: relationship between size dependent photoluminescence and sulfur vacancy trap states, *Physical Chemistry Chemical Physics* 17 (4) (2015) 2850-2858.
- [31] Keuleyan, S.E., Guyot-Sionnest, P., Delerue, C., Allan, G., Mercury Telluride Colloidal Quantum Dots: Electronic Structure, Size-Dependent Spectra, and Photocurrent Detection up to 12 μm , *ACS Nano* 8 (8) (2014) 8676-8682.
- [32] Chen, M.S., Goodman, D.W., The Structure of Catalytically Active Gold on Titania, *Science* 306 (5694) (2004) 252-255.

- [33] Turner, M., Golovko, V.B., Vaughan, O.P.H., Abdulkin, P., Berenguer-Murcia, A., Tikhov, M.S., Johnson, B.F.G., Lambert, R.M., Selective oxidation with dioxygen by gold nanoparticle catalysts derived from 55-atom clusters, *Nature* 454 (2008) 981.
- [34] Daniel, M.-C., Astruc, D., Gold Nanoparticles: Assembly, Supramolecular Chemistry, Quantum-Size-Related Properties, and Applications toward Biology, Catalysis, and Nanotechnology, *Chemical Reviews* 104 (1) (2004) 293-346.
- [35] Gao, N., Chen, Y., Li, L., Guan, Z., Zhao, T., Zhou, N., Yuan, P., Yao, S.Q., Xu, Q.-H., Shape-Dependent Two-Photon Photoluminescence of Single Gold Nanoparticles, *The Journal of Physical Chemistry C* 118 (25) (2014) 13904-13911.
- [36] Cao, S., Tao, F., Tang, Y., Li, Y., Yu, J., Size- and shape-dependent catalytic performances of oxidation and reduction reactions on nanocatalysts, *Chemical Society Reviews* 45 (17) (2016) 4747-4765.
- [37] Orendorff, C.J., Sau, T.K., Murphy, C.J., Shape-Dependent Plasmon-Resonant Gold Nanoparticles, *Small* 2 (5) (2006) 636-639.
- [38] Wang, Y.-N., Wei, W.-T., Yang, C.-W., Huang, M.H., Seed-Mediated Growth of Ultralong Gold Nanorods and Nanowires with a Wide Range of Length Tunability, *Langmuir* 29 (33) (2013) 10491-10497.
- [39] Das, S.K., Dickinson, C., Lafir, F., Brougham, D.F., Marsili, E., Synthesis, characterization and catalytic activity of gold nanoparticles biosynthesized with *Rhizopus oryzae* protein extract, *Green Chemistry* 14 (5) (2012) 1322-1334.
- [40] Xia, F., Zuo, X., Yang, R., Xiao, Y., Kang, D., Vallée-Bélisle, A., Gong, X., Yuen, J.D., Hsu, B.B., Heeger, A.J., Colorimetric detection of DNA, small molecules, proteins, and ions using unmodified gold nanoparticles and conjugated polyelectrolytes, *Proceedings of the National Academy of Sciences* 107 (24) (2010) 10837-10841.
- [41] Lee, J.S., Han, M.S., Mirkin, C.A., Colorimetric detection of mercuric ion (Hg^{2+}) in aqueous media using DNA-functionalized gold nanoparticles, *Angewandte Chemie* 119 (22) (2007) 4171-4174.
- [42] Chen, G.-H., Chen, W.-Y., Yen, Y.-C., Wang, C.-W., Chang, H.-T., Chen, C.-F., Detection of mercury (II) ions using colorimetric gold nanoparticles on paper-based analytical devices, *Analytical chemistry* 86 (14) (2014) 6843-6849.
- [43] Jiang, W., Kim, B.Y.S., Rutka, J.T., Chan, W.C.W., Nanoparticle-mediated cellular response is size-dependent, *Nature Nanotechnology* 3 (2008) 145.
- [44] Ayyappan, S., Philip, J., Raj, B., A facile method to control the size and magnetic properties of CoFe_2O_4 nanoparticles, *Materials Chemistry and Physics* 115 (2) (2009) 712-717.
- [45] Chen, J.P., Sorensen, C.M., Klabunde, K.J., Hadjipanayis, G.C., Devlin, E., Kostikas, A., Size-dependent magnetic properties of MnFe_2O_4 fine particles synthesized by coprecipitation, *Physical Review B* 54 (13) (1996) 9288-9296.
- [46] Sau, T.K., Pal, A., Pal, T., Size Regime Dependent Catalysis by Gold Nanoparticles for the Reduction of Eosin, *The Journal of Physical Chemistry B* 105 (38) (2001) 9266-9272.
- [47] Zhou, X., Xu, W., Liu, G., Panda, D., Chen, P., Size-Dependent Catalytic Activity and Dynamics of Gold Nanoparticles at the Single-Molecule Level, *Journal of the American Chemical Society* 132 (1) (2010) 138-146.

- [48] Shan, Y., Ma, S., Nie, L., Shang, X., Hao, X., Tang, Z., Wang, H., Size-dependent endocytosis of single gold nanoparticles, *Chemical Communications* 47 (28) (2011) 8091-8093.
- [49] Zhang, H., Jin, M., Xiong, Y., Lim, B., Xia, Y., Shape-Controlled Synthesis of Pd Nanocrystals and Their Catalytic Applications, *Accounts of Chemical Research* 46 (8) (2013) 1783-1794.
- [50] Jin, M., Zhang, H., Xie, Z., Xia, Y., Palladium nanocrystals enclosed by {100} and {111} facets in controlled proportions and their catalytic activities for formic acid oxidation, *Energy & Environmental Science* 5 (4) (2012) 6352-6357.
- [51] Huang, X., El-Sayed, I.H., Qian, W., El-Sayed, M.A., Cancer Cell Imaging and Photothermal Therapy in the Near-Infrared Region by Using Gold Nanorods, *Journal of the American Chemical Society* 128 (6) (2006) 2115-2120.
- [52] Dickerson, E.B., Dreaden, E.C., Huang, X., El-Sayed, I.H., Chu, H., Pushpanketh, S., McDonald, J.F., El-Sayed, M.A., Gold nanorod assisted near-infrared plasmonic photothermal therapy (PPTT) of squamous cell carcinoma in mice, *Cancer Letters* 269 (1) (2008) 57-66.
- [53] Song, Q., Zhang, Z.J., Shape Control and Associated Magnetic Properties of Spinel Cobalt Ferrite Nanocrystals, *Journal of the American Chemical Society* 126 (19) (2004) 6164-6168.
- [54] Zhao, Z., Zhou, Z., Bao, J., Wang, Z., Hu, J., Chi, X., Ni, K., Wang, R., Chen, X., Chen, Z., Gao, J., Octapod iron oxide nanoparticles as high-performance T2 contrast agents for magnetic resonance imaging, *Nature Communications* 4 (2013) 2266.
- [55] Liu, X., Cao, K., Chen, Y., Ma, Y., Zhang, Q., Zeng, D., Liu, X., Wang, L.-S., Peng, D.-L., Shape-dependent magnetic and microwave absorption properties of iron oxide nanocrystals, *Materials Chemistry and Physics* 192 (Supplement C) (2017) 339-348.
- [56] Gai, S., Li, C., Yang, P., Lin, J., Recent Progress in Rare Earth Micro/Nanocrystals: Soft Chemical Synthesis, Luminescent Properties, and Biomedical Applications, *Chemical Reviews* 114 (4) (2014) 2343-2389.
- [57] Sun, L.-D., Wang, Y.-F., Yan, C.-H., Paradigms and Challenges for Bioapplication of Rare Earth Upconversion Luminescent Nanoparticles: Small Size and Tunable Emission/Excitation Spectra, *Accounts of Chemical Research* 47 (4) (2014) 1001-1009.
- [58] Dong, H., Sun, L.-D., Yan, C.-H., Energy transfer in lanthanide upconversion studies for extended optical applications, *Chemical Society Reviews* 44 (6) (2015) 1608-1634.
- [59] Dong, H., Du, S.-R., Zheng, X.-Y., Lyu, G.-M., Sun, L.-D., Li, L.-D., Zhang, P.-Z., Zhang, C., Yan, C.-H., Lanthanide Nanoparticles: From Design toward Bioimaging and Therapy, *Chem Rev* 115 (19) (2015) 10725-10815.
- [60] Qin, X., Liu, X., Huang, W., Bettinelli, M., Liu, X., Lanthanide-Activated Phosphors Based on 4f-5d Optical Transitions: Theoretical and Experimental Aspects, *Chemical Reviews* 117 (5) (2017) 4488-4527.
- [61] Heer, S., Kömpe, K., Güdel, H.U., Haase, M., Highly Efficient Multicolour Upconversion Emission in Transparent Colloids of Lanthanide-Doped NaYF₄ Nanocrystals, *Advanced Materials* 16 (23-24) (2004) 2102-2105.
- [62] Wu, S., Butt, H.-J., Near-Infrared-Sensitive Materials Based on Upconverting Nanoparticles, *Advanced Materials* 28 (6) (2016) 1208-1226.

- [63] Auzel, F., Upconversion and Anti-Stokes Processes with f and d Ions in Solids, *Chemical Reviews* 104 (1) (2004) 139-174.
- [64] Haase, M., Schäfer, H., Upconverting Nanoparticles, *Angewandte Chemie International Edition* 50 (26) (2011) 5808-5829.
- [65] Chen, G., Qiu, H., Prasad, P.N., Chen, X., Upconversion Nanoparticles: Design, Nanochemistry, and Applications in Theranostics, *Chemical Reviews* 114 (10) (2014) 5161-5214.
- [66] Zhou, B., Shi, B., Jin, D., Liu, X., Controlling upconversion nanocrystals for emerging applications, *Nat Nano* 10 (11) (2015) 924-936.
- [67] Kobayashi, H., Kosaka, N., Ogawa, M., Morgan, N.Y., Smith, P.D., Murray, C.B., Ye, X., Collins, J., Kumar, G.A., Bell, H., Choyke, P.L., In vivo multiple color lymphatic imaging using upconverting nanocrystals, *Journal of Materials Chemistry* 19 (36) (2009) 6481-6484.
- [68] Yu, M., Li, F., Chen, Z., Hu, H., Zhan, C., Yang, H., Huang, C., Laser Scanning Up-Conversion Luminescence Microscopy for Imaging Cells Labeled with Rare-Earth Nanophosphors, *Analytical Chemistry* 81 (3) (2009) 930-935.
- [69] Lu, Y., Zhao, J., Zhang, R., Liu, Y., Liu, D., Goldys, E.M., Yang, X., Xi, P., Sunna, A., Lu, J., Shi, Y., Leif, R.C., Huo, Y., Shen, J., Piper, J.A., Robinson, J.P., Jin, D., Tunable lifetime multiplexing using luminescent nanocrystals, *Nat Photon* 8 (1) (2014) 32-36.
- [70] Wilhelm, S., Perspectives for Upconverting Nanoparticles, *ACS Nano* (2017).
- [71] Hou, Y., Qiao, R., Fang, F., Wang, X., Dong, C., Liu, K., Liu, C., Liu, Z., Lei, H., Wang, F., NaGdF₄ nanoparticle-based molecular probes for magnetic resonance imaging of intraperitoneal tumor xenografts in vivo, *ACS nano* 7 (1) (2012) 330-338.
- [72] Johnson, N.J., Oakden, W., Stanisiz, G.J., Scott Prosser, R., van Veggel, F.C., Size-tunable, ultrasmall NaGdF₄ nanoparticles: insights into their T1 MRI contrast enhancement, *Chemistry of Materials* 23 (16) (2011) 3714-3722.
- [73] He, M., Huang, P., Zhang, C., Hu, H., Bao, C., Gao, G., He, R., Cui, D., Dual phase-controlled synthesis of uniform lanthanide-doped NaGdF₄ upconversion nanocrystals via an OA/ionic liquid two-phase system for in vivo dual-modality imaging, *Advanced Functional Materials* 21 (23) (2011) 4470-4477.
- [74] Ni, D., Zhang, J., Bu, W., Zhang, C., Yao, Z., Xing, H., Wang, J., Duan, F., Liu, Y., Fan, W., PEGylated NaHoF₄ nanoparticles as contrast agents for both X-ray computed tomography and ultra-high field magnetic resonance imaging, *Biomaterials* 76 (2016) 218-225.
- [75] Ni, D., Bu, W., Zhang, S., Zheng, X., Li, M., Xing, H., Xiao, Q., Liu, Y., Hua, Y., Zhou, L., Single Ho³⁺-Doped Upconversion Nanoparticles for High-Performance T₂-Weighted Brain Tumor Diagnosis and MR/UCL/CT Multimodal Imaging, *Advanced Functional Materials* 24 (42) (2014) 6613-6620.
- [76] Dong, H., Du, S.-R., Zheng, X.-Y., Lyu, G.-M., Sun, L.-D., Li, L.-D., Zhang, P.-Z., Zhang, C., Yan, C.-H., Lanthanide Nanoparticles: From Design toward Bioimaging and Therapy, *Chemical Reviews* 115 (19) (2015) 10725-10815.
- [77] Wu, Y., Sun, Y., Zhu, X., Liu, Q., Cao, T., Peng, J., Yang, Y., Feng, W., Li, F., Lanthanide-based nanocrystals as dual-modal probes for SPECT and X-ray CT imaging, *Biomaterials* 35 (16) (2014) 4699-4705.

- [78] Yang, Y., Sun, Y., Cao, T., Peng, J., Liu, Y., Wu, Y., Feng, W., Zhang, Y., Li, F., Hydrothermal synthesis of NaLuF₄: 153 Sm, Yb, Tm nanoparticles and their application in dual-modality upconversion luminescence and SPECT bioimaging, *Biomaterials* 34 (3) (2013) 774-783.
- [79] Rieffel, J., Chen, F., Kim, J., Chen, G., Shao, W., Shao, S., Chitgupi, U., Hernandez, R., Graves, S.A., Nickles, R.J., Hexamodal Imaging with Porphyrin-Phospholipid-Coated Upconversion Nanoparticles, *Advanced Materials* 27 (10) (2015) 1785-1790.
- [80] Lee, J., Lee, T.S., Ryu, J., Hong, S., Kang, M., Im, K., Kang, J.H., Lim, S.M., Park, S., Song, R., RGD Peptide-Conjugated Multimodal NaGdF₄: Yb³⁺/Er³⁺ Nanophosphors for Upconversion Luminescence, MR, and PET Imaging of Tumor Angiogenesis, *Journal of Nuclear Medicine* 54 (1) (2013) 96-103.
- [81] Sun, Y., Zhu, X., Peng, J., Li, F., Core-Shell Lanthanide Upconversion Nanophosphors as Four-Modal Probes for Tumor Angiogenesis Imaging, *ACS Nano* 7 (12) (2013) 11290-11300.
- [82] Wang, F., Wang, J., Liu, X., Direct Evidence of a Surface Quenching Effect on Size-Dependent Luminescence of Upconversion Nanoparticles, *Angewandte Chemie* 122 (41) (2010) 7618-7622.
- [83] Zhao, J., Lu, Z., Yin, Y., McRae, C., Piper, J.A., Dawes, J.M., Jin, D., Goldys, E.M., Upconversion luminescence with tunable lifetime in NaYF₄:Yb,Er nanocrystals: role of nanocrystal size, *Nanoscale* 5 (3) (2013) 944-952.
- [84] Chen, F., Bu, W., Zhang, S., Liu, X., Liu, J., Xing, H., Xiao, Q., Zhou, L., Peng, W., Wang, L., Shi, J., Positive and Negative Lattice Shielding Effects Co-existing in Gd (III) Ion Doped Bifunctional Upconversion Nanoprobes, *Advanced Functional Materials* 21 (22) (2011) 4285-4294.
- [85] Johnson, N.J.J., Oakden, W., Stanisz, G.J., Scott Prosser, R., van Veggel, F.C.J.M., Size-Tunable, Ultrasmall NaGdF₄ Nanoparticles: Insights into Their T₁ MRI Contrast Enhancement, *Chemistry of Materials* 23 (16) (2011) 3714-3722.
- [86] Park, J.Y., Baek, M.J., Choi, E.S., Woo, S., Kim, J.H., Kim, T.J., Jung, J.C., Chae, K.S., Chang, Y., Lee, G.H., Paramagnetic Ultrasmall Gadolinium Oxide Nanoparticles as Advanced T₁ MRI Contrast Agent: Account for Large Longitudinal Relaxivity, Optimal Particle Diameter, and In Vivo T₁ MR Images, *ACS Nano* 3 (11) (2009) 3663-3669.
- [87] Zhuo, Z., Liu, Y., Liu, D., Huang, P., Jiang, F., Chen, X., Hong, M., Manipulating energy transfer in lanthanide-doped single nanoparticles for highly enhanced upconverting luminescence, *Chemical Science* (2017).
- [88] Ding, B.-B., Peng, H.-Y., Qian, H.-S., Zheng, L., Yu, S.-H., Unique Upconversion Core-Shell Nanoparticles with Tunable Fluorescence Synthesized by a Sequential Growth Process, *Advanced Materials Interfaces* 3 (3) (2016) 1500649-n/a.
- [89] Wen, H.-Q., Peng, H.-Y., Liu, K., Bian, M.-H., Xu, Y.-J., Dong, L., Yan, X., Xu, W.-P., Tao, W., Shen, J.-L., Lu, Y., Qian, H.-S., Sequential Growth of NaYF₄:Yb/Er@NaGdF₄ Nanodumbbells for Dual-Modality Fluorescence and Magnetic Resonance Imaging, *ACS Applied Materials & Interfaces* 9 (11) (2017) 9226-9232.
- [90] Xu, B., Zhang, X., Huang, W., Yang, Y., Ma, Y., Gu, Z., Zhai, T., Zhao, Y., Nd³⁺ sensitized dumbbell-like upconversion nanoparticles for photodynamic therapy application, *Journal of Materials Chemistry B* 4 (16) (2016) 2776-2784.

- [91] Park, J., Joo, J., Kwon, S.G., Jang, Y., Hyeon, T., Synthesis of Monodisperse Spherical Nanocrystals, *Angewandte Chemie International Edition* 46 (25) (2007) 4630-4660.
- [92] van Embden, J., Chesman, A.S.R., Jasieniak, J.J., The Heat-Up Synthesis of Colloidal Nanocrystals, *Chemistry of Materials* 27 (7) (2015) 2246-2285.
- [93] Faraday, M., The Bakerian lecture: experimental relations of gold (and other metals) to light, *Philosophical Transactions of the Royal Society of London* 147 (1857) 145-181.
- [94] Jana, N.R., Gearheart, L., Murphy, C.J., Wet chemical synthesis of high aspect ratio cylindrical gold nanorods, *The Journal of Physical Chemistry B* 105 (19) (2001) 4065-4067.
- [95] Burda, C., Chen, X., Narayanan, R., El-Sayed, M.A., Chemistry and Properties of Nanocrystals of Different Shapes, *Chemical Reviews* 105 (4) (2005) 1025-1102.
- [96] Thanh, N.T.K., Maclean, N., Mahiddine, S., Mechanisms of Nucleation and Growth of Nanoparticles in Solution, *Chemical Reviews* 114 (15) (2014) 7610-7630.
- [97] LaMer, V.K., Dinegar, R.H., Theory, Production and Mechanism of Formation of Monodispersed Hydrosols, *Journal of the American Chemical Society* 72 (11) (1950) 4847-4854.
- [98] Abécassis, B., Bouet, C., Garnero, C., Constantin, D., Lequeux, N., Ithurria, S., Dubertret, B., Pauw, B.R., Pontoni, D., Real-Time in Situ Probing of High-Temperature Quantum Dots Solution Synthesis, *Nano Letters* 15 (4) (2015) 2620-2626.
- [99] Yu, L., Yan, Z., Cai, Z., Zhang, D., Han, P., Cheng, X., Sun, Y., Quantitatively in Situ Imaging Silver Nanowire Hollowing Kinetics, *Nano Letters* 16 (10) (2016) 6555-6559.
- [100] Liao, H.-G., Zheng, H., Liquid Cell Transmission Electron Microscopy, *Annual Review of Physical Chemistry* 67 (1) (2016) 719-747.
- [101] Sun, Y., Ren, Y., In Situ Synchrotron X-Ray Techniques for Real-Time Probing of Colloidal Nanoparticle Synthesis, *Particle & Particle Systems Characterization* 30 (5) (2013) 399-419.
- [102] Harada, M., Kamigaito, Y., Nucleation and Aggregative Growth Process of Platinum Nanoparticles Studied by in Situ Quick XAFS Spectroscopy, *Langmuir* 28 (5) (2012) 2415-2428.
- [103] Ohyama, J., Teramura, K., Higuchi, Y., Shishido, T., Hitomi, Y., Kato, K., Tanida, H., Uruga, T., Tanaka, T., In Situ Observation of Nucleation and Growth Process of Gold Nanoparticles by Quick XAFS Spectroscopy, *ChemPhysChem* 12 (1) (2011) 127-131.
- [104] Sun, Y., Interfaced heterogeneous nanodimers, *National Science Review* 2 (3) (2015) 329-348.
- [105] Wagner, C., Theorie der alterung von niederschlägen durch umlösen (Ostwald-reifung), *Zeitschrift für Elektrochemie, Berichte der Bunsengesellschaft für physikalische Chemie* 65 (7-8) (1961) 581-591.
- [106] Talapin, D.V., Rogach, A.L., Haase, M., Weller, H., Evolution of an Ensemble of Nanoparticles in a Colloidal Solution: Theoretical Study, *The Journal of Physical Chemistry B* 105 (49) (2001) 12278-12285.
- [107] Zhou, J., Liu, Q., Feng, W., Sun, Y., Li, F., Upconversion Luminescent Materials: Advances and Applications, *Chem Rev* 115 (1) (2015) 395-465.
- [108] Wang, F., Liu, X., Recent advances in the chemistry of lanthanide-doped upconversion nanocrystals, *Chem Soc Rev* 38 (4) (2009) 976-989.

- [109] Mai, H.-X., Zhang, Y.-W., Si, R., Yan, Z.-G., Sun, L.-d., You, L.-P., Yan, C.-H., High-Quality Sodium Rare-Earth Fluoride Nanocrystals: Controlled Synthesis and Optical Properties, *Journal of the American Chemical Society* 128 (19) (2006) 6426-6436.
- [110] Zhang, Y.-W., Sun, X., Si, R., You, L.-P., Yan, C.-H., Single-Crystalline and Monodisperse LaF₃ Triangular Nanoplates from a Single-Source Precursor, *Journal of the American Chemical Society* 127 (10) (2005) 3260-3261.
- [111] Du, Y.-P., Zhang, Y.-W., Sun, L.-D., Yan, C.-H., Luminescent Monodisperse Nanocrystals of Lanthanide Oxyfluorides Synthesized from Trifluoroacetate Precursors in High-Boiling Solvents, *The Journal of Physical Chemistry C* 112 (2) (2008) 405-415.
- [112] Du, Y.-P., Zhang, Y.-W., Yan, Z.-G., Sun, L.-D., Yan, C.-H., Highly Luminescent Self-Organized Sub-2-nm EuOF Nanowires, *Journal of the American Chemical Society* 131 (45) (2009) 16364-16365.
- [113] Du, Y.-P., Zhang, Y.-W., Sun, L.-D., Yan, C.-H., Atomically Efficient Synthesis of Self-assembled Monodisperse and Ultrathin Lanthanide Oxychloride Nanoplates, *Journal of the American Chemical Society* 131 (9) (2009) 3162-3163.
- [114] Ye, X., Chen, J., Engel, M., Millan, J.A., Li, W., Qi, L., Xing, G., Collins, J.E., Kagan, C.R., Li, J., Glotzer, S.C., Murray, C.B., Competition of shape and interaction patchiness for self-assembling nanoplates, *Nature Chemistry* 5 (2013) 466.
- [115] Ye, X., Collins, J.E., Kang, Y., Chen, J., Chen, D.T.N., Yodh, A.G., Murray, C.B., Morphologically controlled synthesis of colloidal upconversion nanophosphors and their shape-directed self-assembly, *Proceedings of the National Academy of Sciences* 107 (52) (2010) 22430-22435.
- [116] Wang, X., Zhuang, J., Peng, Q., Li, Y., A general strategy for nanocrystal synthesis, *Nature* 437 (2005) 121.
- [117] Wang, L., Li, Y., Controlled Synthesis and Luminescence of Lanthanide Doped NaYF₄ Nanocrystals, *Chemistry of Materials* 19 (4) (2007) 727-734.
- [118] Wang, L., Li, Y., Na(Y_{1.5}Na_{0.5})F₆ Single-Crystal Nanorods as Multicolor Luminescent Materials, *Nano Letters* 6 (8) (2006) 1645-1649.
- [119] Wang, F., Han, Y., Lim, C.S., Lu, Y., Wang, J., Xu, J., Chen, H., Zhang, C., Hong, M., Liu, X., Simultaneous phase and size control of upconversion nanocrystals through lanthanide doping, *Nature* 463 (7284) (2010) 1061-1065.
- [120] Zhang, F., Wan, Y., Yu, T., Zhang, F., Shi, Y., Xie, S., Li, Y., Xu, L., Tu, B., Zhao, D., Uniform Nanostructured Arrays of Sodium Rare-Earth Fluorides for Highly Efficient Multicolor Upconversion Luminescence, *Angewandte Chemie International Edition* 46 (42) (2007) 7976-7979.
- [121] Mai, H.-X., Sun, L.-D., Zhang, Y.-W., Si, R., Feng, W., Zhang, H.-P., Liu, H.-C., Yan, C.-H., Shape-Selective Synthesis and Oxygen Storage Behavior of Ceria Nanopolyhedra, Nanorods, and Nanocubes, *The Journal of Physical Chemistry B* 109 (51) (2005) 24380-24385.
- [122] Kaneko, K., Inoke, K., Freitag, B., Hungria, A.B., Midgley, P.A., Hansen, T.W., Zhang, J., Ohara, S., Adschiri, T., Structural and Morphological Characterization of Cerium Oxide Nanocrystals Prepared by Hydrothermal Synthesis, *Nano Letters* 7 (2) (2007) 421-425.
- [123] Qian, L., Zhu, J., Du, W., Qian, X., Solvothermal synthesis, electrochemical and photocatalytic properties of monodispersed CeO₂ nanocubes, *Materials Chemistry and Physics* 115 (2) (2009) 835-840.

- [124] Ke, J., Xiao, J.-W., Zhu, W., Liu, H., Si, R., Zhang, Y.-W., Yan, C.-H., Dopant-Induced Modification of Active Site Structure and Surface Bonding Mode for High-Performance Nanocatalysts: CO Oxidation on Capping-free (110)-oriented CeO₂:Ln (Ln = La–Lu) Nanowires, *Journal of the American Chemical Society* 135 (40) (2013) 15191-15200.
- [125] Li, Z., Zhang, Y., An efficient and user-friendly method for the synthesis of hexagonal-phase NaYF₄:Yb, Er/Tm nanocrystals with controllable shape and upconversion fluorescence, *Nanotechnology* 19 (34) (2008) 345606.
- [126] Qian, H.S., Guo, H.C., Ho, P.C.-L., Mahendran, R., Zhang, Y., Mesoporous-Silica-Coated Up-Conversion Fluorescent Nanoparticles for Photodynamic Therapy, *Small* 5 (20) (2009) 2285-2290.
- [127] Li, Z., Zhang, Y., Jiang, S., Multicolor Core/Shell-Structured Upconversion Fluorescent Nanoparticles, *Advanced Materials* 20 (24) (2008) 4765-4769.
- [128] HaiSheng, Q., ZhengQuan, L., Yong, Z., Multicolor polystyrene nanospheres tagged with up-conversion fluorescent nanocrystals, *Nanotechnology* 19 (25) (2008) 255601.
- [129] Shi, F., Wang, J., Zhang, D., Qin, G., Qin, W., Greatly enhanced size-tunable ultraviolet upconversion luminescence of monodisperse [small beta]-NaYF₄:Yb,Tm nanocrystals, *Journal of Materials Chemistry* 21 (35) (2011) 13413-13421.
- [130] Chen, G., Ohulchanskyy, T.Y., Law, W.C., Agren, H., Prasad, P.N., Monodisperse NaYbF₄:Tm³⁺/NaGdF₄ core/shell nanocrystals with near-infrared to near-infrared upconversion photoluminescence and magnetic resonance properties, *Nanoscale* 3 (5) (2011) 2003-2008.
- [131] Das, G.K., Johnson, N.J.J., Cramen, J., Blasiak, B., Latta, P., Tomanek, B., van Veggel, F.C.J.M., NaDyF₄ Nanoparticles as T2 Contrast Agents for Ultrahigh Field Magnetic Resonance Imaging, *The Journal of Physical Chemistry Letters* 3 (4) (2012) 524-529.
- [132] Chen, G., Ohulchanskyy, T.Y., Liu, S., Law, W.-C., Wu, F., Swihart, M.T., Ågren, H., Prasad, P.N., Core/Shell NaGdF₄:Nd³⁺/NaGdF₄ Nanocrystals with Efficient Near-Infrared to Near-Infrared Downconversion Photoluminescence for Bioimaging Applications, *ACS Nano* 6 (4) (2012) 2969-2977.
- [133] Shi, F., Wang, J., Zhai, X., Zhao, D., Qin, W., Facile synthesis of [small beta]-NaLuF₄:Yb/Tm hexagonal nanoplates with intense ultraviolet upconversion luminescence, *CrystEngComm* 13 (11) (2011) 3782-3787.
- [134] Park, Y.I., Kim, H.M., Kim, J.H., Moon, K.C., Yoo, B., Lee, K.T., Lee, N., Choi, Y., Park, W., Ling, D., Na, K., Moon, W.K., Choi, S.H., Park, H.S., Yoon, S.-Y., Suh, Y.D., Lee, S.H., Hyeon, T., Theranostic Probe Based on Lanthanide-Doped Nanoparticles for Simultaneous In Vivo Dual-Modal Imaging and Photodynamic Therapy, *Advanced Materials* 24 (42) (2012) 5755-5761.
- [135] Nam, S.H., Bae, Y.M., Park, Y.I., Kim, J.H., Kim, H.M., Choi, J.S., Lee, K.T., Hyeon, T., Suh, Y.D., Long-Term Real-Time Tracking of Lanthanide Ion Doped Upconverting Nanoparticles in Living Cells, *Angewandte Chemie International Edition* 50 (27) (2011) 6093-6097.
- [136] Wang, F., Deng, R., Wang, J., Wang, Q., Han, Y., Zhu, H., Chen, X., Liu, X., Tuning upconversion through energy migration in core-shell nanoparticles, *Nat Mater* 10 (12) (2011) 968-973.
- [137] Pichaandi, J., Boyer, J.-C., Delaney, K.R., van Veggel, F.C.J.M., Two-Photon Upconversion Laser (Scanning and Wide-Field) Microscopy Using Ln³⁺-Doped NaYF₄ Upconverting Nanocrystals: A

Critical Evaluation of their Performance and Potential in Bioimaging, *The Journal of Physical Chemistry C* 115 (39) (2011) 19054-19064.

[138] Deng, R., Xie, X., Vendrell, M., Chang, Y.-T., Liu, X., Intracellular Glutathione Detection Using MnO₂-Nanosheet-Modified Upconversion Nanoparticles, *Journal of the American Chemical Society* 133 (50) (2011) 20168-20171.

[139] Abel, K.A., Boyer, J.-C., Veggel, F.C.J.M.v., Hard Proof of the NaYF₄/NaGdF₄ Nanocrystal Core/Shell Structure, *Journal of the American Chemical Society* 131 (41) (2009) 14644-14645.

[140] Dong, C., Pichaandi, J., Regier, T., van Veggel, F.C.J.M., Nonstatistical Dopant Distribution of Ln³⁺-Doped NaGdF₄ Nanoparticles, *The Journal of Physical Chemistry C* 115 (32) (2011) 15950-15958.

[141] Wang, F., Deng, R., Liu, X., Preparation of core-shell NaGdF₄ nanoparticles doped with luminescent lanthanide ions to be used as upconversion-based probes, *Nat. Protocols* 9 (7) (2014) 1634-1644.

[142] Liu, C., Wang, H., Zhang, X., Chen, D., Morphology- and phase-controlled synthesis of monodisperse lanthanide-doped NaGdF₄ nanocrystals with multicolor photoluminescence, *Journal of Materials Chemistry* 19 (4) (2009) 489-496.

[143] Liu, C., Wang, H., Li, X., Chen, D., Monodisperse, size-tunable and highly efficient [small beta]-NaYF₄:Yb,Er(Tm) up-conversion luminescent nanospheres: controllable synthesis and their surface modifications, *Journal of Materials Chemistry* 19 (21) (2009) 3546-3553.

[144] Li, X., Gai, S., Li, C., Wang, D., Niu, N., He, F., Yang, P., Monodisperse Lanthanide Fluoride Nanocrystals: Synthesis and Luminescent Properties, *Inorganic Chemistry* 51 (7) (2012) 3963-3971.

[145] Longyi, B., Zhengquan, L., Qingling, T., Jianjian, X., Yuanyuan, M., Yujie, X., Controlled synthesis of uniform LaF₃ polyhedrons, nanorods and nanoplates using NaOH and ligands, *Nanotechnology* 24 (14) (2013) 145604.

[146] Teng, X., Zhu, Y., Wei, W., Wang, S., Huang, J., Naccache, R., Hu, W., Tok, A.I.Y., Han, Y., Zhang, Q., Fan, Q., Huang, W., Capobianco, J.A., Huang, L., Lanthanide-Doped Na_xScF_{3+x} Nanocrystals: Crystal Structure Evolution and Multicolor Tuning, *Journal of the American Chemical Society* 134 (20) (2012) 8340-8343.

[147] Ding, Y., Teng, X., Zhu, H., Wang, L., Pei, W., Zhu, J.-J., Huang, L., Huang, W., Orthorhombic KSc₂F₇:Yb/Er nanorods: controlled synthesis and strong red upconversion emission, *Nanoscale* 5 (23) (2013) 11928-11932.

[148] Sun, X., Zhang, Y.-W., Du, Y.-P., Yan, Z.-G., Si, R., You, L.-P., Yan, C.-H., From Trifluoroacetate Complex Precursors to Monodisperse Rare-Earth Fluoride and Oxyfluoride Nanocrystals with Diverse Shapes through Controlled Fluorination in Solution Phase, *Chemistry – A European Journal* 13 (8) (2007) 2320-2332.

[149] Wang, J., Song, H., Xu, W., Dong, B., Xu, S., Chen, B., Yu, W., Zhang, S., Phase transition, size control and color tuning of NaREF₄:Yb³⁺, Er³⁺ (RE = Y, Lu) nanocrystals, *Nanoscale* 5 (8) (2013) 3412-3420.

[150] Huang, W., Lu, C., Jiang, C., Wang, W., Song, J., Ni, Y., Xu, Z., Controlled synthesis of NaYF₄ nanoparticles and upconversion properties of NaYF₄:Yb, Er (Tm)/FC transparent nanocomposite thin films, *Journal of Colloid and Interface Science* 376 (1) (2012) 34-39.

- [151] Liu, C., Gao, Z., Zeng, J., Hou, Y., Fang, F., Li, Y., Qiao, R., Shen, L., Lei, H., Yang, W., Gao, M., Magnetic/Upconversion Fluorescent NaGdF₄:Yb,Er Nanoparticle-Based Dual-Modal Molecular Probes for Imaging Tiny Tumors in Vivo, *ACS Nano* 7 (8) (2013) 7227-7240.
- [152] Hiramatsu, H., Osterloh, F.E., A Simple Large-Scale Synthesis of Nearly Monodisperse Gold and Silver Nanoparticles with Adjustable Sizes and with Exchangeable Surfactants, *Chemistry of Materials* 16 (13) (2004) 2509-2511.
- [153] Yamada, H., Urata, C., Higashitamori, S., Aoyama, Y., Yamauchi, Y., Kuroda, K., Critical Roles of Cationic Surfactants in the Preparation of Colloidal Mesostructured Silica Nanoparticles: Control of Mesostructure, Particle Size, and Dispersion, *ACS Applied Materials & Interfaces* 6 (5) (2014) 3491-3500.
- [154] Liu, X., Zhang, X., Tian, G., Yin, W., Yan, L., Ruan, L., Yang, Z., Xiao, D., Gu, Z., A simple and efficient synthetic route for preparation of NaYF₄ upconversion nanoparticles by thermo-decomposition of rare-earth oleates, *CrystEngComm* 16 (25) (2014) 5650-5661.
- [155] Ostrowski, A.D., Chan, E.M., Gargas, D.J., Katz, E.M., Han, G., Schuck, P.J., Milliron, D.J., Cohen, B.E., Controlled Synthesis and Single-Particle Imaging of Bright, Sub-10 nm Lanthanide-Doped Upconverting Nanocrystals, *ACS Nano* 6 (3) (2012) 2686-2692.
- [156] Gargas, D.J., Chan, E.M., Ostrowski, A.D., Aloni, S., Altoe, M.V.P., Barnard, E.S., Sanii, B., Urban, J.J., Milliron, D.J., Cohen, B.E., Schuck, P.J., Engineering bright sub-10-nm upconverting nanocrystals for single-molecule imaging, *Nat Nano* 9 (4) (2014) 300-305.
- [157] Huo, Z., Chen, C., Chu, D., Li, H., Li, Y., Systematic Synthesis of Lanthanide Phosphate Nanocrystals, *Chemistry – A European Journal* 13 (27) (2007) 7708-7714.
- [158] Li, P., Peng, Q., Li, Y., Dual-Mode Luminescent Colloidal Spheres from Monodisperse Rare-Earth Fluoride Nanocrystals, *Advanced Materials* 21 (19) (2009) 1945-1948.
- [159] Bu, W., Chen, Z., Chen, F., Shi, J., Oleic Acid/Oleylamine Cooperative-Controlled Crystallization Mechanism for Monodisperse Tetragonal Bipyramid NaLa(MoO₄)₂ Nanocrystals, *The Journal of Physical Chemistry C* 113 (28) (2009) 12176-12185.
- [160] Li, Z., Zeng, J., Li, Y., Solvothermal Route to Synthesize Well-Dispersed YBO₃:Eu Nanocrystals, *Small* 3 (3) (2007) 438-443.
- [161] Wang, X., Zhuang, J., Peng, Q., Li, Y., Hydrothermal Synthesis of Rare-Earth Fluoride Nanocrystals, *Inorganic Chemistry* 45 (17) (2006) 6661-6665.
- [162] Wang, G., Peng, Q., Li, Y., Synthesis and upconversion luminescence of BaY₂F₈:Yb³⁺/Er³⁺ nanobelts, *Chemical Communications* 46 (40) (2010) 7528-7529.
- [163] Wang, L., Li, P., Li, Y., Down- and Up-Conversion Luminescent Nanorods, *Advanced Materials* 19 (20) (2007) 3304-3307.
- [164] Li, S., Xie, T., Peng, Q., Li, Y., Nucleation and Growth of CeF₃ and NaCeF₄ Nanocrystals, *Chemistry – A European Journal* 15 (11) (2009) 2512-2517.
- [165] Wang, G., Peng, Q., Li, Y., Luminescence Tuning of Upconversion Nanocrystals, *Chemistry – A European Journal* 16 (16) (2010) 4923-4931.
- [166] Ye, R., Qingbo, X., Wenqin, L., Renfu, L., Xueyuan, C., Optical properties and luminescence dynamics of Eu³⁺-doped terbium orthophosphate nanophosphors, *Nanotechnology* 22 (27) (2011) 275701.

- [167] Huo, Z., Chen, C., Li, Y., Self-assembly of uniform hexagonal yttrium phosphate nanocrystals, *Chemical Communications* (33) (2006) 3522-3524.
- [168] Zhang, F., Li, J., Shan, J., Xu, L., Zhao, D., Shape, Size, and Phase-Controlled Rare-Earth Fluoride Nanocrystals with Optical Up-Conversion Properties, *Chemistry – A European Journal* 15 (41) (2009) 11010-11019.
- [169] Xia, Y., Gilroy, K.D., Peng, H.-C., Xia, X., Seed-Mediated Growth of Colloidal Metal Nanocrystals, *Angewandte Chemie International Edition* 56 (1) (2017) 60-95.
- [170] Park, J., Lee, E., Hwang, N.-M., Kang, M., Kim, S.C., Hwang, Y., Park, J.-G., Noh, H.-J., Kim, J.-Y., Park, J.-H., Hyeon, T., One-Nanometer-Scale Size-Controlled Synthesis of Monodisperse Magnetic Iron Oxide Nanoparticles, *Angewandte Chemie International Edition* 44 (19) (2005) 2872-2877.
- [171] Jana, N.R., Gearheart, L., Murphy, C.J., Wet chemical synthesis of silver nanorods and nanowires of controllable aspect ratio, *Chemical Communications* (7) (2001) 617-618.
- [172] Jana, N.R., Gearheart, L., Murphy, C.J., Evidence for Seed-Mediated Nucleation in the Chemical Reduction of Gold Salts to Gold Nanoparticles, *Chemistry of Materials* 13 (7) (2001) 2313-2322.
- [173] Jana, N.R., Gearheart, L., Murphy, C.J., Seeding Growth for Size Control of 5–40 nm Diameter Gold Nanoparticles, *Langmuir* 17 (22) (2001) 6782-6786.
- [174] Yao, Q., Yuan, X., Fung, V., Yu, Y., Leong, D.T., Jiang, D.-e., Xie, J., Understanding seed-mediated growth of gold nanoclusters at molecular level, *Nature Communications* 8 (1) (2017) 927.
- [175] Niu, W., Li, Z.-Y., Shi, L., Liu, X., Li, H., Han, S., Chen, J., Xu, G., Seed-Mediated Growth of Nearly Monodisperse Palladium Nanocubes with Controllable Sizes, *Crystal Growth & Design* 8 (12) (2008) 4440-4444.
- [176] Zheng, Y., Zhong, X., Li, Z., Xia, Y., Successive, Seed-Mediated Growth for the Synthesis of Single-Crystal Gold Nanospheres with Uniform Diameters Controlled in the Range of 5–150 nm, *Particle & Particle Systems Characterization* 31 (2) (2014) 266-273.
- [177] Dreaden, E.C., Alkilany, A.M., Huang, X., Murphy, C.J., El-Sayed, M.A., The golden age: gold nanoparticles for biomedicine, *Chemical Society Reviews* 41 (7) (2012) 2740-2779.
- [178] Yang, X., Yang, M., Pang, B., Vara, M., Xia, Y., Gold Nanomaterials at Work in Biomedicine, *Chemical Reviews* 115 (19) (2015) 10410-10488.
- [179] Zhang, Q., Li, W., Moran, C., Zeng, J., Chen, J., Wen, L.-P., Xia, Y., Seed-Mediated Synthesis of Ag Nanocubes with Controllable Edge Lengths in the Range of 30–200 nm and Comparison of Their Optical Properties, *Journal of the American Chemical Society* 132 (32) (2010) 11372-11378.
- [180] Sun, S., Zeng, H., Size-Controlled Synthesis of Magnetite Nanoparticles, *Journal of the American Chemical Society* 124 (28) (2002) 8204-8205.
- [181] Nguyen, K.T., Zhao, Y., Engineered Hybrid Nanoparticles for On-Demand Diagnostics and Therapeutics, *Accounts of Chemical Research* 48 (12) (2015) 3016-3025.
- [182] Kovalenko, M.V., Manna, L., Cabot, A., Hens, Z., Talapin, D.V., Kagan, C.R., Klimov, V.I., Rogach, A.L., Reiss, P., Milliron, D.J., Guyot-Sionnest, P., Konstantatos, G., Parak, W.J., Hyeon, T., Korgel, B.A., Murray, C.B., Heiss, W., Prospects of Nanoscience with Nanocrystals, *ACS Nano* 9 (2) (2015) 1012-1057.

- [183] Khademhosseini, A., Chan, W.W.C., Chhowalla, M., Glotzer, S.C., Gogotsi, Y., Hafner, J.H., Hammond, P.T., Hersam, M.C., Javey, A., Kagan, C.R., Kotov, N.A., Lee, S.-T., Li, Y., Möhwald, H., Mulvaney, P.A., Nel, A.E., Parak, W.J., Penner, R.M., Rogach, A.L., Schaak, R.E., Stevens, M.M., Wee, A.T.S., Brinker, J., Chen, X., Chi, L., Crommie, M., Dekker, C., Farokhzad, O., Gerber, C., Ginger, D.S., Irvine, D.J., Kiessling, L.L., Kostarelos, K., Landes, C., Lee, T., Leggett, G.J., Liang, X.-J., Liz-Marzán, L., Millstone, J., Odom, T.W., Ozcan, A., Prato, M., Rao, C.N.R., Sailor, M.J., Weiss, E., Weiss, P.S., *Nanoscience and Nanotechnology Cross Borders*, ACS Nano 11 (2) (2017) 1123-1126.
- [184] Oldenburg, S.J., Averitt, R.D., Westcott, S.L., Halas, N.J., *Nanoengineering of optical resonances*, Chemical Physics Letters 288 (2) (1998) 243-247.
- [185] Salgueiriño-Maceira, V., Correa-Duarte, M.A., *Increasing the Complexity of Magnetic Core/Shell Structured Nanocomposites for Biological Applications*, Advanced Materials 19 (23) (2007) 4131-4144.
- [186] Balakrishnan, S., Bonder, M.J., Hadjipanayis, G.C., *Particle size effect on phase and magnetic properties of polymer-coated magnetic nanoparticles*, Journal of Magnetism and Magnetic Materials 321 (2) (2009) 117-122.
- [187] Caruso, F., *Nanoengineering of Particle Surfaces*, Advanced Materials 13 (1) (2001) 11-22.
- [188] Phadtare, S., Kumar, A., Vinod, V.P., Dash, C., Palaskar, D.V., Rao, M., Shukla, P.G., Sivaram, S., Sastry, M., *Direct Assembly of Gold Nanoparticle “Shells” on Polyurethane Microsphere “Cores” and Their Application as Enzyme Immobilization Templates*, Chemistry of Materials 15 (10) (2003) 1944-1949.
- [189] Qi, L., Ma, J., Cheng, H., Zhao, Z., *Synthesis and characterization of mixed CdS/ZnS nanoparticles in reverse micelles*, Colloids and Surfaces A: Physicochemical and Engineering Aspects 111 (3) (1996) 195-202.
- [190] Chen, X., Peng, D., Ju, Q., Wang, F., *Photon upconversion in core-shell nanoparticles*, Chemical Society Reviews 44 (6) (2015) 1318-1330.
- [191] Wang, Luo, J., Fan, Q., Suzuki, M., Suzuki, I.S., Engelhard, M.H., Lin, Y., Kim, N., Wang, J.Q., Zhong, C.-J., *Monodispersed Core-Shell Fe₃O₄@Au Nanoparticles*, The Journal of Physical Chemistry B 109 (46) (2005) 21593-21601.
- [192] Xuan, S., Wang, Y.-X.J., Yu, J.C., Leung, K.C.-F., *Preparation, Characterization, and Catalytic Activity of Core/Shell Fe₃O₄@Polyaniline@Au Nanocomposites*, Langmuir 25 (19) (2009) 11835-11843.
- [193] Zanella, R., Sandoval, A., Santiago, P., Basiuk, V.A., Saniger, J.M., *New Preparation Method of Gold Nanoparticles on SiO₂*, The Journal of Physical Chemistry B 110 (17) (2006) 8559-8565.
- [194] Ghosh Chaudhuri, R., Paria, S., *Core/Shell Nanoparticles: Classes, Properties, Synthesis Mechanisms, Characterization, and Applications*, Chemical Reviews 112 (4) (2012) 2373-2433.
- [195] Loo, C., Lin, A., Hirsch, L., Lee, M.-H., Barton, J., Halas, N., West, J., Drezek, R., *Nanoshell-Enabled Photonics-Based Imaging and Therapy of Cancer*, Technology in Cancer Research & Treatment 3 (1) (2004) 33-40.
- [196] Li, J.-F., Yang, Z.-L., Ren, B., Liu, G.-K., Fang, P.-P., Jiang, Y.-X., Wu, D.-Y., Tian, Z.-Q., *Surface-Enhanced Raman Spectroscopy Using Gold-Core Platinum-Shell Nanoparticle Film Electrodes: Toward a Versatile Vibrational Strategy for Electrochemical Interfaces*, Langmuir 22 (25) (2006) 10372-10379.

- [197] Hu, J.-W., Li, J.-F., Ren, B., Wu, D.-Y., Sun, S.-G., Tian, Z.-Q., Palladium-Coated Gold Nanoparticles with a Controlled Shell Thickness Used as Surface-Enhanced Raman Scattering Substrate, *The Journal of Physical Chemistry C* 111 (3) (2007) 1105-1112.
- [198] Hines, M.A., Guyot-Sionnest, P., Synthesis and Characterization of Strongly Luminescing ZnS-Capped CdSe Nanocrystals, *The Journal of Physical Chemistry* 100 (2) (1996) 468-471.
- [199] Peng, X., Schlamp, M.C., Kadavanich, A.V., Alivisatos, A.P., Epitaxial Growth of Highly Luminescent CdSe/CdS Core/Shell Nanocrystals with Photostability and Electronic Accessibility, *Journal of the American Chemical Society* 119 (30) (1997) 7019-7029.
- [200] Dabbousi, B.O., Rodriguez-Viejo, J., Mikulec, F.V., Heine, J.R., Mattoussi, H., Ober, R., Jensen, K.F., Bawendi, M.G., (CdSe)ZnS Core-Shell Quantum Dots: Synthesis and Characterization of a Size Series of Highly Luminescent Nanocrystallites, *The Journal of Physical Chemistry B* 101 (46) (1997) 9463-9475.
- [201] Mokari, T., Banin, U., Synthesis and Properties of CdSe/ZnS Core/Shell Nanorods, *Chemistry of Materials* 15 (20) (2003) 3955-3960.
- [202] Talapin, D.V., Rogach, A.L., Kornowski, A., Haase, M., Weller, H., Highly Luminescent Monodisperse CdSe and CdSe/ZnS Nanocrystals Synthesized in a Hexadecylamine-Trioctylphosphine Oxide-Trioctylphosphine Mixture, *Nano Letters* 1 (4) (2001) 207-211.
- [203] Kudera, S., Zanella, M., Giannini, C., Rizzo, A., Li, Y., Gigli, G., Cingolani, R., Ciccarella, G., Spahl, W., Parak, W.J., Manna, L., Sequential Growth of Magic-Size CdSe Nanocrystals, *Advanced Materials* 19 (4) (2007) 548-552.
- [204] Li, X., Zhang, F., Zhao, D., Lab on upconversion nanoparticles: optical properties and applications engineering via designed nanostructure, *Chemical Society Reviews* 44 (6) (2015) 1346-1378.
- [205] Chen, G., Ågren, H., Ohulchanskyy, T.Y., Prasad, P.N., Light upconverting core-shell nanostructures: nanophotonic control for emerging applications, *Chemical Society Reviews* 44 (6) (2015) 1680-1713.
- [206] Yi, G.-S., Chow, G.-M., Water-Soluble NaYF₄:Yb,Er(Tm)/NaYF₄/Polymer Core/Shell/Shell Nanoparticles with Significant Enhancement of Upconversion Fluorescence, *Chemistry of Materials* 19 (3) (2007) 341-343.
- [207] Xie, X., Gao, N., Deng, R., Sun, Q., Xu, Q.-H., Liu, X., Mechanistic Investigation of Photon Upconversion in Nd³⁺-Sensitized Core-Shell Nanoparticles, *Journal of the American Chemical Society* 135 (34) (2013) 12608-12611.
- [208] Wen, H., Zhu, H., Chen, X., Hung, T.F., Wang, B., Zhu, G., Yu, S.F., Wang, F., Upconverting Near-Infrared Light through Energy Management in Core-Shell-Shell Nanoparticles, *Angewandte Chemie International Edition* 52 (50) (2013) 13419-13423.
- [209] He, S., Johnson, N.J.J., Nguyen Huu, V.A., Cory, E., Huang, Y., Sah, R.L., Jokerst, J.V., Almutairi, A., Simultaneous Enhancement of Photoluminescence, MRI Relaxivity, and CT Contrast by Tuning the Interfacial Layer of Lanthanide Heteroepitaxial Nanoparticles, *Nano Lett* 17 (8) (2017) 4873-4880.
- [210] Zeng, H., Li, J., Wang, Z.L., Liu, J.P., Sun, S., Bimagnetic Core/Shell FePt/Fe₃O₄ Nanoparticles, *Nano Letters* 4 (1) (2004) 187-190.

- [211] Zeng, H., Li, J., Liu, J.P., Wang, Z.L., Sun, S., Exchange-coupled nanocomposite magnets by nanoparticle self-assembly, *Nature* 420 (2002) 395.
- [212] Carnes, C.L., Klabunde, K.J., Unique Chemical Reactivities of Nanocrystalline Metal Oxides toward Hydrogen Sulfide, *Chemistry of Materials* 14 (4) (2002) 1806-1811.
- [213] Han, W., Yi, L., Zhao, N., Tang, A., Gao, M., Tang, Z., Synthesis and Shape-Tailoring of Copper Sulfide/Indium Sulfide-Based Nanocrystals, *Journal of the American Chemical Society* 130 (39) (2008) 13152-13161.
- [214] Radi, A., Pradhan, D., Sohn, Y., Leung, K.T., Nanoscale Shape and Size Control of Cubic, Cuboctahedral, and Octahedral Cu–Cu₂O Core–Shell Nanoparticles on Si(100) by One-Step, Templateless, Capping-Agent-Free Electrodeposition, *ACS Nano* 4 (3) (2010) 1553-1560.
- [215] Huang, C.-C., Yang, Z., Chang, H.-T., Synthesis of Dumbbell-Shaped Au–Ag Core–Shell Nanorods by Seed-Mediated Growth under Alkaline Conditions, *Langmuir* 20 (15) (2004) 6089-6092.
- [216] Zeng, J., Zheng, Y., Rycenga, M., Tao, J., Li, Z.-Y., Zhang, Q., Zhu, Y., Xia, Y., Controlling the Shapes of Silver Nanocrystals with Different Capping Agents, *Journal of the American Chemical Society* 132 (25) (2010) 8552-8553.
- [217] Wang, Y., Wan, D., Xie, S., Xia, X., Huang, C.Z., Xia, Y., Synthesis of Silver Octahedra with Controlled Sizes and Optical Properties via Seed-Mediated Growth, *ACS Nano* 7 (5) (2013) 4586-4594.
- [218] Huang, X., Tang, S., Zhang, H., Zhou, Z., Zheng, N., Controlled Formation of Concave Tetrahedral/Trigonal Bipyramidal Palladium Nanocrystals, *Journal of the American Chemical Society* 131 (39) (2009) 13916-13917.
- [219] Sau, T.K., Rogach, A.L., Jäckel, F., Klar, T.A., Feldmann, J., Properties and Applications of Colloidal Nonspherical Noble Metal Nanoparticles, *Advanced Materials* 22 (16) (2010) 1805-1825.
- [220] Tréguer-Delapierre, M., Majimel, J., Mornet, S., Duguet, E., Ravaine, S., Synthesis of non-spherical gold nanoparticles, *Gold Bulletin* 41 (2) (2008) 195-207.
- [221] Narayanan, R., El-Sayed, M.A., Shape-Dependent Catalytic Activity of Platinum Nanoparticles in Colloidal Solution, *Nano Letters* 4 (7) (2004) 1343-1348.
- [222] Noguez, C., Surface Plasmons on Metal Nanoparticles: The Influence of Shape and Physical Environment, *The Journal of Physical Chemistry C* 111 (10) (2007) 3806-3819.
- [223] Liu, D., Xu, X., Du, Y., Qin, X., Zhang, Y., Ma, C., Wen, S., Ren, W., Goldys, E.M., Piper, J.A., Dou, S., Liu, X., Jin, D., Three-dimensional controlled growth of monodisperse sub-50 nm heterogeneous nanocrystals, *Nature Communications* 7 (2016) 10254.
- [224] Seo, J.T., Yang, Q., Kim, W.-J., Heo, J., Ma, S.-M., Austin, J., Yun, W.S., Jung, S.S., Han, S.W., Tabibi, B., Temple, D., Optical nonlinearities of Au nanoparticles and Au/Ag cores, *Opt. Lett.* 34 (3) (2009) 307-309.
- [225] Kelly, K.L., Coronado, E., Zhao, L.L., Schatz, G.C., The Optical Properties of Metal Nanoparticles: The Influence of Size, Shape, and Dielectric Environment, *The Journal of Physical Chemistry B* 107 (3) (2003) 668-677.
- [226] Ma, Y., Li, W., Cho, E.C., Li, Z., Yu, T., Zeng, J., Xie, Z., Xia, Y., Au@Ag Core–Shell Nanocubes with Finely Tuned and Well-Controlled Sizes, Shell Thicknesses, and Optical Properties, *ACS Nano* 4 (11) (2010) 6725-6734.

- [227] Mayer, M., Scarabelli, L., March, K., Altantzis, T., Tebbe, M., Kociak, M., Bals, S., García de Abajo, F.J., Fery, A., Liz-Marzán, L.M., Controlled Living Nanowire Growth: Precise Control over the Morphology and Optical Properties of AgAuAg Bimetallic Nanowires, *Nano Letters* 15 (8) (2015) 5427-5437.
- [228] Critchley, K., Khanal, B.P., Górzny, M.Ł., Vigderman, L., Evans, S.D., Zubarev, E.R., Kotov, N.A., Near-Bulk Conductivity of Gold Nanowires as Nanoscale Interconnects and the Role of Atomically Smooth Interface, *Advanced Materials* 22 (21) (2010) 2338-2342.
- [229] Sun, Y., Ren, Y., Liu, Y., Wen, J., Okasinski, J.S., Miller, D.J., Ambient-stable tetragonal phase in silver nanostructures, *Nature Communications* 3 (2012) 971.
- [230] Pietrobon, B., McEachran, M., Kitaev, V., Synthesis of Size-Controlled Faceted Pentagonal Silver Nanorods with Tunable Plasmonic Properties and Self-Assembly of These Nanorods, *ACS Nano* 3 (1) (2009) 21-26.

CHAPTER 2 Materials and Methods

2.1 General Chemicals and Reagents

The general chemicals and reagents used in the research work described in this report, with details of their manufacturer are listed in **Table 2.1**.

Table 2.1 Manufacturer details for chemicals and reagents.

Chemicals and Reagents	Purity	CAS number	Manufacturer
Yttrium(III) chloride hexahydrate ($\text{YCl}_3 \cdot 6\text{H}_2\text{O}$)	99.99% trace metals basis	10025-94-2	Sigma-Aldrich (Australia)
Ytterbium(III) chloride hexahydrate ($\text{YbCl}_3 \cdot 6\text{H}_2\text{O}$)	99.998% trace metals basis	10035-01-5	Sigma-Aldrich (Australia)
Thulium(III) chloride hexahydrate ($\text{TmCl}_3 \cdot 6\text{H}_2\text{O}$)	99.99% trace metals basis	1331-74-4	Sigma-Aldrich (Australia)
Erbium(III) chloride hexahydrate ($\text{ErCl}_3 \cdot 6\text{H}_2\text{O}$)	99.995% trace metals basis	10025-75-9	Sigma-Aldrich (Australia)
Dysprosium(III) chloride hexahydrate ($\text{DyCl}_3 \cdot 6\text{H}_2\text{O}$)	99.9% trace metals basis	15059-52-6	Sigma-Aldrich (Australia)
Gadolinium(III) chloride hexahydrate ($\text{GdCl}_3 \cdot 6\text{H}_2\text{O}$)	99% (titration)	13450-84-5	Sigma-Aldrich (Australia)
Lutetium(III) chloride hexahydrate ($\text{LuCl}_3 \cdot 6\text{H}_2\text{O}$)	99.9% trace metals basis	15230-79-2	Sigma-Aldrich (Australia)

Sodium hydroxide (NaOH)	semiconductor grade, 99.99% trace metals basis	1310-73-2	Sigma-Aldrich (Australia)
Ammonium fluoride (NH ₄ F)	≥ 99.99% trace metals basis	12125-01-8	Sigma-Aldrich (Australia)
Sodium fluoride (NaF)	99.99% trace metals basis	7681-49-4	Sigma-Aldrich (Australia)
Sodium Oleate (NaOA)	>97.0%(T)	143-19-1	TCI (Japan)
Oleic Acid (OA)	Technical grade, 90%	112-80-1	Sigma-Aldrich (Australia)
1-Octadecene (ODE)	Technical grade, 90%	112-88-9	Sigma-Aldrich (Australia)
Oleylamine (OM)	Technical grade, 70%	112-90-3	Sigma-Aldrich (Australia)
Ethanol	Undenatured 100%	64-17-5	Chem-Supply (Australia)
Methanol	for HPLC, ≥ 99.9%	67-56-1	Sigma-Aldrich (Australia)
Cyclohexane	for HPLC, ≥ 99.9%	110-82-7	Chem-Supply (Australia)
Tetrahydrofuran (THF)	anhydrous, ≥ 99.9%, inhibitor-free	109-99-9	Sigma-Aldrich (Australia)
Dopamine hydrochloride	98%	62-31-7	Sigma-Aldrich (Australia)

3,4-dihydroxyhydrocinnamic acid	98%	1078-61-1	Sigma-Aldrich (Australia)
mPEG-NHS	99%	NA	JenKem (China)
Biotain-PEG-NHS	98%	NA	JenKem (China)
IGEPAL [®] CO-520	NA	68412-54-4	Sigma-Aldrich (Australia)
Tetraethyl orthosilicate	≥99.0% (GC)	78-10-4	Sigma-Aldrich (Australia)
(3-Aminopropyl)triethoxysilane	≥98%	919-30-2	Sigma-Aldrich (Australia)
Ammonium hydroxide solution	ACS reagent, 28.0-30.0% NH ₃ basis	1336-21-6	Sigma-Aldrich (Australia)

2.2 Instruments and Equipment

The names of equipment and software used by the author and described in this thesis, and their respective manufacturer details, are listed in **Table 2.2**.

Table 2.2 Details of the instrument/equipment manufacturers.

Instrument/Equipment	Property	Manufacturer
Magnetic stirrer	0-1800 rpm	Labquip (Australia)
Heating mantle	Range room temperature to 400 °C	Labquip (Australia)

Temperature controller	Range room temperature to 400 °C	Labquip (Australia)
Three-neck round-bottom flask	50 mL, 100 mL	Synthware (China)
Flow control adapter	19/22	Synthware (China)
Teflon-coated, Elliptical rare earth extra power stir bars	15 × 10 mm	Sigma-Aldrich (Australia)
Micropipettes	ranges: 10–100 µl, 100–1,000 µl and 500–5,000 µl;	Eppendorf (Germany)
Centrifuge	Centrifuge 5424 Centrifuge 5804	Eppendorf (Germany)
Vortex mixer	LSE	Corning (Australia)
Ultrasonic cleaner	Commercial Benchtop Cleaners (FXP) 2.7 Liter	Unisonics (Australia)
Laboratory balance	SJF2104 (0.1 mg)	ProSciTech (Australia)

2.3 Home-made Instruments

2.3.1 Confocal microscope for single nanoparticles [1]

We built a laser scanning confocal microscope for the intensity measurement of single UCNPs as shown in **Fig. 2.1**. [1] The excitation source is a 976 nm single mode polarized laser (229 mW) which is focused onto the sample through a 100x objective lens (NA 1.4). The emission from sample is collecting by same objective lens then refocused into an optical fiber which has a core size matching with system Airy disk. A Single Photon Counting Avalanche Diode (SPAD) detector is connected to the collection optical fiber to detect the emission intensity. The scanning is achieved by moving the 3D piezo stage.

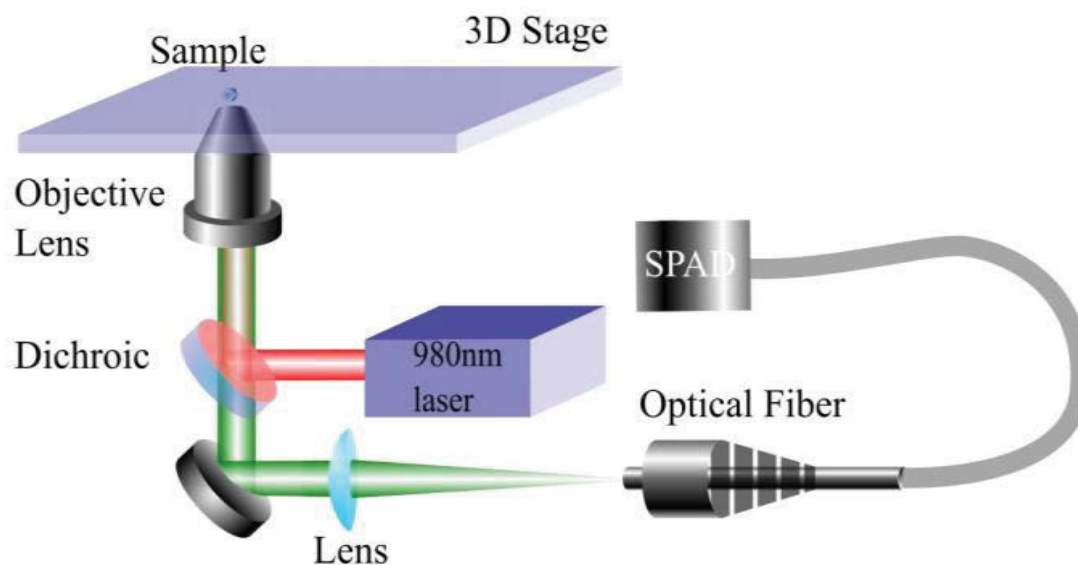


Figure 2.1 Schematic illustration of the system setup for customized scanning confocal microscope. Reproduced with permission from Ref.[1] Copyright (2016) American Chemical Society.

2.3.2 Dual-laser confocal/super-resolution microscope [2]

The optical system was built on a sample scanning configuration employing a 3-axis closed-loop piezo stage (stage body MAX311D/M, piezo controller BPC303; Thorlabs).[2] Illustrated in **Fig. 2.2**, a single-mode fibre-coupled 980 nm diode laser (LE-LS-980-300-FCS, LEO Photonics; maximum output power 300 mW) was used as the excitation source. After collimation, the excitation beam was transmitted through a long-pass dichroic mirror (ZT860lpxr, Chroma), then reflected by a second short-pass dichroic mirror (T750spxrxt, Chroma), and focused through an oil-immersion objective (UPlanAPO, Olympus; 100 \times , NA = 1.4) onto the sample slide. The first dichroic mirror also allowed the 808 nm probing beam from a polarization-maintaining fibre-coupled diode laser (LU0808M250-1C16F30A, Lumics; single mode, linear polarization, maximum output power 250 mW) to merge with the 980 nm beam. The luminescence signal from the sample was collected by the same objective, split from the excitation and probing beams by the second dichroic mirror, before being coupled into a multi-mode fibre (M24L01, Thorlabs). The other end of the fibre was connected to a single-photon avalanche diode (SPAD; SPCM-AQRH-13-FC, PerkinElmer) capable of being time-gated electronically. To select upconversion emission bands, different band-pass filters (FF01-448/20-25 and FF01-660/13-25, Semrock) were inserted in the detection path for both transient response measurement and confocal imaging. The distal end of the multi-

mode fibre could also be switched to a miniature monochromator (MicroHR Auto, Horiba) equipped with a second SPAD for measuring upconversion emission spectra.

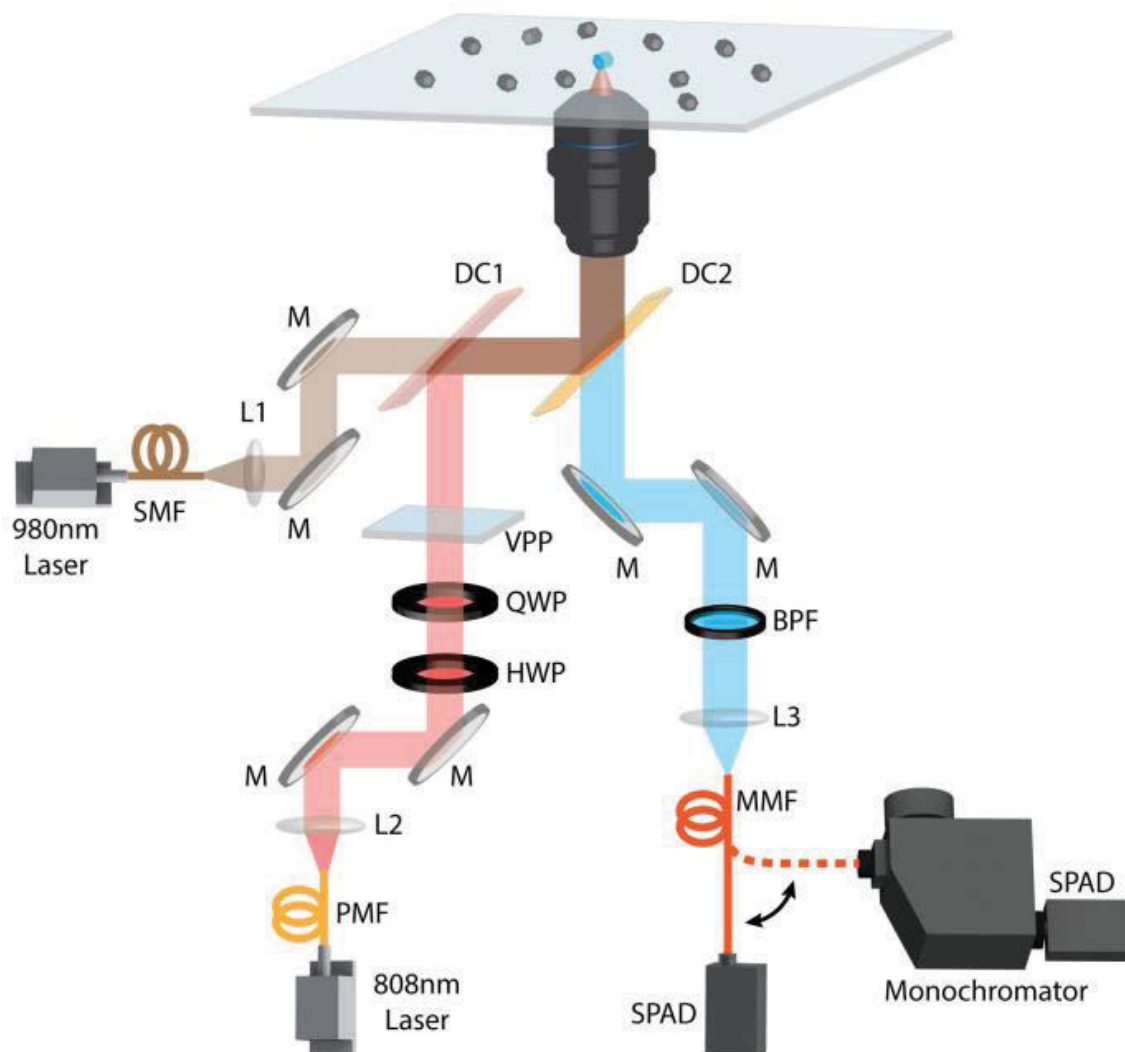


Figure 2.2 Optical layout of the dual-laser confocal/super-resolution microscope for probing $\text{NaYF}_4:\text{Yb,Tm}$ nanocrystals. SMF, single-mode fibre; PMF, polarization-maintaining fibre; MMF, multi-mode fibre; DC1 and DC2, dichroic filters; L1, L2 and L3, collimation/collection lenses; HWP, half-wave plate; QWP, quarter-wave plate; VPP, vortex phase plate; SPAD, single-photon avalanche diode; M, mirror. Reproduced with permission from Ref.[2] Copyright (2017) Macmillan Publishers Limited.

For acquiring optical super-resolution images, a quarter-wave plate (WPQ10M-808, Thorlabs) was used to first transform the 808 nm beam from linear polarization to circular polarization. In practice a half-wave plate (WPH10M-808, Thorlabs) was also used to facilitate the adjustment towards quality circular

polarization. Then, a vortex phase plate (VPP-1a, RPC Photonics) was inserted in the 808 nm beam path, so that a doughnut-shaped PSF was generated at the focal plane. In both cases of dual-laser confocal and super-resolution imaging, the two beams of 980 and 808 nm were carefully aligned to ensure precise overlapping of their PSFs in both X - Y and Z directions.

2.3.3 Multi-photon near-infrared emission saturation nanoscopy [3]

All the measurements were performed on a home-built microscopy system equipped with a 3-axis closed-loop piezo stage (stage body MAX311D/M, piezo controller BPC303; Thorlabs) and a vortex phase plate (VPP, VPP-1a, RPC Photonics). A schematic drawing of the experimental setup was presented in **Fig. 2.3**. [3] UCNPs were excited by a polarization-maintaining single-mode fiber-coupled 980 nm diode laser (BL976-PAG900, controller CLD1015, Thorlabs). The first half wave plate (HWP, WPH05M-980, Thorlabs) and polarized beam splitter (PBS, CCM1-PBS252/M, Thorlabs) were employed to precisely adjust the excitation power by rotating HWP electronically. The purpose of the second HWP was to turn the polarization from horizontal (P polarized) to vertical (S polarized). A doughnut-shaped point spread function (PSF) at the focal plane was generated by a VPP. Confocal scanning was acquired without the VPP via the auxiliary two flexible mirrors as shown in the dotted portion of **Figure** . After collimation, the excitation beam was reflected by the first short-pass dichroic mirror (DM 1, T875spxrxt-UF1, Chroma), and focused through a high numerical aperture objective (UPlanSApo, 100 \times /1.40 oil, Olympus) to the sample slide. A quarter-wave plate (QWP, WPQ05M-980, Thorlabs) was adopted to transform the excitation beam from linear polarization to circular polarization to obtain optical super-resolution images. Photoluminescence was collected by the same objective and split from the excitation beams by DM 1. The emission signals were filtered by band pass filters (BPF, ET805/20M, ET445/30M, Chroma; FF01-475/35-25, Semrock; ET750sp-2p8, Chroma with FGL695, Thorlabs) or short pass filter (SPF, FF01-842/SP-25, Semrock). Different emission bands were split from the fluorescence beam by the second short-pass dichroic mirror (DM 2, ZT785spxrxt-UF1, Chroma) and coupled into multi-mode fiber (MMF, M24L02, Thorlabs), then detected by a single-photon counting avalanche photodiode (SPAD, SPCM-AQRH-14-FC, Excelitas). The MMF could also be switched to a miniature monochromator (iHR550, Horiba) for measuring upconversion emission spectra. Typical excitation powers for the recording of super-resolution NIREs images varied from 5 mW to 100 mW. All powers were measured at the back aperture of the objective lens. Pixel dwell times were adjusted to be about 3 ms.

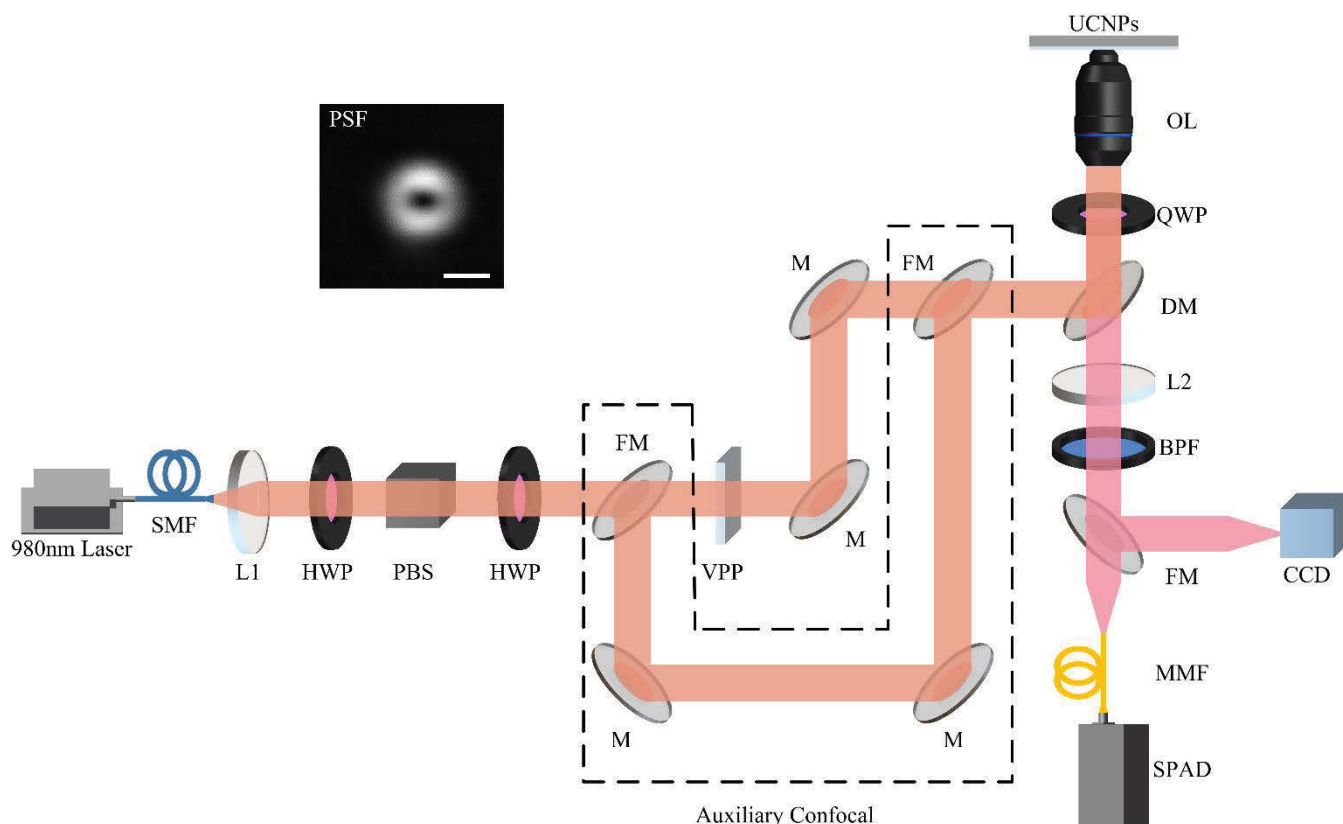


Figure 2.3 The experimental setup for NIREs nanoscopy (SMF, single-mode fiber; MMF, multi-mode fiber; L1, collimation lens; L2, collection lens; HWP, half-wave plate; QWP, quarter-wave plate; PBS, polarized beam splitter; VPP, vortex phase plate; M, mirror; FM, flexible mirror; DM, dichroic mirror; OL, objective lens; BPF, band pass filter; SPAD, single-photon avalanche diode; CCD, charge coupled device). The dotted portion is designed for an auxiliary confocal with two flexible mirrors to bypass the VPP in the main optical path. The inset: point spread function (PSF) of the NIREs is measured by light-scattering from 50 nm gold beads in reflection (its path is not shown). The scale bar: 500 nm. Reproduced from Ref.[3].

2.4 General NaREF₄ Nanocrystals Synthesis

2.4.1 One-pot synthesis

The precipitation of monodisperse nanoparticles in solution is governed by a temporal nucleation followed by growth of nanocrystals.[4] Due to the low energy difference between crystal nucleation and its growth, the synthesis of uniform NaREF₄ nanocrystals requires strict consideration of several experimental variables. These include its surfactant, reaction time, temperature and so on. The facile synthesis of NaREF₄ nanocrystals, performed by the author for this work, uses the co-precipitation of

$\text{Ln}(\text{OA})_3$ complexes prompted by NH_4F and NaOH reagents. Nucleation and growth phases are well separated by performing the reaction in two steps: one at a low ($50\text{ }^\circ\text{C}$) temperature and the other at a high ($300\text{ }^\circ\text{C}$) temperature. Long-chain hydrocarbons (ODE) and unsaturated fatty acids (OA) are used as the high boiling point solvent in this method.[4] OA also acts as the surfactant to control the nanocrystals growth and subsequently stabilizes the produced nanocrystals. Thanks to the small lattice mismatch between different type of NaREF_4 , different NaREF_4 lanthanide ions can be easily incorporated into one nanocrystal by varying the composition of the $\text{Ln}(\text{OA})_3$ precursors added. This enables the fine-tunable optical properties of the formed multifunctional nanocrystal as well as their cutting-edge sensing and imaging applications.

2.4.2 Core@shell nanostructure synthesis

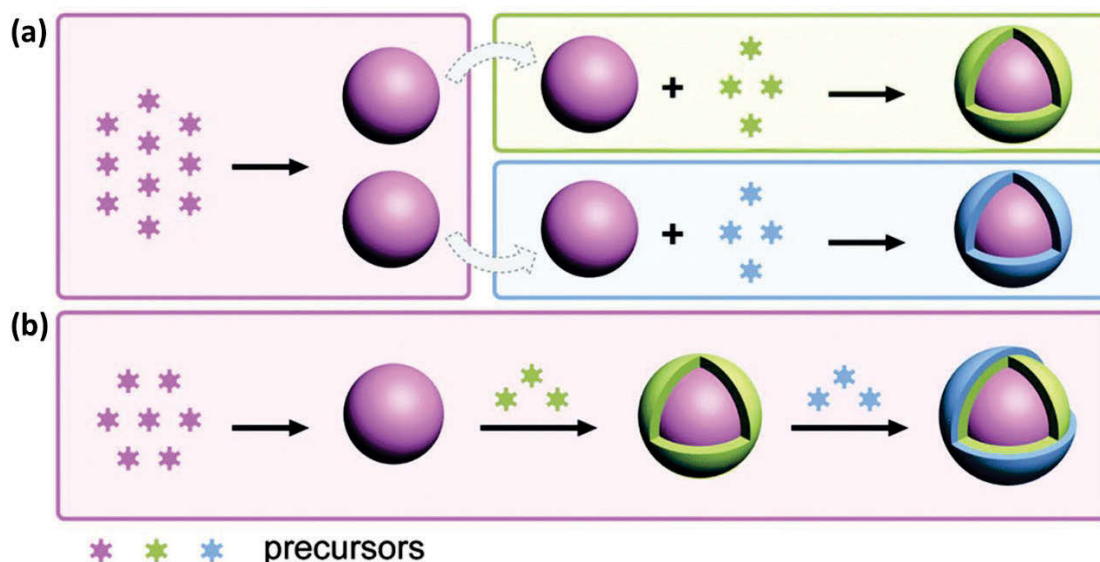


Figure 2.4 Common strategies for synthesis of core@shell nanoparticles via seed-mediated growth. (a) Facile tuning of the shell composition through a parallel heat-up of pre-synthesized core nanoparticles with varying shell precursors. (b) Rapid synthesis of multi-shelled nanoparticles through serial hot-injections of diverse shell precursors. Reproduced with permission from Ref.[7] Copyright (2015) Royal Society of Chemistry.

The usefulness of multifunctional core@shell UCNPs has led to significant improvements in their synthesis.[5, 6] Similar chemical procedure for seed nanocrystals synthesis can be employed for the shells growth, except that the precursors growth straight on the surface of preformed seed nanocrystals without the nucleation process. The classification of seed-mediated epitaxial growth approaches on UCNPs nanocrystal is commonly based on the process of combining the shell precursors in the reaction system. Therefore, the conventional core@shell synthesis procedures can be classified as the heat-up method and

hot-injection method (**Fig. 2.4**).[7, 8] In the heat-up method, the shell precursors are mixed with the preformed seed nanocrystals in high boiling point solvents. It is then heated to elevated temperatures to induce shell growth following an identical protocol for the seed synthesis (**Fig. 2.4a**). With hot-injection, shell precursors are injected directly into a fresh reaction solution containing pre-synthesized seed nanocrystals at higher temperatures (**Fig. 2.4b**). The major difference between each approach is the amount of shell precursor available in the growth solution and the growth rate of the nanocrystals that each produces.

2.4.2.1 Heat-up method

The idea of heat-up procedure to make core@shell nanocrystals was reported by Yan et al. and refined by Zhang et al. in 2008.[9, 10] In both studies, the seed nanocrystals were first synthesized and separated from their solvent. Shell precursors were fabricated and added to these seeds and subsequently heated to a high temperature to grow the shell layer. In this process, the monomer of shells in the growth solution were gradually deposited onto the seed particles to form shell layers. Also, the shell thickness can be fine-tuning by changing the ratio of shell precursors to seeds in the reaction mix. For instance, Zhao et al. reported the precise control over the shell thickness by heating NaYF₄:Yb/Er nanoparticles in OA and ODE solution by adjusting the amount of NaGdF₄ precursor added.[11] A spherical model was used to calculate the amount of shell precursor to be added. NaYF₄:Yb/Er@NaGdF₄ core@shell nanocrystals with 1 to 10 Gd atomic thicknesses were produced. A precise control over the thin shell thickness was also reported by Wang et al. [12]

The heat-up approach has been considered to be a simple method and widely employed for the core@shell fabrication. However, for producing multi-shelled nanostructures, different shell layers are successively coated by a sequence of independent syntheses by repeating the precise synthetic protocol (**Fig. 2.5a**). Therefore, core@multishell structure fabrication will need prolonged heating, volatile solvent removal, multiple centrifuging and washing for coating of different shells. This is time-consuming, laborious, and user unfriendly. Also, van Veggel et al. reported that the shell layer of core@shell nanoparticles from heat-up approach are not uniform, which means that the core NPs cannot be protected efficiently to suppress the surface luminescence quenching. Furthermore, growing nanocrystals with relative thicker shells (above 5 nm) can also create an anisotropically shaped shell with a wider size distribution.

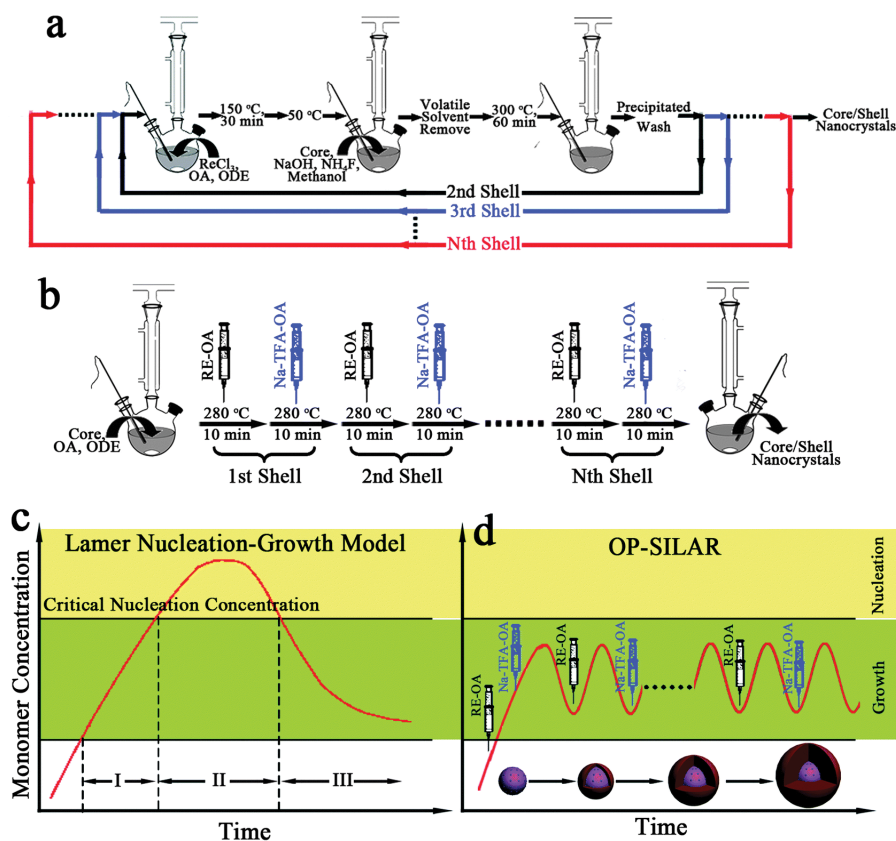


Figure 2.5 (a, b) Schematic depiction of conventional heating-up multi-cycle method (a), and the successive layer-by-layer method (b) for the synthesis of core@shell UCNPs. (c, d) Schematic illustration of the LaMer plot and the successive layer-by-layer method for the controlled synthesis of core@shell UCNPs by using this method. Reproduced with permission from Ref.[6] Copyright (2015) Royal Society of Chemistry.

2.4.2.2 Hot-injection method

The hot-injection method originally developed for fabrication of core@shell semiconductor nanocrystals was first employed to synthesize $\text{NaYF}_4:\text{Yb/Er(Tm)}@\text{NaYF}_4$ core@shell nanocrystals by Yi et al. in 2007.[13] In their experiment, $\text{NaYF}_4:\text{Yb/Er}$ core nanoparticles were made by the thermal decomposition of NaTFA , Y(TFA)_3 , Yb(TFA)_3 , and Er(TFA)_3 in OM at 340°C . An OM solution of NaTFA and Y(TFA)_3 were added as shell precursors. This caused the epitaxial growth of an inert NaYF_4 shell layer. Several core@shell nanostructures were made this way, including $\text{NaYbF}_4@\text{CaF}_2$,[14] $\text{NaGdF}_4@\text{NaGdF}_4$,[15] and $\text{LiLuF}_4@\text{LiLuF}_4$.[16]

As a distinct advantage, the hot-injection method enables one-pot synthesis of multi-shelled nanoparticles by succeeding addition of a sequence of shell precursors (Fig. 2.4b), which overcomes the

limitations of the heat-up approach.[17] Shell thickness can be controlled further by adjusting the injection dosage of the precursors. A one-pot method for the successive layer-by-layer growth approach was reported, which realizes the successive shell coating by continuous injection of shell precursors (**Fig. 2.5b**). In this methods, the precursors concentration was kept relatively low in the growth process to avoid the homogeneous nucleation (**Fig. 2.5d**). This developed approach is flexible to deposit the uniform multi-shell by continuous addition of the different shell precursors. Also, the shell thickness of nanocrystals can be well controlled from 0.36 to 8 nm by adjusting the ratio of the shell precursors and the seed nanoparticles. Moreover, the location of dopant can be well controlled by changing the species and injection sequence of the shell precursors.

In principle, there are two factors determining the quality of the core@shell nanoparticles during the seeded growth: (1) the elimination of additional nucleation (this can be controlled by using a relatively low shell precursor concentration); and (2) the uniform multilayer growth for high-quality core@shell nanostructure fabrication. This can be controlled by controlling the injection rate of the shell precursors. Hence, the facile hot-injection approach is useful. It can control the precursor concentration as well as the growth rate of the crystals. For instance, Zhang et al. reported that a layer-by-layer deposition can make homogeneous shells. A higher emission intensity and a longer lifetime were seen in core/shell nanocrystals made with a hot-injection procedure rather than a one-step shell coating method.[17]

2.5 Synthesis Protocol

2.5.1 Stock solution preparation

LnCl_3 was dissolved in methanol using an ultrasonic cleaning bath and used as the lanthanide stock solution. The concentrations for different LnCl_3 solutions are ranging from 0.1 to 0.4 M. They were then stored in plastic tubes at $-20\text{ }^\circ\text{C}$ until needed. They could be stored this way for up to 12 months without precipitating.

Stock solutions of NaOH and NH_4F were prepared by dissolving NaOH or NH_4F in methanol to make 0.5 M or 0.4 M concentrations respectively. These were stored in plastic tubes at $-20\text{ }^\circ\text{C}$ until needed. Solutions could be stored for up to 2 months without precipitation.

2.5.2 Reaction set up

A 50-ml flask equipped with an inert gas adapter, a stir bar and a thermocouple probe for monitoring and maintaining the temperature was used for the reaction. A magnetic stirrer was used to mix the reactants. A heating mantle with a temperature controller system was employed to heat the flask.

2.5.3 One-pot NaREF₄ synthesis

Typically, for 1 mmol NaYF₄:20%Yb,2%Er nanocrystal synthesis, 1.95 mL YCl₃ stock solution (0.4 M), 1 mL YbCl₃ stock solution (0.2 M), and 0.2 mL ErCl₃ stock solution (0.1 M) were added to a flask containing 6 ml OA and 15 ml ODE. The flask was fitted with a thermocouple temperature sensor and connected to Ar gas with a Schlenk line. Ultra-high purity argon gas is required for quality NaREF₄ synthesis. The mix was heated to 170 °C under an argon flow and vigorous stirring and held for 30 min to obtain a clear solution. After that, the reaction mixture was cooled to room temperature under the stirring. Subsequently, 5 mL methanol solution of NH₄F (4 mmol) and NaOH (2.5 mmol) was added to the reaction solution. After being held for 30 min while stirring, the reaction solution was heated to 80 °C under argon and held for 20 min to remove methanol. It was then heated to 300 °C and held for another 90 min under an argon flow and vigorous stirring. Finally, the reaction solution was cooled again to room temperature.

Step 1



Step 2

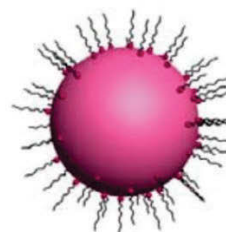


Figure 2.6 Schematic illustration of the co-precipitation strategy for the synthesis of lanthanide-doped NaREF₄ nanocrystals. Lanthanide-oleate precursors are prepared by the reaction of lanthanide chloride and oleic acid at 150 °C. The precipitation of the lanthanide-oleate precursors by sodium and fluoride at low temperature and

subsequent annealing in high boiling solvent afford monodisperse NaREF₄ nanocrystals. Reproduced with permission from Ref.[4] Copyright (2014) Macmillan Publishers Limited.

For purification, the reaction solution was added with an equal volume of ethanol. This led to the precipitation of the nanocrystals. This was transferred to two 15-ml centrifuge tubes. After centrifugation (at 9000 rpm for 5 min), the supernatant was discarded. The particles were purified by dispersing their precipitate in 3 ml cyclohexane. Subsequently, the nanocrystals were precipitated again by adding ethanol and methanol and by centrifugation. After 3 to 4 washing cycles, the processed nanocrystals were dispersed in 5 mL cyclohexane.

2.5.4 Core@shell synthesis.

Step 1



Step 2

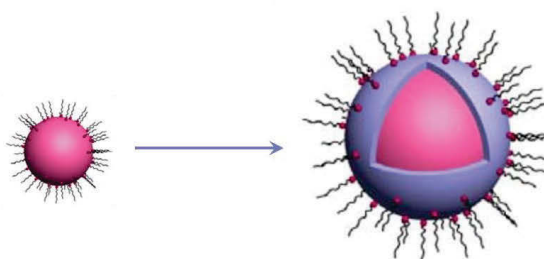


Figure 2.7 Schematic illustration of the co-precipitation strategy for the synthesis of lanthanide-doped NaREF₄ core@shell nanocrystals. Lanthanide-oleate precursors are prepared by the reaction of lanthanide chloride and oleic acid at 150 °C. The precipitation of the lanthanide-oleate precursors by sodium and fluoride at low temperature as shell precursor and subsequent annealing in high boiling solvent with core nanocrystals afford monodisperse NaREF₄ core@shell nanocrystals. Reproduced with permission from Ref.[4] Copyright (2014) Macmillan Publishers Limited.

2.5.4.1 Heat-up method

Shell precursors were firstly prepared. 0.2 mmol of YCl₃·6H₂O was added to a flask containing 4 ml of OA and 10 ml of ODE. This mix was heated to 170 °C under an argon flow. It was then stirred vigorously for 30 min to obtain a clear solution before it was cooled to about 50 °C. Next, a methanol solution of

NH₄F (0.8 mmol) and NaOH (0.5 mmol) was added. Then pre-synthesized core nanocrystals (0.2 mmol in 1 mL cyclohexane) were added to seed growth. This differs from the one-pot core nanocrystal approach. After stirring for 30 min, the solution was heated to 80 °C under argon and held for 20 min to remove methanol. Then the solution was further heated to 300 °C and held for another 90 min under an argon flow and with vigorous stirring. Finally, the reaction solution was cooled back to room temperature. The inert core@shell precipitate was purified the same way as the NaYF₄ core particles.

2.5.4.2 Hot-injection method

Shell precursors were first prepared. 6.0 mmol of YCl₃·6H₂O was added to a flask containing 40 ml of OA and 40 ml of ODE. The mixture was heated to 170 °C under an argon flow and vigorously stirred for 30 min to obtain a clear solution. It was then cooled to about 50 °C. A methanol solution of NH₄F (24.0 mmol) and NaOH (24.0 mmol) was added. After stirring for 30 min, the solution was heated to 80 °C under argon and held for 20 min to remove methanol. The solution was further heated to 150 °C and held for 30 min under an argon flow while vigorously stirring. Finally, the reaction solution was cooled to room temperature. It was then labeled as NaYF₄ shell precursors. Likewise, NaREF₄ with different constituent shell precursors were synthesized using RECl₃ at a corresponding ratio.

For the epitaxial growth of NaREF₄ on the core of NaYF₄, 0.075 mmol of synthesized NaYF₄ core particles was further heated to 300 °C under an argon flow and vigorously stirred. Then, 0.2 mL of NaREF₄ shell precursors were added to the reaction mixture and ripened at 300 °C for 3 min. This was followed by several repeats of this injection and ripening cycle to form the core@shell nanocrystals. Finally, the reaction solution was cooled to room temperature and the formed inert core@shell nanostructures were purified the same way as the NaYF₄ core particles.

It should be noted that core@multi-shell nanocrystals could be easily synthesized using this protocol. For instance, for the epitaxial growth of multiple layers of NaREF₄ onto a core of NaYF₄, 0.075 mmol of NaYF₄ core particles was heated to 300 °C under an argon flow while vigorously stirred. Then, 0.2 mL of shell precursor was added to the reaction mix and ripened at 300 °C for 3 min. The procedure was repeated several times to form the core@first-shell. Then, 0.2 mL of second shell precursor was added to the reaction mixture and ripened at 300 °C for 3 min. The procedure was repeated several times to form the core@first-shell@second-shell. Similarly, a third shell and a forth shell et al. were made by this one-

pot hot-injection coating method. When it was completed, the reaction mix was cooled to room temperature. The core@multi-shell precipitate was purified the same way as the NaYF₄ core particles.

2.6 Characterization

Transmission electron microscope (TEM) measurements were performed with a Philips CM10 TEM that had an Olympus Sis Megaview G2 Digital Camera. The microscope had an accelerating voltage of 100 kV. Samples were prepared by drying nanoparticles on a copper grid coated with a thin layer of carbon. To avoid agglomeration, particles were diluted with cyclohexane. [1]

Powder X-ray diffraction (XRD) measurements were collected using a Bruker D8 Discover diffractometer. Data was recorded using a slit of 0.02° at a scanning speed of 2° min⁻¹ and Cu K α radiation ($\lambda=1.5406$ Å).

To measure upconverting luminescence, a modified photoluminescence spectrometer coupled with a 980-nm continuous-wave laser was used. The spectra emitting with a 10-mm path length from colloidal solutions in quartz cuvettes were acquired with a Fluorolog-Tau3 spectrofluorometer (Jobin Yvon Horiba). This was equipped with an external 980 nm CW diode laser at a pump power of 250mW. Samples were at the same concentration in cyclohexane. This was done by weighing and then adding the same amount of the UCNPs to the solution. [1]

Sample slides of dispersed UCNPs were prepared for single nanoparticle measurement.[2] To optimally image these particles, an embedding medium with a refractive index matching that of the immersion oil was used. 2.4 g of Mowiol 4-88 (Sigma-Aldrich) was mixed with 6 g of glycerol in a 50-ml centrifuge tube. After stirring on a magnetic stirrer for 1 h, 6 ml of Milli-Q water was added. The stirring was continued for another 2 h. Then, 12 ml tris(hydroxymethyl)aminomethane (Tris)-HCl buffer (at 0.2 M at pH 8.5) was added. The solution was water-bathed at 50 °C under constant agitation until the Mowiol was dissolved. Any remaining solids were removed by centrifuging at 7,500g for 30 min. To prepare a sample on a slide, a cover-slip was washed with pure ethanol and then Milli-Q water under ultrasonication. It was then treated with 50 μ l of polylysine solution (at 0.1% in H₂O w/v). After 30 min, the polylysine was washed off with Milli-Q water, and the cover-slip was air-dried. 20 μ l of UCNPs (diluted to 0.01 mg ml⁻¹ in cyclohexane) was dropped onto the treated surface. This was immediately washed with 500 μ l of cyclohexane twice. After air-drying, the cover-slip was put on a clean glass slide spread with 10 μ l of as-

prepared embedding medium. Air bubbles were squeezed out by a gentle force. The slide with the sample was kept at room temperature for another 24 h to ensure complete dryness before measurement.

2.7 General Surface Modification

UCNPs have emerged as a promising new family of luminescent nanomaterials attracting a large amount of research interests in the biomedical field, due to their capability to convert low energy NIR photons into visible ones. However, most of the high-quality UCNPs are formed in the organic solution and have the hydrophobic surface. Transferring them with hydrophilic surface is a requirement in their applications for bioimaging, labeling, and bioassays.[18]

2.7.1 Silica coating

Following an oil in water reverse microemulsion process, 1 mL Igepal CO-520 was dispersed in 20 mL cyclohexane. Afterwards, UCNPs in cyclohexane solution (1.5 mL, 25 mg/mL) was added. After sonication for 15 min, 140 μ L of ammonia (at 30% concentration) was added dropwise while the mix was vigorously stirred for another 2 h. Then 130 μ L of tetraethyl orthosilicate was added dropwise. The mixture was stirred for 24 h before the addition of methanol to terminate reaction. The formed UCNPs@SiO₂ nanoparticles were washed with cyclohexane and ethanol for 3 times to remove excess Igepal CO-520, and finally dispersed in 4 mL deionized water.[19-21]

2.7.2 POEGA-b-PMAEP polymer modified UCNPs [22, 23]

POEGA-b-PMAEP polymer was prepared and characterized following procedures described in reports elsewhere.[22, 23] Nanocrystal surfaces were modified with this polymer. NaYF₄:Yb/Er nanocrystals (20 mg) were dispersed in 1 mL of tetrahydrofuran. A solution of POEGA-b-PMAEP polymer (50 mg) in tetrahydrofuran (2 mL) was individually added to the dispersed NaYF₄:Yb/Er nanocrystals. This was sonicated for 1 min and incubated in a shaker overnight at 40 °C. The polymer coated NaYF₄:Yb/Er nanocrystals were purified by centrifuging three times at 14 000 rpm for 10 min. The supernatant was removed, and the nanoparticles were dispersed in an aqueous media.

2.7.3 3,4-dihydroxyhydrocinnamic acid modified UCNPs [24]

3,4-dihydroxyhydrocinnamic acid (100 mg) was dissolved in 8 mL of tetrahydrofuran in a flask and heated to 50 °C under the argon flow. Then UCNPs (30 mg) dispersed in 5 mL of tetrahydrofuran was

added and the mix was stirred for another 4 h. After that, 400 μL of NaOH (0.5 M) was added to precipitate the nanoparticles. Finally, the surface modified UCNPs was collected by centrifugation and re-dispersed in 5 mL of water.[24]

2.7.4 Dopamine modified UCNPs [25]

Dopamine (100 mg) was dissolved in 500 μL of deionized water. 5 mL of tetrahydrofuran was then added. The mix was transferred to a flask with 5 mL of tetrahydrofuran and heated to 50 $^{\circ}\text{C}$ under an argon flow. Then UCNPs (30 mg) dispersed in tetrahydrofuran (5 mL) were added. The mix was stirred for another 4 h. After this, 200 μL of HCl (1 M) was added to the mix to form a precipitate. Finally, the surface modified UCNPs was collected by centrifugation and re-dispersed in 5 mL of water.[25]

2.7.5 Biotin modified UCNPs

To add biotin to particle surfaces, dopamine modified UCNPs in water solution were firstly prepared. Then, 1.5 mL of water containing BIOTIN-PEG-NHS (15 mg) was added while it was magnetically stirred at room temperature for 30 min. Subsequently, 1.5 mL of water containing mPEG-NHS (25 mg) was added, and the reaction was continued overnight under stirring. Finally, the modified nanocrystals were collected by centrifugation and re-dispersed in 5 mL of water.

2.8 References

- [1] Ma, C., Xu, X., Wang, F., Zhou, Z., Wen, S., Liu, D., Fang, J., Lang, C.I., Jin, D., Probing the Interior Crystal Quality in the Development of More Efficient and Smaller Upconversion Nanoparticles, *The Journal of Physical Chemistry Letters* 7 (16) (2016) 3252-3258.
- [2] Liu, Y., Lu, Y., Yang, X., Zheng, X., Wen, S., Wang, F., Vidal, X., Zhao, J., Liu, D., Zhou, Z., Ma, C., Zhou, J., Piper, J.A., Xi, P., Jin, D., Amplified stimulated emission in upconversion nanoparticles for super-resolution nanoscopy, *Nature* 543 (7644) (2017) 229-233.
- [3] Chen, C., Wang, F., Wen, S., Su, Q. P., Wu, M. C. L., Liu, Y., Wang, B., Li, D., Shan, X., Kianinia, M., Aharonovich, I., Toth, M., Jackson, S. P., Xi, P., Jin, D., Multi-photon near-infrared emission saturation nanoscopy using upconversion nanoparticles. *Nature Communications* 9 (1) (2018) 3290.
- [4] Wang, F., Deng, R., Liu, X., Preparation of core-shell NaGdF₄ nanoparticles doped with luminescent lanthanide ions to be used as upconversion-based probes, *Nat. Protocols* 9 (7) (2014) 1634-1644.

- [5] Chen, D., Zhou, Y., Wan, Z., Ji, Z., Huang, P., Tuning into single-band red upconversion luminescence in Yb³⁺/Ho³⁺ activated nano-glass-ceramics through Ce³⁺ doping, *Dalton Transactions* 44 (12) (2015) 5288-5293.
- [6] Li, X., Zhang, F., Zhao, D., Lab on upconversion nanoparticles: optical properties and applications engineering via designed nanostructure, *Chemical Society Reviews* 44 (6) (2015) 1346-1378.
- [7] Chen, X., Peng, D., Ju, Q., Wang, F., Photon upconversion in core-shell nanoparticles, *Chemical Society Reviews* 44 (6) (2015) 1318-1330.
- [8] Johnson, N.J.J., van Veggel, F.C.J.M., Sodium lanthanide fluoride core-shell nanocrystals: A general perspective on epitaxial shell growth, *Nano Research* 6 (8) (2013) 547-561.
- [9] Mai, H.-X., Zhang, Y.-W., Sun, L.-D., Yan, C.-H., Highly Efficient Multicolor Up-Conversion Emissions and Their Mechanisms of Monodisperse NaYF₄:Yb,Er Core and Core/Shell-Structured Nanocrystals, *The Journal of Physical Chemistry C* 111 (37) (2007) 13721-13729.
- [10] Qian, H.-S., Zhang, Y., Synthesis of Hexagonal-Phase Core-Shell NaYF₄ Nanocrystals with Tunable Upconversion Fluorescence, *Langmuir* 24 (21) (2008) 12123-12125.
- [11] Zhang, F., Che, R., Li, X., Yao, C., Yang, J., Shen, D., Hu, P., Li, W., Zhao, D., Direct Imaging the Upconversion Nanocrystal Core/Shell Structure at the Subnanometer Level: Shell Thickness Dependence in Upconverting Optical Properties, *Nano Letters* 12 (6) (2012) 2852-2858.
- [12] Wang, F., Deng, R., Wang, J., Wang, Q., Han, Y., Zhu, H., Chen, X., Liu, X., Tuning upconversion through energy migration in core-shell nanoparticles, *Nat Mater* 10 (12) (2011) 968-973.
- [13] Yi, G.-S., Chow, G.-M., Water-Soluble NaYF₄:Yb,Er(Tm)/NaYF₄/Polymer Core/Shell/Shell Nanoparticles with Significant Enhancement of Upconversion Fluorescence, *Chemistry of Materials* 19 (3) (2007) 341-343.
- [14] Chen, G., Shen, J., Ohulchanskyy, T.Y., Patel, N.J., Kutikov, A., Li, Z., Song, J., Pandey, R.K., Ågren, H., Prasad, P.N., Han, G., (α -NaYbF₄:Tm³⁺)/CaF₂ Core/Shell Nanoparticles with Efficient Near-Infrared to Near-Infrared Upconversion for High-Contrast Deep Tissue Bioimaging, *ACS Nano* 6 (9) (2012) 8280-8287.
- [15] Vetrone, F., Naccache, R., Mahalingam, V., Morgan, C.G., Capobianco, J.A., The Active-Core/Active-Shell Approach: A Strategy to Enhance the Upconversion Luminescence in Lanthanide-Doped Nanoparticles, *Advanced Functional Materials* 19 (18) (2009) 2924-2929.
- [16] Huang, P., Zheng, W., Zhou, S., Tu, D., Chen, Z., Zhu, H., Li, R., Ma, E., Huang, M., Chen, X., Lanthanide-Doped LiLuF₄ Upconversion Nanoprobes for the Detection of Disease Biomarkers, *Angew. Chem. Int. Ed.* 53 (5) (2014) 1252-1257.
- [17] Li, X., Shen, D., Yang, J., Yao, C., Che, R., Zhang, F., Zhao, D., Successive Layer-by-Layer Strategy for Multi-Shell Epitaxial Growth: Shell Thickness and Doping Position Dependence in Upconverting Optical Properties, *Chemistry of Materials* 25 (1) (2013) 106-112.
- [18] Muhr, V., Wilhelm, S., Hirsch, T., Wolfbeis, O.S., Upconversion Nanoparticles: From Hydrophobic to Hydrophilic Surfaces, *Accounts of Chemical Research* 47 (12) (2014) 3481-3493.

- [19] Fan, W., Shen, B., Bu, W., Zheng, X., He, Q., Cui, Z., Zhao, K., Zhang, S., Shi, J., Design of an intelligent sub-50 nm nuclear-targeting nanotheranostic system for imaging guided intranuclear radiosensitization, *Chemical Science* 6 (3) (2015) 1747-1753.
- [20] Xing, H., Bu, W., Zhang, S., Zheng, X., Li, M., Chen, F., He, Q., Zhou, L., Peng, W., Hua, Y., Shi, J., Multifunctional nanoprobe for upconversion fluorescence, MR and CT trimodal imaging, *Biomaterials* 33 (4) (2012) 1079-1089.
- [21] Liu, J., Bu, W., Pan, L., Shi, J., NIR-Triggered Anticancer Drug Delivery by Upconverting Nanoparticles with Integrated Azobenzene-Modified Mesoporous Silica, *Angewandte Chemie International Edition* 52 (16) (2013) 4375-4379.
- [22] Chen, Y., Duong, H.T.T., Wen, S., Mi, C., Zhou, Y., Shimoni, O., Valenzuela, S.M., Jin, D., Exonuclease III-Assisted Upconversion Resonance Energy Transfer in a Wash-Free Suspension DNA Assay, *Analytical Chemistry* 90 (1) (2018) 663-668.
- [23] Duong, H., Chen, Y., Tawfik, S.A., Wen, S., Parviz, M., Ford, M.J., Shimoni, O., Jin, D., Systematic Investigation of Functional Ligands for Colloidal Stable Upconversion Nanoparticles, (2017).
- [24] Liu, Y., Chen, T., Wu, C., Qiu, L., Hu, R., Li, J., Cansiz, S., Zhang, L., Cui, C., Zhu, G., You, M., Zhang, T., Tan, W., Facile Surface Functionalization of Hydrophobic Magnetic Nanoparticles, *Journal of the American Chemical Society* 136 (36) (2014) 12552-12555.
- [25] Liu, Y., Purich, D.L., Wu, C., Wu, Y., Chen, T., Cui, C., Zhang, L., Cansiz, S., Hou, W., Wang, Y., Yang, S., Tan, W., Ionic Functionalization of Hydrophobic Colloidal Nanoparticles To Form Ionic Nanoparticles with Enzymelike Properties, *Journal of the American Chemical Society* 137 (47) (2015) 14952-14958.

CHAPTER 3 One-Nanometer-Scale Size-Controlled Synthesis of UCNPs by Seed-Mediated Growth

3.1 Introduction

UCNPs are capable of converting two or more lower-energy photons into one high energy photon.[1-3] Due to their anti-Stokes property, they have the advantages of negligible background auto-fluorescence, narrow emission bandwidths, non-photobleaching, non-blinking, tunable lifetime, and less light scattering.[1, 3, 4] These nanomaterials, typically lanthanide ions doped rare-earth nanocrystals, have been manifested in many important applications, such as highly sensitive biomolecular detection, cell labeling, and in vivo tumor imaging.[3, 5] Therefore, an increasing number of research groups have devoted their energies to this area. Recent years witnessed the fast development of this field, especially for the high-quality nanocrystals fabrication.

Yet, producing nanocrystals to an intended size is challenging. Particles can vary between lots made from the same starting materials using the same methods. Using the RECl_3 as the precursor in a co-precipitation synthesis, different research groups have produced $\text{NaYF}_4:20\%\text{Yb},2\%\text{Er}$ nanocrystals with varied sizes. For example, the size of 20 nm was reported by Zhang's group,[6-8] 30 nm in diameter by Qin's group,[9] 24 nm in diameter by Jang's group[10] and 28 nm in diameter by Shi's group.[11] A similar variance in size were reported by groups that used the same method, but different starting materials. Hyeon's group added $\text{RE}(\text{OA})_3$ as a RE precursor,[12] whereas the groups of Liu [13-23] and van Veggel [24-28] added $\text{RE}(\text{Ac})_3$ as a precursor. The authors made a series of uniform nanocrystals using identical reagents, methods and conditions. But the samples at the different reports have various diameters, which indicates the relatively large synthesis-to-synthesis variation.[29]

Suter II et al. used *in situ* analysis to observe synthesis processs in a co-precipitation method.[29] As shown in **Fig. 3.1a**, the authors implement the capability to monitor the upconversion luminescence of the reaction mixture during the synthesis process. The size distribution of the nanocrystals for each of the six experiments is ranged from 32.9 to 41.0 nm (**Fig. 3.1b**), which indicates the relatively large synthesis-to-synthesis variation. The green upconversion luminescence, in real time, is collected during six separate

synthesis, which could uncover the time for NaYF₄:Yb,Er nuclear and growth process. As shown in **Fig. 3.1c**, once nucleation and growth occurs, conversion time is about 15 min for all samples. But there is variation in the time taken before nucleation and growth begin. This is from 40 to 98 min, which is more than a factor of 2 across the six experiments. There is no correlation between the final size of the NaYF₄ nanoparticles produced and the reaction time, which indicated the complicated nanocrystals formation process in the one-pot synthesis approach.

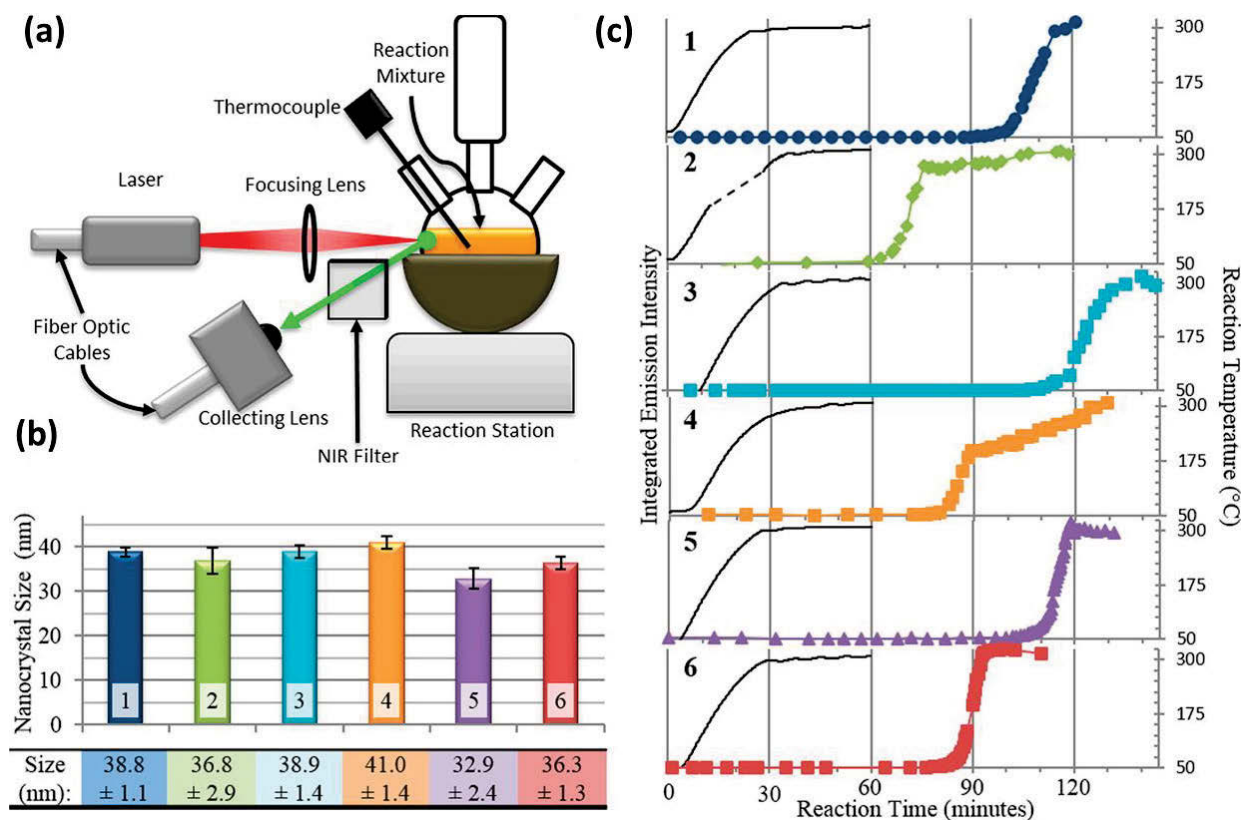


Figure 3.1 (a) Schematic representation of the experimental set up for real-time-monitoring of upconversion nanocrystal synthesis. (b) Final size distribution of product NaYF₄ nanocrystals obtained for 6 batches of synthesis. (c) Integrated emission intensity of green upconversion emission versus reaction time for 6 separate reactions where $t = 0$ min is defined as the initiation of heat-up. The heating profile for each experiment is also shown (solid black line). Reproduced with permission from Ref.[29] Copyright (2014) American Chemical Society.

Reproducibility is important for studying the properties of nanocrystals and their applications. Hence, it is important to control their sizes at the one-nanometer-scale. Seed-mediated growth, described before, is a powerful method for the fine-tuning of nanocrystals size compared with the conventional one-pot

synthesis. We, therefore, introduce the seed-mediated growth method in this Chapter to fabricate the nanocrystals with exact sizes (one-nanometer-scale). The results show that this approach can achieve the desired control over particle's size. This control allows the measurement and comparison of same-sized, but variously doped UCNPs at single nanoparticle level.

3.2 Experimental Section

3.2.1. Synthesis of NaYF₄:20%Yb,2%Er core nanocrystals

NaYF₄:20%Yb,2%Er has been synthesized through the co-precipitation approach similar to our previously reported process.[30, 31] In a typical experiment, 1 mmol RECl₃ (RE = Y, Yb, and Er) was added to a flask containing 6 ml OA and 15 ml ODE. The mixture was heated to 170 °C under an argon flow and vigorously stirred for 30 min to obtain a clear solution. It was then cooled to 50 °C, followed by the addition of 5 mL of a methanol solution of NH₄F (4 mmol) and NaOH (2.5 mmol). After stirring for 30 min, the solution was heated to 80 °C under argon and held for 20 min to remove methanol. The solution was further heated to 300 °C and held for another 90 min under argon flow while vigorously stirred. Finally, the reaction solution was cooled to room temperature. It was then diluted with an equal volume of ethanol, which is led to precipitation of the nanocrystals. After centrifugation, the precipitate was purified by redispersion in 3 ml cyclohexane, followed by precipitation with ethanol and separation by centrifugation. After 3 to 4 washing cycles, the nanocrystals were dispersed in 5 mL cyclohexane.

3.2.2. Seed-mediated growth of nanocrystals

The epitaxial growth of NaREF₄ onto seeds of NaYF₄:20%Yb,2%Er was conducted *via* a successive layer-by-layer hot-injection method. The precursors were prepared first. 1.5 mmol YCl₃·6H₂O was added to a flask containing 10 ml of OA and 10 ml of ODE. The mixture was heated to 170 °C under an argon flow and vigorously stirred for 30 min to obtain a clear solution. It was then cooled to about 50 °C, followed by the addition of methanol solution of NH₄F (6.0 mmol) and NaOH (1.5 mmol). After stirring for 30 min, the solution was heated to 80 °C under argon and held for 20 min to remove the methanol. The solution was further heated to 150 °C and held for 30 min under an argon flow while vigorously stirred. Finally, the solution was cooled to room temperature. It was labeled as NaYF₄:20%Yb,2%Er precursors.

For the epitaxial growth of NaREF₄ on the core of NaYF₄:20%Yb,2%Er, 0.075 mmol synthesized core particles was heated to 300 °C under an argon flow while vigorously stirred. Then, 0.2 mL of NaYF₄:20%Yb,2%Er precursors were immediately injected into the reaction mixture and ripened at 300 °C for 3 min. The injection and ripening cycle was repeated several times to get the core@shell nanocrystals. Finally, the reaction solution was cooled to room temperature. The formed core@shell nanocrystals were purified according to the procedures used for the purification of NaYF₄: 20%Yb, 2%Er core particles.

3.3. Results and Discussion

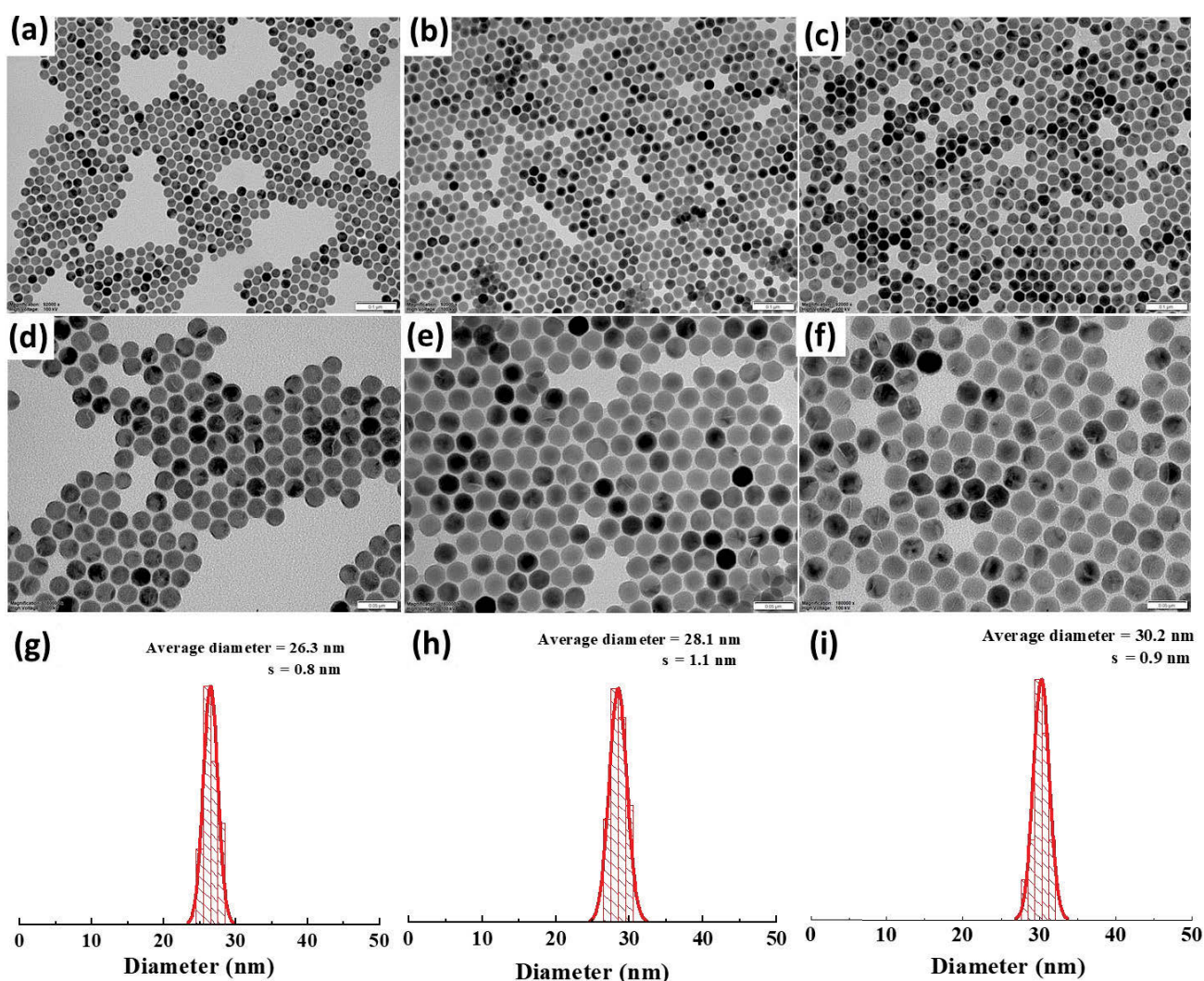


Figure 3.2 (a-c) Extensive TEM images, (d-f) high resolution TEM images, and (g-i) size distribution histogram of the UCNP1 (a,d,g), UCNP2 (b,e,h), and UCNP3 (c,f,i). Scale bar for (a-c) and (d-f) are 100 and 50 nm, respectively.

Using the co-precipitation method, we synthesize three batches of NaYF₄:20%Yb,2%Er (labelled as UCNP1, UCNP2, and UCNP3, respectively) with the same reaction conditions. The robustness of the one-pot synthesis approach was demonstrated. As shown in **Fig. 3.2a-f**, three batches of the NaYF₄:20%Yb,2%Er each contains uniform nanocrystals and has a narrow size distribution ($\sigma_r \leq 5\%$). However, the mean diameter of the nanocrystals differs with 26.3 nm for UCNP1, 28.1 nm for UCNP2, and 30.2 nm for UCNP3, respectively, as shown in the size distribution histogram (**Fig. 3.2g-i**). This indicates the relatively large synthesis-to-synthesis variation, in agree with the previous report. [29]

The size of the UCNPs significantly affects their emission intensity. UCNPs with a small size have an increased surface phonon activity. An increase in activity quenches its luminescence. To quantify and compare the upconversion emission intensity of each batches of UCNPs, we prepared the dispersion samples of the as-synthesized UCNP1, UCNP2, and UCNP3 in cyclohexane with the same mass concentration. Their integrated luminescence emission intensities was tested using Fluorolog spectrometer. We find that the upconversion luminescent intensity of the nanocrystals increases as the size of the UCNPs increased from 26.3 to 30.2 nm (**Fig. 3.3**). It is notable that the intensity of UCNP3 is around 1.68 times as high as that of UCNP1 with the same concentration, even there are with only less than 4 nm difference in the diameter of two samples.

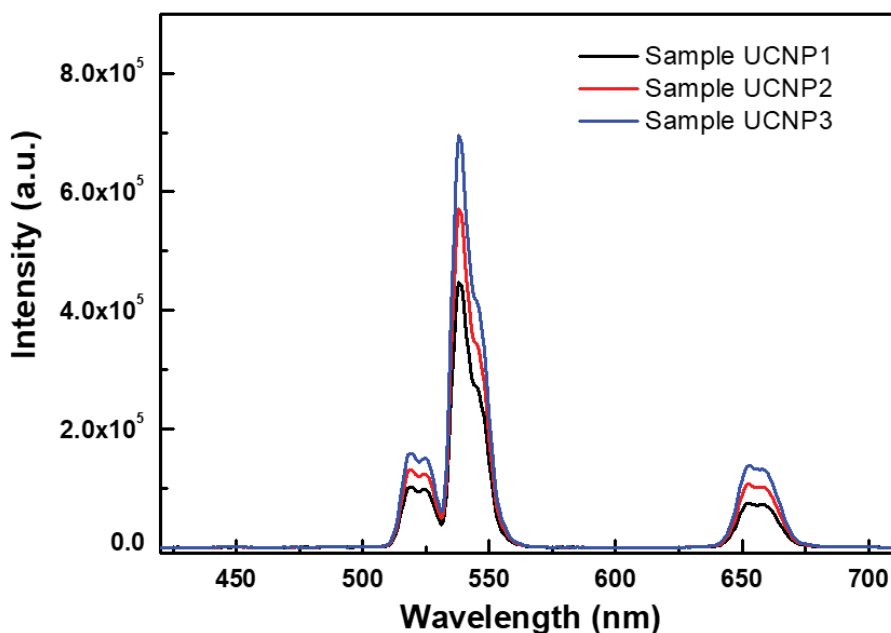


Figure 3.3 Upconversion luminescence spectra of UCNP1, UCNP2 and UCNP3 measured by Fluorolog spectrometer.

To make the nanocrystals have the same size, we apply the seed-mediated growth approach to fine tune the size of the obtained nanocrystals as shown in **Fig. 3.4**. In this design, small nanocrystals are continuously grown by adding precursors. The size of the final product can be controlled by the addition of different amount of precursors and in turn the reaction time for the injection. The amount of the precursor added is calculated using the following equation:

$$V = \frac{4}{3}\pi r^3 \quad 3.1$$

$$V_{precursor} = V_{target} - V_{seed} \quad 3.2$$

Where V_{seed} is the volume of the seed nanocrystals, V_{target} is the volume of the target nanocrystals, and $V_{precursor}$ is the volume of the precursor needed for the growth process.

From **Eq. 3.2**, the volume ratio of precursor and seed is derived:

$$\frac{V_{precursor}}{V_{seed}} = \frac{V_{precursor}}{V_{seed}} - 1 \quad 3.3$$

When **Eq. 3.1** is added to **Eq. 3.3**, **Eq. 3.4** is formulated:

$$\frac{V_{precursor}}{V_{seed}} = \left(\frac{r_{target}}{r_{seed}}\right)^3 - 1 \quad 3.4$$

Then

$$V = \frac{m}{\rho} \quad 3.5$$

$$m = nM \quad 3.6$$

The mole ratio of the precursors and the seeds can be calculated using **Eq. 3.7**:

$$\frac{V_{precursor}}{V_{seed}} = \frac{n_{precursor}}{n_{seed}} \quad 3.7$$

$$\frac{n_{precursor}}{n_{seed}} = \left(\frac{r_{target}}{r_{seed}}\right)^3 - 1 \quad 3.8$$

Therefore, the amount of precursor needed can be calculated by knowing the amount of seed added, its size as well as the final size of the target nanocrystals required.

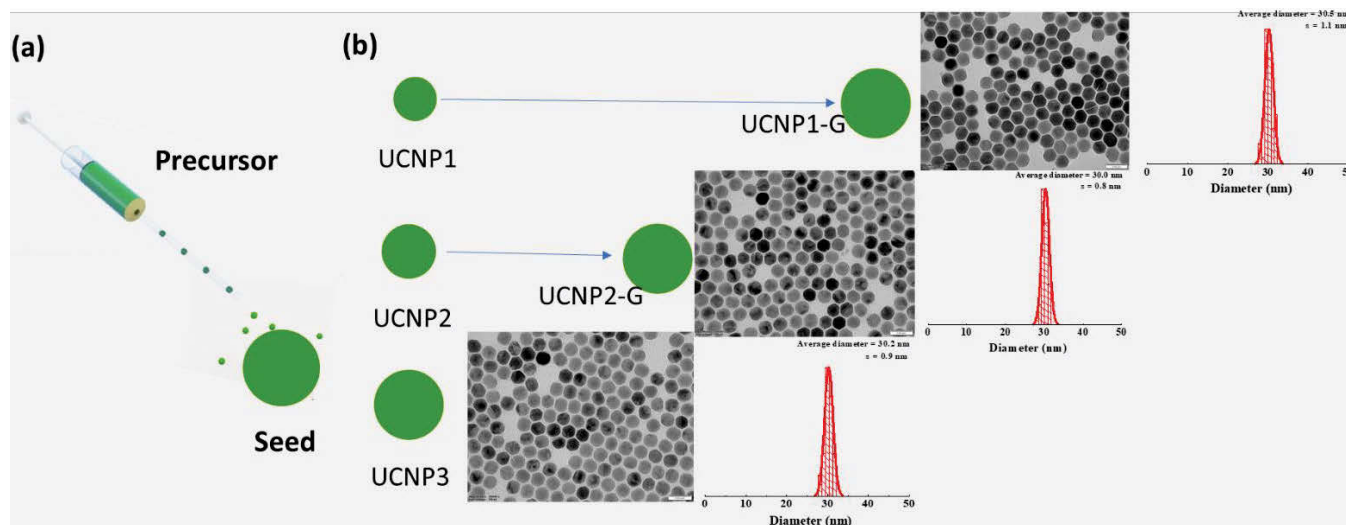


Figure 3.4 (a) Schematic representation of the seed-mediated growth approach to obtain the nanocrystals with the desired size. (b) Schematic representation of the growth time with seeds with different sizes. TEM images and final size distribution of final nanocrystals obtained by fine-tuning. Scale bar, 50 nm.

Through facile seed-mediated growth, we get the nanocrystals of UCNP1-G (UCNP1 seeded growth) and UCNP2-G (UCNP2 seeded growth) that are similar in size to UCNP3. This result is shown in **Fig. 3.4**. Injection time and the number of precursors added depend on the size and the number of seeds added. It is notable the two samples were within one-nanometer-scale of the target nanocrystals (UCNP3). It is, therefore, possible to apply them together as one batch sample.

The optical properties of the three samples are compared. Their upconversion emission intensity is shown in **Fig. 3.5**. The nanocrystals made with a growth approach is found to be optically similar to those made with the one-pot chemical method. The seed-mediated growth approach can make lots of UCNP3s with matching sizes and properties. The doping-dependent optical properties of these similar nanocrystals can be more easily compared.

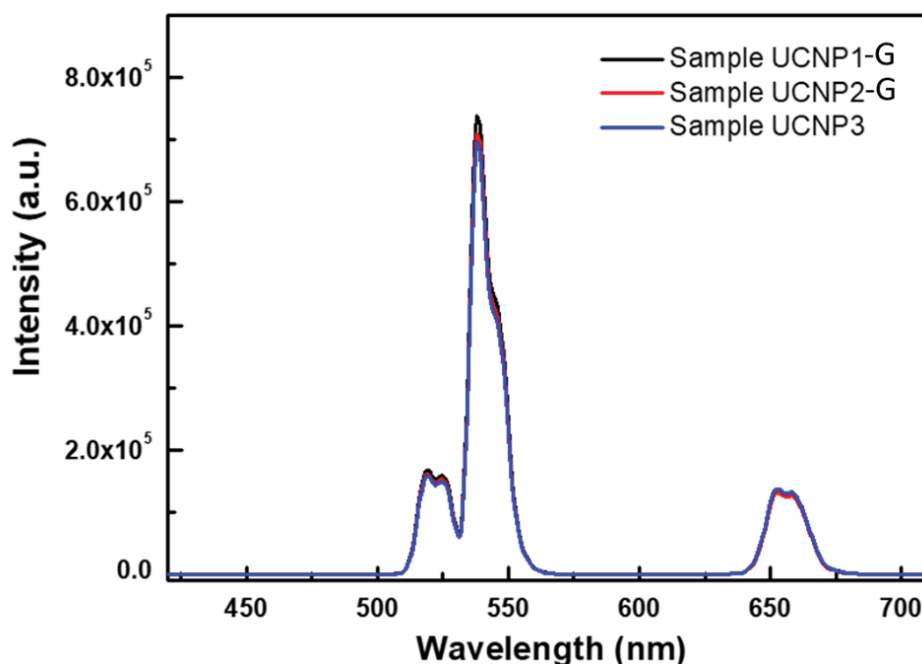


Figure 3.5 Upconversion luminescence spectra of UCNP1-G, UCNP2-G and UCNP3 measured by Fluorolog spectrometer.

The growth approach can make differently composed nanocrystals at the same size. It can also make nanocrystals with the same composition but at different sizes, which are helpful to test the relationship between size and a crystal's properties. More importantly, a series of nanoparticles with different sizes could be obtained through one-pot hot-injection approach. To make these particles, a fraction of the sample is taken out of a reaction mix at different times during the injection process. To prove the advantage of the this approach, we synthesize the nanocrystals with the size as bigger as 70 nm through seed-mediated growth approach. The intermediate products are taken out at different times during this process as shown in **Fig. 3.6**. The seed used in this experiment is 32 nm NaYF₄:20%Yb,8%Tm nanocrystals obtained by the one-pot synthesis. Interestingly, we find that the growth of seeds with the shell precursor did not start immediately. At first, the shell precursors grow by themselves as α -phase nanocrystals, while the size of the seeds becomes slightly reduced to around 30 nm. At about 25 min later, the seeds start to growth and the small α -phase nanocrystals become reduced. These results indicate that there are more complicated growth mechanism during the seeded growth process, which will be introduced in the next Chapter. All these results suggest that nanocrystals can be made over a range of sizes through this developed approach, which is helpful for the size-dependent property studies.

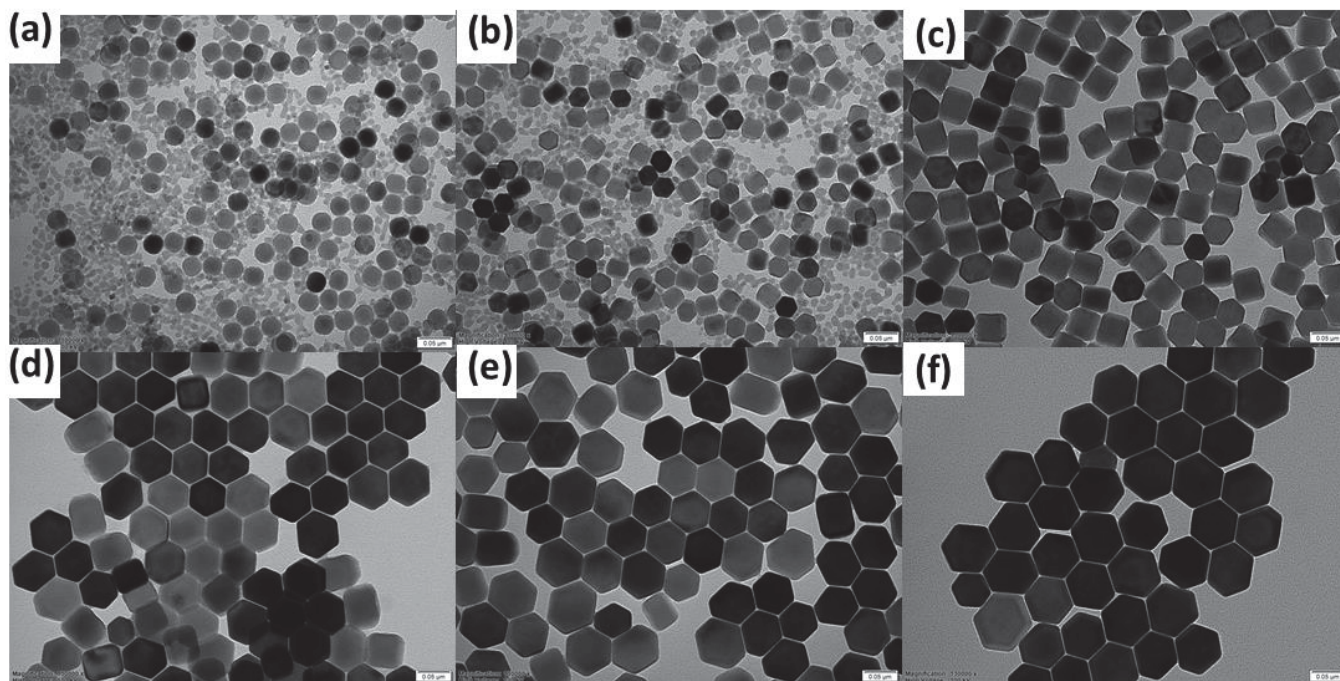


Figure 3.6 TEM images of UCNPs samples with different size and same Yb/Tm doping concentration. The sizes of the nanocrystals are 30 nm, 30.5 nm, 40 nm, 50 nm, 60 nm, and 70 nm from (a) to (f), respectively. Scale bar, 50 nm.

3.4 Applications in Joint Projects

Single-nanoparticle fluorescence characterization provides new insights into the optical properties of individual nanoparticles instead of the ensemble averaging. This technique requires ultra-sensitive single photon detection systems and the controlled synthesis of particles. The 2014 chemistry Nobel Prize was awarded to ‘the development of super-resolved fluorescence microscopy’. The award highlights the importance of microscopy at single molecule resolution. This technique has allowed nanoscale structures to be visualized beyond the ‘diffraction limit’ of light that enabled live cell optical studies with unprecedented resolutions. It has made new applications of fluorescent nanoparticles possible.

Uniform nanocrystals at specific sizes are needed for their characterization at a single level. The seed-mediated growth approach makes this possible. To test this, we synthesized a series of batches of nanocrystals. Each is done with a slightly different activator concentrations. These particles are then used in three joint collaborations: STED-based super-resolution imaging, NIRES-based super-resolution imaging, and single nanoparticle tracking.

3.4.1 STED-based super-resolution imaging [31]

To determine the critical Tm^{3+} doping concentration for enhanced population inversion, a series of ten batches of 40-nm UCNPs are synthesized with incremental Tm^{3+} concentrations from 0.5 mol% to 8 mol% (Fig. 3.7). [31]

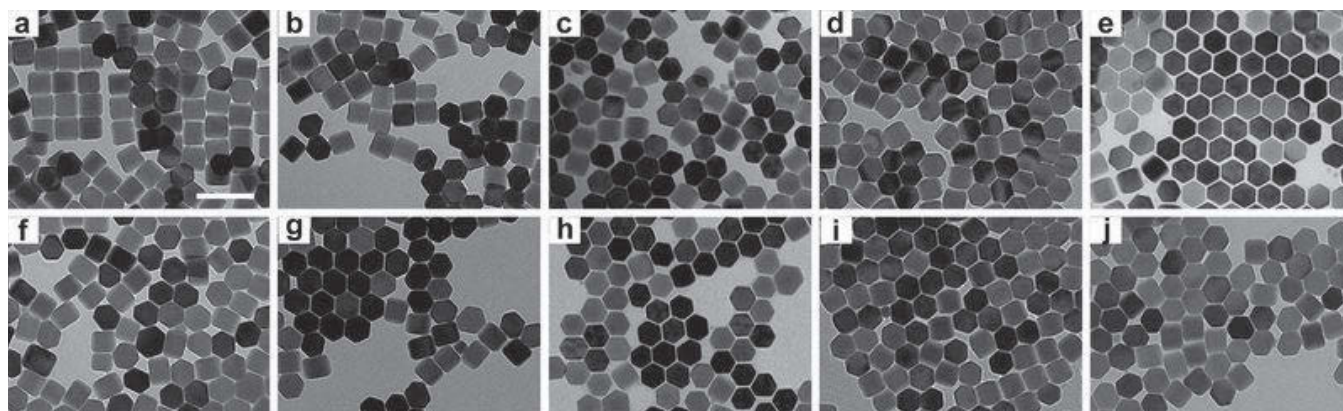


Figure 3.7 TEM images of ten batches of UCNPs samples with the same Yb^{3+} doping concentration (20 mol%) and different Tm^{3+} doping concentration. The Tm^{3+} concentrations are respectively 0.5, 1, 1.5, 2, 2.5, 3, 3.5, 4, 6 and 8 mol% from a to j, respectively. All nanocrystals have average sizes around 40 nm. Scale bar: 100 nm. Reproduced with permission from Ref.[31] Copyright (2017) Macmillan Publishers Limited.

The optical depletion ratio is the ratio of the emission from a sample with an 808 nm depletion probe compared to the emission from a sample without a probe. Under dual-laser illumination, the optical depletion ratio of the 455 nm emission is measured as a function of the 808 nm intensity in single nanoparticle.[31] As shown in Fig. 3.8a, within the available power range of the 808 nm laser, only UCNPs with Tm^{3+} doping concentration $>2\%$ can have more than 50% of their emission switched off. For Tm^{3+} doping concentrations above 4%, optimum depletion ratios above 90% can be achieved. The saturation intensities, denoting the particular values of the probe intensity that halve the upconverted emission, are calculated from a plot of the inverse of the depletion ratio against the 808 nm intensity via linear curve fitting (Fig. 3.8b). The linearity found for UCNPs with Tm^{3+} doping $\geq 3.5\%$ holds only at low 808 nm intensity; at greater intensities, the fit becomes dual- or multi-segment, which suggests that the depletion efficiency for the highly-doped UCNPs is power dependent, and can be substantially amplified by the photon-avalanche-like effect. Those data points appearing with a linear fit in the low 808 nm

intensity range show reduction of saturation intensities by more than two orders of magnitude (from 71.4 MW cm^{-2} to 0.19 MW cm^{-2}) as the Tm^{3+} doping increases from 0.5% to 8%.

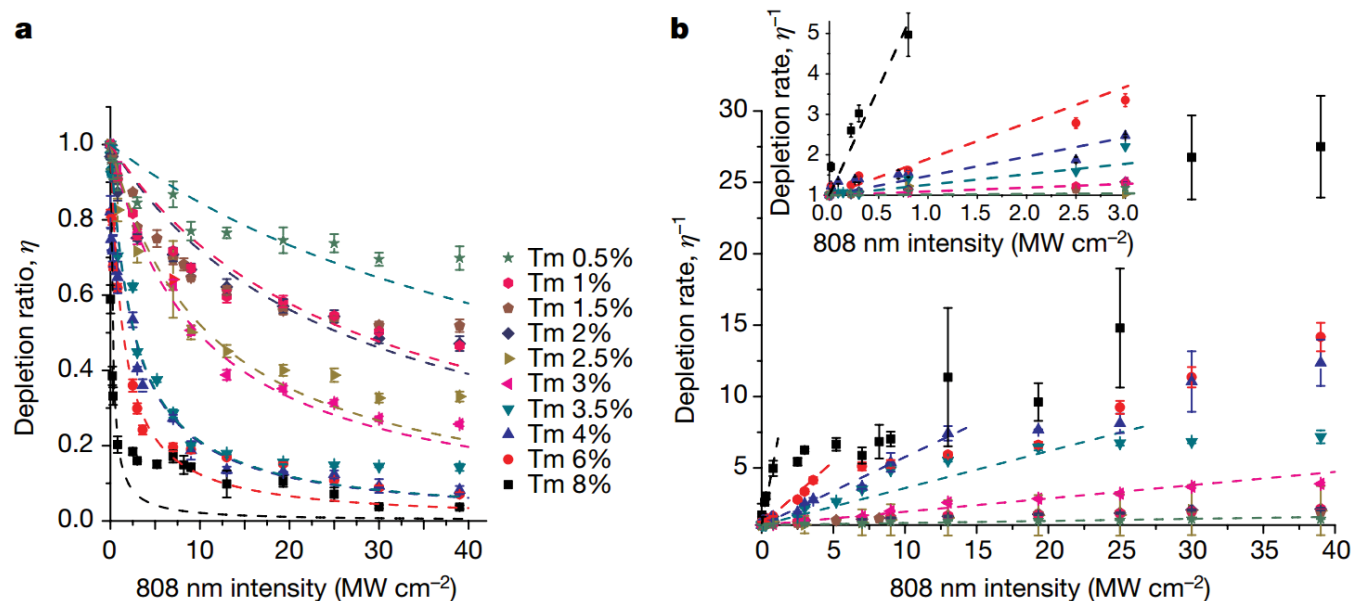


Figure 3.8 Depletion ratio of the upconversion emission at 455 nm, as a result of intermediate-level stimulated emission, under continuous-wave 980 nm excitation at a fixed intensity of 0.66 MW cm^{-2} and 808 nm intensities up to 39 MW cm^{-2} , measured for a series of UCNPs with incremental Tm^{3+} doping concentrations from 0.5 to 8 mol%. Dashed lines are fitted curves using the form $\eta = (1 + I_{808}/I_{\text{sat}})^{-1}$, where I_{sat} denotes the saturation intensity. **b**, The depletion ratio data in **a** are inverted to illustrate the linear relation $\eta^{-1} = 1 + I_{808}/I_{\text{sat}}$. In the inset, the dashed lines are fitted using all data points; in the main panel, linear curve fitting for Tm concentrations $\geq 3.5\%$ uses only data points at low 808 nm intensity. At high 808 nm intensity, the reciprocals of depletion ratio start to deviate from linearity towards plateaus. Error bars in **a** and **b**, ± 1 s.d. with $n = 5$ each. Reproduced with permission from Ref.[31] Copyright (2017) Macmillan Publishers Limited.

We further explore the use of highly doped UCNPs for optical super-resolution imaging; the 808 nm beam is spatially modulated to produce a doughnut-shaped point spread function (PSF) that overlapped with the Gaussian PSF of the 980 nm excitation beam at the focal plane (illustrated in **Fig. 3.9a**).[31] As shown in **Fig. 3.9b**, a region with a size comparable to the optical diffraction limit but containing three 40-nm UCNPs is selected, and a sequence of far-field optical super-resolution images that clearly resolve the adjacent UCNPs are recorded. Spot sizes of 48.3 nm are obtained by our upconversion-STED

microscopy at an 808 nm intensity of 9.75 MW cm^{-2} (**Fig. 3.9c**). As the measured full-width at half-maximum (FWHM) is a convolution between the theoretical resolution and the physical size of the nanoparticle, this only gives the upper bound of the actual PSF size. Deconvolution based on the simple Pythagorean equation shows this result corresponds to a markedly improved resolution of 27.4 nm, representing a 13-fold improvement over the optical diffraction limit, or 1/36 of the excitation wavelength. Compared with earlier use of UCNP in super-resolution microscopy, the upconversion-STED we report here is superior in two respects: it has a simple set-up involving two near-infrared diode lasers, and offering multiple colours and luminescence lifetimes to realize multiplexing. In addition to excellent photostability, sensitivity and versatility, highly doped UCNP now offer efficient optical switching with saturation intensity as low as 0.19 MW cm^{-2} . These engineered nanocrystals offer saturation intensity two orders of magnitude lower than those of fluorescent probes currently employed in stimulated emission depletion microscopy ($1\text{-}240 \text{ MW cm}^{-2}$), suggesting a new way of alleviating the square-root law that typically limits the resolution that can be practically achieved by such techniques.

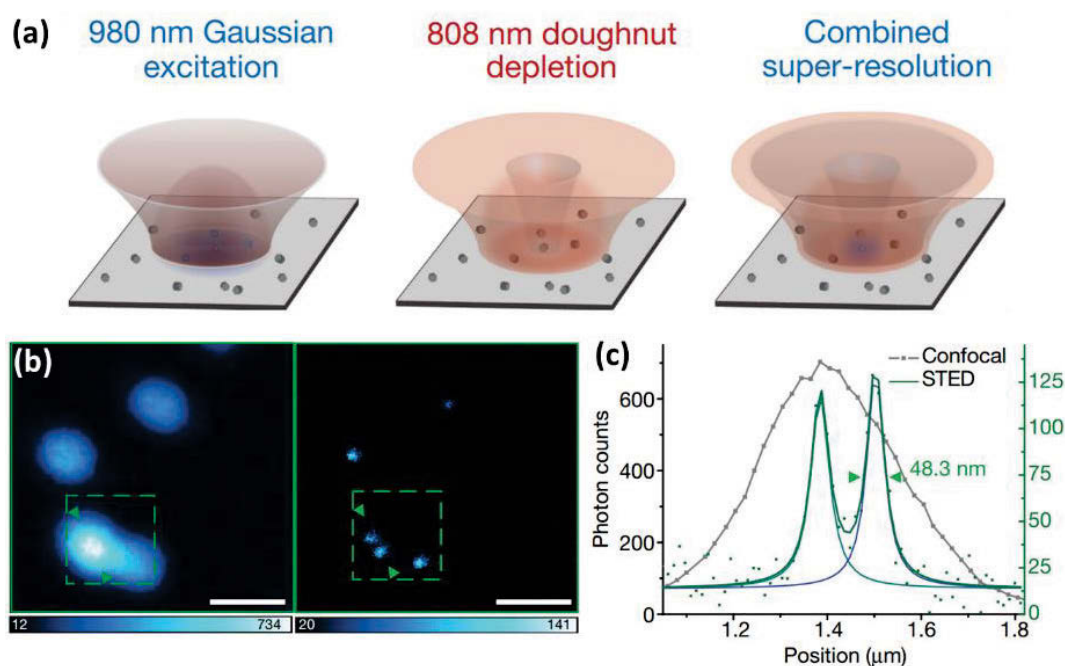


Figure 3.9 (a) Diagrams of the upconversion-STED super-resolution imaging, in which a Gaussian excitation profile (980 nm) and a Gauss–Laguerre mode ‘doughnut’ depletion profile (808 nm) at far field are employed. (b) Confocal (left) and super-resolution (right) images of the 40-nm 8% Tm^{3+} -doped UCNP. The 980 nm and 808 nm intensities are 0.66 and 9.75 MW cm^{-2} , respectively. Pixel dwell time, 4 ms; scale bars, 500 nm. Dashed boxes mark an area containing closely spaced 13-nm UCNP that can be resolved in upconversion-STED but not in confocal imaging.

(c), Intensity profiles between the arrows across two UCNPs in **b**, showing an FWHM of 48.3 nm after Gaussian fitting. Reproduced with permission from Ref.[31] Copyright (2017) Macmillan Publishers Limited.

3.4.2 NIREs-based super-resolution imaging [32]

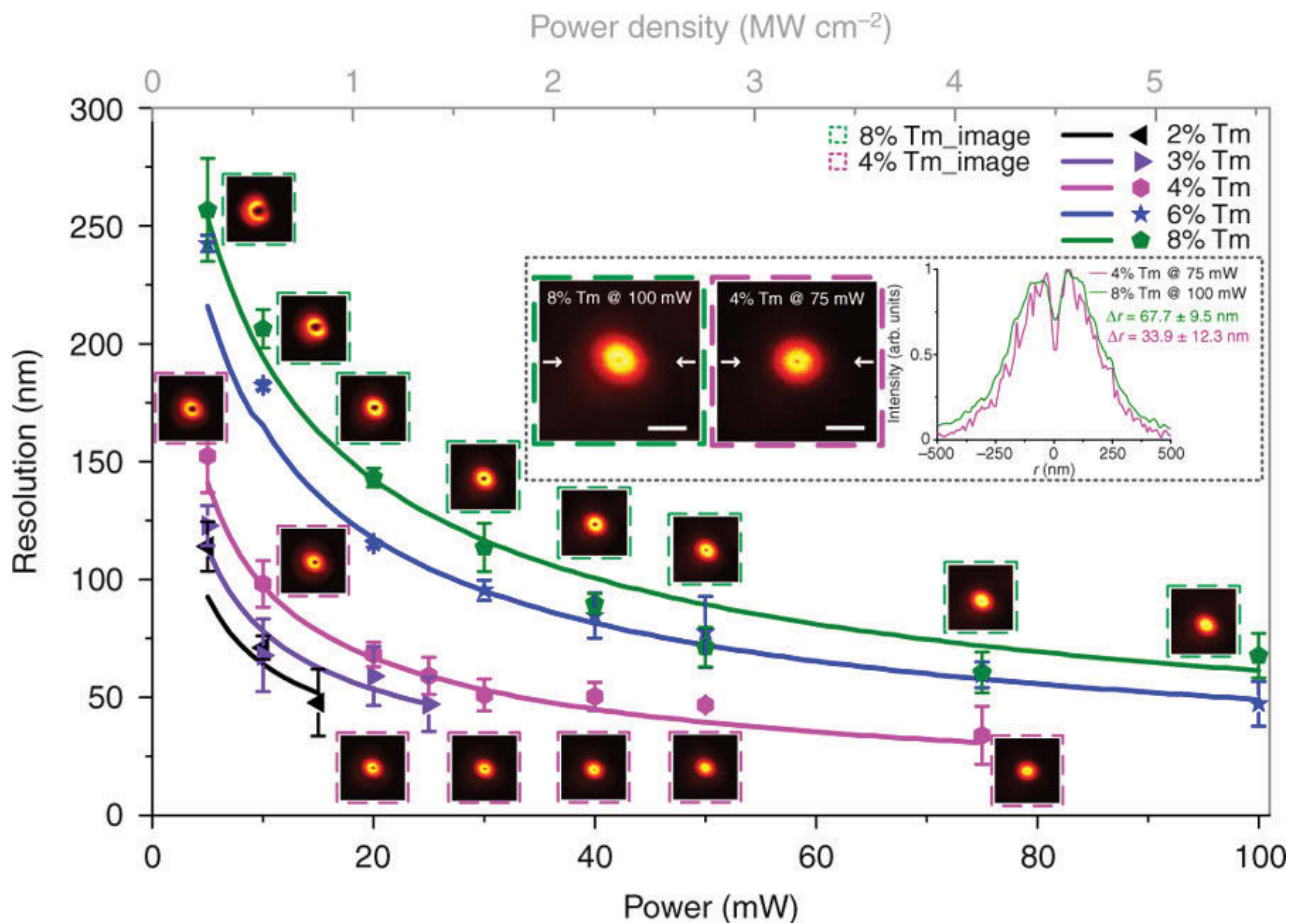


Figure 3.10 Super-resolution scaling Δr of UCNPs ($\text{NaYF}_4:20\% \text{Yb}^{3+}$, $x\% \text{Tm}^{3+}$, ~ 40 nm in diameter; $x = 2, 3, 4, 6, 8$) as a function of the excitation power (intensity). The dots of experimental data are fitted well to the simulation results. Error bars indicate standard deviations from line profiles of several measurements. Insets, NIREs images of 8% Tm^{3+} doping UCNPs at 5.5 MW/cm^2 (left), 4% Tm^{3+} at 4 MW/cm^2 (middle), and the corresponding cross section profile lines (right). Pixel dwell time, 3 ms; pixel size, 10 nm. Scale bar is 500 nm. Reproduced from Ref.[32].

An important application of UCNPs is multi-photon near-infrared emission saturation nanoscopy. [32] We find that setting the 980-nm excitation laser to create a doughnut beam can realize the super-resolution imaging of single UCNPs. Coherent excitation by a 980-nm doughnut beam will easily saturate the metastable level which has a NIR emission (800 nm), so that excited state saturation, or ‘negative’ Ground

State Depletion (GSD)-like mode, can be achieved at excited states of Tm^{3+} activators. This NIR emission band is found brighter and more efficient being saturated at lower laser power, therefore ideal for MPM super-resolution imaging, with remarkable light penetration depth, ultra-low auto-fluorescence background and minimum photo-toxicity. We further demonstrated a novel approach by modifying the material properties of UCNPs to enhance optical resolution, which might be adopted to other super resolution probes (**Fig. 3.10**).

3.4.3 Single nanoparticle tracking [33]

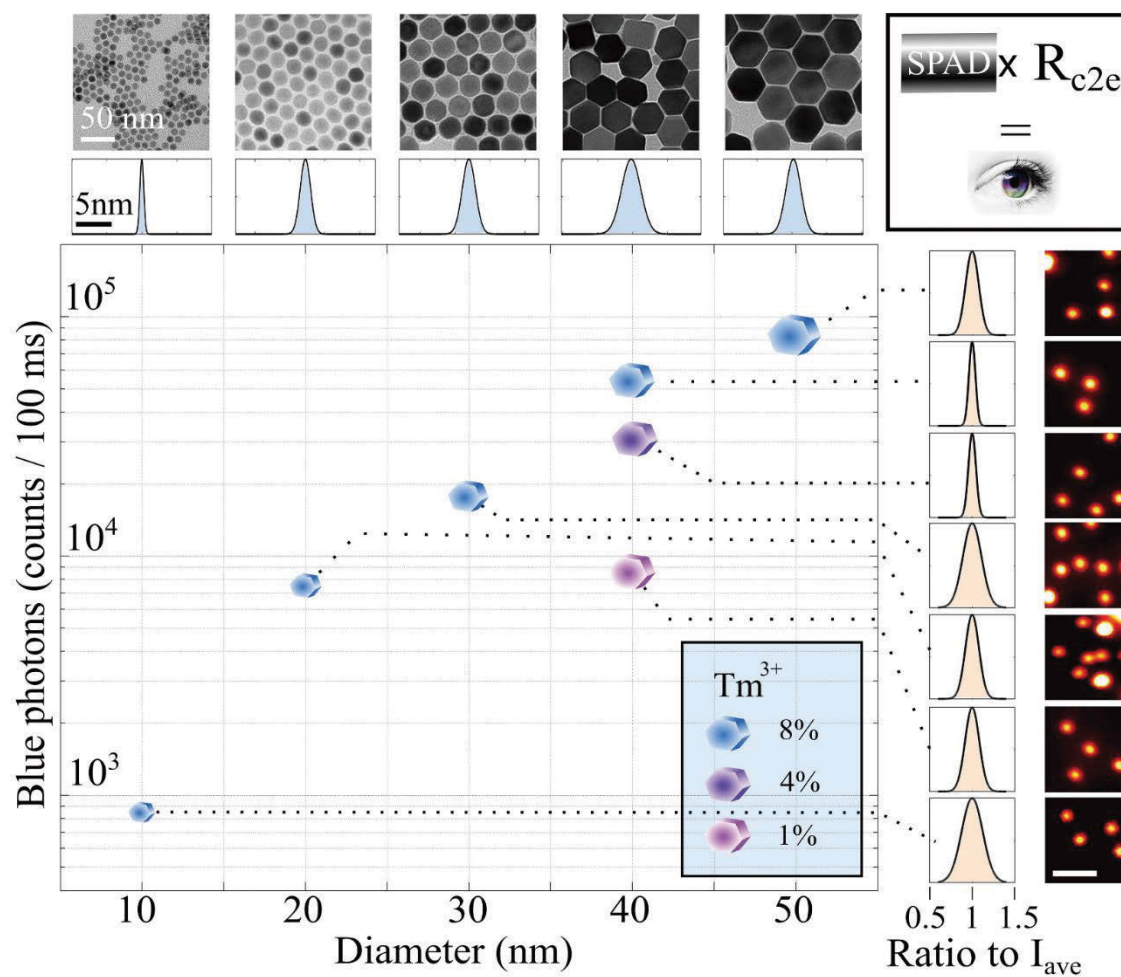


Figure 3.11 the size (transmission electron microscope images) and intensity (confocal scanning) at the blue band of a library of precisely controlled synthesized UCNPs, including peak sizes of 9.98 nm, 22.25 nm, 31.96 nm, 39.78 nm, and 50.21 nm and different Tm^{3+} doping concentrations of 1 mol%, 4 mol% and 8 mol% for the ~40 nm UCNPs.

The standard derivation (SD) of the size varied from 6.23% to 17.4% from the average intensity (I_{ave}). The photon counts used in this paper are the photon counts that reach a human cornea (I_{eye}). Reproduced from Ref.[33].

Due to its optical diffraction limit, conventional far-field fluorescence microscopy does not have sufficient resolution to determine the number of nanoparticles when they are too close to each other. Approaches such as correlative electron microscopy[34] or the recently reported MINFLUX method[35] can be applied to improve the resolution. High-level UCNPs uniformity makes it possible for observers to identify the threshold intensity for single-UCNP detection.[33] **Fig. 3.11** shows a series of different batches of UCNPs purposely synthesized to cover a large range of representative sizes and emission properties. Remarkably, emission across various particles is highly uniform, which provides the foundation for distinguishing single UCNPs from their clusters. Notably, single UCNPs can be detected at low excitation power densities.

The emitters with a brightness higher than the threshold value will be identified as several nanoparticles within the diffraction limit region (e.g., labeled by orange dots in **Fig. 3.12a**).[33] The threshold value measured by the system enables automatic single-nanoparticle detection (**Fig. 3.12a**, processed data) in real-time by computer processing of a wide-field fluorescence image. Note that the processed computer data compensates for the non-uniform excitation field and provides an accurate single identification accuracy (100% accuracy). Remarkably, due to the background-free detection with the NIR excitation, non-blinking and non-bleaching features of the UCNPs, the human eye can also identify this threshold and recognize single UCNPs during microscopic inspection (**Fig. 3.12a**, eye vision). The importance of the real-time observation of single cellular event comes from the detection of sub-cellular vesicles and protein movements and understanding their interactions in the complex cellular function. There are a myriad of models[36] that propose different sub-cellular functions, including cytoskeleton re-arrangement[37], protein dynamics, organelle movement and cooperation[38, 39], but until now, options for the real-time observation of these models in living cells have been limited. As **Fig. 3.12b** shows, in the three typical 2-dimensional images taken at different heights, the high brightness of the photostable UCNPs is detectable not only in a dark room but also under bright-field illumination, providing the ability to identify the position of a single nanoparticle within a living cell and establishing a powerful tool for examining intercellular re-organization and trafficking. By recording the data and offline analysis of nanoparticles inside living cells, the 3-dimensional trajectories of seven spots of single particles (# 2, 3, 4, and 6) and clusters (# 1, 5, and 7) within a single cell for an observation period of 21 s (**Fig. 3.12c**) clearly

show the heterogeneous dynamics of each single nanoparticle and cluster, highlighting the ability to precisely distinguish the transition between different dynamic phases of the transport of a single nanoparticle.

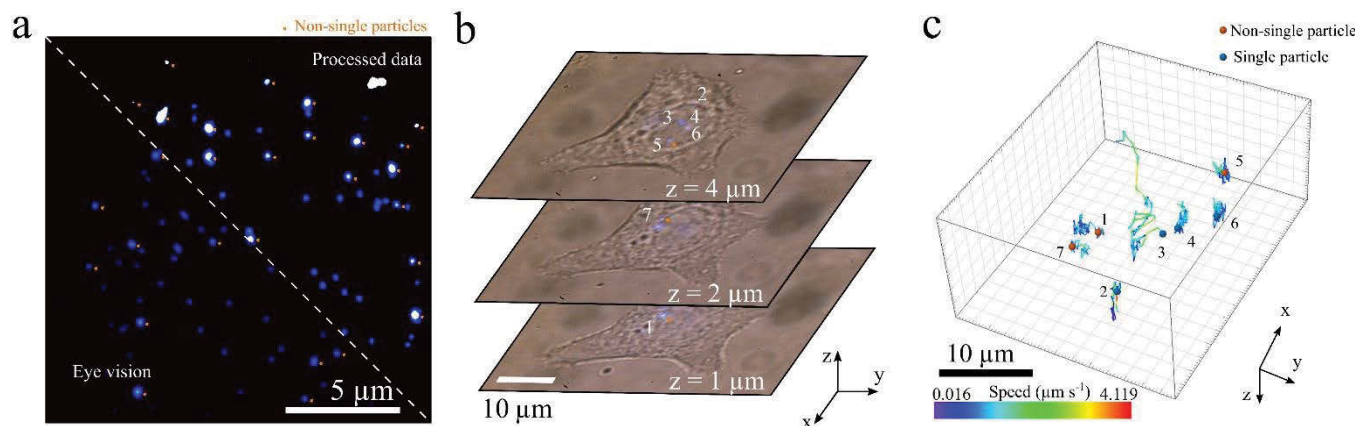


Figure 3.12 Wide-field upconversion fluorescence microscopy method for determining single nanoparticles for long-term 3D tracking and measurement of the local intracellular viscosity. (a) The bottom left image was recorded by a CCD camera (Nikon DS-2Mv) and adjusted (exposure time 150 ms; gain at 4) to show the equivalent intensity level of the image observed by the eye. The top right image was recorded by the same CCD image, and the intensity of each nanoparticle spot is compensated by considering the Gaussian excitation pattern and the power-dependent emission property of the UCNPs (doped with 1 mol% Tm³⁺). Both half images allow for the determination of single UCNPs and clusters or spots containing more than one UCNP, marked by an orange dot. (b) Three representative single-cell images containing 7 UCNP spots (doped with 4 mol% Tm³⁺) at different heights of 1, 2 and 4 μm recorded by a CCD camera in video mode (4.75 frames per second; the exposure time of each frame is 150 ms; gain at 4) during the z-axis scanning process. The high brightness of each single UCNP allows for the real-time recording of the upconversion fluorescence images under bright-field illumination. (c) 3D trajectories of seven numbered upconversion spots, including four single UCNPs (#2, 3, 4, and 6), marked by blue dots, and three non-single UCNPs (#1, 5, and 7), marked by orange dots, observed for 21 s by a 368.85 s tracked video. Reproduced from Ref.[33].

3.5 Conclusion

This chapter introduces a seed-mediated UCNP growth method that provided nano-scale size control. The uniformity of the nanocrystals is confirmed with TEM and upconversion luminescence imaging. This ability makes UCNP possible in the application of STED-/NIRFS-based super-resolution imaging.

This approach is not limited to homogeneous lanthanide doped UCNPs. Because the small lattice mismatches between different types of NaREF₄, it is practical to precisely fabricate heterogeneous core@shell nanoparticles through injection of different NaREF₄ precursors. The hierarchical design of core@shell UCNPs with various shells and features produce particles better tailored to their end-use than conventional UCNPs.

One open question this chapter raised is why seeds start growing 30 min after their injection at 300 °C. A more in-depth study of this intriguing observation will be introduced in next Chapter.

3.6 References

- [1] Zhou, J., Liu, Q., Feng, W., Sun, Y., Li, F., Upconversion Luminescent Materials: Advances and Applications, *Chem Rev* 115 (1) (2015) 395-465.
- [2] Zhou, B., Shi, B., Jin, D., Liu, X., Controlling upconversion nanocrystals for emerging applications, *Nat Nano* 10 (11) (2015) 924-936.
- [3] Dong, H., Du, S.-R., Zheng, X.-Y., Lyu, G.-M., Sun, L.-D., Li, L.-D., Zhang, P.-Z., Zhang, C., Yan, C.-H., Lanthanide Nanoparticles: From Design toward Bioimaging and Therapy, *Chem Rev* 115 (19) (2015) 10725-10815.
- [4] Lu, Y., Zhao, J., Zhang, R., Liu, Y., Liu, D., Goldys, E.M., Yang, X., Xi, P., Sunna, A., Lu, J., Shi, Y., Leif, R.C., Huo, Y., Shen, J., Piper, J.A., Robinson, J.P., Jin, D., Tunable lifetime multiplexing using luminescent nanocrystals, *Nat Photon* 8 (1) (2014) 32-36.
- [5] Yan, C., Zhao, H., Perepichka, D.F., Rosei, F., Lanthanide Ion Doped Upconverting Nanoparticles: Synthesis, Structure and Properties, *Small* 12 (29) (2016) 3888-3907.
- [6] Li, Z., Zhang, Y., An efficient and user-friendly method for the synthesis of hexagonal-phase NaYF₄:Yb, Er/Tm nanocrystals with controllable shape and upconversion fluorescence, *Nanotechnology* 19 (34) (2008) 345606.
- [7] HaiSheng, Q., ZhengQuan, L., Yong, Z., Multicolor polystyrene nanospheres tagged with up-conversion fluorescent nanocrystals, *Nanotechnology* 19 (25) (2008) 255601.
- [8] Qian, H.-S., Zhang, Y., Synthesis of Hexagonal-Phase Core–Shell NaYF₄ Nanocrystals with Tunable Upconversion Fluorescence, *Langmuir* 24 (21) (2008) 12123-12125.
- [9] Shi, F., Wang, J., Zhang, D., Qin, G., Qin, W., Greatly enhanced size-tunable ultraviolet upconversion luminescence of monodisperse [small beta]-NaYF₄:Yb,Tm nanocrystals, *Journal of Materials Chemistry* 21 (35) (2011) 13413-13421.

- [10] Na, H., Woo, K., Lim, K., Jang, H.S., Rational morphology control of [small beta]-NaYF₄:Yb,Er/Tm upconversion nanophosphors using a ligand, an additive, and lanthanide doping, *Nanoscale* 5 (10) (2013) 4242-4251.
- [11] Liu, J., Bu, W., Zhang, S., Chen, F., Xing, H., Pan, L., Zhou, L., Peng, W., Shi, J., Controlled Synthesis of Uniform and Monodisperse Upconversion Core/Mesoporous Silica Shell Nanocomposites for Bimodal Imaging, *Chemistry – A European Journal* 18 (8) (2012) 2335-2341.
- [12] Park, Y.I., Kim, J.H., Lee, K.T., Jeon, K.-S., Na, H.B., Yu, J.H., Kim, H.M., Lee, N., Choi, S.H., Baik, S.-I., Kim, H., Park, S.P., Park, B.-J., Kim, Y.W., Lee, S.H., Yoon, S.-Y., Song, I.C., Moon, W.K., Suh, Y.D., Hyeon, T., Nonblinking and Nonbleaching Upconverting Nanoparticles as an Optical Imaging Nanoprobe and T1 Magnetic Resonance Imaging Contrast Agent, *Advanced Materials* 21 (44) (2009) 4467-4471.
- [13] Wang, F., Deng, R., Wang, J., Wang, Q., Han, Y., Zhu, H., Chen, X., Liu, X., Tuning upconversion through energy migration in core-shell nanoparticles, *Nat Mater* 10 (12) (2011) 968-973.
- [14] Su, Q., Han, S., Xie, X., Zhu, H., Chen, H., Chen, C.-K., Liu, R.-S., Chen, X., Wang, F., Liu, X., The Effect of Surface Coating on Energy Migration-Mediated Upconversion, *Journal of the American Chemical Society* 134 (51) (2012) 20849-20857.
- [15] Xie, X., Gao, N., Deng, R., Sun, Q., Xu, Q.-H., Liu, X., Mechanistic Investigation of Photon Upconversion in Nd³⁺-Sensitized Core-Shell Nanoparticles, *Journal of the American Chemical Society* 135 (34) (2013) 12608-12611.
- [16] Wang, F., Deng, R., Liu, X., Preparation of core-shell NaGdF₄ nanoparticles doped with luminescent lanthanide ions to be used as upconversion-based probes, *Nat. Protocols* 9 (7) (2014) 1634-1644.
- [17] Deng, R., Qin, F., Chen, R., Huang, W., Hong, M., Liu, X., Temporal full-colour tuning through non-steady-state upconversion, *Nat Nano* 10 (3) (2015) 237-242.
- [18] Zhou, B., Yang, W., Han, S., Sun, Q., Liu, X., Photon Upconversion Through Tb³⁺-Mediated Interfacial Energy Transfer, *Advanced Materials* 27 (40) (2015) 6208-6212.
- [19] Brites, C.D.S., Xie, X., Debasu, M.L., Qin, X., Chen, R., Huang, W., Rocha, J., Liu, X., Carlos, L.D., Instantaneous ballistic velocity of suspended Brownian nanocrystals measured by upconversion nanothermometry, *Nat Nano* 11 (10) (2016) 851-856.
- [20] Deng, R., Wang, J., Chen, R., Huang, W., Liu, X., Enabling Förster Resonance Energy Transfer from Large Nanocrystals through Energy Migration, *Journal of the American Chemical Society* 138 (49) (2016) 15972-15979.
- [21] Rodríguez-Sevilla, P., Zhang, Y., Haro-González, P., Sanz-Rodríguez, F., Jaque, F., Solé, J.G., Liu, X., Jaque, D., Thermal Scanning at the Cellular Level by an Optically Trapped Upconverting Fluorescent Particle, *Advanced Materials* 28 (12) (2016) 2421-2426.
- [22] Chen, Q., Xie, X., Huang, B., Liang, L., Han, S., Yi, Z., Wang, Y., Li, Y., Fan, D., Huang, L., Liu, X., Confining Excitation Energy in Er³⁺-Sensitized Upconversion Nanocrystals through Tm³⁺-Mediated Transient Energy Trapping, *Angewandte Chemie International Edition* 56 (26) (2017) 7605-7609.

- [23] Liu, X., Wang, Y., Li, X., Yi, Z., Deng, R., Liang, L., Xie, X., Loong, D.T.B., Song, S., Fan, D., All, A.H., Zhang, H., Huang, L., Liu, X., Binary temporal upconversion codes of Mn²⁺-activated nanoparticles for multilevel anti-counterfeiting, *Nature Communications* 8 (1) (2017) 899.
- [24] Abel, K.A., Boyer, J.-C., Veggel, F.C.J.M.v., Hard Proof of the NaYF₄/NaGdF₄ Nanocrystal Core/Shell Structure, *Journal of the American Chemical Society* 131 (41) (2009) 14644-14645.
- [25] Dong, C., Pichaandi, J., Regier, T., van Veggel, F.C.J.M., Nonstatistical Dopant Distribution of Ln³⁺-Doped NaGdF₄ Nanoparticles, *The Journal of Physical Chemistry C* 115 (32) (2011) 15950-15958.
- [26] Johnson, N.J.J., Oakden, W., Stanisz, G.J., Scott Prosser, R., van Veggel, F.C.J.M., Size-Tunable, Ultrasmall NaGdF₄ Nanoparticles: Insights into Their T₁ MRI Contrast Enhancement, *Chemistry of Materials* 23 (16) (2011) 3714-3722.
- [27] Johnson, N.J.J., Korinek, A., Dong, C., van Veggel, F.C.J.M., Self-Focusing by Ostwald Ripening: A Strategy for Layer-by-Layer Epitaxial Growth on Upconverting Nanocrystals, *Journal of the American Chemical Society* 134 (27) (2012) 11068-11071.
- [28] Fischer, S., Johnson, N.J.J., Pichaandi, J., Goldschmidt, J.C., Veggel, F.C.J.M.v., Upconverting core-shell nanocrystals with high quantum yield under low irradiance: On the role of isotropic and thick shells, *Journal of Applied Physics* 118 (19) (2015) 193105.
- [29] Suter, J.D., Pekas, N.J., Berry, M.T., May, P.S., Real-Time-Monitoring of the Synthesis of β-NaYF₄:17% Yb,3% Er Nanocrystals Using NIR-to-Visible Upconversion Luminescence, *The Journal of Physical Chemistry C* 118 (24) (2014) 13238-13247.
- [30] Liu, D., Xu, X., Du, Y., Qin, X., Zhang, Y., Ma, C., Wen, S., Ren, W., Goldys, E.M., Piper, J.A., Dou, S., Liu, X., Jin, D., Three-dimensional controlled growth of monodisperse sub-50 nm heterogeneous nanocrystals, *Nature Communications* 7 (2016) 10254.
- [31] Liu, Y., Lu, Y., Yang, X., Zheng, X., Wen, S., Wang, F., Vidal, X., Zhao, J., Liu, D., Zhou, Z., Ma, C., Zhou, J., Piper, J.A., Xi, P., Jin, D., Amplified stimulated emission in upconversion nanoparticles for super-resolution nanoscopy, *Nature* 543 (7644) (2017) 229-233.
- [32] Chen, C., Wang, F., Wen, S., Su, Q. P., Wu, M. C. L., Liu, Y., Wang, B., Li, D., Shan, X., Kianinia, M., Aharonovich, I., Toth, M., Jackson, S. P., Xi, P., Jin, D., Multi-photon near-infrared emission saturation nanoscopy using upconversion nanoparticles. *Nature Communications* 9 (1) (2018) 3290.
- [33] Wang, F., Wen, S., He, H., Wang, B., Zhou, Z., Shimoni, O., Jin, D., Microscopic inspection and tracking of single upconversion nanoparticles in living cells, *light: science & applications*, 7 (4) (2018) 18007.
- [34] Albanese, A., Chan, W.C.W., Effect of Gold Nanoparticle Aggregation on Cell Uptake and Toxicity, *ACS Nano* 5 (7) (2011) 5478-5489.
- [35] Balzarotti, F., Eilers, Y., Gwosch, K.C., Gynnå, A.H., Westphal, V., Stefani, F.D., Elf, J., Hell, S.W., Nanometer resolution imaging and tracking of fluorescent molecules with minimal photon fluxes, *Science* 355 (6325) (2017) 606-612.
- [36] Frauenfelder, H., Chen, G., Berendzen, J., Fenimore, P.W., Jansson, H., McMahon, B.H., Stroer, I.R., Swenson, J., Young, R.D., A unified model of protein dynamics, *Proceedings of the National Academy of Sciences* 106 (13) (2009) 5129-5134.

- [37] Fakhri, N., Wessel, A.D., Willms, C., Pasquali, M., Klopfenstein, D.R., MacKintosh, F.C., Schmidt, C.F., High-resolution mapping of intracellular fluctuations using carbon nanotubes, *Science* 344 (6187) (2014) 1031-1035.
- [38] Chu, B.-B., Liao, Y.-C., Qi, W., Xie, C., Du, X., Wang, J., Yang, H., Miao, H.-H., Li, B.-L., Song, B.-L., Cholesterol Transport through Lysosome-Peroxisome Membrane Contacts, *Cell* 161 (2) (2015) 291-306.
- [39] Valm, A.M., Cohen, S., Legant, W.R., Melunis, J., Hershberg, U., Wait, E., Cohen, A.R., Davidson, M.W., Betzig, E., Lippincott-Schwartz, J., Applying systems-level spectral imaging and analysis to reveal the organelle interactome, *Nature* 546 (7656) (2017) 162-167.

CHAPTER 4 Fabrication of Bright and Ultra-small Core@shell UCNPs by Seed-mediated *in-situ* Growth

4.1 Preamble

In Chapter 3, we employ the seed-mediated isotropic growth approach to produce a series of the homogeneous nanocrystals with fine-tunable sizes. Through this work, we investigate conditions for controlled epitaxial growth of core@shell nanostructures. We find that the epitaxial growth of seeds does not start immediately with the shell precursors at 300 °C. Instead, the shell precursors first nucleate and grow by themselves into the α -phase nanocrystals and the size of seeds slightly reduces. Till around 25 min later, the seeds start to re-grow and the amount of small α -phase nanocrystals decreases quickly with time. This observation is a significant indication that explains two challenges in synthesis: (1) the dissolved surface layers from the seed nanocrystals will introduce incomplete coating of heterogeneous shell nanostructure that significantly affects the optical properties of core@shell nanocrystals; (2) it is hard to grow high quality shells onto the sub-10 nm seeds nanocrystals, as the small size cannot survive during this relatively long time before the growth process re-starts.

In this Chapter, we systematically investigate various factors to identify the key to facilitating the controlled epitaxial growth of shells. We find that the reaction mix plays an essential role in catalyzing the epitaxial growth. Using this approach, we successfully fabricate both the integrated heterogeneous core@shell nanocrystals with improved luminescence performance and the sub-10 nm core@shell nanocrystals.

4.2 Introduction

The advances made in producing small and bright UCNPs have enabled many emerging bio-applications towards highly sensitive molecular detection, single-molecule tracking and super resolution imaging of subcellular structures. One of the ongoing efforts is to enhance their brightness and upconversion efficiency, especially when many *in vivo* studies require the size of nanocrystals smaller than the size of biomolecules, e.g. in the sub-10 nm range. Generally speaking, smaller UCNPs have increased number of surface quenchers with structural and compositional discontinuities, which decreases their brightness.

The strategy is to passivate the active core from the surface quenchers with an inert shell. Several groups have reported some remarkably enhanced upconversion emissions through inert shell coating. The enhancement factors range from several to hundreds of folds,[1-10] largely depending on the dissimilar core size, doping concentration, and excitation power density. The shell thickness has also been found to play an important role in the enhancement.[3, 11] Zhao et al. systematically studied a series of NaYF₄:Yb/Er@NaGdF₄ nanoparticles with shell thickness of 0 to 2.5 nm, and detected a linear dependence of upconversion emission intensity on the NaGdF₄ shell thickness.[11] The emission intensity often reaches a plateau at a shell thickness of ~3 nm, corresponding to the critical distance required for the effective interactions between surface oscillators and lanthanide ions.

Indeed, growing the thin shell onto an upconversion-active core has been further extended into multiple shell architectures. This allows the design of arbitrary combination of optical ‘insulation’ layers and energy migration layers within a single nanoparticle of just a few tens of nanometers.[12-18] The fine tuning of upconversion emission colors through energy migration has been demonstrated using Gd³⁺ sublattice structure to bridge efficient energy transfer across the core@shell interface of NaYbF₄:Gd³⁺,Tm³⁺@NaGdF₄@CaF₂:Ce³⁺ nanostructures. This approach has further shifted the excitation wavelength to ~800 nm with Nd³⁺ sensitizers for efficient delivery of light through deep tissue by the so-called transparent biological window.[12] To effectively reduce the cross-relaxation and back energy transfer from activators to Nd³⁺ sensitizers, Zhong et al. has designed NaYF₄:Yb³⁺,Er³⁺@NaYF₄:Yb³⁺@NaNdF₄:Yb³⁺ nanostructure, in which the intermediate NaYF₄:Yb³⁺ shell successfully separates Er³⁺ activators and Nd³⁺ primary upconversion sensitizers.[19] Further coating with an inert NaYF₄ shell has been demonstrated with largely enhanced brightness and quantum yield.[20] Also, the control in doping location with optical ‘insulation’ layers has been demonstrated to emit the

orthogonal emissions,[21-23] spectral/lifetime multiplexing,[24] up-converting/down-shifting,[25] multimode imaging,[26] and multi-optical functions (NIR-induced heat conversion, luminescence, and thermometry) in single particles.[27] For example, by design and synthesis of $\text{NaGdF}_4:\text{Nd}^{3+}@\text{NaYF}_4@\text{NaGdF}_4:\text{Nd}^{3+},\text{Yb}^{3+},\text{Er}^{3+}@\text{NaYF}_4$ nanoparticles, both upconversion and down-shifting luminescence, sensitized by highly doped Nd^{3+} , can be achieved without cross interference.[25]

The importance of design and synthesis of single- and multi- shell coated UCNPs has necessitated a comprehensive study to under the mechanism of epitaxial growth of thin shells. The chemical and structural characteristics at the interface between the core and the layer of shell within a nanocrystal will determine their upconversion properties and performance toward the design of more efficient upconversion nanostructure system.[28, 29] The issue of intermixing and diffusion of dopants between the core and the shell has been identified as an issue.

Chen et al. has developed and validated a spectroscopic method to assess the integrity of core@shell nanocrystals by using Tb^{3+} and Ce^{3+} as luminescent probes.[30] They concluded that the dopant ions were firmly confined in the designed areas within the as-synthesized core@shell nanoparticles, but heat treatment at high temperatures (above 350 °C) promoted the diffusion and migration of dopant ions, which degraded the structural integrity. Haase et al. employed an optical spectroscopy approach to confirm there were a small amount of Eu^{3+} ions existing on the shell of $\text{NaEuF}_4@\text{NaGdF}_4$ particles.[31] The intermixing of dopants between the core and the shell material has be investigated by studying the energy transfer process between Eu^{3+} and Gd^{3+} , between neighboring Eu^{3+} , and between the surface ligands and Eu^{3+} exposed on the nanoparticle surface. The difference may come from the size of the starting core nanocrystals, which determines the length of diffusion at the interface. Additionally, it is also valid to question the effect of the method used for the epitaxial growth of the shell, which may affect the degree of cation intermixing.

Indeed, when we looked into the literature, the core@shell structured UCNPs have been widely fabricated by different methods, such as the heating-up methods, hot-injection methods. Also different Na^+ and F^- sources could be used in the precursors, such as NaOH and NH_4F , or a single-source NaOOCF_3 . [3, 17, 24, 32-36] As long as the issue of cation intermixing effect is concerned in single- and multi- shell nanocrystals, by using different size and doping concentrations, there remains a massive amount of work to be done in terms of understanding the cause of intermixing and exploration of strategies

to optimize the design and the synthesis of the single- and multi- shell UCNPs, when changing conditions, such as the size, the shape, and the chemical composition, in different synthesis routes.[28, 31]

Most recently, Hudry et al. systematically characterized the core@shell UCNPs with different shell thickness.[28] They did the local chemical and structure study by different technologies, including scanning TEM with energy dispersive X-ray spectroscopy, selected area electron diffraction, X-ray total scattering, and pair distribution function analyses. Their results indicated that the strong intermixing between the core and shell materials is induced by a partial seed dissolution and recrystallization process. This study emphasizes the importance of reducing the thickness of the intermixing layer or avoid the formation of this layer, as the key to improving the brightness of UCNPs, particularly towards producing the bright and ultra-small nanocrystals for biomedical applications.

In this Chapter, we systematically investigate the roles of various factors and identify the key to minimize the intermixing between the core and the shell compartments. The results show that the reaction mix, after the core being synthesized, plays an important role in reducing the time for the successive epitaxial growth of shells in the seed-mediated growth method. As a result, we have successfully fabricated the high quality integrated heterogeneous core@shell nanocrystals with improved luminescence performance. More importantly, the sub-10 nm core nanocrystals have been successfully coated with the inert shell to produce the ultra-small core@shell nanocrystals.

4.3 Experimental Section

4.3.1 Synthesis of NaYF₄:20%Yb,2%Er nanocrystals

NaYF₄:20%Yb,2%Er has been synthesized similarly to our previously reported method.[37, 38] In a typical experiment, 0.5 mmol RECl₃ (RE = Y, Yb, Er) was added to a flask containing 6 ml OA and 15 ml ODE. The mixture was heated to 170 °C under argon for 30 min to obtain a clear solution and then cooled down to about 50 °C, followed by the addition of 5 mL methanol solution of NH₄F (2 mmol) and NaOH (1.25 mmol). After stirring for 30 min, the solution was heated to 80 °C under argon for 20 min to remove methanol, and then the solution was further heated to 300 °C for another 90 min. Finally, the reaction solution was cooled down to room temperature. It was then diluted with an equal volume of ethanol, which is led to precipitation of the nanocrystals. After centrifugation, the precipitate was purified by re-dispersion in 3 ml cyclohexane, followed by precipitation with ethanol and separation by centrifugation. After 3 to 4 washing cycles, the nanocrystals were dispersed in 5 mL cyclohexane.

4.3.2 Core@shell nanocrystals synthesis

The epitaxial growth of NaREF₄ onto the core of NaYF₄ was conducted via a successive layer-by-layer hot-injection protocol. Firstly, shell precursors were prepared. 6.0 mmol YCl₃·6H₂O was added to a flask containing 40 ml OA and 40 ml ODE. The mixture was heated to 170 °C under argon for 30 min to obtain a clear solution and then cooled down to about 50 °C, followed by the addition of methanol solution of NH₄F (24.0 mmol) and NaOH (6.0 mmol). After stirring for 30 min, the solution was heated to 80 °C under argon for 20 min to remove methanol, and then the solution was further heated to 150 °C for another 30 min. Finally, the reaction solution was cooled down to room temperature and labelled as NaYF₄ shell precursors.

For the epitaxial growth process, two approaches were employed: *ex situ* growth method and *in situ* growth methods. For *ex situ* growth, 0.2 mmol pre-synthesized and purified NaYF₄ core particles was put in a bottle with 3.6 mL OA and 9.2 mL ODE. Then the mixture was further heated to 300 °C. After that, 1.0 mL of NaYF₄ shell precursors was immediately injected into the reaction mixture and ripened at 300 °C for different time to get the core@shell nanocrystals. For the real-time monitor of the reaction process, around 0.5 ml sample was taken out from the reaction solution at different time points, then these samples were subjected to the washing process and followed with the TEM characterization.

In terms of *in situ* growth methods, NaYF₄:Yb,Er has been synthesized first. 0.2 mmol YCl₃ was added to a flask containing 3.6 ml OA and 9.2 ml ODE. The mixture was heated to 170 °C under argon for 30 min to obtain a clear solution and then cooled down to about 50 °C, followed by the addition of 1 mL methanol solution of NH₄F (0.8 mmol) and NaOH (0.5 mmol). After stirring for 30 min, the solution was heated to 80 °C under argon for 20 min to remove methanol, and then the solution was further heated to 300 °C for another 90 min. Next, 1 mL of NaYF₄ shell precursors was immediately injected into the reaction mixture and ripened at the same temperature. For the real-time monitor of the reaction process, around 0.5 ml sample was taken out from the reaction solution at different time points, then these samples were subjected to the washing process and followed with the TEM characterization.

4.3.3 Small core@shell nanocrystals synthesis

10 nm NaYF₄: 60%Yb³⁺, 2%Tm³⁺ nanocrystals was synthesized according to previously report.[39] In a typical experiment, 0.4 mmol RECl₃ (RE = Y, Yb, Tm) with the molar ratio of 38:60:2 was added to a

50 mL flask containing 6 mL OA and 6 mL ODE. The mixture was heated to 160 °C under argon for 30 min to obtain a clear solution and then cooled down to about 70 °C, followed by the addition of 1.00 g of NaOA and 0.17 g NH₄F. After stirring for 30 min, the solution was heated to 150 °C under argon for 20 min, and then the solution was further heated to 300 °C for another 45 min. Finally, the reaction solution was cooled down to room temperature, and nanoparticles were purified, and the core@shell nanocrystals were synthesized according to the same procedure as mentioned above.

4.3.4 Characterization techniques

The morphology of the formed materials was characterized *via* transmission electron microscopy (TEM) imaging (Philips CM10 TEM with Olympus Sis Megaview G2 Digital Camera) with an operating voltage of 100 kV. The samples were prepared by placing a drop of a dilute suspension of nanocrystals onto copper grids.

The upconversion luminescence spectra were obtained using of a Fluorolog-Tau3 spectrofluorometer (JobinYvon-Horiba) equipped with an external 980 nm CW diode laser with a pump power density of 500 mW/cm². The upconversion nanocrystals were dispersed in the cyclohexane and were prepared to the concentration of 1 mg/ml. The dispersion was transferred to quartz cuvettes with 10 mm path length and three measurements were conducted for each sample.

4.4 Results and Discussion

As discussed in Chapter 3, using the injected shell precursors, the core nanocrystal does not immediately grow into core-shell structure at 300 °C. The shell precursors first nucleate and grow by themselves into the α -phase nanocrystals and the size of seeds slightly reduces, as shown in **Fig. 4.1a** and **4.1b**. To understand the growth mechanism, we firstly synthesize the core@shell nanocrystals using the seed-mediated growth approach developed in Chapter 3, in which the core nanocrystals are pre-synthesized, separated from the reacted solution, and stored in the solvent of OA/ODE. When being heated to 300 °C, the shell precursors are injected (shown in **Fig. 4.1a**). As the core nanocrystals are transferred from their original solvent into the new solvent of OA/ODE as the seeds, we named this method as the *ex situ* growth approach. The TEM result at 10 min shows that shell precursor growth by themselves as the α -phase nanocrystals, while the size of seeds slightly reduces from 24 nm to 22.5 nm (**Fig. 4.1f**). With the relatively longer reaction time, the final nanocrystals become bigger, and the small α -phase nanocrystals disappear

around 45 min (**Fig. 4.1e**). These results indicate that the epitaxial growth process does not start immediately for the formation of core@shell nanocrystals (**Fig. 4.1a** and **4.1b**), but with an intermediate state (**Fig. 4.1c**). This period of time (around 30 minutes) is needed for the reaction to overcome the energy barrier to activate the epitaxial growth.

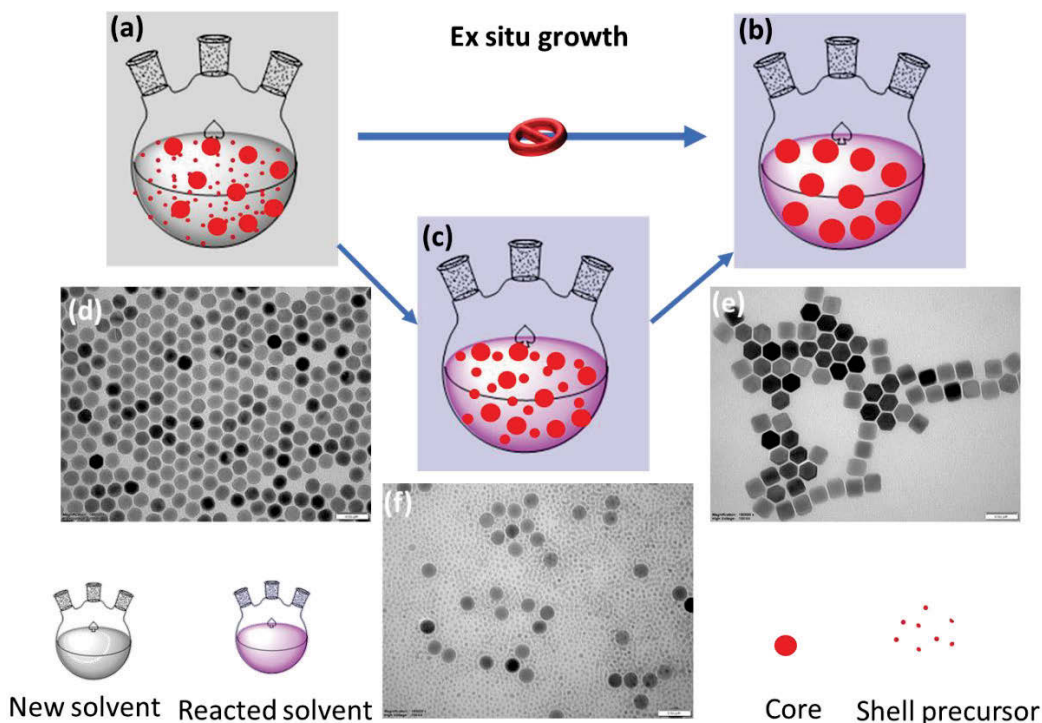


Figure 4.1 The schematic growth process (**a-c**) and corresponding TEM images (**d-f**) of the formation of α - NaYF_4 nanocrystals during the *ex situ* epitaxial growth.

To systematically study the growth process, I take a fraction of samples from the reaction solution at different time points (2, 5, 15, 25, 35, and 45 min) to monitor the reaction process. These samples are subjected to TEM characterization of their size and morphology. As shown in **Fig. 4.2**, the size of the core nanocrystals does not increase with the first 15 min, while the size of α -phase nanocrystals is formed by the precursor. At the time point of 25 min, the shape of the core nanocrystals changes from sphere to hexagon, while the overall size of the nanocrystal does not change significantly (**Fig. 4.2e**). This indicates the seeds are set and ready to grow in the solution. Then, around 35 min, the core nanocrystals start grow and the amount of small α -phase nanocrystals is reduced quickly (**Fig. 4.2f**). And the growth process is completed at 45 min as the α -phase nanocrystals completely disappear (**Fig. 4.2g**). These results suggest

that the growth process itself is relatively quick (within 10 min), but the preparing process take longer (around 30 min).

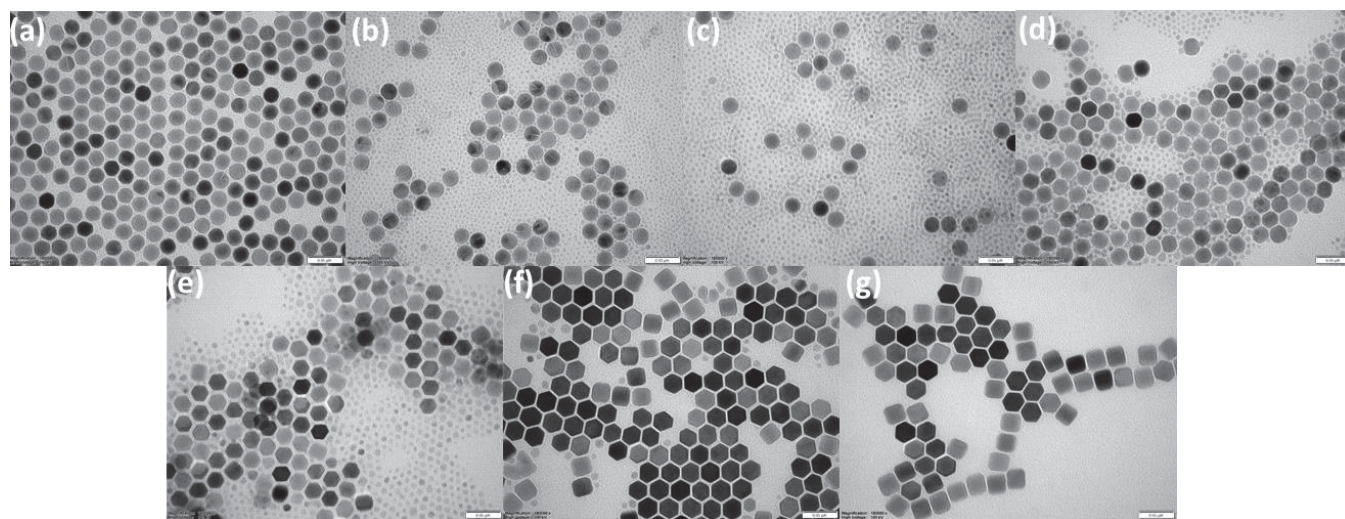


Figure 4.2 The TEM images of the NaYF₄ core (a) and the formation of nanocrystals at different reaction time (b: 2 min, c: 10 min, d: 15 min, e: 25 min, f: 35 min, g: 45 min), during the *ex situ* epitaxial growth process.

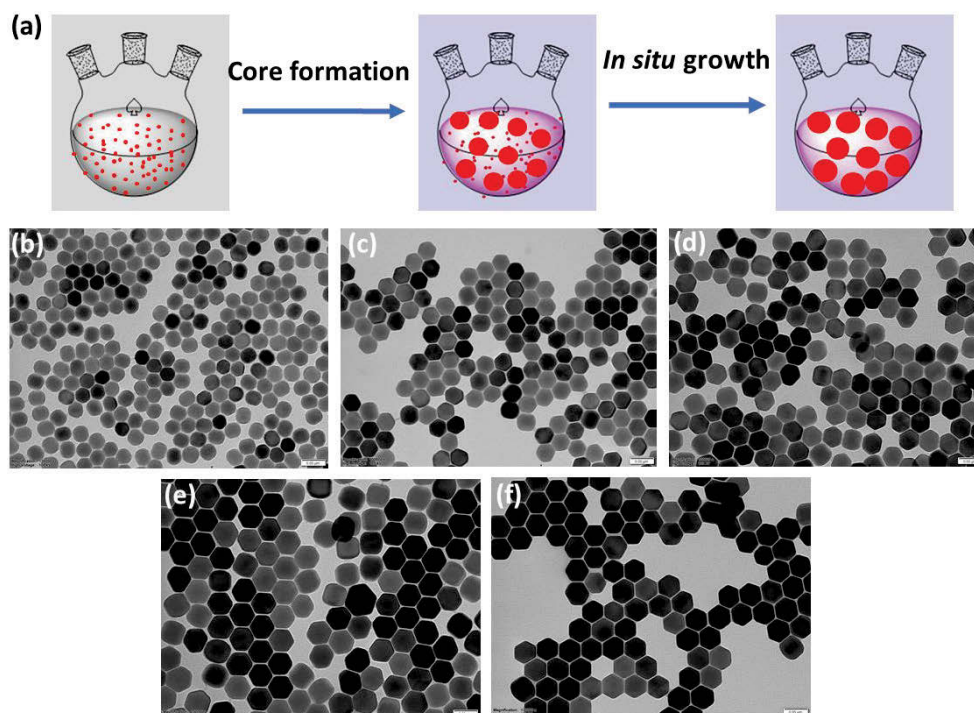


Figure 4.3 (a) The schematic process of *in situ* growth approach after the formation of the core nanocrystals, (b-f) TEM images of the formed NaYF₄ core nanocrystal, and after *in situ* growth with different amount of shell precursors (c: 0.1 mmol, d: 0.2 mmol, e: 0.3 mmol, and f: 0.4 mmol).

Next, we perform the *in situ* growth, in which the precursors are injected into the reaction solution just after the formation of the core nanocrystals at 300 °C. Surprisingly, we find that the growth process happens immediately after the injection of the precursor. As shown in the **Fig. 4.3b**, even 5 min after the injection, we can see that the size of the seeds increases significantly and there are no α -phase nanocrystals nucleated by the shell precursors. Through the continues injection of the precursors, the nanocrystals continue to grow and become bigger (from 34.0 nm to 50.1 nm) with the addition of the precursors (**Fig. 4.3b-f**). It is noted that in the *ex situ* growth process, the nanocrystals can also grow immediately after the injection of the precursor in the continues growth process once they are set to grow (around 45 min after the first injection). As shown in the **Fig. 4.4**, even 3 min after the injection, we can see that the size of the seeds increases significantly and there are no α -phase nanocrystals, which means the followed growth process have the similar behavior with that of the *in situ* growth. Also, with the continues injection of the precursors, the nanocrystals continue their growth with the size increased from 33 nm to 42 nm (**Fig. 4.4b-e**).

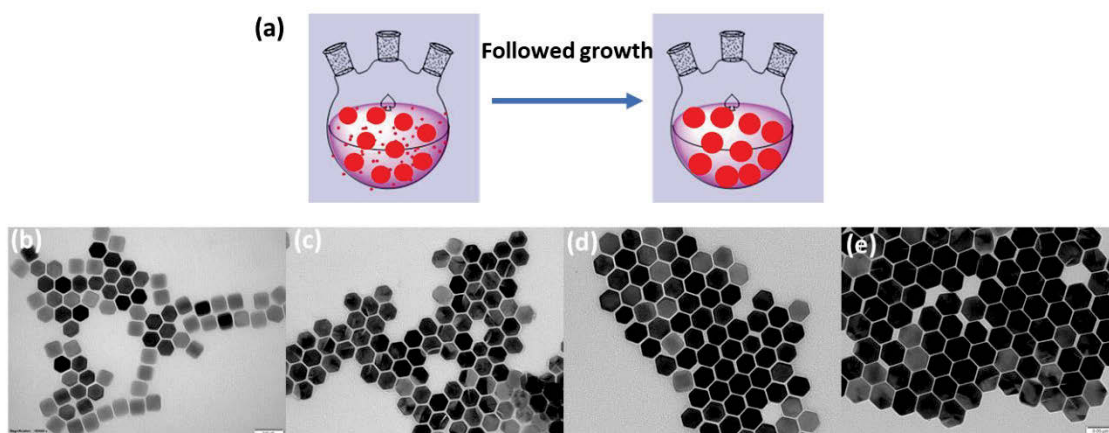


Figure 4.4 (a) The schematic process of followed growth process after the first growth in the *ex situ* approach, (b-e) TEM images of the NaYF₄ nanocrystal after growth with different amount of shell precursors (b: 0.1 mmol, c: 0.2 mmol, d: 0.3 mmol, and e: 0.4 mmol).

As there are same amount of the seeds and the injected shell precursors in the *ex situ* and *in situ* growth approach, the dramatically different behaviors of formation between the two growth methods may be attributed to three scenarios: (1) the “annealing-like” process for the seeds in *ex situ* growth makes the surface of the nanocrystals inactive while the seeds in the *in situ* growth is active without the “annealing-like” process, (2) the environmental (reacted) solution of the seeds in the *in situ* growth facilitates the

growth process but the co-solvent OA-ODE used to store the seeds in the *ex situ* growth does not have the elements, or (3) is just a combination of both.

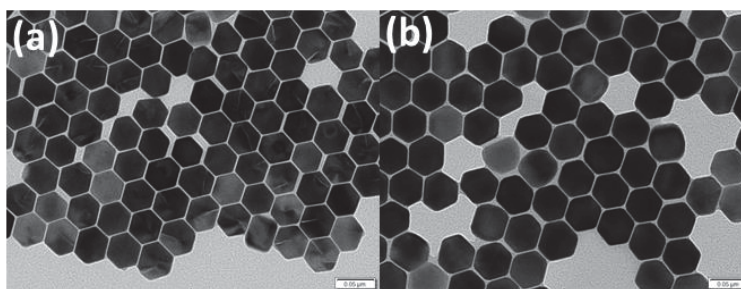


Figure 4.5 The TEM images of NaYF₄ nanocrystal seeds (a), and the nanocrystals formatted 5 min later after the precursor injection at 300 °C after the “anneal” (cooling and reheating to 300 °C) process (b).

To further explore the formation mechanism, we first rule out the possible mechanism that the “annealing-like” process has affected the seed mediated growth. To do this, we cool down the reaction solution to room temperature and re-heat it to 300 °C, and the shell precursors are injected. As shown in **Fig. 4.5b**, the TEM results show that the growth process starts immediately after the injection of the shell precursors. This means that the “annealing-like” process (cooling and re-heating) for the seeds does not play a role in the prompt epitaxial growth of the shell.

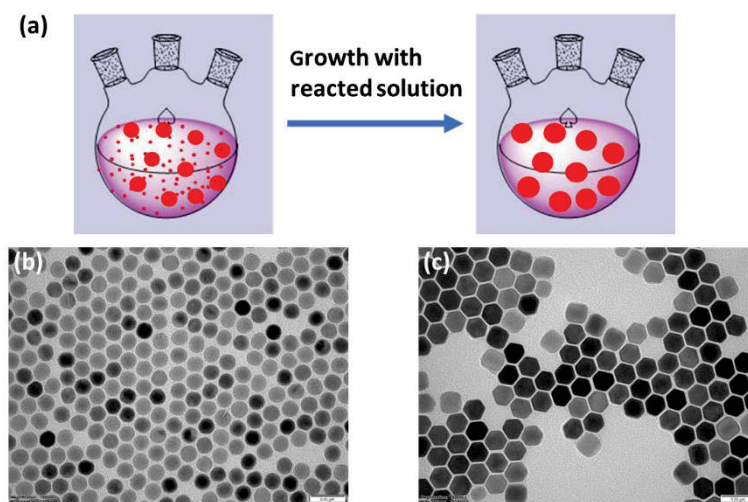


Figure 4.6 (a) The schematic process of growth with reacted solution, TEM images of the β -NaYF₄ nanocrystal before (b) and after growth with 0.1 mmol shell precursors for 5 min (c).

Then, we directly prove that it is the original reacted solution, where the seeds are formed, plays the essential role in facilitating immediate epitaxial growth of the shell, in the *in situ* growth approach. As shown in **Fig. 4.6a**, we separate the formed seeds from the reacted solution by centrifugation and washing,

and the seeds are added back to a bottle containing the reacted solution. After the reaction temperature reaches 300 °C, the shell precursors are injected. The result shows that the seeds are growth immediately after the shell injection and there are no α -phase nanocrystals nucleated by the shell precursors (**Fig. 4.6c**).

These results clearly indicate that the reacted solution, in which the seeds are synthesized, shows the catalyst-like function during the epitaxial growth process as shown in **Fig. 4.7**. The solution has overcome the energy barriers quickly after the temperature reaching to 300 °C. In terms of the *ex situ* approach, the activation energy is much higher than that of *in situ* one, and in turn longer time is needed to obtain enough energy to overcome the energy barriers. During this period, a partial seed dissolution processes as proved by the results in *ex situ* approach, in which the size of the seeds decreases at first. The dissolution from the seeds will mix together with shell precursor and grow on the surface of the seeds. Therefore, a strong intermixing mechanism happens, which explains the observed chemical and structural characteristics of the synthesized core@shell UCNPs, while using the *in situ* approach, the seeds will not have a chance to be dissolved, suggesting the reduced degree of intermixing between the core and the shell.

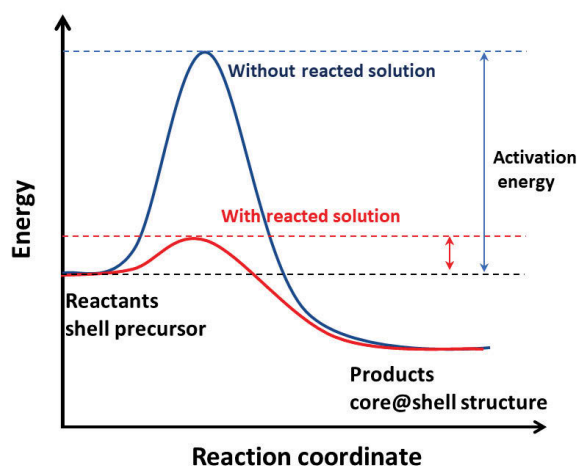


Figure 4.7 Free energy diagram of seed mediated growth with and without reacted solution.

To prove this, we further compare the high-quality core@shell nanostructure synthesized by the *in situ* growth approach with the ones using the *ex situ* approach. In this work, Er^{3+} is used as the active dopant ion for its rich energy level system that offers multiple excitation and emission pathways spanning the visible to the NIR wavelengths. We choose $\text{NaYF}_4: 20\% \text{Yb}, 2\% \text{Er}$ as the core and NaYF_4 as the inert shell. TEM micrographs shown that the core nanocrystals have the size around 24 nm with the relatively narrow size distribution (**Fig. 4.8a**). After the NaYF_4 shell coating through *ex situ* and *in situ* growth approaches, two batches of core@shell nanocrystals have the similar size around 28 nm (**Fig. 4.8b** and **4.8c**), which

makes the luminescence intensities of the two nanocrystals are comparable at the same concentration. We then measure the upconversion emission properties of the core@shell nanocrystals under 980 nm continuous-wave diode laser excitation. As shown in **Fig. 4.8d**, the luminescent intensity of NaYF₄:20%Yb,2%Er@NaYF₄ obtained by the *in situ* growth is almost double that of the nanocrystals formed by the *ex situ* growth approach.

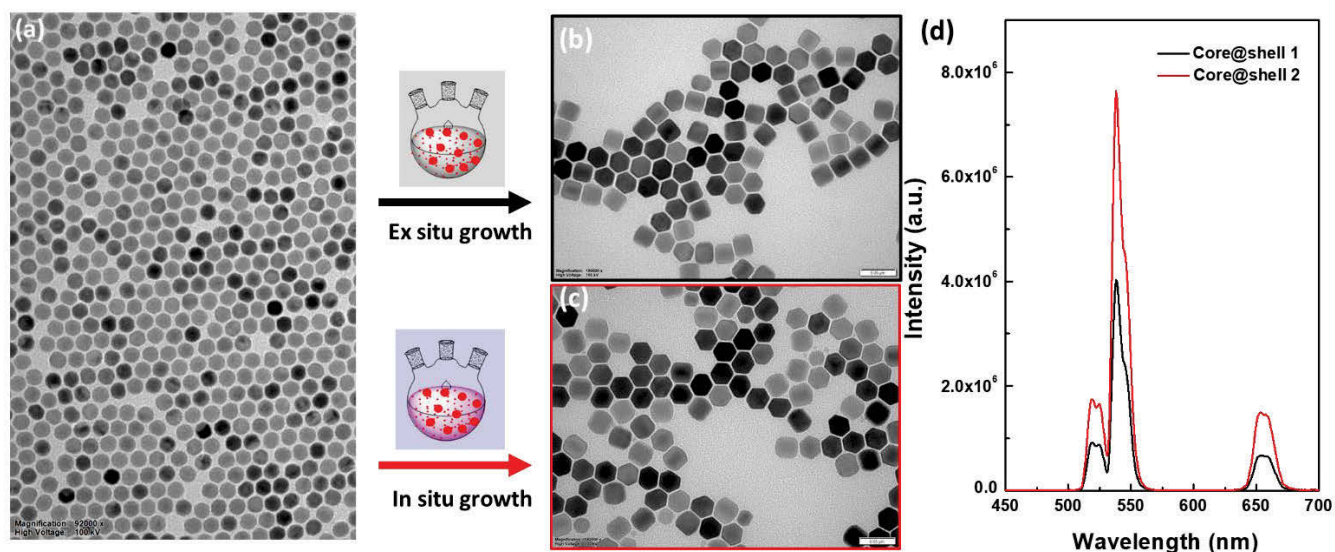


Figure 4.8 TEM images of the NaYF₄:20%Yb,2%Er core nanocrystals (a), and the NaYF₄:20%Yb,2%Er@NaYF₄ core@shell nanocrystals through *ex situ* (b) and *in situ* (c) growth approaches, respectively, (d) Upconversion luminescence spectra of core@shell 1 (*ex situ* growth) and core@shell 2 (*in situ* growth) measured by Fluorolog spectrometer.

Apart from fabricating the high-quality core@shell nanocrystals with the improved optical performance, the *in situ* growth method also offers a feasible method for the fabrication of the small core@shell nanocrystals from the sub-10 nm nanocrystals as the core. While typically due to the low stability of sub-10-nm nanocrystals (**Fig. 4.9a**) in the reaction mix, it is hard to use sub-10-nm nanocrystals as the seeds if using the conventional *ex situ* growth method. As shown in **Fig. 4.9b**, the size of the core nanocrystals will become nonuniform at 10 min before the growth process. With extended reaction time and more precursor injected, bigger particles are formed with the relatively broad size distribution. When the *in situ* growth method is employed, the small core@shell nanocrystals with fine-tuning shell thickness can be formed (**Fig. 4.9d** and **4.9e**) at different reaction time.

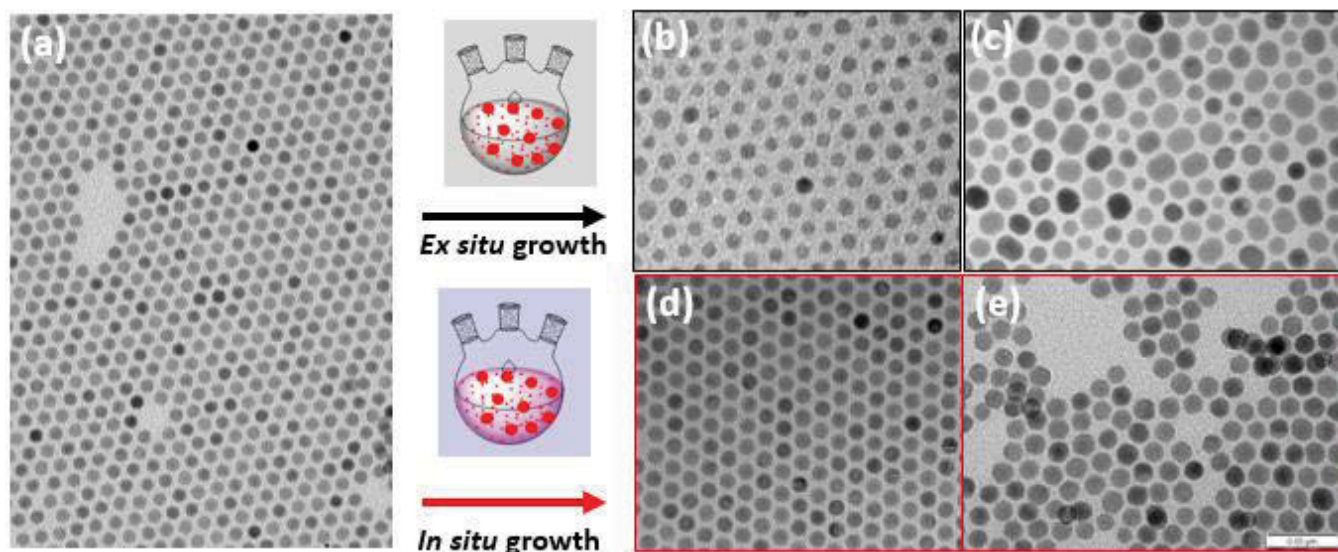


Figure 4.9 TEM images of the 10 nm NaYF₄:20%Yb,2%Er core nanocrystals (a), and the NaYF₄:20%Yb,2%Er@NaYF₄ core@shell nanocrystals using the *ex situ* (b,c) and *in situ* (d,e) growth approach, respectively.

4.5 Conclusion

To conclude, we find that it is the reacted solution that facilitates a prompt growth of the shells around the core nanocrystals. Using the *in situ* growth method, we demonstrate a successful synthesis of the high quality core@shell nanocrystals, and the bright and ultra-small core@shell nanocrystals, ideal for nanomedicine applications.

4.6 References

- [1] Wang, F., Wang, J., Liu, X., Direct Evidence of a Surface Quenching Effect on Size-Dependent Luminescence of Upconversion Nanoparticles, *Angewandte Chemie International Edition* 49 (41) (2010) 7456-7460.
- [2] Yi, G.-S., Chow, G.-M., Water-Soluble NaYF₄:Yb,Er(Tm)/NaYF₄/Polymer Core/Shell/Shell Nanoparticles with Significant Enhancement of Upconversion Fluorescence, *Chemistry of Materials* 19 (3) (2007) 341-343.
- [3] Johnson, N.J.J., Korinek, A., Dong, C., van Veggel, F.C.J.M., Self-Focusing by Ostwald Ripening: A Strategy for Layer-by-Layer Epitaxial Growth on Upconverting Nanocrystals, *Journal of the American Chemical Society* 134 (27) (2012) 11068-11071.
- [4] Liu, Y., Tu, D., Zhu, H., Li, R., Luo, W., Chen, X., A Strategy to Achieve Efficient Dual-Mode Luminescence of Eu³⁺ in Lanthanides Doped Multifunctional NaGdF₄ Nanocrystals, *Advanced Materials* 22 (30) (2010) 3266-3271.

- [5] Boyer, J.-C., van Veggel, F.C.J.M., Absolute quantum yield measurements of colloidal NaYF₄: Er³⁺, Yb³⁺ upconverting nanoparticles, *Nanoscale* 2 (8) (2010) 1417-1419.
- [6] Chen, G., Shen, J., Ohulchanskyy, T.Y., Patel, N.J., Kutikov, A., Li, Z., Song, J., Pandey, R.K., Ågren, H., Prasad, P.N., Han, G., (α -NaYbF₄:Tm³⁺)/CaF₂ Core/Shell Nanoparticles with Efficient Near-Infrared to Near-Infrared Upconversion for High-Contrast Deep Tissue Bioimaging, *ACS Nano* 6 (9) (2012) 8280-8287.
- [7] Wang, Y.-F., Sun, L.-D., Xiao, J.-W., Feng, W., Zhou, J.-C., Shen, J., Yan, C.-H., Rare-Earth Nanoparticles with Enhanced Upconversion Emission and Suppressed Rare-Earth-Ion Leakage, *Chemistry – A European Journal* 18 (18) (2012) 5558-5564.
- [8] Shen, J., Chen, G., Ohulchanskyy, T.Y., Kesseli, S.J., Buchholz, S., Li, Z., Prasad, P.N., Han, G., Tunable Near Infrared to Ultraviolet Upconversion Luminescence Enhancement in (α -NaYF₄:Yb,Tm)/CaF₂ Core/Shell Nanoparticles for In situ Real-time Recorded Biocompatible Photoactivation, *Small* 9 (19) (2013) 3213-3217.
- [9] Damasco, J.A., Chen, G., Shao, W., Ågren, H., Huang, H., Song, W., Lovell, J.F., Prasad, P.N., Size-Tunable and Monodisperse Tm³⁺/Gd³⁺-Doped Hexagonal NaYbF₄ Nanoparticles with Engineered Efficient Near Infrared-to-Near Infrared Upconversion for In Vivo Imaging, *ACS Applied Materials & Interfaces* 6 (16) (2014) 13884-13893.
- [10] Sun, T., Ma, R., Qiao, X., Fan, X., Wang, F., Shielding Upconversion by Surface Coating: A Study of the Emission Enhancement Factor, *ChemPhysChem* 17 (5) (2016) 766-770.
- [11] Zhang, F., Che, R., Li, X., Yao, C., Yang, J., Shen, D., Hu, P., Li, W., Zhao, D., Direct Imaging the Upconversion Nanocrystal Core/Shell Structure at the Subnanometer Level: Shell Thickness Dependence in Upconverting Optical Properties, *Nano Letters* 12 (6) (2012) 2852-2858.
- [12] Wang, Y.-F., Liu, G.-Y., Sun, L.-D., Xiao, J.-W., Zhou, J.-C., Yan, C.-H., Nd³⁺-Sensitized Upconversion Nanophosphors: Efficient In Vivo Bioimaging Probes with Minimized Heating Effect, *ACS Nano* 7 (8) (2013) 7200-7206.
- [13] Xie, X., Gao, N., Deng, R., Sun, Q., Xu, Q.-H., Liu, X., Mechanistic Investigation of Photon Upconversion in Nd³⁺-Sensitized Core–Shell Nanoparticles, *Journal of the American Chemical Society* 135 (34) (2013) 12608-12611.
- [14] Chen, G., Damasco, J., Qiu, H., Shao, W., Ohulchanskyy, T.Y., Valiev, R.R., Wu, X., Han, G., Wang, Y., Yang, C., Ågren, H., Prasad, P.N., Energy-Cascaded Upconversion in an Organic Dye-Sensitized Core/Shell Fluoride Nanocrystal, *Nano Letters* 15 (11) (2015) 7400-7407.
- [15] Chen, G., Shao, W., Valiev, R.R., Ohulchanskyy, T.Y., He, G.S., Ågren, H., Prasad, P.N., Efficient Broadband Upconversion of Near-Infrared Light in Dye-Sensitized Core/Shell Nanocrystals, *Advanced Optical Materials* 4 (11) (2016) 1760-1766.
- [16] Deng, R., Qin, F., Chen, R., Huang, W., Hong, M., Liu, X., Temporal full-colour tuning through non-steady-state upconversion, *Nat Nano* 10 (3) (2015) 237-242.
- [17] Wang, F., Deng, R., Wang, J., Wang, Q., Han, Y., Zhu, H., Chen, X., Liu, X., Tuning upconversion through energy migration in core–shell nanoparticles, *Nat Mater* 10 (12) (2011) 968-973.

- [18] Hao, S., Chen, G., Yang, C., Shao, W., Wei, W., Liu, Y., Prasad, P.N., Nd³⁺-Sensitized multicolor upconversion luminescence from a sandwiched core/shell/shell nanostructure, *Nanoscale* 9 (30) (2017) 10633-10638.
- [19] Zhong, Y., Tian, G., Gu, Z., Yang, Y., Gu, L., Zhao, Y., Ma, Y., Yao, J., Elimination of Photon Quenching by a Transition Layer to Fabricate a Quenching-Shield Sandwich Structure for 800 nm Excited Upconversion Luminescence of Nd³⁺-Sensitized Nanoparticles, *Advanced Materials* 26 (18) (2014) 2831-2837.
- [20] Zhou, B., Yang, W., Han, S., Sun, Q., Liu, X., Photon Upconversion Through Tb³⁺-Mediated Interfacial Energy Transfer, *Advanced Materials* 27 (40) (2015) 6208-6212.
- [21] Lai, J., Zhang, Y., Pasquale, N., Lee, K.-B., An Upconversion Nanoparticle with Orthogonal Emissions Using Dual NIR Excitations for Controlled Two-Way Photoswitching, *Angewandte Chemie International Edition* 53 (52) (2014) 14419-14423.
- [22] Li, X., Guo, Z., Zhao, T., Lu, Y., Zhou, L., Zhao, D., Zhang, F., Filtration Shell Mediated Power Density Independent Orthogonal Excitations–Emissions Upconversion Luminescence, *Angewandte Chemie International Edition* 55 (7) (2016) 2464-2469.
- [23] Wen, H., Zhu, H., Chen, X., Hung, T.F., Wang, B., Zhu, G., Yu, S.F., Wang, F., Upconverting Near-Infrared Light through Energy Management in Core–Shell–Shell Nanoparticles, *Angewandte Chemie International Edition* 52 (50) (2013) 13419-13423.
- [24] Dong, H., Sun, L.-D., Feng, W., Gu, Y., Li, F., Yan, C.-H., Versatile Spectral and Lifetime Multiplexing Nanoplatform with Excitation Orthogonalized Upconversion Luminescence, *ACS Nano* 11 (3) (2017) 3289-3297.
- [25] Zhang, Y., Liu, X., Nanocrystals: Shining a light on upconversion, *Nat Nano* 8 (10) (2013) 702-703.
- [26] He, S., Johnson, N.J.J., Nguyen Huu, V.A., Cory, E., Huang, Y., Sah, R.L., Jokerst, J.V., Almutairi, A., Simultaneous Enhancement of Photoluminescence, MRI Relaxivity, and CT Contrast by Tuning the Interfacial Layer of Lanthanide Heteroepitaxial Nanoparticles, *Nano Lett* 17 (8) (2017) 4873-4880.
- [27] Marciniak, L., Pilch, A., Arabasz, S., Jin, D., Bednarkiewicz, A., Heterogeneously Nd³⁺ doped single nanoparticles for NIR-induced heat conversion, luminescence, and thermometry, *Nanoscale* 9 (24) (2017) 8288-8297.
- [28] Hudry, D., Busko, D., Popescu, R., Gerthsen, D., Abeykoon, A.M.M., Kübel, C., Bergfeldt, T., Richards, B.S., Direct Evidence of Significant Cation Intermixing in Upconverting Core@Shell Nanocrystals: Toward a New Crystallochemical Model, *Chemistry of Materials* 29 (21) (2017) 9238-9246.
- [29] Chen, G., Agren, H., Ohulchanskyy, T.Y., Prasad, P.N., Light upconverting core-shell nanostructures: nanophotonic control for emerging applications, *Chem Soc Rev* 44 (6) (2015) 1680-1713.
- [30] Chen, B., Peng, D., Chen, X., Qiao, X., Fan, X., Wang, F., Establishing the Structural Integrity of Core–Shell Nanoparticles against Elemental Migration using Luminescent Lanthanide Probes, *Angewandte Chemie International Edition* 54 (43) (2015) 12788-12790.
- [31] Dühnen, S., Haase, M., Study on the Intermixing of Core and Shell in NaEuF₄/NaGdF₄ Core/Shell Nanocrystals, *Chemistry of Materials* 27 (24) (2015) 8375-8386.

- [32] Ai, F., Ju, Q., Zhang, X., Chen, X., Wang, F., Zhu, G., A core-shell-shell nanoplatfrom upconverting near-infrared light at 808 nm for luminescence imaging and photodynamic therapy of cancer, 5 (2015) 10785.
- [33] Chen, X., Peng, D., Ju, Q., Wang, F., Photon upconversion in core-shell nanoparticles, Chemical Society Reviews 44 (6) (2015) 1318-1330.
- [34] Mai, H.-X., Zhang, Y.-W., Sun, L.-D., Yan, C.-H., Highly Efficient Multicolor Up-Conversion Emissions and Their Mechanisms of Monodisperse NaYF₄:Yb,Er Core and Core/Shell-Structured Nanocrystals, The Journal of Physical Chemistry C 111 (37) (2007) 13721-13729.
- [35] Dong, H., Sun, L.-D., Wang, Y.-F., Xiao, J.-W., Tu, D., Chen, X., Yan, C.-H., Photon upconversion in Yb³⁺-Tb³⁺ and Yb³⁺-Eu³⁺ activated core/shell nanoparticles with dual-band excitation, Journal of Materials Chemistry C 4 (19) (2016) 4186-4192.
- [36] Huang, B., Sun, M., Dougherty, A.W., Dong, H., Xu, Y.-J., Sun, L.-D., Yan, C.-H., Unravelling the energy transfer of Er³⁺-self-sensitized upconversion in Er³⁺-Yb³⁺-Er³⁺ clustered core@shell nanoparticles, Nanoscale 9 (46) (2017) 18490-18497.
- [37] Liu, D., Xu, X., Du, Y., Qin, X., Zhang, Y., Ma, C., Wen, S., Ren, W., Goldys, E.M., Piper, J.A., Dou, S., Liu, X., Jin, D., Three-dimensional controlled growth of monodisperse sub-50 nm heterogeneous nanocrystals, Nature Communications 7 (2016) 10254.
- [38] Liu, Y., Lu, Y., Yang, X., Zheng, X., Wen, S., Wang, F., Vidal, X., Zhao, J., Liu, D., Zhou, Z., Ma, C., Zhou, J., Piper, J.A., Xi, P., Jin, D., Amplified stimulated emission in upconversion nanoparticles for super-resolution nanoscopy, Nature 543 (7644) (2017) 229-233.
- [39] Rinkel, T., Raj, A.N., Dühnen, S., Haase, M., Synthesis of 10 nm β-NaYF₄:Yb,Er/NaYF₄ Core/Shell Upconversion Nanocrystals with 5 nm Particle Cores, Angew. Chem. Int. Ed. 55 (3) (2016) 1164-1167.

CHAPTER 5 Optimal Sensitizer-Activator Doping Concentration in Single Upconversion Nanocrystals via Seeded Growth Approach

5.1 Preamble

In last chapter, we employ the seed-mediated isotropic growth to produce the homogeneous nanocrystals, which shows the fine-tuning in size. As discussed in the introduction chapter, heterogeneous core@shell structure has become an immense scientific and technological interest due to its unique controlled deposition of different elements across the nanocrystals. Integrating different elements into a nanoplatform will not only enable multi-functionality to be built into one, but also enable new and enhanced properties that could not be found in their parent homogeneous nanoparticles.

In terms of upconversion nanomaterials, a sensitizer with a sufficient absorption cross-section in the NIR region is usually co-doped with the activator ions to enhance the upconversion luminescence. The optimization of the doping concentration of both sensitizer and activator is the key to get the high efficiency upconversion nanocrystals. However, the increase of the concentration of commonly used sensitizer ions (Yb^{3+}) will significantly increase the nanocrystal size (from around 25 nm for 20% Yb^{3+} to around 200 nm for 98% Yb^{3+}), due to Yb^{3+} -varied crystal growth rate via the modification of electron charge density on the nanoparticle surface. This makes it impossible to directly compare the upconversion efficiency of the nanocrystals with different Yb^{3+} doping concentration.

Fortunately, this problem could be solved by the seed-mediated growth, by keeping the size of the doped layer the same for comparing the brightness at a single nanocrystal level. More importantly, this design of heterogeneous core@shell structures provides an inert layer of shell to isolate the surface quenchers. Therefore, the facile seeded growth approach allows us to optimize the sensitizer and activator doping concentrations in UCNPs.

5.2 Introduction

The nonlinear photon upconversion process to combine two or more lower-energy photons into one high energy photon, in lanthanide doped nanomaterials, has enabled a range of new nanophotonics and biophotonics applications.[1-8] The nature of their anti-stokes photon upconversion process offers a list of superior advantages for bio-applications, including negligible auto-fluorescence background, narrow emission bandwidth, exceptional photo-stability, and deep tissue penetration through optical transparent biological windows. The current focus in this field is on maximizing their high brightness as the single molecule probes and sensors for nanoscale biomolecular assays, super resolution fluorescence microscopy and multi-modal *in vivo* bio-imaging applications.[2, 3, 6, 9-17]

Since the photon upconversion process involves mutual interactions and energy transfers within a network of photon sensitizers and activators, their concentrations play an essential role in the luminescent properties of UCNPs.[1] Increasing the doping concentration of dopant ions (either sensitizer or activator) within a nanoparticle could improve the efficiency of cascade energy transfer process, but it also short-circuits the sensitized photon energies to the quenchers through non-radiative pathways. This is the reason why a relatively low concentration of sensitizers (Yb^{3+} ions below 20 mol%) and activators (Er^{3+} ions below 2 mol% and Tm^{3+} ions below 1 mol%) had been used in $\beta\text{-NaYF}_4$ nanocrystals to avoid the cross-relaxation and concentration quenching effects induced by the energy back transfer between each ions.[10, 18, 19]

Only recently, high-irradiance excitation was employed to alleviate concentration quenching in high activator doped upconversion nanocrystals,[20-22] and inert shells were used to further increase the concentrations of Yb^{3+} sensitizers and Er^{3+} activators.[22-24] Because the thresholds of concentration quenching for each sensitizer and activator ions are highly dependent on the excitation power, and direct growth of NaYF_4 nanocrystals with increasing the doping percentage of Yb^{3+} and Tm^{3+} from the conventional doped nanocrystals (low concentration) to highly doped nanocrystals will end up with different sizes that incorporate different amount of photon players as well as quenching factors from the surface, it justifies a more systematic investigation on the synthesis and characterizations to identify the optimal concentration and combination in order to produce brighter nanocrystals at a different excitation power densities applied in different applications.

In this Chapter, through a careful seed-mediated synthesis, we fabricate the heterogeneous core@shell@shell sandwich nanostructure with various doping concentration but same size. These highly controlled samples enables the systematic study of the doping concentrations of both sensitizers and activators, which guarantees the same amount of active photon conversion layer between an inert core template and an inert layer of shell that isolates the surface quenchers.[24-26] This allows us to directly compare and identify the optimum combination of sensitizers (Yb^{3+}) and emitters (Tm^{3+}) as a guideline to synthesize a range of the bright single UCNPs smaller than the size of antibody (~ 15 nm) optimized for different excitation regimes.

5.3 Experimental Section

5.3.1 Synthesis of NaYF_4 core nanocrystals

NaYF_4 had been synthesized similarly to our previously reported method.[27, 28] In a typical experiment, 3 mmol $\text{YCl}_3 \cdot 6\text{H}_2\text{O}$ were added to a flask containing 36 ml OA and 90 ml ODE. The mixture was heated to 170°C under argon for 30 min to obtain a clear solution and then cooled down to about 50°C , followed by the addition of 15 mL methanol solution of NH_4F (12 mmol) and NaOH (7.5 mmol). After stirring for 30 min, the solution was heated to 80°C under argon for 20 min to remove methanol, and then the solution was further heated to 300°C for another 90 min. Finally, the reaction solution was cooled down to room temperature, and nanoparticles were precipitated by ethanol and washed with cyclohexane, ethanol and methanol for 3 times to get the NaYF_4 core nanoparticles.

5.3.2 Core@shell@shell nanocrystals synthesis

The epitaxial growth of multiple layers of NaREF_4 onto the core of NaYF_4 was conducted via a successive layer-by-layer hot-injection protocol. Firstly, shell precursors were prepared. 6.0 mmol $\text{YCl}_3 \cdot 6\text{H}_2\text{O}$ were added to a flask containing 40 ml OA and 40 ml ODE. The mixture was heated to 170°C under argon for 30 min to obtain a clear solution and then cooled down to about 50°C , followed by the addition of methanol solution of NH_4F (24.0 mmol) and NaOH (6.0 mmol). After stirring for 30 min, the solution was heated to 80°C under argon for 20 min to remove methanol, and then the solution was further heated to 150°C for another 30 min. Finally, the reaction solution was cooled down to room temperature and labelled as NaYF_4 shell precursors. Similarly, the $\text{NaYbF}_4:x\%\text{Tm}$ ($x= 4, 6, 8, 12, \text{ and } 16$) shell precursors were synthesized using same method.

For the epitaxial growth of multiple layers of NaREF₄ on the core of NaYF₄, 0.075 mmol synthesized NaYF₄ core particles was further heated to 300 °C. Then, 0.2 mL of NaYbF₄:x%Tm shell precursors were immediately injected into the reaction mixture and ripened at 300 °C for 3 min followed by the same injection and ripening cycles for 15 times to get the core@NaYbF₄:x%Tm. After 1 ml sample were taken out, the NaYF₄ inert shell was coated similar with that for active shell coating. Finally, the reaction solution was cooled down to room temperature and the formed inert-core@active-shell@inert-shell nanostructure were purified according to the procedures used for the purification of core particles.

5.3.3 Small core@shell nanocrystals synthesis

Sub-10 nm NaYF₄:60%Yb, 2%Tm nanocrystals was synthesized according to previously report.[29] In a typical experiment, 0.4 mmol RECl₃ (RE=Y, Yb, Tm) with the molar ratio of 38:60:2 were added to a 50 mL flask containing 6 mL OA and 6 mL ODE. The mixture was heated to 160 °C under argon for 30 min to obtain a clear solution and then cooled down to about 70 °C, followed by the addition of 1.00 g of NaOA and 0.17 g NH₄F. After stirring for 30 min, the solution was heated to 150 °C under argon for 20 min, and then the solution was further heated to 300 °C for another 45 min. Finally, the reaction solution was cooled down to room temperature and nanoparticles were purified. The core-shell nanocrystals were synthesized according to the same procedure as mentioned in chapter 4.

5.3.4 Characterization techniques

The morphology of the formed materials was characterized *via* transmission electron microscopy (TEM) imaging (Philips CM10 TEM with Olympus Sis Megaview G2 Digital Camera) with an operating voltage of 100 kV. The samples were prepared by placing a drop of a dilute suspension of nanocrystals onto copper grids.

The emission of single UCNPs has been measured by a purpose-build scanning confocal system. A 976.5 nm laser was used to excite the UCNPs, with a home build power control unit including a half wave plate and a polarizer. The emission of UCNPs was collected by a high NA objective lens (Olympus, NA=1.4), then focused by a tube lens to an optical fibre (working as confocal aperture Airy disk = 1.01), which was linked to a single photon avalanche detector (SPAD). The scanning was achieved by x-y movement of the stage. The photon counts per second of each Gaussian spot was used to represent the brightness of that single particle.

5.4 Results and Discussion

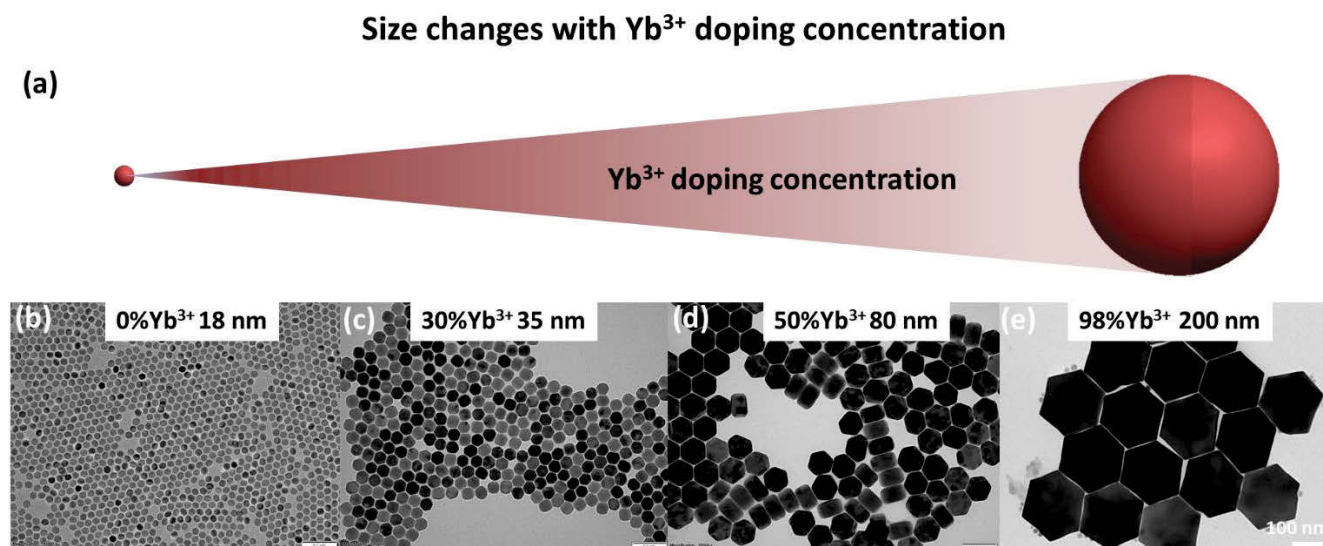


Figure 5.1 (a) The size of the NaYF₄:Yb nanocrystals changes with the Yb³⁺ doping concentration. (b-e) Typical TEM images and average sizes (insert) of the NaYF₄ (b), NaYF₄:30%Yb (c), NaYF₄:50%Yb (d), and NaYF₄:98%Yb (e).

In the upconversion system, Yb³⁺ with high absorption cross-section has been commonly employed as a sensitizer and co-doped along with the activator to enable the efficient energy transfer upconversion process for enhanced luminescence. The optimization of the doping concentration of both Yb³⁺ and activator is the key to get the high efficiency upconversion nanocrystals. However, the increase of the concentration of Yb³⁺ will significantly increase the nanocrystal size, due to Yb³⁺-varied crystal growth rate via the modification of electron charge density on the nanoparticle surface. As shown in **Fig. 5.1**, the size of the NaYF₄:Yb³⁺ increases from 18 nm to around 200 nm when the Yb³⁺ doping concentration rises from 0 to 98%. This makes it impossible to directly compare the upconversion efficiency of the nanocrystals with different Yb³⁺ doping concentration, due to different surface to volume ratio.

To make the size in control with different Yb³⁺ doping concentration, we design the seed-mediated synthesis to fabricate the heterogeneous core@shell@shell sandwich nanostructure with various doping concentrations in the intern shell (**Fig. 5.2a**). In this work, Tm³⁺ is used as the active dopant ion for its rich energy level system that offers multiple excitation and emission pathways spanning the visible to the NIR wavelengths. Using a layer-by-layer hot injection method,[15, 30] we demonstrate a precise control in step-by-step epitaxial growth of multiple layers to form an inert-core@active-shell@inert-shell nanostructure. TEM micrographs are used to reveal the successful control in the size of the

core@shell@shell nanoparticles with different Yb^{3+} doping concentration. **Fig. 5.2b-d** show the size of each step of synthesis to produce $\text{NaYF}_4@ \text{NaYF}_4:20\% \text{Yb}, 1\% \text{Tm}^{3+}@ \text{NaYF}_4$ UCNPs with a size increasing from 18.1 nm to 26.3 nm and to 31.2 nm, indicating the thickness of photon active shell of 4 nm and the thickness of inert shell of 2.5 nm. Interestingly, when both the doping concentrations of the Yb^{3+} and Tm^{3+} are increased, the obtained $\text{NaYF}_4@ \text{NaYF}_4:60\% \text{Yb}, 2\% \text{Tm}^{3+}$ nanocrystals (**Fig. 5.2e**) have the same size with that of the conventional one with the low doping concentration (**Fig. 5.2c and 5.2d**). All the nanocrystals have the relatively narrow size distribution and the standard derivation of the sizes across all the samples is below 1.0 nm (**Fig. 5.2c-f**, insert). This provides opportunity for quantitative study of the upconversion intensity of single nanocrystals when doped with different concentrations of sensitizer and activator ions.

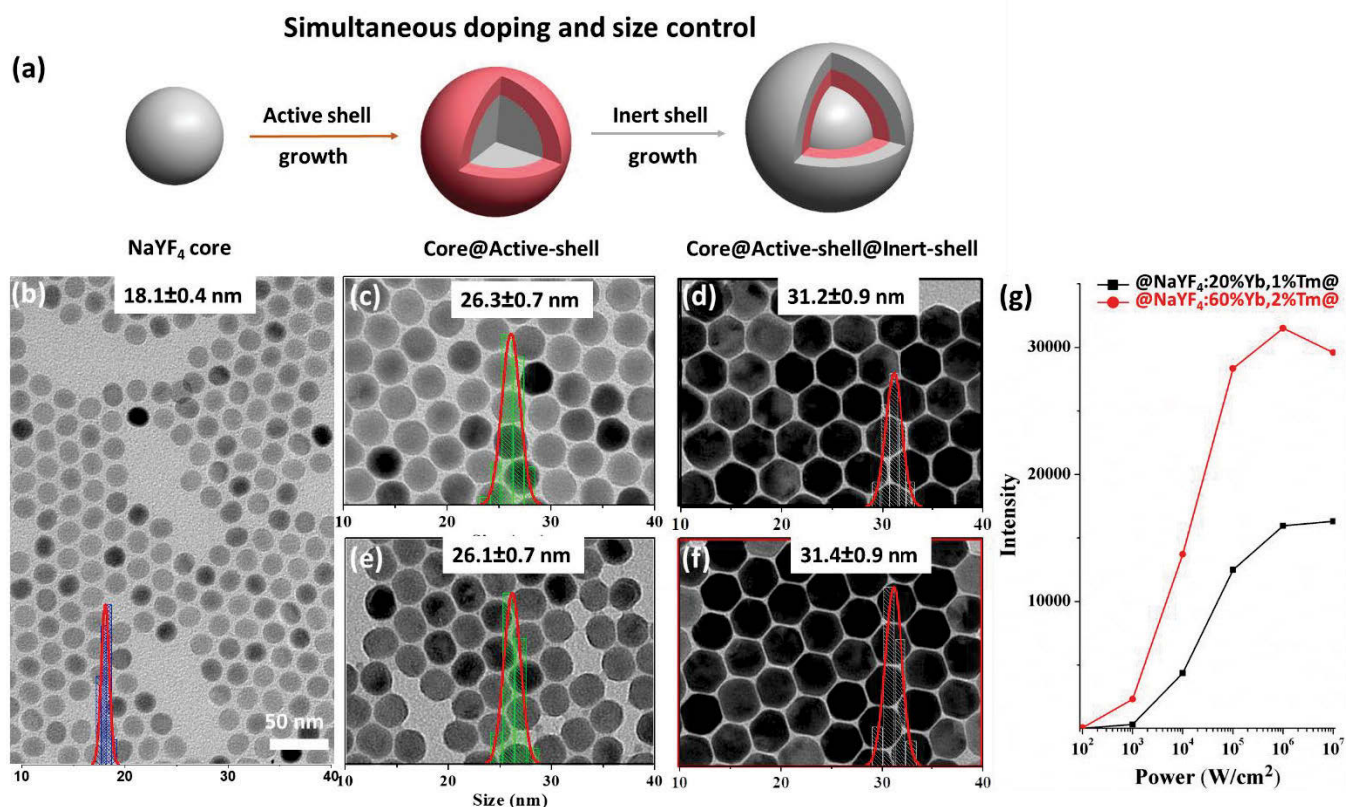


Figure 5.2 (a) Schematic design of the synthesis process for multishell nanostructure with doping and size control, (b-f) Typical TEM images and size distribution histograms (insert) of the core (b), core@active-shell (c,e), and core@active-shell@inert-shell (d,f) with different active shell of NaYF₄:20%Yb, 1%Tm (c,d) and NaYF₄:60%Yb, 2%Tm (e,f). (g) The measured upconversion luminescence intensities (c.p.s) of single UCNPs under different excitation power density.

We firstly investigate the upconversion emission properties of the core nanocrystals using a purpose-built confocal microscope under 980 nm continuous-wave diode laser excitation.[22] The brightness of single UCNPs doped with different concentrations of sensitizer and activator ions and at different excitation power density regimes has been systematically measured. As shown in **Fig. 5.2g**, even at a much lower excitation power density (10^2 W/cm²), upconversion photons from single UCNPs with high concentrations of sensitizer ions are still detectable. There are 89 counts per second (c.p.s) detected from UCNPs with 2 mol% Tm³⁺ and 60 mol% Yb³⁺, which are more than 2 times higher than the conventional one (40 c.p.s for 1 mol% Tm³⁺ and 20 mol% Yb³⁺). Slightly increasing the excitation power density to 10^3 W/cm² (much lower than most of standard wide-field fluorescence microscopy),[14] the luminescent intensity of UCNPs with 2 mol% Tm³⁺ and 60 mol% Yb³⁺ is increased dramatically to 2336 c.p.s, which is 6 times higher than that of the conventional one (338 c.p.s) at this power range. When the excitation power further increases to 10^5 W/cm², the luminescent intensities of both NaYF₄@NaYF₄:60%Yb,2%Tm@NaYF₄ and NaYF₄@NaYF₄:20%Yb,1%Tm@NaYF₄ are increased significantly to 28362 and 12509 c.p.s, respectively. After that, the intensity of conventional one reaches to a saturation point due to the relatively lower doping concentration. Interestingly, the luminescent intensity of NaYF₄@NaYF₄:60%Yb,2%Tm@NaYF₄ shows a decrease after a peak intensity the power range of 10^6 - 10^7 W/cm². This indicates that the relatively low concentration of activator (2% Tm³⁺) limits the brightness of the nanocrystals at higher power range.

To systematically study and compare the effect of Tm³⁺ doping concentration with high sensitizer Yb³⁺ concentration on their brightness at different excitation power, we design another 3 combinations with increased activators concentrations following this core@shell@shell structure: NaYF₄@NaYF₄:60%Yb,4%Tm@NaYF₄, NaYF₄@NaYF₄:60%Yb,8%Tm@NaYF₄ and NaYF₄@NaYF₄:60%Yb,16%Tm@NaYF₄. As shown in **Fig. 5.3**, when the doping concentration of the Tm³⁺ increases, the obtained core@active-shell nanocrystals (**Fig. 5.3a,c,e**) have the same sizes with that of the NaYF₄@NaYF₄:60%Yb,2%Tm (**Fig. 5.2e**). Also, the core@active-shell@inert-shell (**Fig. 5.3b,d,f**) have the same sizes with that of NaYF₄@NaYF₄:60%Yb,2%Tm@NaYF₄ (**Fig. 5.2f**). Similarly, all the nanocrystals have the relatively narrow size distribution (**Fig. 5.3a-f**, insert) for quantitative measurements.

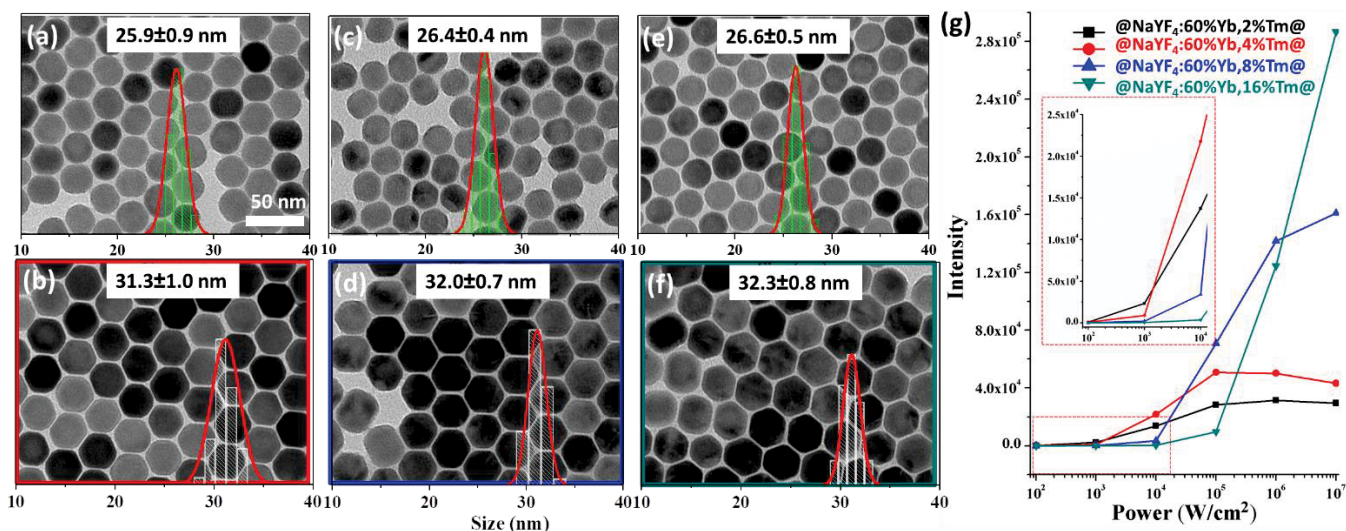


Figure 5.3 (a-f) Typical TEM images and size distribution histograms (insert) of the core@active-shell (a,c,e), and core@active-shell@inert-shell (b,d,f) with different active shell of NaYF₄:60%Yb,4%Tm (a,b), NaYF₄:60%Yb,8%Tm (c,d) and NaYF₄:60%Yb,16%Tm (e,f). (g) The measured upconversion luminescence intensities (c.p.s) of single UCNPs under different excitation power density. Inset shows the enlarged part at lower excitation power range.

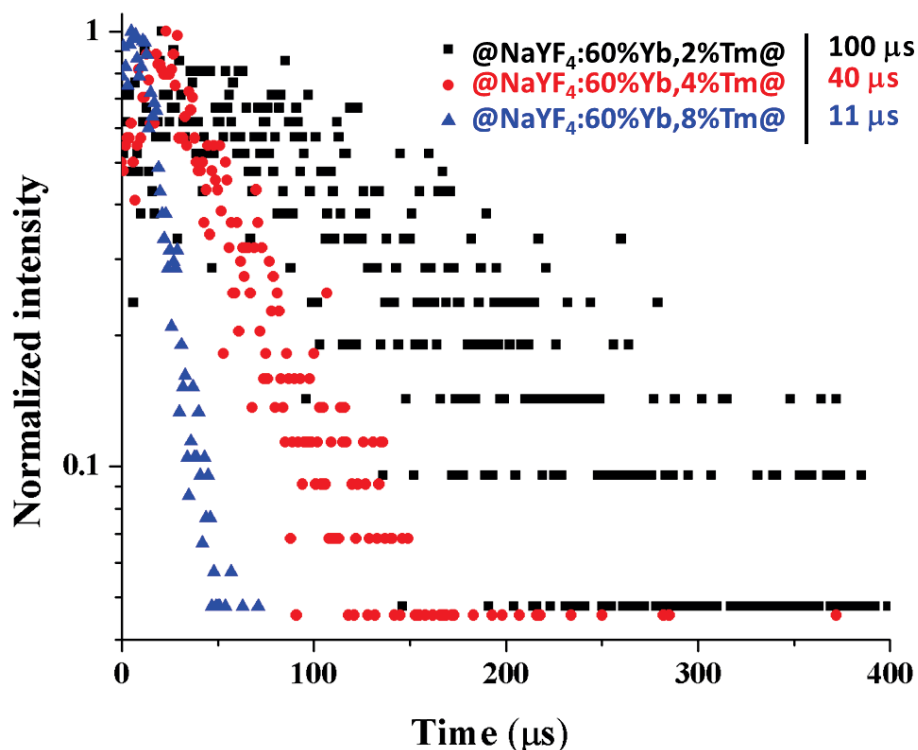


Figure 5.4 Luminescence decay at 455 nm with variable Tm³⁺ dopant concentration and their corresponding lifetime values at excitation power of 10⁷ W/cm².

Fig. 5.3g summarizes the upconversion luminescence intensities of four kinds of nanocrystals with same Yb doping concentration (60%) and increased Tm^{3+} doping concentrations (2%, 4%, 8% and 16%), showing significantly enhanced upconversion for Tm^{3+} highly doped UCNPs at the higher excitation power (10^7 W/cm^2), though their intensities are barely detectable at the lower power range ($<10^3 \text{ W/cm}^2$). Under the excitation power of 10^3 W/cm^2 , the intensity of 4% Tm^{3+} doped one starts to surpass that of the 2% Tm^{3+} doped one, and the intensity of 8% Tm^{3+} doped one becomes the brightest nanocrystals with the intensity of 70820 c.p.s at 10^5 W/cm^2 . These results indicate that the increase of the Tm^{3+} doping concentration only dramatically improves the luminescence intensity at the relatively higher excitation power to overcome the concentration quenching.

Since concentration quenching can be evidenced by the decreased lifetime, we examine the time-resolved population of the blue emission under 980 nm excitation for the nanocrystals with different Tm^{3+} doping concentration. As shown in **Fig. 5.4**, the luminescence lifetime decreases from 100 to 11 μs as the Tm^{3+} concentration increases from 2% to 8%. As the inert shell has been employed to eliminate energy migration to the surface, this decrease in lifetime should be attributed to the increased probability of cross-relaxation when increasing the dopant concentration.

Apart from the effect of Tm^{3+} concentration, we also study the role of Yb^{3+} concentration on the brightness of the samples at different excitation power. Another 2 samples have been designed by varying the sensitizer concentrations with fixed Tm^{3+} concentration (8%) following this core@shell@shell structure: $\text{NaYF}_4@\text{NaYF}_4:30\%\text{Yb},8\%\text{Tm}@\text{NaYF}_4$, and $\text{NaYF}_4@\text{NaYF}_4:92\%\text{Yb},8\%\text{Tm}@\text{NaYF}_4$. The upconversion luminescence intensities, shown in **Fig. 5.5e** suggests that the optimum concentration of Yb^{3+} ions at the high excitation power range ($>10^6 \text{ W/cm}^2$) should be around 60%. Further increasing the Yb^{3+} concentration 92%, the luminescence intensity only slightly increases. **Fig. 5.6** displays nearly unchanged luminescence lifetimes around 11 μs for all the 8% Tm^{3+} doped UCNPs though the Yb^{3+} concentration increases from 30% to 92%. This suggests that the increase of Yb^{3+} concentration does not introduce the cross-relaxation process. Taking the results from the samples with different Tm^{3+} concentration (**Fig. 5.4**) into the considerations, we can conclude that the cross-relaxation is primarily associated with the activator's concentration. Therefore, NaYbF_4 has been identified as the better host for Tm^{3+} -based upconversion system.

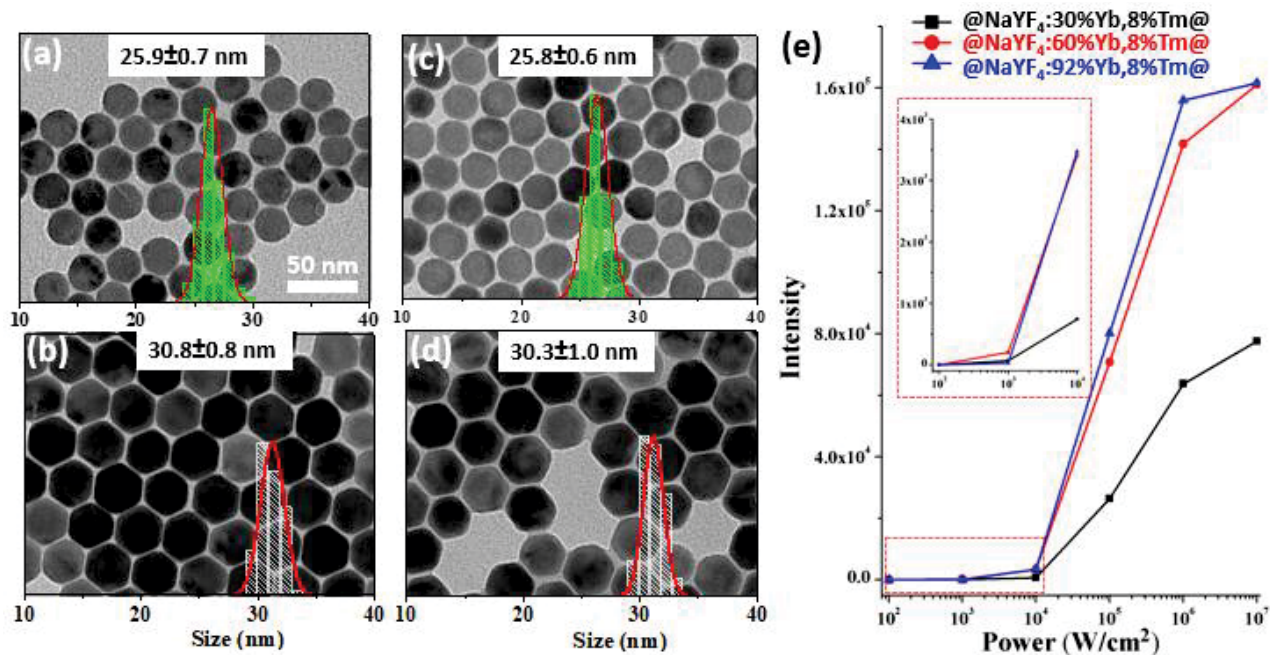


Figure 5.5 (a-d) Typical TEM images and size distribution histograms (insert) of the core@active-shell (a,c), and core@active-shell@inert-shell (b,d) with different active shell of NaYF₄:30%Yb,8%Tm (a,b), and NaYF₄:92%Yb,8%Tm (c,d). (e) The measured upconversion luminescence intensities (c.p.s) of single UCNPs under different excitation power density. Inset shows the enlarged part at lower excitation power range.

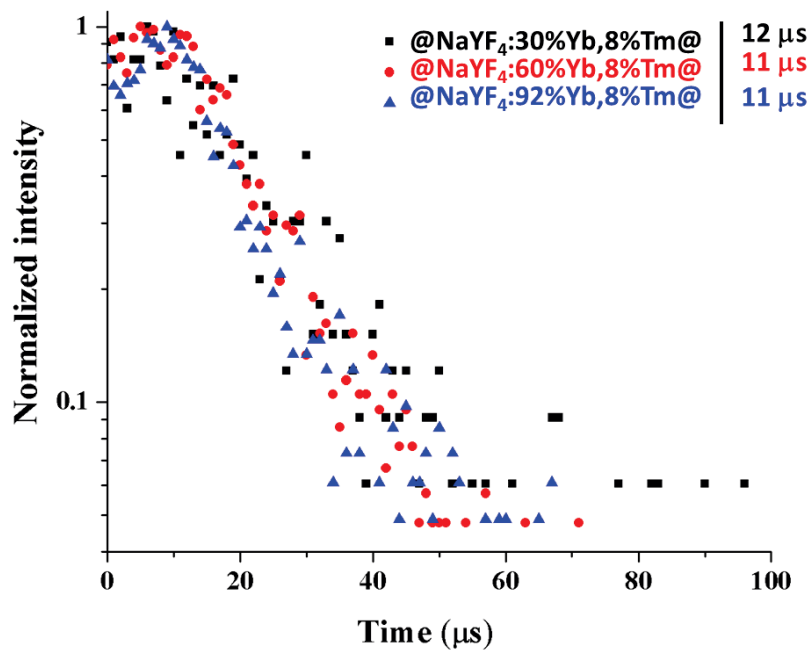


Figure 5.6 Luminescence decay at 455 nm with variable Yb³⁺ dopant concentration and their corresponding lifetime values at excitation power of 10⁷ W/cm².

To systematically identify the optimized Tm^{3+} concentration in the NaYbF_4 host, we further design four samples with different activators concentrations by filling the active upconversion shell within the inert core and inert shell structure: $\text{NaYF}_4@\text{NaYbF}_4:4\%\text{Tm}@\text{NaYF}_4$, $\text{NaYF}_4@\text{NaYbF}_4:6\%\text{Tm}@\text{NaYF}_4$, $\text{NaYF}_4@\text{NaYbF}_4:12\%\text{Tm}@\text{NaYF}_4$, and $\text{NaYF}_4@\text{NaYbF}_4:16\%\text{Tm}@\text{NaYF}_4$. As shown in **Fig. 5.7**, all the core@active-shell (**Fig. 5.7a,c,e,g**) and the core@active-shell@inert-shell (**Fig. 5.7b,d,f,h**) have the well-controlled size with a relatively narrow size distribution (**Fig. 5.7a-h**, insert). Similar with the results from the samples with different Tm^{3+} doping concentration with the same Yb^{3+} concentration, the upconversion luminescence intensities of the nanocrystals improve significantly with the increase of Tm^{3+} doping concentration at the higher excitation power range, particularly at 10^7 W/cm^2 (**Fig. 5.8**). Remarkably, the $\text{NaYF}_4@\text{NaYbF}_4:12\%\text{Tm}@\text{NaYF}_4$ nanocrystals show the brightest luminescence at the excitation of 10^7 W/cm^2 with the intensity of 320278 c.p.s.

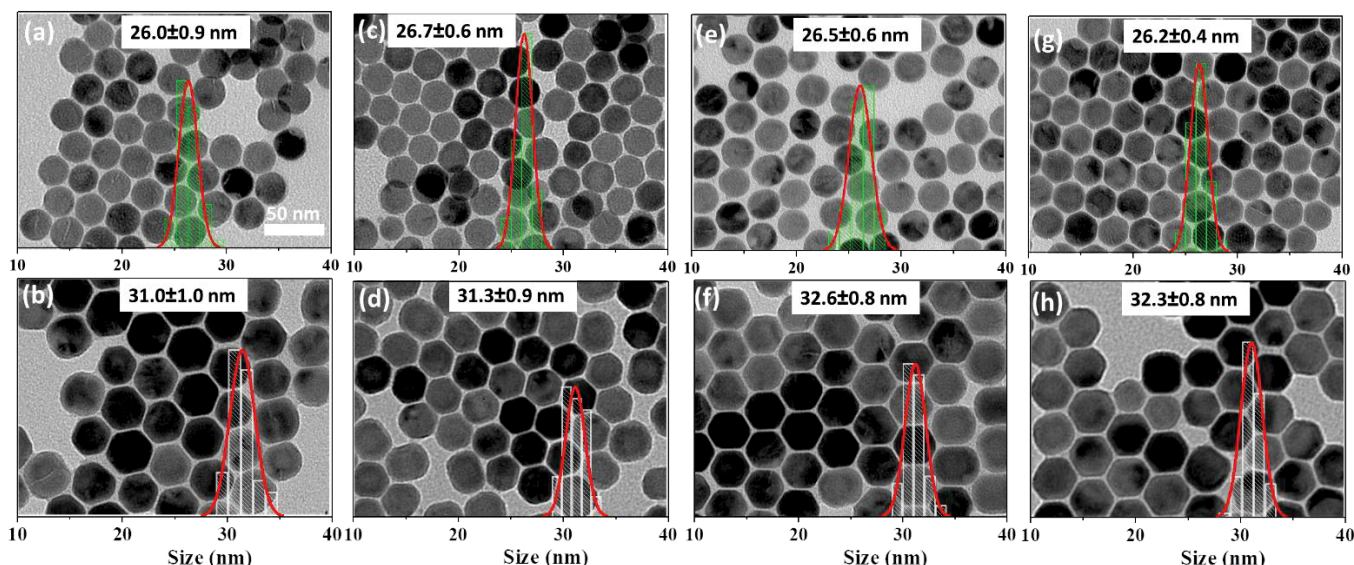


Figure 5.7 Typical TEM images and size distribution histograms (insert) of the core@active-shell (**a,c,e,g**), and core@active-shell@inert-shell (**b,d,f,h**) with different active shell of $\text{NaYbF}_4:4\%\text{Tm}$ (**a,b**), $\text{NaYbF}_4:6\%\text{Tm}$ (**c,d**), $\text{NaYbF}_4:12\%\text{Tm}$ (**e,f**), and $\text{NaYbF}_4:16\%\text{Tm}$ (**g,h**).

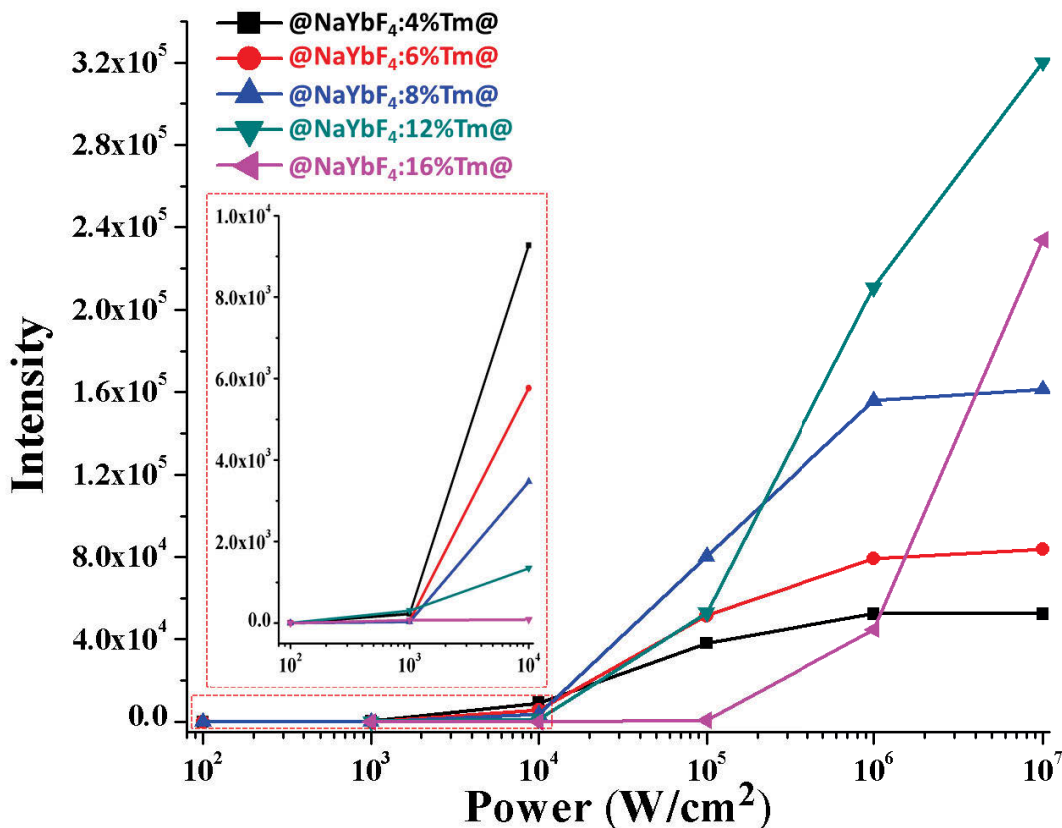


Figure 5.8 The measured upconversion luminescence intensities (c.p.s) of single UCNPs under different excitation power density. Inset shows the enlarged part at lower excitation power range.

The luminescence intensities of nanocrystals with different Tm^{3+} and Yb^{3+} doping at varies excitation power are summarised in **Table 5.1**. Only $\text{NaYF}_4@/\text{NaYF}_4:60\%\text{Yb},2\%\text{Tm}@/\text{NaYF}_4$ and $\text{NaYF}_4@/\text{NaYF}_4:60\%\text{Yb},4\%\text{Tm}@/\text{NaYF}_4$ nanocrystals display the detectable luminescent signals at 10^2 W/cm^2 from single nanocrystals. Slightly increasing the excitation power density to 10^3 W/cm^2 , all single UCNPs become bright enough to be imaged. UCNPs with 2 mol% Tm^{3+} and 60 mol% Yb^{3+} are still the brightest nanocrystals (2336 c.p.s) among all the study samples at this power range. With the excitation power density increasing to 10^4 W/cm^2 , the optimum doping concentration of Tm^{3+} has been shifted to 4 mol% and emit stronger upconversion luminescence (21764 c.p.s). The brightest upconversion luminescence is emitted from NaYbF_4 UCNPs with the optimum Tm^{3+} concentrations shifted to 8 mol% and 12 mol%, when the excitation power density further increased to 10^5 , 10^6 , and 10^7 W/cm^2 . Remarkably each single $\text{NaYbF}_4:12\%\text{Tm}$ UCNP emits 320278 c.p.s, around 20 times brighter than the conventional one (16326 c.p.s). More interestingly, compared with the conventional 20 mol% Yb^{3+} and 1 mol% Tm^{3+} co-doped NaYF_4 UCNPs, our quantitative measurements show that the optimum concentrations of Tm^{3+} ,

once passivated by inert shells, are always above the conventional value, and higher excitation power could activate higher concentrations of Tm^{3+} ions (from 2 mol% to 12 mol%) with overall intensities enhanced by orders of magnitudes.

Table 5.1. The measured upconversion luminescence intensities (c.p.s) of single UCNPs (the brightest Tm^{3+} ones under each excitation power density were highlighted in blue colours)

Tm^{3+} Concentration (mol %)	Yb^{3+} Concentration (mol %)	980 nm Excitation Power Density (W/cm^2)					
		10^2	10^3	10^4	10^5	10^6	10^7
1	20	40	338	4374	12509	15967	16326
2	60	89	2336	13726	28362	31506	29593
4	60	73	882	21764	50841	50233	43183
4	96		221	9272	38241	52417	52286
6	94		50	5768	51573	79262	83939
8	30		66	743	26446	63778	77603
8	60		202	3407	70820	141767	161053
8	92		29	3475	80250	155903	161517
12	88		304	1343	52887	210796	320278
16	60		45	342	9674	124522	286434
16	84		70	80	896	44823	234102

Fig. 5.9 selectively shows the confocal microscopy images and spectrum profiles of single UCNPs highlighted in **Table 5.1**. At the much lower excitation power density ($10^2 \text{ W}/\text{cm}^2$), single optimized Tm^{3+} doped UCNPs is detectable (**Fig. 5.9a**) with emission peak at 800 nm. When the excitation power density increasing to $10^3 \text{ W}/\text{cm}^2$, single Tm^{3+} doped UCNPs shows a high signal to noise ratio (26.7). Under an excitation power density of $10^4 \text{ W}/\text{cm}^2$, Tm^{3+} doped nanocrystals become one order of magnitude brighter with remarkable four-photon emission at 455 nm (**Fig. 5.9c**). Under higher excitation power density ranges, $10^6 \text{ W}/\text{cm}^2$ and above, the spectra of single Tm^{3+} doped nanocrystals become clearly detectable (**Fig. 5.9e** and **5.9f**) with the huge enhanced emissions at 455 nm.

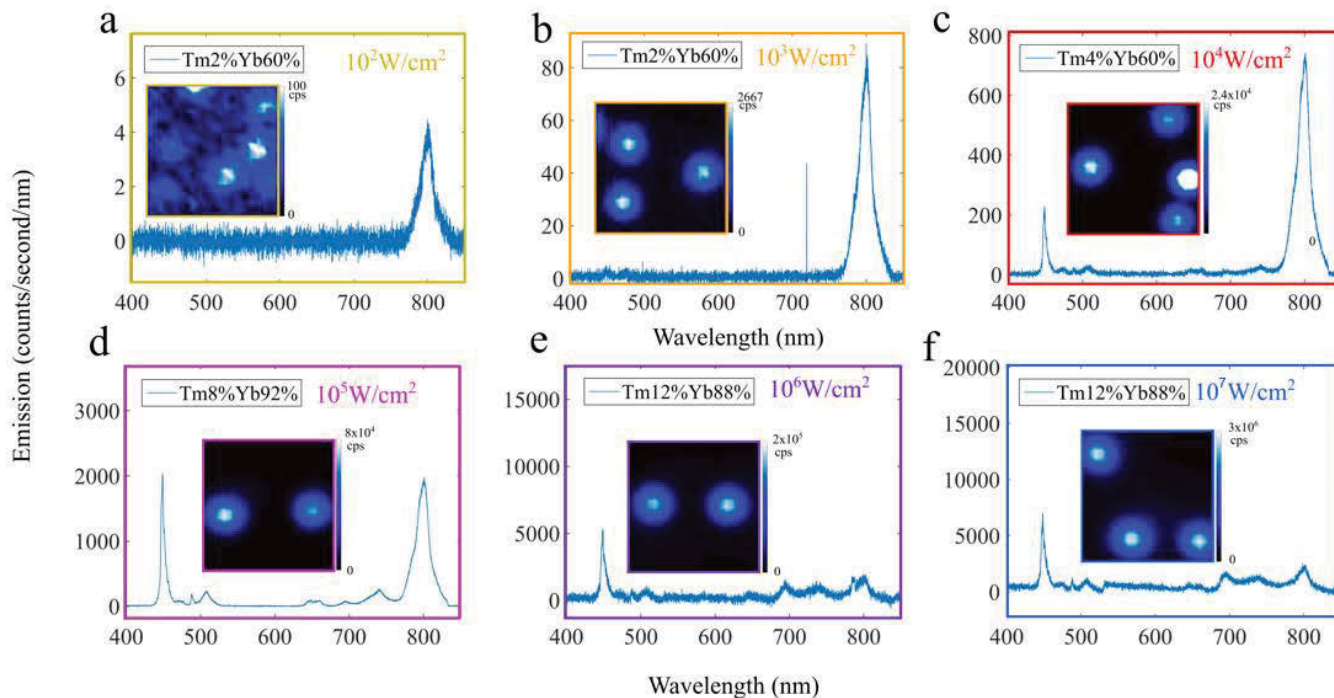


Figure 5.9. Confocal microscopy images and spectrum profiles of the brightest UCNPs highlighted in table 5.1 under the different power densities of 10^2 W/cm² (a), 10^3 W/cm² (b), 10^4 W/cm² (c), 10^5 W/cm² (d), 10^6 W/cm² (e), and 10^7 W/cm² (f). Note: pseudocolours of blue was used to indicate the single nanoparticle images of Tm³⁺ doped UCNPs. (e,f) showed the spectra of single UCNPs, and (a,b,c,d) were the spectrum profiles measured from the ensembles but calibrated from the total photon counts intensities to show the comparison intensities at different emission peaks.

UCNPs have been well-recognized as the most efficient multi-photon fluorescent probes for highly sensitive molecular detection,[13] non-blinking single-molecule tracking[31, 32], and super resolution imaging.[28, 33] In order to truly enable many intracellular applications, the size of each UCNPs should be smaller than the size of biomolecules, ideally comparable with the organic dye and QDs.[34-37] By calculating the volume of the active shell (4 nm active shell), we could give a theoretical value of brightness (12 times dimmer) if a smaller active-core@inert-shell UCNPs (10 nm core; 2.5 nm shell) will be synthesized, and a 15 nm NaYF₄:60%Yb³⁺,2%Tm@NaYF₄ UCNP should be detectable at the power range of 10^2 - 10^3 W/cm².

Using the developed *in situ* seed-mediated growth method, we synthesize the sub-10 nm active core of (NaYF₄:60%Yb,2%Tm),[29] coated with 2.5 nm inert shell (illustrated in **Fig. 5.10a**). Both the core and the active-core@shell nanocrystals have the well-controlled sizes and the relatively narrow size

distributions (**Fig. 5.10b-c**, insert). Interestingly, these small UCNPs are detectable at single level under an excitation density as low as 114 W/cm^2 (**Fig. 5.10d**). With the increase of the excitation power, the luminescence intensity of single UCNPs rises significantly to around 100 c.p.s at excitation power of 573 W/cm^2 , and the single nanocrystals can be seen with high signal-to-noise-ratio. When the excitation increasing further to 5730 W/cm^2 , the luminescent intensity of the nanocrystals witnesses a steep rise to above 1500 c.p.s. There brighter and smaller nanocrystals will pave the way for their bioimaging applications.[3, 38-41]

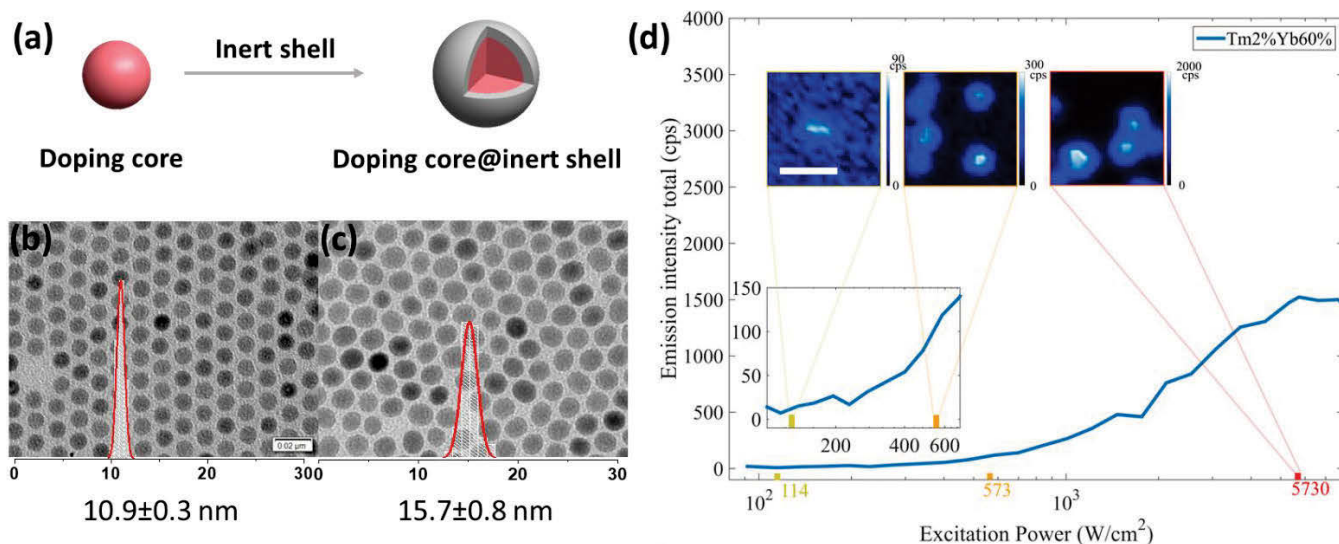


Figure 5.10 Small core@shell structure design (a) and TEM images of $\text{NaYF}_4:60\%\text{Yb},2\%\text{Tm}$ (b), $\text{NaYF}_4:60\%\text{Yb},2\%\text{Tm}@NaYF_4$ (c); (d) Integrated upconversion luminescence intensity as a function of excitation irradiance for $\text{NaYF}_4:60\%\text{Yb},2\%\text{Tm}@NaYF_4$ nanocrystals. Inset shows the confocal microscopy quantitative measurement of whole spectrum luminescence emission of single $\text{NaYF}_4:60\%\text{Yb},2\%\text{Tm}@NaYF_4$ at the excitation power of 114 W/cm^2 , 573 W/cm^2 , and 5730 W/cm^2 . Scale bar: 20 nm.

5.5 Conclusion

To conclude, using a precisely controlled synthesis approach, we fabricate a new library of inert core@active-shell@inert-shell nanostructures. These nanocrystals enable the systematic study of the upconversion luminescent properties of the nanocrystals with varied doping concentrations of Yb^{3+} and Tm^{3+} . The results demonstrate that the higher doping concentrations of Yb^{3+} and Tm^{3+} can significantly enhance the upconversion luminescence at relatively high excitation power range, while the relatively lower doping concentration of Tm^{3+} should be used to produce the brighter nanocrystals at lower

excitation power to avoid the cross-relaxation. Through the systematic synthesis and optical study, we provide a library of brightest nanocrystals with optimum doping concentrations at different excitation densities. This observation has further guided us to synthesize the sub-10 nm active core nanocrystals (after 2.5 nm inert shell passivation the final size of UCNPs are similar to the size of an IgG antibody ~ 15 nm).

5.6 References

- [1] Zhou, B., Shi, B., Jin, D., Liu, X., Controlling upconversion nanocrystals for emerging applications, *Nat Nano* 10 (11) (2015) 924-936.
- [2] Zhou, J., Liu, Q., Feng, W., Sun, Y., Li, F., Upconversion Luminescent Materials: Advances and Applications, *Chem Rev* 115 (1) (2015) 395-465.
- [3] Dong, H., Du, S.-R., Zheng, X.-Y., Lyu, G.-M., Sun, L.-D., Li, L.-D., Zhang, P.-Z., Zhang, C., Yan, C.-H., Lanthanide Nanoparticles: From Design toward Bioimaging and Therapy, *Chem Rev* 115 (19) (2015) 10725-10815.
- [4] Chen, G., Agren, H., Ohulchanskyy, T.Y., Prasad, P.N., Light upconverting core-shell nanostructures: nanophotonic control for emerging applications, *Chem Soc Rev* 44 (6) (2015) 1680-1713.
- [5] Fan, W., Shen, B., Bu, W., Zheng, X., He, Q., Cui, Z., Ni, D., Zhao, K., Zhang, S., Shi, J., Intranuclear biophotonics by smart design of nuclear-targeting photo-/radio-sensitizers co-loaded upconversion nanoparticles, *Biomaterials* 69 (Supplement C) (2015) 89-98.
- [6] Lu, Y., Zhao, J., Zhang, R., Liu, Y., Liu, D., Goldys, E.M., Yang, X., Xi, P., Sunna, A., Lu, J., Shi, Y., Leif, R.C., Huo, Y., Shen, J., Piper, J.A., Robinson, J.P., Jin, D., Tunable lifetime multiplexing using luminescent nanocrystals, *Nat Photon* 8 (1) (2014) 32-36.
- [7] Deng, R., Qin, F., Chen, R., Huang, W., Hong, M., Liu, X., Temporal full-colour tuning through non-steady-state upconversion, *Nat Nano* 10 (3) (2015) 237-242.
- [8] Dong, H., Sun, L.-D., Feng, W., Gu, Y., Li, F., Yan, C.-H., Versatile Spectral and Lifetime Multiplexing Nanoplatfrom with Excitation Orthogonalized Upconversion Luminescence, *ACS Nano* 11 (3) (2017) 3289-3297.
- [9] Yan, C., Zhao, H., Perepichka, D.F., Rosei, F., Lanthanide Ion Doped Upconverting Nanoparticles: Synthesis, Structure and Properties, *Small* 12 (29) (2016) 3888-3907.
- [10] Tu, L., Liu, X., Wu, F., Zhang, H., Excitation energy migration dynamics in upconversion nanomaterials, *Chem Soc Rev* 44 (6) (2015) 1331-1345.
- [11] He, S., Johnson, N.J.J., Nguyen Huu, V.A., Cory, E., Huang, Y., Sah, R.L., Jokerst, J.V., Almutairi, A., Simultaneous Enhancement of Photoluminescence, MRI Relaxivity, and CT Contrast by Tuning the Interfacial Layer of Lanthanide Heteroepitaxial Nanoparticles, *Nano Lett* 17 (8) (2017) 4873-4880.
- [12] Cao, C., Xue, M., Zhu, X., Yang, P., Feng, W., Li, F., Energy Transfer Highway in Nd³⁺-Sensitized Nanoparticles for Efficient near-Infrared Bioimaging, *ACS Appl Mater Interfaces* 9 (22) (2017) 18540-18548.

- [13] Su, Q., Feng, W., Yang, D., Li, F., Resonance Energy Transfer in Upconversion Nanoplatfoms for Selective Biodetection, *Acc. Chem. Res.* 50 (1) (2017) 32-40.
- [14] Park, Y.I., Lee, K.T., Suh, Y.D., Hyeon, T., Upconverting nanoparticles: a versatile platform for wide-field two-photon microscopy and multi-modal in vivo imaging, *Chem Soc Rev* 44 (6) (2015) 1302-1317.
- [15] Huang, P., Zheng, W., Zhou, S., Tu, D., Chen, Z., Zhu, H., Li, R., Ma, E., Huang, M., Chen, X., Lanthanide-Doped LiLuF₄ Upconversion Nanoprobes for the Detection of Disease Biomarkers, *Angew. Chem. Int. Ed.* 53 (5) (2014) 1252-1257.
- [16] Bang, D., Jo, E.-J., Hong, S., Byun, J.-Y., Lee, J.Y., Kim, M.-G., Lee, L.P., Nanocrescent antenna for nanofocusing of excitation radiation and generating asymmetric frequency upconverted emission, *Nano Lett* (2017).
- [17] Lee, K.-T., Park, J.-H., Kwon, S.J., Kwon, H.-K., Kyhm, J., Kwak, K.-W., Jang, H.S., Kim, S.Y., Han, J.S., Lee, S.-H., Shin, D.-H., Ko, H., Han, I.-K., Ju, B.-K., Kwon, S.-H., Ko, D.-H., Simultaneous Enhancement of Upconversion and Downshifting Luminescence via Plasmonic Structure, *Nano Lett* 15 (4) (2015) 2491-2497.
- [18] Wang, F., Liu, X., Recent advances in the chemistry of lanthanide-doped upconversion nanocrystals, *Chem Soc Rev* 38 (4) (2009) 976-989.
- [19] Wang, F., Liu, X., Upconversion Multicolor Fine-Tuning: Visible to Near-Infrared Emission from Lanthanide-Doped NaYF₄ Nanoparticles, *J Am Chem Soc* 130 (17) (2008) 5642-5643.
- [20] Zhao, J., Jin, D., Schartner, E.P., Lu, Y., Liu, Y., Zvyagin, A.V., Zhang, L., Dawes, J.M., Xi, P., Piper, J.A., Goldys, E.M., Monroe, T.M., Single-nanocrystal sensitivity achieved by enhanced upconversion luminescence, *Nat Nano* 8 (10) (2013) 729-734.
- [21] Gargas, D.J., Chan, E.M., Ostrowski, A.D., Aloni, S., Altoe, M.V.P., Barnard, E.S., Sani, B., Urban, J.J., Milliron, D.J., Cohen, B.E., Schuck, P.J., Engineering bright sub-10-nm upconverting nanocrystals for single-molecule imaging, *Nat Nano* 9 (4) (2014) 300-305.
- [22] Ma, C., Xu, X., Wang, F., Zhou, Z., Liu, D., Zhao, J., Guan, M., Lang, C.I., Jin, D., Optimal Sensitizer Concentration in Single Upconversion Nanocrystals, *Nano Lett* 17 (5) (2017) 2858-2864.
- [23] Shen, B., Cheng, S., Gu, Y., Ni, D., Gao, Y., Su, Q., Feng, W., Li, F., Revisiting the optimized doping ratio in core/shell nanostructured upconversion particles, *Nanoscale* 9 (5) (2017) 1964-1971.
- [24] Johnson, N.J.J., He, S., Diao, S., Chan, E.M., Dai, H., Almutairi, A., Direct Evidence for Coupled Surface and Concentration Quenching Dynamics in Lanthanide-Doped Nanocrystals, *J Am Chem Soc* 139 (8) (2017) 3275-3282.
- [25] Wang, F., Wang, J., Liu, X., Direct Evidence of a Surface Quenching Effect on Size-Dependent Luminescence of Upconversion Nanoparticles, *Angewandte Chemie* 122 (41) (2010) 7618-7622.
- [26] Fischer, S., Bronstein, N.D., Swabeck, J.K., Chan, E.M., Alivisatos, A.P., Precise Tuning of Surface Quenching for Luminescence Enhancement in Core-Shell Lanthanide-Doped Nanocrystals, *Nano Lett* 16 (11) (2016) 7241-7247.

- [27] Liu, D., Xu, X., Du, Y., Qin, X., Zhang, Y., Ma, C., Wen, S., Ren, W., Goldys, E.M., Piper, J.A., Dou, S., Liu, X., Jin, D., Three-dimensional controlled growth of monodisperse sub-50 nm heterogeneous nanocrystals, *Nature Communications* 7 (2016) 10254.
- [28] Liu, Y., Lu, Y., Yang, X., Zheng, X., Wen, S., Wang, F., Vidal, X., Zhao, J., Liu, D., Zhou, Z., Ma, C., Zhou, J., Piper, J.A., Xi, P., Jin, D., Amplified stimulated emission in upconversion nanoparticles for super-resolution nanoscopy, *Nature* 543 (7644) (2017) 229-233.
- [29] Rinkel, T., Raj, A.N., Dühnen, S., Haase, M., Synthesis of 10 nm β -NaYF₄:Yb,Er/NaYF₄ Core/Shell Upconversion Nanocrystals with 5 nm Particle Cores, *Angew. Chem. Int. Ed.* 55 (3) (2016) 1164-1167.
- [30] Li, X., Wang, R., Zhang, F., Zhao, D., Engineering Homogeneous Doping in Single Nanoparticle To Enhance Upconversion Efficiency, *Nano Lett* 14 (6) (2014) 3634-3639.
- [31] Nam, S.H., Bae, Y.M., Park, Y.I., Kim, J.H., Kim, H.M., Choi, J.S., Lee, K.T., Hyeon, T., Suh, Y.D., Long-Term Real-Time Tracking of Lanthanide Ion Doped Upconverting Nanoparticles in Living Cells, *Angewandte Chemie* 123 (27) (2011) 6217-6221.
- [32] Wu, S., Han, G., Milliron, D.J., Aloni, S., Altoe, V., Talapin, D.V., Cohen, B.E., Schuck, P.J., Non-blinking and photostable upconverted luminescence from single lanthanide-doped nanocrystals, *Proc Natl Acad Sci U S A* 106 (27) (2009) 10917-10921.
- [33] Liang, L., Liu, X., STED Nanoscopy Goes Low Power, *Chem* 2 (3) (2017) 331-333.
- [34] Blom, H., Widengren, J., Stimulated Emission Depletion Microscopy, *Chem Rev* 117 (11) (2017) 7377-7427.
- [35] Chen, O., Zhao, J., Chauhan, V.P., Cui, J., Wong, C., Harris, D.K., Wei, H., Han, H.-S., Fukumura, D., Jain, R.K., Bawendi, M.G., Compact high-quality CdSe–CdS core–shell nanocrystals with narrow emission linewidths and suppressed blinking, *Nat Mater* 12 (5) (2013) 445-451.
- [36] Pinaud, F., Clarke, S., Sittner, A., Dahan, M., Probing cellular events, one quantum dot at a time, *Nat Meth* 7 (4) (2010) 275-285.
- [37] Resch-Genger, U., Grabolle, M., Cavaliere-Jaricot, S., Nitschke, R., Nann, T., Quantum dots versus organic dyes as fluorescent labels, *Nat Meth* 5 (9) (2008) 763-775.
- [38] Qin, Q.-S., Zhang, P.-Z., Sun, L.-D., Shi, S., Chen, N.-X., Dong, H., Zheng, X.-Y., Li, L.-M., Yan, C.-H., Ultralow-power near-infrared excited neodymium-doped nanoparticles for long-term in vivo bioimaging, *Nanoscale* 9 (14) (2017) 4660-4664.
- [39] Near-Infrared Fluorescent Nanomaterials for Bioimaging and Sensing, *Advanced Optical Materials* 5 (2) (2017) 1600446.
- [40] Xia, M., Zhou, D., Yang, Y., Yang, Z., Qiu, J., Synthesis of Ultrasmall Hexagonal NaGdF₄: Yb³⁺+Er³⁺@ NaGdF₄: Yb³⁺@ NaGdF₄: Nd³⁺ Active-Core/Active-Shell/Active-Shell Nanoparticles with Enhanced Upconversion Luminescence, *ECS Journal of Solid State Science and Technology* 6 (4) (2017) R41-R46.
- [41] Cao, C., Xue, M., Zhu, X., Yang, P., Feng, W., Li, F., Energy Transfer Highway in Nd³⁺-Sensitized Nanoparticles for Efficient near-Infrared Bioimaging, *ACS Applied Materials & Interfaces* 9 (22) (2017) 18540-18548.

CHAPTER 6 Single-axis Epitaxial Growth of Barcoded Heterogeneous Nanorods

6.1 Preamble

While spherical core-shell nanoparticles have enabled many design of nanomaterials and applications, fabricating arbitrary non-spherical nanorods will further advance catalysis, electronics, photonics, energy conversion, and nanomedicine. The key is to enable directional control of elemental composition with atomic scale precision. Here, we systematically investigate the varied roles of the surfactant molecule OA, and report that absolute one-direction growth of nanorods can be achieved by fine tuning of surfactant molecules' relative stabilities on the desired crystal facet. On-demand deposition of precursors along the longitudinal direction has produced a series of nanorods in the range of 24 nm to 242 nm. Combination with heterogenous growth, we demonstrate a library of multifunctional contrast agents for multimode bioimaging, with each functionalization being maximized and logically assembled within a single barcoded nanorod. This suggests future heterogeneous nanocrystals with integrated functions can be realized by the programmable growth of multifunctional barcode crystals with tunable size, composition, and properties.

6.2 Introduction

Precision in bottom-up atomic scale controlled synthesis of nanomaterials will enable arbitrary design and fabrication of heterogeneous nanostructures with multifunctional properties.[1-8] Compared with zero-dimensional spherical nanoparticles, 1-dimensional nanostructure, especially the heterogeneous nanorods, provides a versatile design platform to incorporate multi-functional units, enhance interplays between different materials compositions, and produce a range of previously inaccessible nanomaterials with high monodispersity and choice of complex shapes.[9-18] Heterogeneous nanorods have shown larger surface to volume ratio, improved charge transfer and carrier mobility, and superior efficiencies in targeted drug delivery. [11, 15, 17]

Currently demonstrated nanorods, including gold and semiconductor (e.g. ZnO) nanorods, are formed using a core-shell design but with anisotropic thickness of shells along all directions.[19-28] To our best knowledge, none of these nanomaterials has achieved single-direction growth only along one crystalline axis.

In this Chapter, we report our achievement in single-axis directional epitaxial growth of heterogeneous nanorods in lanthanide doped hexagonal-phase NaYF₄ nanocrystals. Choosing this material system is due to their matured wet-chemistry synthesis strategies. And monodisperse hexagonal nanocrystals have well-defined (001) and (100)/(010) facets on their end and side surfaces, respectively. As the new generation of functional nanomaterials, there found a broad range of applications in biomolecular sensing, microscopy imaging, multimodal bio-imaging (fluorescence, MRI, CT, SPECT, and so on.), and light-triggered nanomedicine therapy, and as the next step of developments there is a trend in developing new strategies to integrate multi-functions into one nanoplatform.

6.3 Experimental Section

6.3.1 Synthesis of NaYF₄:Yb,Er core nanocrystals

NaYF₄:Yb,Er core nanocrystals were synthesized according to our previously reported method.[29, 30] In a typical experiment, 2 mmol RECl₃ (RE = Y, Yb, Er) with the molar ratio of 78:20:2 was added to a 100 mL flask containing 13 mL OA and 30 mL ODE. The mixture was heated to 170 °C under argon for

30 min to obtain a clear solution and then cooled down to about 50 °C, followed by the addition of 10 mL methanol solution of NH₄F (8 mmol) and NaOH (5 mmol). After stirring for 30 min, the solution was heated to 80 °C under argon for 20 min to remove methanol, and then the solution was further heated to 310 °C for another 90 min. Finally, the reaction solution was cooled down to room temperature, and nanoparticles were precipitated by ethanol and washed with cyclohexane, ethanol and methanol for 3 times to get the NaYF₄:Yb,Er nanoparticles.

6.3.2 Longitudinal growth of NaREF₄ onto the core of NaYF₄:Yb,Er nanocrystals

The longitudinal growth of NaREF₄ onto the core of NaYF₄:Yb,Er nanocrystals was conducted via a successive layer-by-layer hot-injection protocol. Firstly, shell precursors were prepared. 1.0 mmol YCl₃6H₂O was added to a 50 mL flask containing 4 mL OA and 10 mL ODE. The mixture was heated to 170 °C under argon for 30 min to obtain a clear solution and then cooled down to about 50 °C, followed by the addition of 5 mL methanol solution of NH₄F (4.0 mmol) and NaOH (4.5 mmol). After stirring for 30 min, the solution was heated to 80 °C under argon for 20 min to remove methanol, and then the solution was further heated to 150 °C for another 30 min. Finally, the reaction solution was cooled down to room temperature and labelled as NaYF₄ shell precursors. Similarly, the NaGdF₄ and NaDyF₄ shell precursors were synthesized using 1.0 mmol GdCl₃6H₂O and 1.0 mmol DyCl₃6H₂O, instead of YCl₃6H₂O.

For the longitudinal growth of NaYF₄, 0.1 mmol NaYF₄:Yb,Er core particles were added to a 50 mL flask containing 3 mL OA, 7 mL ODE, 124.2 mg NaOH. The mixture was heated to 170 °C under argon for 30 min, and then the solution was further heated to 310 °C. After that, 0.15 mL of NaYF₄ shell precursors were immediately injected into the reaction mixture and ripened at 310 °C for 2.5 min followed by the same injection and ripening cycles for different times to get the nanorods with different length. Finally, the reaction solution was cooled down to room temperature and the formed nanorod were purified according to the procedures used for the purification of NaYF₄:Yb,Er core particles.

6.3.3 Programmable growth of versatile nanoring-coated nanodumbbell

For the nanoring-coated-nanodumbbell synthesis, the NaYF₄:Yb,Er@NaLuF₄@NaDyF₄ rods were first formed according to method 6.3.2. Then 0.15 mmol GdCl₃ was added to a 50 mL flask with 6 mL OA and 6 mL ODE. The mixture was heated to 170 °C under argon for 30 min to obtain a clear solution and cooled down to about 50 °C, followed by the addition of 4 mL methanol solution of NH₄F (0.6 mmol), NaOH

(0.1875 mmol). After stirring for 30 min, the formed NaYF₄:Yb,Er@NaLuF₄@NaDyF₄ rods (0.05 mmol in cyclohexane) were added and the solution was heated to 80 °C under argon for 20 min to remove methanol and cyclohexane, and then the solution was further heated to 310 °C for another 90 min. Finally, the reaction solution was cooled down to room temperature and the formed nanoparticles were purified according to the procedures used for the purification of NaYF₄:Yb,Er core particles.

6.3.4 Characterization techniques

The morphology of the formed materials was characterized *via* TEM imaging (Philips CM10 TEM with Olympus Sis Megaview G2 Digital Camera) with an operating voltage of 100 kV. The samples were prepared by placing a drop of a dilute suspension of nanocrystals onto copper grids. The high resolution TEM measurements were performed using an aberration corrected analytical TEM (JEOL ARM-200F) with an operating voltage of 100 kV. High-angle annular dark-field (HAADF) scanning transmission electron microscope (STEM) images and corresponding element mapping images were collected with the same TEM equipped with a Centurio SSD energy-dispersive X-ray spectroscopy (EDS) detector at 77 K. The upconversion luminescence spectra of colloidal solutions in quartz cuvettes with 10 mm path length were acquired using a Fluorolog-Tau3 spectrofluorometer (JobinYvon-Horiba) equipped with an external 980 nm CW diode laser with a pump power of 278 mW. The T₁-weighted MR images were acquired with a conventional spin echo acquisition in a 0.5 T systems (MiniMR60, Shanghai Niumag Corporation) at room temperature (FOVRead = 100 mm, FOVPhase = 100 mm, Averages = 2, TR = 1000 ms, TE = 20 ms, Slices = 1, and Slices width = 5 mm). T₁ relaxometry was measured in a 0.5 T magnetic field (PQ001, Shanghai Niumag Corporation) at room temperature (P90 (us) = 16.00, P180 (us) = 28.00, TD = 1024, SW(KHz) = 200, TR (ms) = 10000, RG1 = 20, RG2 = 3, NS = 2, D1 (ms) = 1300). The r₁ relaxivity was determined by a linear fit of the inverse T₁ relaxation time as a function of the Gd(III) concentration. T₂ relaxometry was performed in a 0.5 T magnetic field (MiniMR60, Shanghai Niumag Corporation) at room temperature (P90(us) = 18.00, P180 (us) = 34.00, TD = 1034094, SW (KHz) = 200, TR (ms) = 10000, RG1 = 20, RG2 = 3, NS = 2, DL1 = 0.5 ms, NECH = 5000). The r₂ relaxivity was also calculated through the curve fitting of 1/T₂ as a function of Dy(III) concentration. To examine the X-ray attenuation property, solutions of the formed product and Omnipaque (iohexol 300, GE Healthcare) with different Ln or I concentrations were prepared. CT scans were performed using a GE LightSpeed VCT imaging system (GE Medical Systems, Milwaukee, WI) with 100 kV, 220 mA, and a

slice thickness of 1.25 mm. Contrast enhancement was evaluated in Hounsfield units (HU) for each concentration of the samples or Omnipaque.

6.3.5 Cytotoxicity assay

The cytotoxicity of the multifunctional nanocrystals was evaluated by MTT viability assay of SKOV-3 cells. SKOV-3 cells were continuously grown in RPMI 1640 cell culture medium supplemented with streptomycin (100 $\mu\text{g}/\text{mL}$), penicillin (100 U/mL), and 10% FBS. Approximately 1×10^4 cells per well were seeded into a 96-well plate and cultured overnight to bring the cells to confluence. Then, the medium was replaced with fresh medium containing nanoparticles at different concentrations (0, 2.5, 5, 10, 20, 40, 80 $\mu\text{g}/\text{ml}$, respectively). After 24 h incubation, 20 μL MTT (5 mg/mL) in PBS was added to each well. The assays were carried out according to the manufacturer's instructions using a Thermo Scientific Multiskan MK3 ELISA reader (Thermo Scientific, USA) at 570 nm. For each sample, mean and standard deviation for the triplicate wells were reported.

6.3.6 In vivo multimode imaging of SKOV-3 xenograft tumor model.

Animal experiments were carried out at Shanghai General Hospital (Shanghai, China) according to protocols approved by the institutional committee for animal care and also in accordance with the policy of the National Ministry of Health. For in vivo imaging of tumors, a SKOV-3 xenografted tumor model was established by subcutaneously injecting 1×10^6 SKOV-3 cells/mouse in the right side of the Balb/c nude mice. When the tumor nodules reached a volume of 0.2-0.5 cm^3 at approximately 4 weeks post injection, nanomaterials (100 μL in PBS, 20 mg/ml) was intratumor delivered to the mice. MR imaging was performed using a GE 3.0 T Signa EXCITE TwinSpeed HD MR system with a custom-built rodent receiver coil (Chenguang Med Tech, Shanghai, China). At 10 min after injection, 2D spin-echo T₁- and T₂-weighted MR images were obtained with a matrix size of 256×128 , slice thickness of 2.6 mm, and field of view (FOV) of $40 \text{ mm} \times 40 \text{ mm}$. For CT imaging, a GE LightSpeed VCT imaging system was used with the same parameters as the in vitro characterization. The UCL imaging was performed with a Kodak camera under an external 1 W continuous wave infrared laser (980 nm, Shanghai Connet Fiber Optics Co., China) as the excited source.

6.4 Results and Discussion

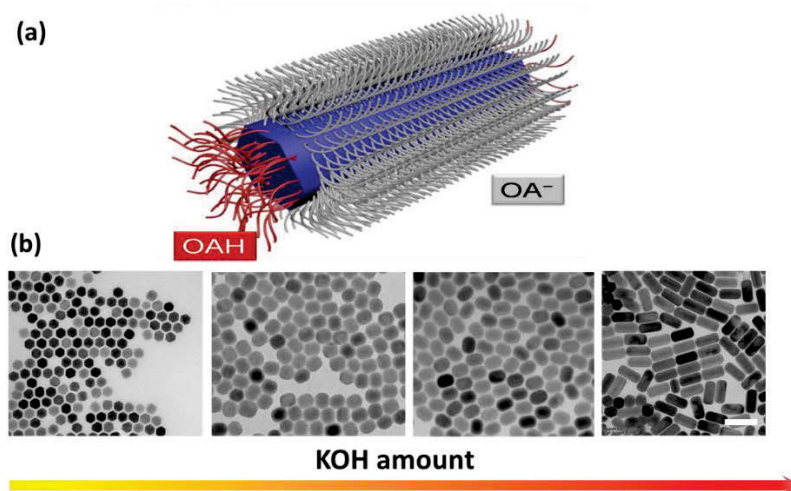


Figure 6.1 (a) the proposed OAH and OA^- distribution on the surface of the β - NaYF_4 nanocrystal, (b) TEM shows the morphology change of the nanocrystals with the different amount of KOH during the seed-mediated growth process. Scale bar: 100 nm.

According to our recent report,[29] surfactant ligands of oleic acid molecules (OAH) and oleic cations (OA^-) are preferably bond onto (001) and (100)/(010) facets of a NaYF_4 nanocrystal (**Fig. 6.1a**). To further prove these scenarios, the effect of OA^- concentration is systematically studied (**Fig. 6.1b**). It is obviously that the aspect ratio of the formed nanocrystals increases (from 1 to 2.8) with the concentration of OA^- (**Fig. 6.1b**), which demonstrate the key role of the OA^- on the facet selectively growth. However, even with the optimized OA^- concentration and the temperature, the width of the nanorods is bigger than that of the seed. This means the selective growth in this case is only the preferred direction control through the heating up epitaxial growth method, in which the relatively high concentration of shell precursor will make the precise growth direction impossible.

To improve this situation, we employ the layer-by-layer hot injection method,[31-33] which makes the concentration of the shell precursor relatively consistent and highly tunable during the growth process (**Fig. 6.2**). This approach allows us to systematically optimize the effect of the shell precursor's concentration on the facet selective growth behaviour. As shown in **Fig. 6.3**, when the shell precursor concentration is relatively low (there were less amount of the injected shell precursors to meet the demand in depositing a single atomic layer on both (001) facets of each seed nanocrystals), the growth behaviour becomes much more controllable than the heating up methods.

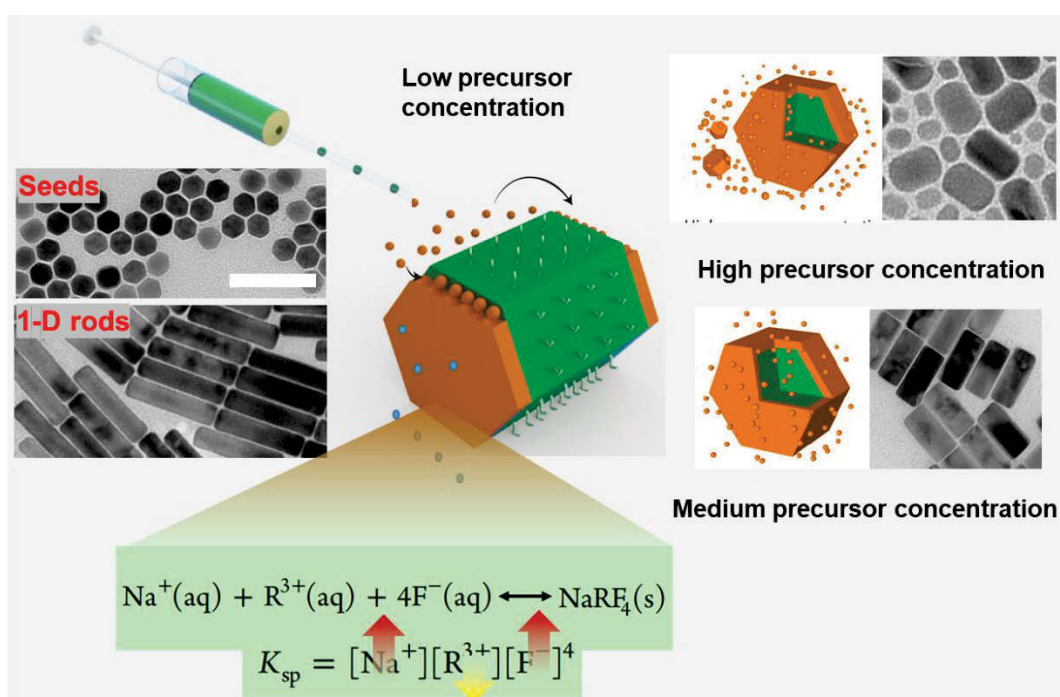


Figure 6.2 Schematic diagram of the developed one-dimensional growth of the nanocrystals through the layer-by-layer hot injection method, and TEM images of the nanorods obtained under different injection rate. Scale bar: 100 nm.

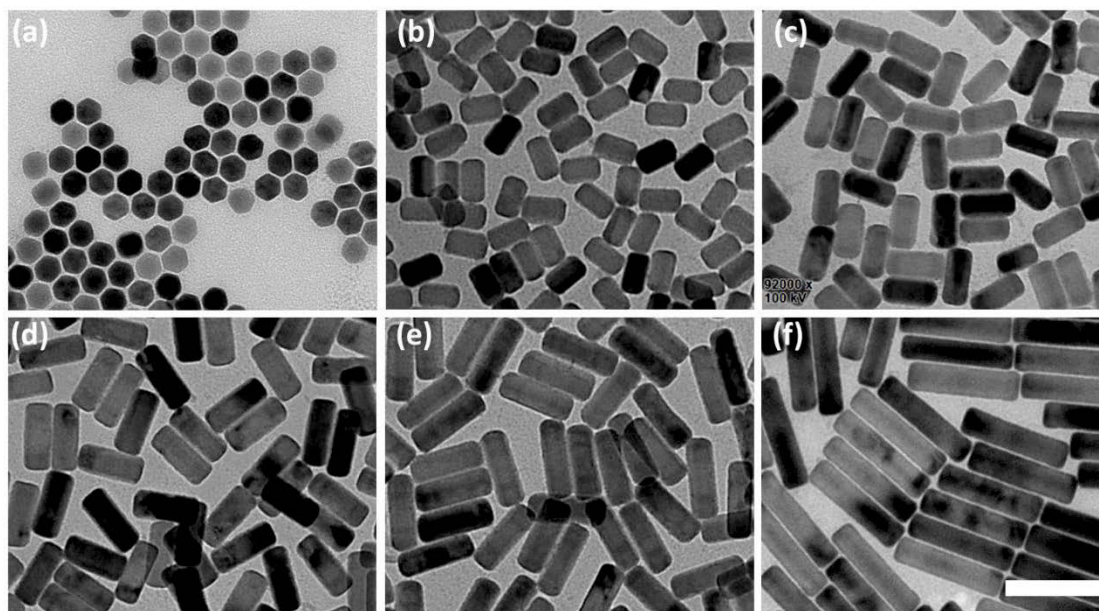


Figure 6.3 TEM images of the homogeneous NaYF_4 nanorods under the low concentration of the shell precursor with different amount of shell precursors injected, core (a), 2 mL (b), 4 mL (c), 6 mL (d), 8 mL (e), and 12 mL (f). Scale bar: 100 nm.

When the injection amount is increased by 2.5 times (medium precursor concentration), the width grows significantly, which suggests part of the shell precursors started to grow onto the non-preferred (100)/(010) facets as shown in **Fig. 6.4**. Interestingly, if the injection amount is further increased by 5 times (high precursor concentration), not only the width grows significantly, but also there are some new smaller nanocrystals formed (**Fig. 6.5**). This indicate too much shell precursors are used to form new crystals through nuclear and growth process.

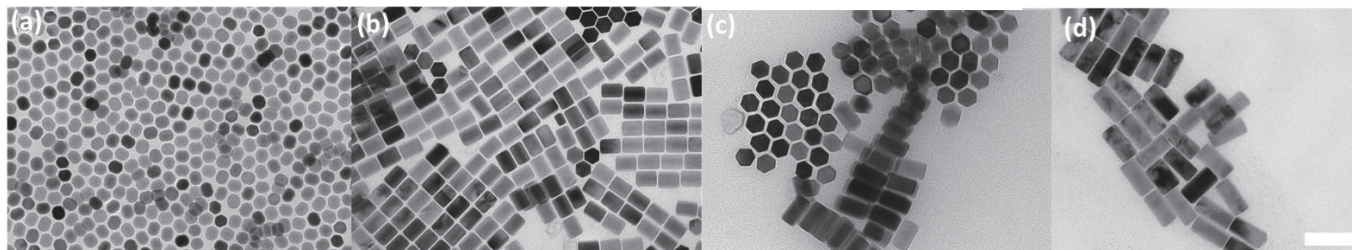


Figure 6.4 TEM images of the homogeneous NaYF₄ nanorods under the low concentration of the shell precursor with different amount of shell precursors injected, core (a), 2 mL (b), 4 mL (c), and 6 mL (d). Scale bar: 100 nm.

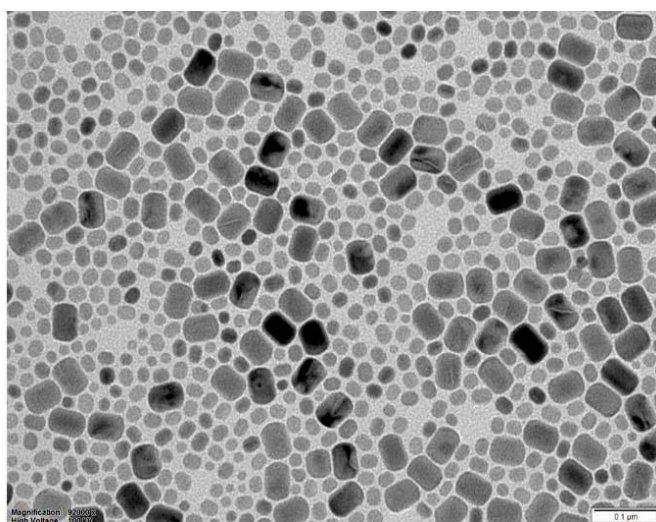


Figure 6.5 TEM images of the homogeneous NaYF₄ nanorods under the high concentration of the shell precursor (4 mL injected). Scale bar: 100 nm.

To further relatively lower the precursor's concentration for the precise growth control, and leverage the law of reciprocal proportions to shift the reaction more to the right side (**Fig. 6.2**), we provide more F⁻ and Na⁺ ions in the reaction solution. To prove this, we first study the concentration of Na⁺ ions on the growth behaviors by replacing some of NaOH with KOH while keeping the same concentration of OA⁻ in the solution. The result shown in **Fig. 6.6** indicates that the NaOH-only system provided better control

along the longitudinal direction than the NaOH/KOH system though the amount of OH^- is the same, illustrating the role of the concentration of Na^+ ions. Also, the volume of the formed nanocrystals from the NaOH/KOH system is smaller than that from the NaOH only system, further indicating that the high concentration of Na^+ ions could shift the reaction to the right side. Similar trend is observed after addition of more F^- ions in the reaction solution by keeping the amounts of Na^+ and OA^- the same.

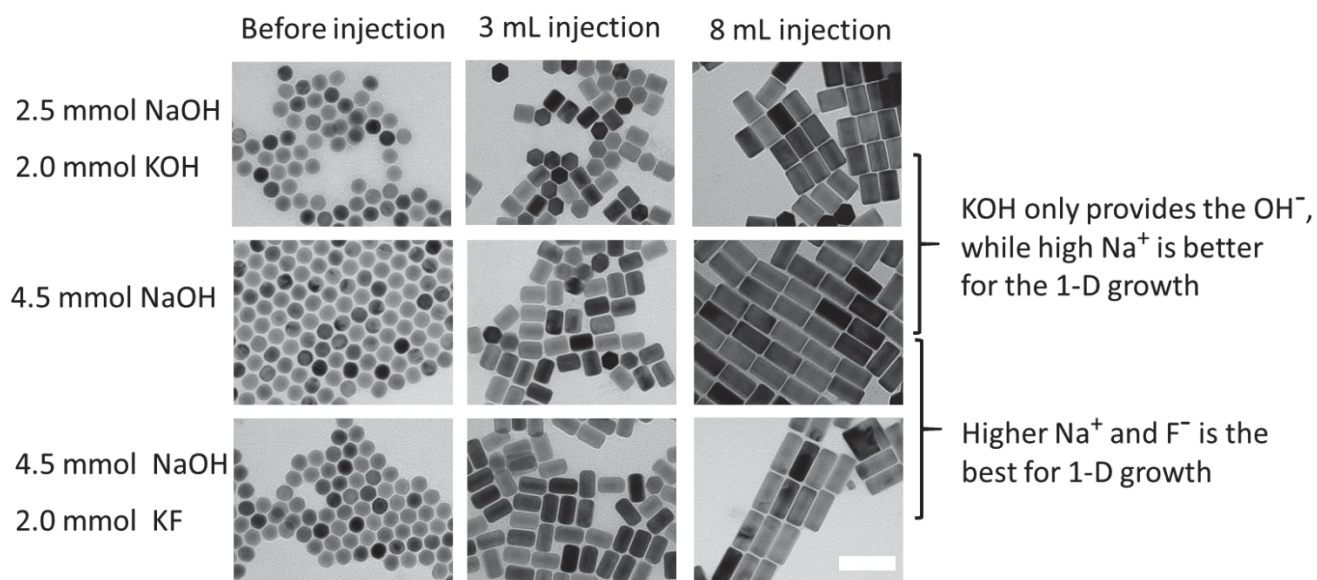


Figure 6.6 TEM images of a series of nanocrystals samples grown from varied concentrations of Na^+ and F^- ions while keeping the concentration of OA^- the same. Scale bar: 100 nm.

Through careful controls in the injection amounts of shell precursors, Na^+ and F^- ions, with the assistance of optimized OA^- concentration and reaction temperature, precisely controlled epitaxial growth in longitudinal direction have been achieved. **Fig. 6.7** shows a library of NaYF_4 nanorods with tunable width from 20 nm to 60 nm (determined by the starting size of the seed nanocrystals) and length from 24 to 242 nm (by the number of successive injection cycles).

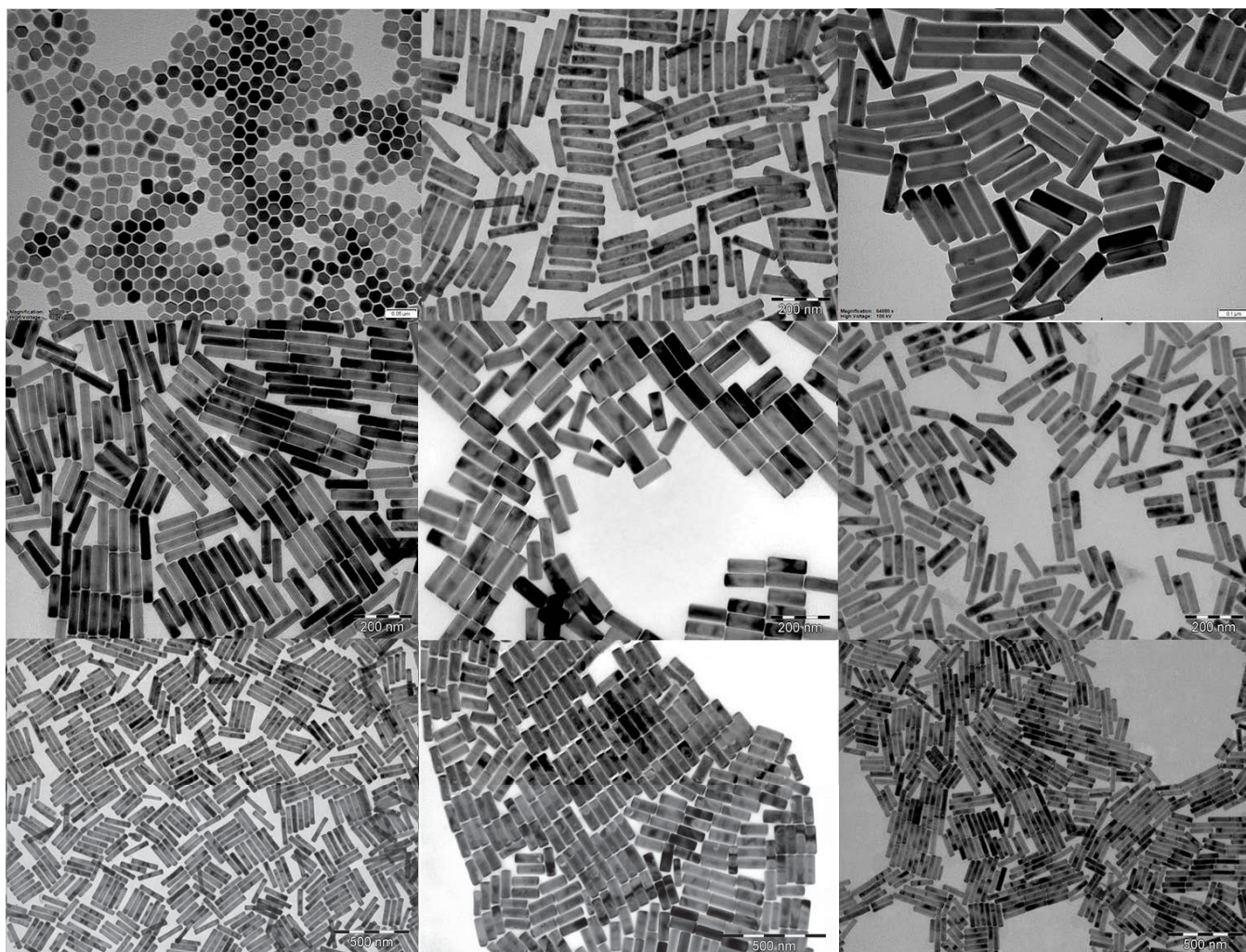


Figure 6.7 TEM images of a series of controlled synthesis of nanorods with the continuously tunable length and width, obtained by the seed-mediated growth approach.

The technique enabling precise control in the 1-D growth of homogeneous nanorods has further enabled a series of arbitrary design and synthesis of heterogeneous nanocrystals with multifunctional properties. As a demonstration, we first synthesize a structure of nine-section NaYF_4 , Yb,Er-NaYF_4 , NaDyF_4 , NaYF_4 , NaGdF_4 nanorods, following the layer-by-layer hot injection approach, with different lanthanide shell precursors injected each step (**Fig. 6.8**). TEM micrographs (**Fig. 6.8b-e**) show the structure of epitaxial growth of shells along the longitudinal direction of the core nanocrystals (**Fig. 6.8a**). The length of nanorods continuously increased to 120 nm, and the width of the nanocrystals does not show any apparent changes, remained at around 30 nm for the whole reaction process. The elemental mapping analysis confirms the elemental distribution of Gd^{3+} , Dy^{3+} , and Y^{3+} of the formed nanorods (**Fig. 6.8f-j**), consistent with our design. The line scan maps (**Fig. 6.9**) further confirm the rods with different elements at different

parts, indicating the successful synthesis the heterogeneous nanoparticles with the facile one-pot hot injection method.

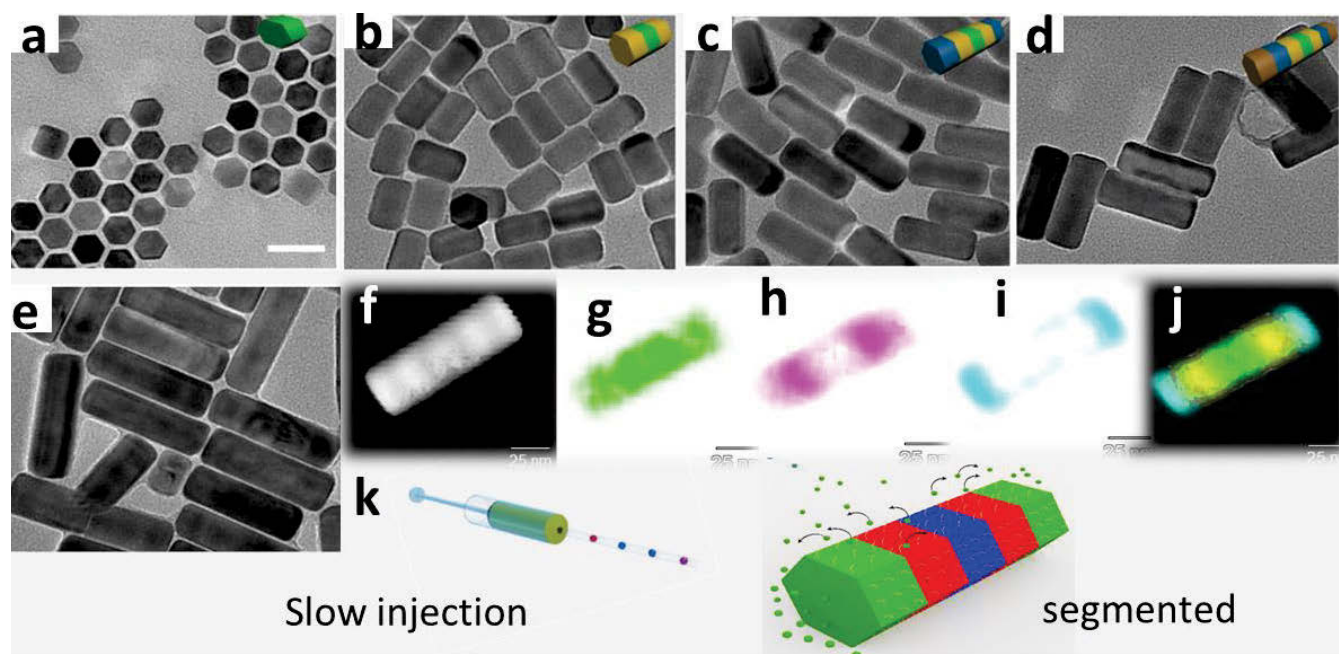


Figure 6.8 TEM images of NaYF₄,Yb,Er core nanocrystals (a), three-section NaYF₄,Yb,Er-NaYF₄ nanorods (b), five-section NaYF₄,Yb,Er-NaYF₄-NaDyF₄ nanorods (c), seven-section NaYF₄,Yb,Er-NaYF₄-NaDyF₄-NaYF₄ nanorods (d), and final nine-section NaYF₄,Yb,Er-NaYF₄-NaDyF₄-NaYF₄-NaGdF₄ nanorods (e); (f-j) HAADF-STEM image (f) and elemental mapping of Y³⁺, Dy³⁺, and Gd³⁺ in the final nine-section nanorods; (k) Schematic diagram of the nanorod synthesis through layer-by-layer hot injection with different lanthanide shell precursor. Scale bar: 50 nm.

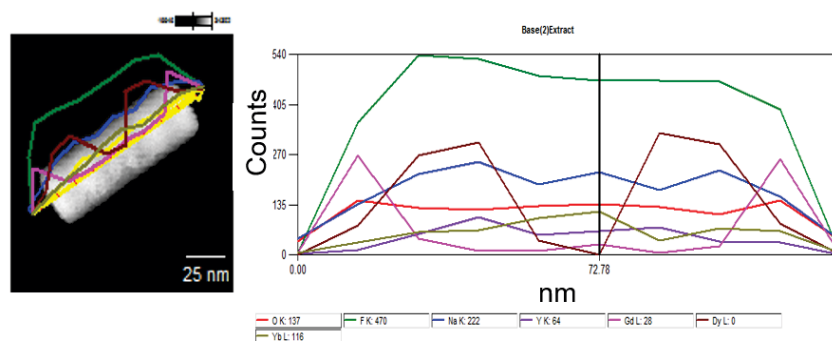


Figure 6.9 Line scan maps of the single NaYF₄,Yb,Er-NaYF₄-NaDyF₄-NaYF₄-NaGdF₄ further confirmed the rods with different elements at different part, indicating the successful synthesis the heterogeneous nanoparticles with facile one-pot hot injection methods.

Lanthanide materials have been used as the most common contrast agents for MRI [34-36] CT [37-41] and optical bio-imaging applications.[36, 38-40, 42-45] The programmable design, synthesis and integration of multiple functions and materials compositions will provide an integrated contrast agent for multi-modal bio-imaging, in which optimizing the performance of each contrast modality is the key.[44, 46] Using the facile synthesis approach developed from this work, we further demonstrate a design and on-demand synthesis of desirable composites to form multifunctional nanostructures, with a series of synergetic strategies to optimize the performance of each functions.

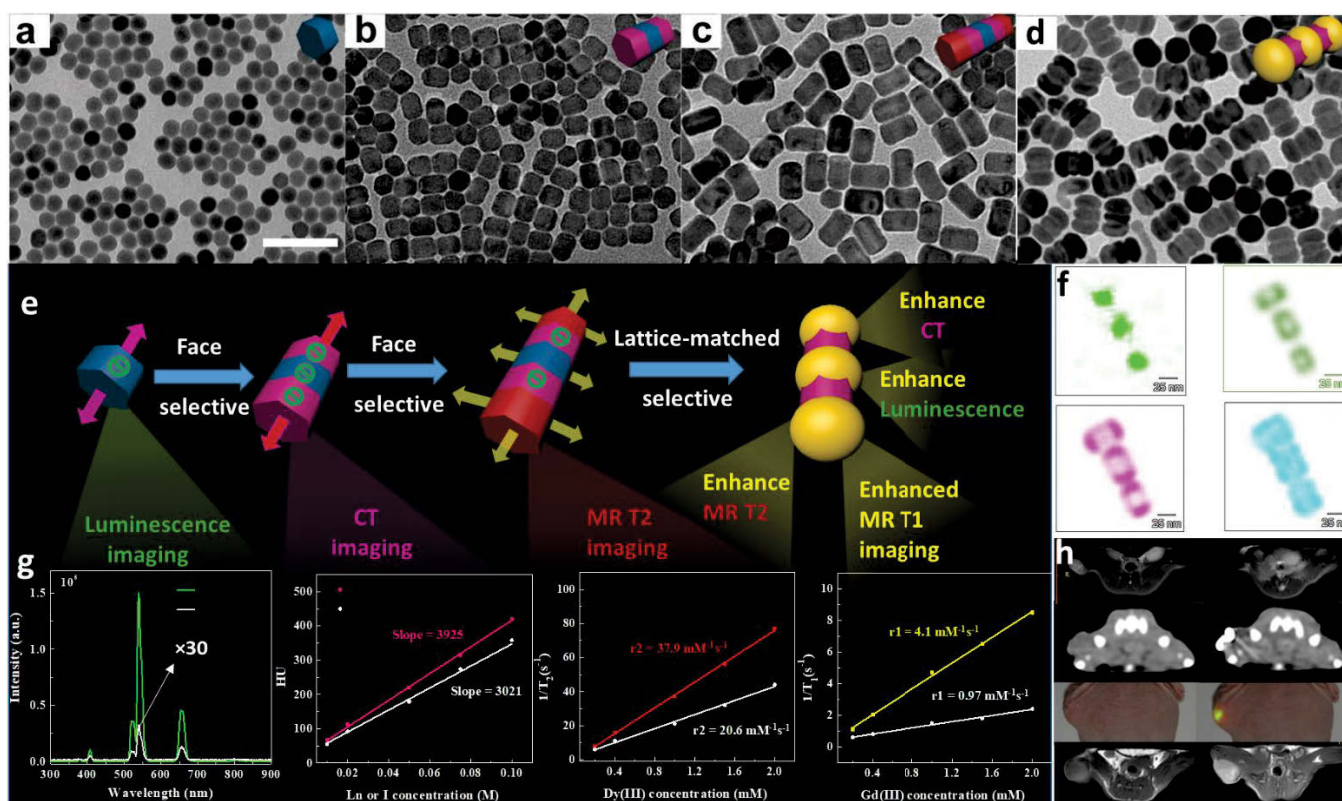


Figure 6.10 (a-d) TEM images of core nanocrystals (a), NaYF₄:Yb,Er-NaLuF₄ nanorods (b), NaYF₄:Yb,Er-NaLuF₄-NaDyF₄ nanorods (c), and NaYF₄:Yb,Er-NaLuF₄-NaDyF₄-NaGdF₄ nanoring-coated-dumbbells (d). (e) Schematic diagram of the growth mechanism of NaYF₄:Yb,Er-NaLuF₄-NaDyF₄-NaGdF₄ nanoring-coated-dumbbells, (f) STEM elemental mapping of a single nanoring-coated-dumbbell, (g) photoluminescence, MR T1, and MR T2 relaxation properties of the formed nanoring-coated-dumbbells compared with that of the homogeneous NaYF₄:Yb,Dy,Gd,Lu,Er nanorods. The X-ray attenuation property of the nanoring-coated-dumbbells compared with the clinically used CT contrast agent (Iohexol). (h) *In vivo* MR T2, CT, photoluminescence, and MR T1 images (from top to bottom) of a xenografted tumor model before (left) and after injection (right) of nanoring-coated-dumbbells.

For example, **Fig. 6.10** shows the design logic and synthesis procedure of nanoring-coated-dumbbells, and their significantly improved performance for multi-modality bio-imaging. Luminescent NaYF₄:Yb,Er nanocrystals (**Fig. 6.10a**) have been synthesized first as the seed, followed by an NaLuF₄ being selectively growth on the (001) facet of the seed for enhanced CT imaging (**Fig. 6.10b**) and a further epitaxial growth of NaDyF₄ for MR T2 imaging (**Fig. 6.10c**). The section of NaLuF₄ has been designed to isolate the NaYF₄:Yb,Er and NaDyF₄ and to avoid Dy³⁺ induced luminescence quenching. At the last step, NaGdF₄ nanocrystals, as the MR T1 imaging agent, are introduced. It is well known that exposing Gd³⁺ ions on the surface will significantly enhance the MR relaxivity.[47-49] The NaGdF₄ as inert shell will also benefit the luminescence of NaYF₄:Yb,Er. The epitaxial growth becomes selective for NaGdF₄ coating, directed by the lattice match, and eventually formed an architecture of nanoring-coated-dumbbells (**Fig. 6.10d**). This design has resulted in a synergetic enhancement of photoluminescence (reducing the surface quenching of NaYF₄:Yb,Er), MR T1 (making most of NaGdF₄ on the surface) and T2 relaxivity (passivating NaDyF₄ from surface water molecules), and CT contrast (inducing the heavy lanthanide atom Lu, Dy and Gd). The elemental mapping analysis has confirmed the elemental distribution of Gd³⁺, Dy³⁺, Lu³⁺, and Y³⁺ ions across the formed nanoring-coated-dumbbell (**Fig. 6.10f**), consistent with our initial design of the heterogeneous structure (**Fig. 6.10e**).

To evaluate the synergetic enhancement of multiple physical properties, we systematically and quantitatively characterize the photoluminescence, MR T1, and MR T2 relaxation properties of the formed nanoring-coated-dumbbells, compared with that of the homogeneous NaYF₄:Yb,Dy,Gd,Lu,Er nanorods (**Fig. 6.10g**). The photoluminescence intensity of the formed nanocrystals is two orders of magnitude (110 times) brighter than that of homogeneous one, which is attributed to both the effective surface passivation and isolation of Dy³⁺ induced cross relaxation effects. The r1 relaxivity of our designed structure is more than 4 times stronger than that of the homogeneous one. Interestingly, the r2 relaxivity from Dy³⁺ using heterogeneous controlled synthesis has also shown a better performance, because of the separation of Gd³⁺ and Dy³⁺ ions and large distance of separation between Dy³⁺ and water molecules. The X-ray attenuation property of the nanoring-coated-dumbbells is slightly better than the clinically used CT contrast agent (Iohexol), due to the higher attenuation of lanthanide element than that of iodine. This synergetic enhancement in four parameters have suggested a powerful solution for four modality bio-imaging applications.

To demonstrate the multimode imaging application using the nanoring-coated-dumbbells, their cytotoxicity is first evaluated by the standard MTT viability assay. The results show no significant

cytotoxicity of the nanoring-coated-dumbbells even at the concentration of the particles as high as 80 ug/mL, when compared to the cells treated with PBS. We then conduct the *in vivo* multimodal imaging of a xenografted tumor model. As shown in **Fig. 6.10h**, the tumor region shows a high contrast signal to the background in all the four imaging modes after intratumor injection, compared with that before the injection.

6.5 Conclusion

To conclude, we find that the strong binding of oleate cations played an important role in inhibiting the nanocrystal growth on (100)/(010) facets but it is insufficient for precisely controlled growth of nanorods along one direction. After verifying the roles of temperature and the ratio of seed crystal and precursors' concentrations, we develop a synthesis strategy based on a hot injection approach. We show that the architectures of homogenous and heterogeneous nanorods can be longitudinally engineered, with their shape, size and the element spatial arrangement precisely controlled. Through the facile one-pot hot-injection method, programmable heterogeneous nanorods and other sophisticated structures can be formed via selection of different lanthanide element doping. The partitioned heterogeneous nanocrystals, featured with a synergetic enhancement of multiple physical properties, become a nanoplatform for multi-modal imaging. This suggests a new scope for the up-scale controlled engineering of heterogeneous nanocrystals to integrate multiple functions towards many emerging nanotechnology applications.

6.6 References

- [1] Huang, X., Zeng, Z., Bao, S., Wang, M., Qi, X., Fan, Z., Zhang, H., Solution-phase epitaxial growth of noble metal nanostructures on dispersible single-layer molybdenum disulfide nanosheets, *Nature Communications* 4 (2013) 1444.
- [2] Jiang, R., Li, B., Fang, C., Wang, J., Metal/Semiconductor Hybrid Nanostructures for Plasmon-Enhanced Applications, *Advanced Materials* 26 (31) (2014) 5274-5309.
- [3] Huang, X., Tan, C., Yin, Z., Zhang, H., 25th Anniversary Article: Hybrid Nanostructures Based on Two-Dimensional Nanomaterials, *Advanced Materials* 26 (14) (2014) 2185-2204.
- [4] Donega, C.d.M., Synthesis and properties of colloidal heteronanocrystals, *Chemical Society Reviews* 40 (3) (2011) 1512-1546.
- [5] Nakonechnyi, I., Sluydts, M., Justo, Y., Jasieniak, J., Hens, Z., Mechanistic Insights in Seeded Growth Synthesis of Colloidal Core/Shell Quantum Dots, *Chemistry of Materials* 29 (11) (2017) 4719-4727.

- [6] Fantechi, E., Roca, A.G., Sepúlveda, B., Torruella, P., Estradé, S., Peiró, F., Coy, E., Jurga, S., Bastús, N.G., Nogués, J., Puentes, V., Seeded Growth Synthesis of Au–Fe₃O₄ Heterostructured Nanocrystals: Rational Design and Mechanistic Insights, *Chemistry of Materials* 29 (9) (2017) 4022-4035.
- [7] Slejko, E.A., Sayevich, V., Cai, B., Gaponik, N., Lughì, V., Lesnyak, V., Eychmüller, A., Precise Engineering of Nanocrystal Shells via Colloidal Atomic Layer Deposition, *Chemistry of Materials* 29 (19) (2017) 8111-8118.
- [8] Kovalenko, M.V., Manna, L., Cabot, A., Hens, Z., Talapin, D.V., Kagan, C.R., Klimov, V.I., Rogach, A.L., Reiss, P., Milliron, D.J., Guyot-Sionnest, P., Konstantatos, G., Parak, W.J., Hyeon, T., Korgel, B.A., Murray, C.B., Heiss, W., Prospects of Nanoscience with Nanocrystals, *ACS Nano* 9 (2) (2015) 1012-1057.
- [9] Tian, J., Zhao, Z., Kumar, A., Boughton, R.I., Liu, H., Recent progress in design, synthesis, and applications of one-dimensional TiO₂ nanostructured surface heterostructures: a review, *Chemical Society Reviews* 43 (20) (2014) 6920-6937.
- [10] Wang, X., Li, Z., Shi, J., Yu, Y., One-Dimensional Titanium Dioxide Nanomaterials: Nanowires, Nanorods, and Nanobelts, *Chemical Reviews* 114 (19) (2014) 9346-9384.
- [11] Xiao, F.-X., Miao, J., Tao, H.B., Hung, S.-F., Wang, H.-Y., Yang, H.B., Chen, J., Chen, R., Liu, B., One-Dimensional Hybrid Nanostructures for Heterogeneous Photocatalysis and Photoelectrocatalysis, *Small* 11 (18) (2015) 2115-2131.
- [12] Zhao, Q., Zhao, M., Qiu, J., Lai, W.-Y., Pang, H., Huang, W., One Dimensional Silver-based Nanomaterials: Preparations and Electrochemical Applications, *Small* 13 (38) (2017) 1701091-n/a.
- [13] Ge, M., Li, Q., Cao, C., Huang, J., Li, S., Zhang, S., Chen, Z., Zhang, K., Al-Deyab, S.S., Lai, Y., One-dimensional TiO₂ Nanotube Photocatalysts for Solar Water Splitting, *Advanced Science* 4 (1) (2017) 1600152-n/a.
- [14] Gong, S., Cheng, W., One-Dimensional Nanomaterials for Soft Electronics, *Advanced Electronic Materials* 3 (3) (2017) 1600314-n/a.
- [15] Wei, Q., Xiong, F., Tan, S., Huang, L., Lan, E.H., Dunn, B., Mai, L., Porous One-Dimensional Nanomaterials: Design, Fabrication and Applications in Electrochemical Energy Storage, *Advanced Materials* 29 (20) (2017) 1602300-n/a.
- [16] Lei, D., Benson, J., Magasinski, A., Berdichevsky, G., Yushin, G., Transformation of bulk alloys to oxide nanowires, *Science* 355 (6322) (2017) 267-271.
- [17] Li, J., Zheng, G., One-Dimensional Earth-Abundant Nanomaterials for Water-Splitting Electrocatalysts, *Advanced Science* 4 (3) (2017) 1600380-n/a.
- [18] Yi, X., Shi, X., Gao, H., A Universal Law for Cell Uptake of One-Dimensional Nanomaterials, *Nano Letters* 14 (2) (2014) 1049-1055.
- [19] He, J., Zheng, W., Ligmajer, F., Chan, C.-F., Bao, Z., Wong, K.-L., Chen, X., Hao, J., Dai, J., Yu, S.-F., Lei, D.Y., Plasmonic enhancement and polarization dependence of nonlinear upconversion emissions from single gold nanorod@SiO₂@CaF₂:Yb³⁺,Er³⁺ hybrid core-shell-satellite nanostructures, *Light Sci Appl.* 6 (2017) e16217.

- [20] Yin, Z., Zhou, D., Xu, W., Cui, S., Chen, X., Wang, H., Xu, S., Song, H., Plasmon-Enhanced Upconversion Luminescence on Vertically Aligned Gold Nanorod Monolayer Supercrystals, *ACS Applied Materials & Interfaces* 8 (18) (2016) 11667-11674.
- [21] Lee, C., Hwang, H.S., Lee, S., Kim, B., Kim, J.O., Oh, K.T., Lee, E.S., Choi, H.-G., Youn, Y.S., Rabies Virus-Inspired Silica-Coated Gold Nanorods as a Photothermal Therapeutic Platform for Treating Brain Tumors, *Advanced Materials* 29 (13) (2017) 1605563-n/a.
- [22] Walsh, M.J., Tong, W., Katz-Boon, H., Mulvaney, P., Etheridge, J., Funston, A.M., A Mechanism for Symmetry Breaking and Shape Control in Single-Crystal Gold Nanorods, *Accounts of Chemical Research* 50 (12) (2017) 2925-2935.
- [23] Jana, N.R., Gearheart, L., Murphy, C.J., Wet chemical synthesis of high aspect ratio cylindrical gold nanorods, *The Journal of Physical Chemistry B* 105 (19) (2001) 4065-4067.
- [24] Wang, Y.-N., Wei, W.-T., Yang, C.-W., Huang, M.H., Seed-Mediated Growth of Ultralong Gold Nanorods and Nanowires with a Wide Range of Length Tunability, *Langmuir* 29 (33) (2013) 10491-10497.
- [25] Xu, S., Wang, Z.L., One-dimensional ZnO nanostructures: Solution growth and functional properties, *Nano Research* 4 (11) (2011) 1013-1098.
- [26] Chang, H., Sun, Z., Ho, K.Y.-F., Tao, X., Yan, F., Kwok, W.-M., Zheng, Z., A highly sensitive ultraviolet sensor based on a facile in situ solution-grown ZnO nanorod/graphene heterostructure, *Nanoscale* 3 (1) (2011) 258-264.
- [27] Weintraub, B., Zhou, Z., Li, Y., Deng, Y., Solution synthesis of one-dimensional ZnO nanomaterials and their applications, *Nanoscale* 2 (9) (2010) 1573-1587.
- [28] Spencer, M.J.S., Gas sensing applications of 1D-nanostructured zinc oxide: Insights from density functional theory calculations, *Progress in Materials Science* 57 (3) (2012) 437-486.
- [29] Liu, D., Xu, X., Du, Y., Qin, X., Zhang, Y., Ma, C., Wen, S., Ren, W., Goldys, E.M., Piper, J.A., Dou, S., Liu, X., Jin, D., Three-dimensional controlled growth of monodisperse sub-50 nm heterogeneous nanocrystals, *Nature Communications* 7 (2016) 10254.
- [30] Liu, D., Xu, X., Wang, F., Zhou, J., Mi, C., Zhang, L., Lu, Y., Ma, C., Goldys, E., Lin, J., Jin, D., Emission stability and reversibility of upconversion nanocrystals, *Journal of Materials Chemistry C* 4 (39) (2016) 9227-9234.
- [31] Wang, R., Li, X., Zhou, L., Zhang, F., Epitaxial Seeded Growth of Rare-Earth Nanocrystals with Efficient 800 nm Near-Infrared to 1525 nm Short-Wavelength Infrared Downconversion Photoluminescence for In Vivo Bioimaging, *Angewandte Chemie International Edition* 53 (45) (2014) 12086-12090.
- [32] Li, X., Shen, D., Yang, J., Yao, C., Che, R., Zhang, F., Zhao, D., Successive Layer-by-Layer Strategy for Multi-Shell Epitaxial Growth: Shell Thickness and Doping Position Dependence in Upconverting Optical Properties, *Chemistry of Materials* 25 (1) (2013) 106-112.
- [33] Li, X., Wang, R., Zhang, F., Zhao, D., Engineering Homogeneous Doping in Single Nanoparticle To Enhance Upconversion Efficiency, *Nano Lett* 14 (6) (2014) 3634-3639.
- [34] Park, Y.I., Kim, J.H., Lee, K.T., Jeon, K.-S., Na, H.B., Yu, J.H., Kim, H.M., Lee, N., Choi, S.H., Baik, S.-I., Kim, H., Park, S.P., Park, B.-J., Kim, Y.W., Lee, S.H., Yoon, S.-Y., Song, I.C., Moon, W.K.,

Suh, Y.D., Hyeon, T., Nonblinking and Nonbleaching Upconverting Nanoparticles as an Optical Imaging Nanoprobe and T1 Magnetic Resonance Imaging Contrast Agent, *Advanced Materials* 21 (44) (2009) 4467-4471.

[35] Feng, L., Yang, D., He, F., Gai, S., Li, C., Dai, Y., Yang, P., A Core–Shell-Satellite Structured Fe₃O₄@g-C₃N₄-UCNPs-PEG for T1/T2-Weighted Dual-Modal MRI-Guided Photodynamic Therapy, *Advanced Healthcare Materials* 6 (18) (2017) 1700502-n/a.

[36] Yi, Z., Li, X., Xue, Z., Liang, X., Lu, W., Peng, H., Liu, H., Zeng, S., Hao, J., Remarkable NIR Enhancement of Multifunctional Nanoprobes for In Vivo Trimodal Bioimaging and Upconversion Optical/T2-Weighted MRI-Guided Small Tumor Diagnosis, *Advanced Functional Materials* 25 (46) (2015) 7119-7129.

[37] Liu, Z., Li, Z., Liu, J., Gu, S., Yuan, Q., Ren, J., Qu, X., Long-circulating Er³⁺-doped Yb₂O₃ up-conversion nanoparticle as an in vivo X-Ray CT imaging contrast agent, *Biomaterials* 33 (28) (2012) 6748-6757.

[38] Tian, G., Zheng, X., Zhang, X., Yin, W., Yu, J., Wang, D., Zhang, Z., Yang, X., Gu, Z., Zhao, Y., TPGS-stabilized NaYbF₄:Er upconversion nanoparticles for dual-modal fluorescent/CT imaging and anticancer drug delivery to overcome multi-drug resistance, *Biomaterials* 40 (2015) 107-116.

[39] Zeng, S., Tsang, M.-K., Chan, C.-F., Wong, K.-L., Hao, J., PEG modified BaGdF₅:Yb/Er nanoprobes for multi-modal upconversion fluorescent, in vivo X-ray computed tomography and biomagnetic imaging, *Biomaterials* 33 (36) (2012) 9232-9238.

[40] Xing, H., Bu, W., Zhang, S., Zheng, X., Li, M., Chen, F., He, Q., Zhou, L., Peng, W., Hua, Y., Shi, J., Multifunctional nanoprobes for upconversion fluorescence, MR and CT trimodal imaging, *Biomaterials* 33 (4) (2012) 1079-1089.

[41] Liu, Y., Ai, K., Liu, J., Yuan, Q., He, Y., Lu, L., A High-Performance Ytterbium-Based Nanoparticulate Contrast Agent for In Vivo X-Ray Computed Tomography Imaging, *Angewandte Chemie International Edition* 51 (6) (2012) 1437-1442.

[42] Zhou, J., Liu, Z., Li, F., Upconversion nanophosphors for small-animal imaging, *Chemical Society Reviews* 41 (3) (2012) 1323-1349.

[43] Wang, F., Banerjee, D., Liu, Y., Chen, X., Liu, X., Upconversion nanoparticles in biological labeling, imaging, and therapy, *Analyst* 135 (8) (2010) 1839-1854.

[44] Chen, G., Qiu, H., Prasad, P.N., Chen, X., Upconversion Nanoparticles: Design, Nanochemistry, and Applications in Theranostics, *Chemical Reviews* 114 (10) (2014) 5161-5214.

[45] Shen, J., Zhao, L., Han, G., Lanthanide-doped upconverting luminescent nanoparticle platforms for optical imaging-guided drug delivery and therapy, *Advanced Drug Delivery Reviews* 65 (5) (2013) 744-755.

[46] He, S., Johnson, N.J.J., Nguyen Huu, V.A., Cory, E., Huang, Y., Sah, R.L., Jokerst, J.V., Almutairi, A., Simultaneous Enhancement of Photoluminescence, MRI Relaxivity, and CT Contrast by Tuning the Interfacial Layer of Lanthanide Heteroepitaxial Nanoparticles, *Nano Lett* 17 (8) (2017) 4873-4880.

- [47] Xing, H., Zhang, S., Bu, W., Zheng, X., Wang, L., Xiao, Q., Ni, D., Zhang, J., Zhou, L., Peng, W., Zhao, K., Hua, Y., Shi, J., Ultrasmall NaGdF₄ Nanodots for Efficient MR Angiography and Atherosclerotic Plaque Imaging, *Advanced Materials* 26 (23) (2014) 3867-3872.
- [48] Johnson, N.J.J., Oakden, W., Stanisz, G.J., Scott Prosser, R., van Veggel, F.C.J.M., Size-Tunable, Ultrasmall NaGdF₄ Nanoparticles: Insights into Their T₁ MRI Contrast Enhancement, *Chemistry of Materials* 23 (16) (2011) 3714-3722.
- [49] Chen, F., Bu, W., Zhang, S., Liu, X., Liu, J., Xing, H., Xiao, Q., Zhou, L., Peng, W., Wang, L., Shi, J., Positive and Negative Lattice Shielding Effects Co-existing in Gd (III) Ion Doped Bifunctional Upconversion Nanoprobes, *Advanced Functional Materials* 21 (22) (2011) 4285-4294.

CHAPTER 7 Conclusion and Future Scope

7.1 Conclusion

In this thesis, I focus on exploring nanomaterials science for controlled upconversion nanocrystals synthesis and their performance study. The developed seed-mediated growth approach is very promising for on-demand production of various multifunctional nanocrystals. This approach offers high precision in controlled synthesis of homogeneous and heterogeneous nanocrystals with desirable size, shape and deposition of dopants. In particular, I demonstrate that UCNPs with fine-tuning the size and different activator concentration could be fabricated, which enables the directly comparison of their performance at single particle level for super-resolution imaging and *in vivo* nanoparticle tracking. Also, the nanocrystals with heterogenous core@shell@ structures enables the simultaneous sensitizer doping and size control, which paves the way for optimizing sensitizer-activator doping concentration and the design of bright and small UCNPs. Moreover, I show the absolute one-direction growth of nanorods can be achieved by fine tuning of surfactant molecules' relative stabilities on the desired crystal facet, which enables the fabrication of on-demand heterogeneous nanorods for multimode bioimaging.

The key results of this PhD work can be summarized below:

1) I demonstrate the seed-mediated growth method for fabricating homogeneous nanocrystals doped with different concentrations of activator ions. The size of the nanocrystals could be precisely controlled (one nanometer resolution) with this method, which makes it possible to compare the doping-dependent optical properties of the nanocrystals with the same size. To determine the critical Tm^{3+} doping concentration for super-resolution imaging applications, a series of ten batches of 40-nm UCNPs are synthesized with incremental Tm^{3+} concentrations from 0.5 mol% to 8 mol%. This forms the foundation for a range of single nanocrystal measurements and evaluations of their optical properties towards a series of novel applications in nanoscopy.

2) In term of the growth mechanism, I discover that the solution mix, after the core being synthesized, plays an important role in reducing the reaction time for the successive epitaxial growth of shells. Leveraging this finding, I successfully fabricate the integrated heterogeneous core@shell nanocrystals with the luminescence intensity almost double than of the nanocrystals formed in the conventional methods.

3) Small core@shell nanocrystals with sub-10-nm nanocrystals as the core can be formed with the assistance of the solution mix and in turn the reduced reaction time. These core@shell nanocrystals cannot be fabricated using conventional methods due to the low stability of sub-10-nm nanocrystals in the reaction mix. These bright and ultra-small core@shell UCNPs will pave the way for nanomedicine applications.

4) I find the heterogeneous seed-mediated growth approach can be used to fabricate the core@shell@shell nanoparticles with various sensitizer and activator doping concentration but at the same size. These nanocrystals enable the systematic study of the upconversion luminescent properties of the nanocrystals with varied doping concentrations of Yb^{3+} and Tm^{3+} . I demonstrate that the higher doping concentrations of Yb^{3+} and Tm^{3+} can significantly enhance the upconversion luminescence at relatively high excitation power range, while the relatively lower doping concentration of Tm^{3+} and higher doping concentration of Yb^{3+} should be used to produce the brighter nanocrystals at lower excitation power to avoid the cross-relaxation.

5) Through the systematic synthesis and optical study, I provide a library of brightest nanocrystals with optimum doping concentrations at different excitation densities. This observation has further guided us to synthesize the bright 15 nm core@shell nanocrystals with 10 nm active core nanocrystals, which is similar to the size of an IgG antibody.

6) I find that the surfactant molecule of OAH and OA^- has different bonding ability on different facets of the nanocrystals, which enables the growth direction control of upconversion nanocrystals in the seed-mediated growth method. Through fine-tuning of the amount of surfactant molecules and the concentration of the shell precursor, I achieve the absolute one-direction growth of UCNPs nanorods by the layer-by-layer deposition of precursor on the desired crystal facet. On-demand deposition of arbitrary kind of precursors along the longitudinal direction has resulted in a series of homogeneous nanorods in the length range from 24 nm to 242 nm.

7) Through directional controlled growth approach, I also demonstrate the fabrication of heterogeneous barcoded nanorods as multifunctional contrast agents for multimodal bioimaging. Through carefully design, each lanthanide element for different imaging is logically assembled within a single barcode to maximize the multi-functionalization. These heterogeneous nanorods can be used as a nanoplatform for multi-modal *in vivo* tumor imaging. This suggests future heterogeneous nanocrystals with integrated functions can be realized by the programmable growth of multifunctional barcode crystals with tunable size, composition, and properties.

The UCNPs with controlled size, shape and properties is the first step towards real excellent applications of fluorescent microscopy, nanoscale thermometry, photodynamic therapy, optogenetics, security inks, photovoltaic converters, and 3-D volumetric displays. Under the base of this work, more specific application related research projects are ready to start.

7.2 Future Scope

My PhD thesis, by exploring the seed-mediated growth approach for highly controlled engineering of NaReF₄ nanocrystals, suggests a new field in controlled growth of high quality of highly doped UCNPs and hybrid nanocrystals. These advanced nanomaterials will enable various exist as well as emerging applications possible.

7.2.1 Developing highly doped UCNPs

The development of nanoscience and nanotechnology makes the precision in doping control during the synthesis, which has resulted in a library of programmable heterogeneous multilayer doped nanostructures, particularly in UCNPs.[1] These include the doping location evolution (from heterogeneous to homogeneous, then to programmable heterogeneous doping in the core-shell system) and dopant species evolution (from single to dual/multi-doping, from homo-valence ion to hetero-valence ion doping).

The **doping location** in the elaborated multilayer nanosystem was adjusted to enhance the performance of the luminescent nanomaterials. Also, the emerging graded doping[2-5] will open the door for further tuning of the doping concentration and location at each layer of the multilayer nanosystem, then to continue their improvement in brighter and multi-functional nanomaterials. Thus far, only the sphere-like core-shell structure was employed to control the energy transfer, while the study on the emerging heterogenous nanorods as well as the nanoplate is scarce.[6] The ultimate frontier for the doping location control is enabling the 3-D programmable arranging different kind of dopants in different location of the host materials, which will make it possible to study the performance of a single dopant and the direct interaction between different dopants.

Recent progress witnesses the **dopant species** evolution (from single to dual/multi-doping, from homo-valence ion to hetero-valence ion doping). Different dopant species could be employed to control phase structures, sizes, shapes as well as properties of functional nanomaterials.[7] Multi-dopant doping was employed in some nanomaterials systems to simultaneously tune the excitation wavelength as well as the

emitting spectrum.[8-11] More recently, doping was adopted from homo-valence ion to hetero-valence ion doping.[12-14] For example, apart from the Fe³⁺ doping,[15] transition metal Mn²⁺ doping was also employed to obtain the enhanced red emission from Er³⁺.[16, 17] With the advances in wet-chemical synthesis, it is possible to extend the dopant species to whatever needed for better performance. Apart from the active dopants (Er³⁺, Tm³⁺, Yb³⁺, Nd³⁺, Mn²⁺, Ce³⁺, and Cr³⁺), some passive dopants (e.g. K⁺ and Li⁺), which do not participate in ET but change the nanocrystal structure, also have affected the brightness of the UCNPs.

7.2.2 Development of hybrid system

During the past decade, **hybrid nanocomposites** have been of immense scientific and technological interest in the area of biomedicine.[18-20] This is largely due to the unique structural properties related to different elements in the nanocrystals. Integrating different elements into a nanoplatform can introduce new and enhanced properties, or multi-functionality, which could not be found in the parent homogeneous nanoparticles. Therefore, the ultimate front for nanomaterials science is the development of a programmable diversity of nanosystem with the desired functionalities and performance, which has always been the challenge for chemists and materials scientists.

The large surface-to-volume ratio of nanomaterials makes their surfaces the dominant player in many physical and chemical processes, as evidenced in the **organic-inorganic hybrid nanomaterials**.[21] The surface ligands — molecules that bind to the surface — are an essential component of nanomaterial synthesis, which can significantly alter luminescence properties and generate completely new effects.[22] For example, for upconversion luminescence, lanthanide-doped inorganic nanocrystals exhibit narrowband (FWHM around 20 nm) and unfortunately low (10^{-20} cm⁻²) absorption/emission, neither blinking nor photobleaching, require low excitation power ($<10^4$ W/cm²) and do not interfere with cellular/tissue autofluorescence. On the other hand, organic dyes have the advantages of broad spectral window, significantly larger absorption cross section and quantum efficiency. Therefore, the organic-inorganic hybrid nanomaterials (i.e. dye-sensitized upconversion nanosystem) bridge the gap and combine the advantages.[23] Similarly, the common triplet energy transfer could happened between the inorganic nanocrystals and dye attached to the surface.[24-27] This strategy enables direct excitonic energy transfer from ‘dark’ triplets in the organic semiconductor tetracene to colloidal PbS nanocrystals, thereby successfully harnessing molecular triplet excitons in the near infrared.[26] To make the energy transfer effective, not only the distance between sensitizers, sensitizers and activators, and activators themselves

should be concerned (leveraging long-range energy migration)[28], but also the orientation of the surface organic dye should be controlled (employ the MOF technology).[29, 30].

Apart from the inorganic-organic system, the **inorganic-inorganic nanosystem** also shows the in-depth development. For example, PbS colloidal quantum dots were doped into the MAPbI₃ film to produce the ‘dots-in-a-matrix’ crystals in the solution phase through heteroepitaxy,[31] which enables the combination of the electrical transport properties of the perovskite matrix with the high radiative efficiency of the quantum dots. Similarly, Cargnello et al. showed that gold nanocrystals act as substitutional dopants in superlattices of host nanocrystals (CdSe or PbSe) with the similar size through nanocrystal self-assembly.[32] The gold nanocrystals occupy random positions in the superlattice with a widely controllable density, which makes the conductivity of PbSe films can be manipulated over at least six orders of magnitude. Interestingly, the number, distance and the form shape of the nanocrystals dopants could be well controllable on each host nanocrystal with the advantages of the wet-chemical synthesis and post-synthesis process.

7.2.3 Exploring new applications

The advanced materials fabrication methods and in turn the emerging of on-demand nanoparticles will further push their real applications in super-resolution microscopy, in vivo multimode imaging, optogenetics, and single nanoparticle tracking, photovoltaics, Nanothermometry and laser refrigeration.

Super-resolution microscopy, including Single-Molecule Localization Microscopy (such as STORM, dSTORM, PALM, FPALM, GSDIM) and STED, SIM provides direct insight into fundamental biological processes occurring at length scales smaller than light’s diffraction limit. The advent of super resolution has revolutionized biological fluorescence microscopy and the associated field at large. However, much of that excitement has been tempered by prohibitive imaging requirements. Achieving super resolution entails certain sacrifices, namely imaging speed, choice of fluorophore, ease of multicolor and three-dimensional imaging, and generally more complex instrumentation as compared to standard widefield or confocal imaging techniques. Therefore, the new luminescent nanomaterials providing more choice of the fluorophore will boost the development of the super-resolution nanoscopy if only small size and bright emission will be managed. The on-demand design of multifunctional doped nanosystem will enable the multiplexing of the nanoscopy, which is of great importance to study the protein interaction as well as physiological and pathological process at the nanoscale.

In vivo optical imaging is a powerful methodology allowing users to monitor molecular and functional events noninvasively in a broad array of applications from cancer biology to microbiology using either bioluminescent or fluorescent reporters. In comparison with other *in vivo* imaging techniques (such as MRI, echography and CT imaging), optical approaches offer high sensitivity and high spatial resolution. This resolution scale is by no means a fundamental limit, as shown by progress in the growing field of super resolution microscopy. Therefore, the luminescent nanomaterials, as the contrast agent, will boost the clinical application of the optical imaging.

The emergence of **optogenetics** in the field of neuroscience has witnessed tremendous progress in the past decade. There, progress in optical microscopy, combined with the development of new genetic markers that can make specific gene populations optically active, has provided neuroscientists with a powerful means to better understand brain behavior. Given such promising developments, the luminescent nanomaterials are driven both by the refinement of optical techniques and by the development of new contrast mechanisms.

Single-nanoparticle tracking reveals the machinery of motion by molecular motors disclosed fundamental information about the dynamics and the interplay of different membrane components in living cells. Essential features of sub-cellular structures and interactions between biomolecules have been revealed thanks to the implementation of single-nanoparticle tracking techniques inside living cells. More recently, the need for accurate molecular localization has been further pushed by the development of super-resolution microscopies based on localization. Here, the intensity and uniformity of the luminescent nanomaterials is the key for its ultimate success.

In **photovoltaics**, achieving a high optical absorption of solar light is the key to the outstanding performance of the cells. This needs the combination of both downconversion and upconversion luminescent nanomaterials with high quantum yield at appropriately low irradiance (several 0.1 W/cm^2), which is a mandatory precondition to achieve a significant impact of the upconverter on the overall device performance. These photons can then be utilized by the solar cell. Theoretically, the efficiency of a crystalline silicon solar cell can be enhanced by UC from 30% to 40% (33% relative). In more comprehensive studies, considering up to date and more realistic parameters for silicon solar cells and Er-doped upconverter materials, the predicted efficiency enhancement is around 15% relative.

Nanothermometry aims to extract knowledge of the local temperature of a given system with sub-micrometric spatial resolution. The recent development of nanotechnology and nanomedicine brought

about the appearance of a large number of such systems.[33] In micro/nano-electronics, the reduced dimensions of electrical conduction channels lead to relevant resistances in such a way that the Joule heating effect becomes non-negligible. Another area that could benefit greatly from the high-resolution and high-sensitivity of nanothermometry is biomedicine, in which temperature is known to play a crucial role in determining its dynamics and properties. Fortunately, many luminescent nanothermometers enable the accurate and sensitive temperature sensing even in living cells.[34, 35]

Recent **laser refrigeration** of solids results have achieved cryogenic temperatures through a vibration-free, anti-Stokes photoluminescence process.[36][37] These upconversion nanosystem, including high Yb^{3+} concentration doped NaYF_4 Nanowires (down to 9 °C),[38] have shown excellent laser refrigeration performance. This technology enables a range of potential future applications, including single-molecule biophysics and integrated photonic, electronic, and microfluidic devices. Also, it has been demonstrated that single-beam laser trapping can be used to induce and quantify the local refrigeration of physiological media by >10 °C following the emission of photoluminescence from upconverting yttrium lithium fluoride nanocrystals.[37] This trend will open the door for the study of the bio-process in living cells under lower temperatures. The challenge, here, is the relatively large size of the laser refrigeration reagent (100 - 1000nm), which will hinder the protein labeling and the interaction and process study in succession.

7.3 References

- [1] Liu, D., Xu, X., Du, Y., Qin, X., Zhang, Y., Ma, C., Wen, S., Ren, W., Goldys, E.M., Piper, J.A., Dou, S., Liu, X., Jin, D., Three-dimensional controlled growth of monodisperse sub-50 nm heterogeneous nanocrystals, *Nature Communications* 7 (2016) 10254.
- [2] Hadar, I., Philbin, J.P., Panfil, Y.E., Neyshtadt, S., Lieberman, I., Eshet, H., Lazar, S., Rabani, E., Banin, U., Semiconductor Seeded Nanorods with Graded Composition Exhibiting High Quantum-Yield, High Polarization, and Minimal Blinking, *Nano Letters* 17 (4) (2017) 2524-2531.
- [3] Zhong, Y., Rostami, I., Wang, Z., Dai, H., Hu, Z., Energy Migration Engineering of Bright Rare-Earth Upconversion Nanoparticles for Excitation by Light-Emitting Diodes, *Advanced Materials* 27 (41) (2015) 6418-6422.
- [4] Huang, H., Dai, B., Wang, W., Lu, C., Kou, J., Ni, Y., Wang, L., Xu, Z., Oriented Built-in Electric Field Introduced by Surface Gradient Diffusion Doping for Enhanced Photocatalytic H_2 Evolution in CdS Nanorods, *Nano Letters* 17 (6) (2017) 3803-3808.
- [5] Tian, W., Leng, J., Zhao, C., Jin, S., Long-Distance Charge Carrier Funneling in Perovskite Nanowires Enabled by Built-in Halide Gradient, *Journal of the American Chemical Society* 139 (2) (2017) 579-582.

- [6] Zhuo, Z., Liu, Y., Liu, D., Huang, P., Jiang, F., Chen, X., Hong, M., Manipulating energy transfer in lanthanide-doped single nanoparticles for highly enhanced upconverting luminescence, *Chemical Science* (2017).
- [7] Wang, F., Han, Y., Lim, C.S., Lu, Y., Wang, J., Xu, J., Chen, H., Zhang, C., Hong, M., Liu, X., Simultaneous phase and size control of upconversion nanocrystals through lanthanide doping, *Nature* 463 (7284) (2010) 1061-1065.
- [8] Wang, F., Liu, X., Upconversion Multicolor Fine-Tuning: Visible to Near-Infrared Emission from Lanthanide-Doped NaYF₄ Nanoparticles, *J Am Chem Soc* 130 (17) (2008) 5642-5643.
- [9] Wang, Y.-F., Liu, G.-Y., Sun, L.-D., Xiao, J.-W., Zhou, J.-C., Yan, C.-H., Nd³⁺-Sensitized Upconversion Nanophosphors: Efficient In Vivo Bioimaging Probes with Minimized Heating Effect, *ACS Nano* 7 (8) (2013) 7200-7206.
- [10] Deng, R., Qin, F., Chen, R., Huang, W., Hong, M., Liu, X., Temporal full-colour tuning through non-steady-state upconversion, *Nat Nano* 10 (3) (2015) 237-242.
- [11] Wang, F., Liu, X., Multicolor Tuning of Lanthanide-Doped Nanoparticles by Single Wavelength Excitation, *Accounts of Chemical Research* 47 (4) (2014) 1378-1385.
- [12] Stavrinadis, A., Pelli Cresi, J.S., d'Acapito, F., Magén, C., Boscherini, F., Konstantatos, G., Aliovalent Doping in Colloidal Quantum Dots and Its Manifestation on Their Optical Properties: Surface Attachment versus Structural Incorporation, *Chemistry of Materials* 28 (15) (2016) 5384-5393.
- [13] Begum, R., Parida, M.R., Abdelhady, A.L., Murali, B., Alyami, N.M., Ahmed, G.H., Hedhili, M.N., Bakr, O.M., Mohammed, O.F., Engineering Interfacial Charge Transfer in CsPbBr₃ Perovskite Nanocrystals by Heterovalent Doping, *Journal of the American Chemical Society* 139 (2) (2017) 731-737.
- [14] Stavrinadis, A., Rath, A.K., de Arquer, F.P.G., Diedenhofen, S.L., Magén, C., Martinez, L., So, D., Konstantatos, G., Heterovalent cation substitutional doping for quantum dot homojunction solar cells, 4 (2013) 2981.
- [15] Tang, J., Chen, L., Li, J., Wang, Z., Zhang, J., Zhang, L., Luo, Y., Wang, X., Selectively enhanced red upconversion luminescence and phase/size manipulation via Fe³⁺ doping in NaYF₄:Yb,Er nanocrystals, *Nanoscale* 7 (35) (2015) 14752-14759.
- [16] Tian, G., Gu, Z., Zhou, L., Yin, W., Liu, X., Yan, L., Jin, S., Ren, W., Xing, G., Li, S., Zhao, Y., Mn²⁺ Dopant-Controlled Synthesis of NaYF₄:Yb/Er Upconversion Nanoparticles for in vivo Imaging and Drug Delivery, *Advanced Materials* 24 (9) (2012) 1226-1231.
- [17] Zeng, S., Yi, Z., Lu, W., Qian, C., Wang, H., Rao, L., Zeng, T., Liu, H., Liu, H., Fei, B., Hao, J., Simultaneous Realization of Phase/Size Manipulation, Upconversion Luminescence Enhancement, and Blood Vessel Imaging in Multifunctional Nanoprobes Through Transition Metal Mn²⁺ Doping, *Advanced Functional Materials* 24 (26) (2014) 4051-4059.
- [18] Nguyen, K.T., Zhao, Y., Engineered Hybrid Nanoparticles for On-Demand Diagnostics and Therapeutics, *Accounts of Chemical Research* 48 (12) (2015) 3016-3025.
- [19] Kovalenko, M.V., Manna, L., Cabot, A., Hens, Z., Talapin, D.V., Kagan, C.R., Klimov, V.I., Rogach, A.L., Reiss, P., Milliron, D.J., Guyot-Sionnest, P., Konstantatos, G., Parak, W.J., Hyeon, T., Korgel,

B.A., Murray, C.B., Heiss, W., Prospects of Nanoscience with Nanocrystals, *ACS Nano* 9 (2) (2015) 1012-1057.

[20] Khademhosseini, A., Chan, W.W.C., Chhowalla, M., Glotzer, S.C., Gogotsi, Y., Hafner, J.H., Hammond, P.T., Hersam, M.C., Javey, A., Kagan, C.R., Kotov, N.A., Lee, S.-T., Li, Y., Möhwald, H., Mulvaney, P.A., Nel, A.E., Parak, W.J., Penner, R.M., Rogach, A.L., Schaak, R.E., Stevens, M.M., Wee, A.T.S., Brinker, J., Chen, X., Chi, L., Crommie, M., Dekker, C., Farokhzad, O., Gerber, C., Ginger, D.S., Irvine, D.J., Kiessling, L.L., Kostarelos, K., Landes, C., Lee, T., Leggett, G.J., Liang, X.-J., Liz-Marzán, L., Millstone, J., Odom, T.W., Ozcan, A., Prato, M., Rao, C.N.R., Sailor, M.J., Weiss, E., Weiss, P.S., *Nanoscience and Nanotechnology Cross Borders*, *ACS Nano* 11 (2) (2017) 1123-1126.

[21] Kagan, C.R., Mitzi, D.B., Dimitrakopoulos, C.D., *Organic-Inorganic Hybrid Materials as Semiconducting Channels in Thin-Film Field-Effect Transistors*, *Science* 286 (5441) (1999) 945-947.

[22] Boles, M.A., Ling, D., Hyeon, T., Talapin, D.V., *The surface science of nanocrystals*, *Nat Mater* 15 (2) (2016) 141-153.

[23] Chen, G., Damasco, J., Qiu, H., Shao, W., Ohulchanskyy, T.Y., Valiev, R.R., Wu, X., Han, G., Wang, Y., Yang, C., Ågren, H., Prasad, P.N., *Energy-Cascaded Upconversion in an Organic Dye-Sensitized Core/Shell Fluoride Nanocrystal*, *Nano Letters* 15 (11) (2015) 7400-7407.

[24] Mongin, C., Garakyaraghi, S., Razgoniaeva, N., Zamkov, M., Castellano, F.N., *Direct observation of triplet energy transfer from semiconductor nanocrystals*, *Science* 351 (6271) (2016) 369-372.

[25] Wu, M., Congreve, D.N., Wilson, M.W.B., Jean, J., Geva, N., Welborn, M., Van Voorhis, T., Bulović, V., Bawendi, M.G., Baldo, M.A., *Solid-state infrared-to-visible upconversion sensitized by colloidal nanocrystals*, *Nat Photon* 10 (1) (2016) 31-34.

[26] Tabachnyk, M., Ehrler, B., Gélinas, S., Böhm, M.L., Walker, B.J., Musselman, K.P., Greenham, N.C., Friend, R.H., Rao, A., *Resonant energy transfer of triplet excitons from pentacene to PbSe nanocrystals*, *Nat Mater* 13 (11) (2014) 1033-1038.

[27] Huang, Z., Li, X., Mahboub, M., Hanson, K.M., Nichols, V.M., Le, H., Tang, M.L., Bardeen, C.J., *Hybrid Molecule–Nanocrystal Photon Upconversion Across the Visible and Near-Infrared*, *Nano Letters* 15 (8) (2015) 5552-5557.

[28] Deng, R., Wang, J., Chen, R., Huang, W., Liu, X., *Enabling Förster Resonance Energy Transfer from Large Nanocrystals through Energy Migration*, *Journal of the American Chemical Society* 138 (49) (2016) 15972-15979.

[29] Sun, C.-Y., Wang, X.-L., Zhang, X., Qin, C., Li, P., Su, Z.-M., Zhu, D.-X., Shan, G.-G., Shao, K.-Z., Wu, H., Li, J., *Efficient and tunable white-light emission of metal–organic frameworks by iridium-complex encapsulation*, 4 (2013) 2717.

[30] Yang, X., Lin, X., Zhao, Y., Zhao, Y.S., Yan, D., *Lanthanide Metal–Organic Framework Microrods: Colored Optical Waveguides and Chiral Polarized Emission*, *Angewandte Chemie* (2017) n/a-n/a.

[31] Ning, Z., Gong, X., Comin, R., Walters, G., Fan, F., Voznyy, O., Yassitepe, E., Buin, A., Hoogland, S., Sargent, E.H., *Quantum-dot-in-perovskite solids*, *Nature* 523 (7560) (2015) 324-328.

- [32] Cargnello, M., Johnston-Peck, A.C., Diroll, B.T., Wong, E., Datta, B., Damodhar, D., Doan-Nguyen, V.V.T., Herzing, A.A., Kagan, C.R., Murray, C.B., Substitutional doping in nanocrystal superlattices, *Nature* 524 (7566) (2015) 450-453.
- [33] Brites, C.D.S., Xie, X., Debasu, M.L., Qin, X., Chen, R., Huang, W., Rocha, J., Liu, X., Carlos, L.D., Instantaneous ballistic velocity of suspended Brownian nanocrystals measured by upconversion nanothermometry, *Nat Nano* 11 (10) (2016) 851-856.
- [34] Zhu, X., Feng, W., Chang, J., Tan, Y.-W., Li, J., Chen, M., Sun, Y., Li, F., Temperature-feedback upconversion nanocomposite for accurate photothermal therapy at facile temperature, *Nature Communications* 7 (2016) 10437.
- [35] Kucsko, G., Maurer, P.C., Yao, N.Y., Kubo, M., Noh, H.J., Lo, P.K., Park, H., Lukin, M.D., Nanometre-scale thermometry in a living cell, *Nature* 500 (7460) (2013) 54-58.
- [36] Ha, S.-T., Shen, C., Zhang, J., Xiong, Q., Laser cooling of organic–inorganic lead halide perovskites, *Nat Photon* 10 (2) (2016) 115-121.
- [37] Roder, P.B., Smith, B.E., Zhou, X., Crane, M.J., Pauzauskie, P.J., Laser refrigeration of hydrothermal nanocrystals in physiological media, *Proceedings of the National Academy of Sciences* 112 (49) (2015) 15024-15029.
- [38] Zhou, X., Smith, B.E., Roder, P.B., Pauzauskie, P.J., Laser Refrigeration of Ytterbium-Doped Sodium–Yttrium–Fluoride Nanowires, *Advanced Materials* 28 (39) (2016) 8658-8662.

8. Appendix---Review

Advances in highly doped upconversion nanoparticles

(This work published in *Nature Communications*: 2018, 9, 2415)

Abstract: Upconversion nanomaterials are typically doped with lanthanide ions, capable of converting near-infrared light into visible and ultraviolet one. The restraint of ‘concentration quenching’ has been long challenging the community for the development of brighter nanoparticles with a large amount of dopants. This review surveys the mechanism and strategies that bypass the quenching effect to create highly doped upconversion nanocrystals. Importantly, many new and inspiring optical properties have been discovered out of these nanocrystals, showing a revolutionary impact in the field of ultra-sensitive detection, optical multiplexing and super resolution nanoscopy, towards an array of novel enabling technologies.

8.1 Introduction

Upconversion nanoparticles (UCNPs) are typically doped with lanthanide ions with multiple energy levels, which up-converts two or more lower-energy photons into one high energy photon¹⁻³. This unique anti-Stokes’ optical property enables a broad range of applications spanning background-free bio-labelling and bio-sensing, light-triggered drug delivery, multimodal bio-imaging, full-color 3D display, and solar energy harvesting⁴⁻⁶. To enhance its upconversion efficiency, it requires co-doping of both the sensitizer with a large absorption cross-section and the activator with an intermediate excited state matching that of sensitizer ions to achieve efficient energy transfer⁷⁻⁹. This process involves mutual interactions of the sensitizer and activator ions, which is sensitive to the operating distance. Therefore, the doping concentration, determining factor of dopant ions distance, significantly affects the energy transfer process and the luminescent properties of UCNPs⁹⁻¹¹.

The primary goal to increase the concentration of co-dopants is to directly improve the brightness of luminescence nanomaterials. However, the restraint of concentration quenching that limits the amount of the dopants usable, has been known for years in bulk (e.g. Nd doped YAG laser) materials¹², and tuning the luminescence properties and applications have been largely constrained by the relatively low

concentrations of dopants (Figure 1a)^{2,13}. This issue becomes particularly outstanding in nanomaterials with relatively large ratios of surface to volume, where high doping concentration will induce both cross-relaxation energy loss and energy migration to the large amount of surface quenchers, which explains the much-reduced luminescence quantum yield in upconversion nanomaterial¹⁴⁻¹⁶. Fortunately, over the last decade, a great amount of research efforts has been devoted to studying the concentration quenching mechanisms (Figure 1b) and building brighter luminescence nanomaterials through raised emitters content, which opens the door for many new applications^{2,10,17,18}.

In this review, we discuss the phenomenon of concentration quenching and its mechanism (Figure 1 and Box 1), review general and emerging strategies for overcoming concentration quenching (Box 2), and summarize the revolutionary impact of highly doped UCNPs on promoting their brightness and new properties for a range of new applications (Figure 2). In particular, we discuss the use of heterogeneously doped core@shell design to manipulate the energy migration and overcome the concentration quenching (Figure 3) and new ways to apply intentionally induced cross-relaxation in highly doped nanocrystals (Figure 4). We outlook the challenges and opportunities of highly doped systems to create smaller and brighter nanoparticles, and discuss the urgent needs in hybrid and heterogeneous materials as well as device technologies for synergetic multi-functional applications.

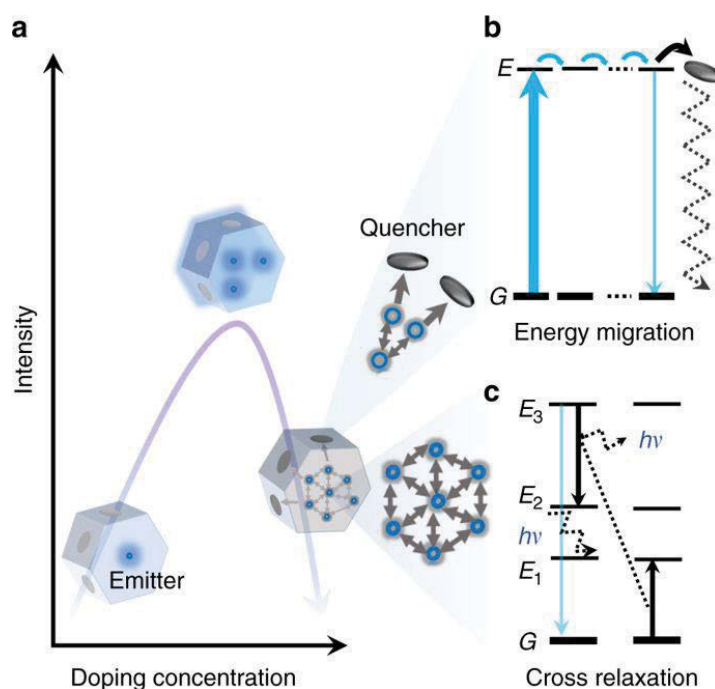


Figure 1 | Concentration quenching in upconversion nanoparticles. a, Increasing the doping concentration of dopant ions (either sensitizer or activator) in the nanoparticles could increase the emission brightness to a certain

level, but further embedding more dopants could lead to the cascade energy transfer process less effective, as too much dopants will render concentration quenching dominating. **b**, in a highly doped lanthanide upconversion system, the cause of concentration quenching includes: energy migration to surface quencher (top) and cross-relaxation energy loss (down). The term $h\nu$ represents the phonon energy.

8.2 Concentration Quenching

For a long history, the restraint of concentration quenching has been challenging the field of luminescent materials^{12,19}. The theory of concentration quenching in inorganic phosphors was introduced by Dexter and Schulman in 1954, who suggest that the considerable quenching may arise when the activator concentration reaches 10^{-3} to 10^{-2} M in bulk materials¹⁹. Different mechanisms (resonance energy transfer²⁰, molecular interactions²¹, and intermolecular photo-induced electron transfer²²) of concentration quenching in organic dye have been studied since early 1980s. It has affected the maximum number of fluorophores used in dye-doped silica nanoparticles²³. The detrimental effect of concentration quenching lies in the fact that it largely limits the concentration of activators in luminescent materials, which in turn restricts the access to a high level of luminescence intensity, in consequence broadly hindering further applications.

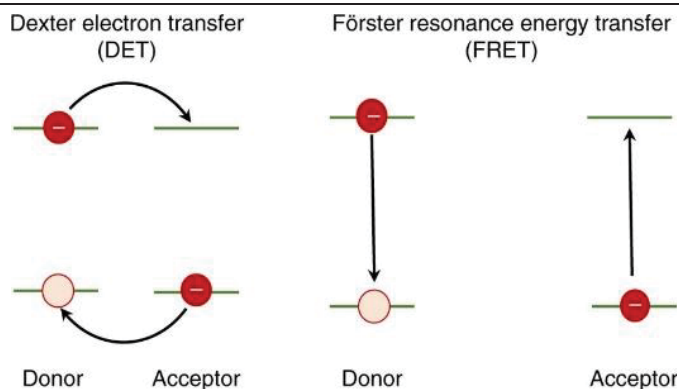
The limitation set by the threshold of concentration quenching becomes a real problem for nanoscale luminescent materials. As illustrated in [Figure 1b](#), the cause of this follows that high doping concentration (shorter distance) leads to increased occasion of energy transfer process between dopants^{5,7}, the excited state electrons can be quickly ‘short-circuited’ to the surface of nanomaterials where exist a relatively large amount of quenchers, and therefore lead to dramatic decrease of luminescence intensity ([Figure 1b](#)). More specifically, the high doping concentration facilitates the energy transfer process, through either energy migration of excited photons to the surface quenchers^{15,24,25} or inter-dopant cross-relaxation with emission loss each time^{7,13}.

To avoid the quenching of luminescence, conventionally, the doping level has been kept relatively low to ensure a sizable separation between the dopants to prevent parasitic interaction. Accordingly the critical distance (Förster critical distance) is typically in the range of 2–6 nm²⁶, meaning that the doping range should be below 10^{-3} M for organic dye-doped SiO₂²³ and 10^{-2} M for UCNPs¹³. For an efficient upconversion to proceed, the relatively low concentrations of sensitizers (typically around 20 mol %) and activators (below 2 mol %) are generally used in hexagonal-phase alkaline rare-earth fluoride nanocrystals.

This is the key roadblock to yield smaller and brighter luminescent nanomaterials²⁷⁻²⁹, which requires changing canonical approach to the composition of nanoparticles and photoexcitation schemes^{4,6}.

Box 1. The mechanism of concentration quenching

The notorious photophysical phenomenon of concentration quenching can be frequently observed from a solution of organic dyes when increasing its concentration to a certain level, typically 10^{-3} to 10^{-2} M^{7,9,19,20}. The leading factors behind concentration quenching are related to Förster resonance energy transfer (FRET) and Dexter electron transfer (also known as exchange or collisional energy transfer).



FRET is based on classical dipole-dipole interactions between the transition dipoles of the donor(D)-acceptor(A) distance, R , falling off at a rate of $1/R^6$ as well as spectral overlap of D's emission and A's absorption. Dexter energy transfer is a short-range phenomenon that falls off exponentially with distance (proportional to e^{-kR} where k is a constant that depends on the inverse of the van der Waals radius of the atom) and depends on spatial overlap of donor and quencher molecular orbitals¹⁶. The concentration quenching between phosphors is expressed by the rate constant, k_{CQ} , determined from the equation for η_{PL} :³⁰

$$\eta_{PL} = \eta_{et}\eta_{isc} \frac{k_{ph}}{k_{ph}+k_{nr}+k_{CQ}}; \quad k = \frac{1}{\tau_{PL}} \left(\frac{R_0}{R}\right)^6; \quad R_0 = \sqrt[6]{\frac{9000c^4 \ln 10x^2 \eta_{PL}}{128\pi^5 n^4 N_A} \int f_D(v) \epsilon_A(v) \frac{dv}{v^4}}$$

where η_{et} is the efficiency of the energy transfer from a host to a dopant, η_{isc} is the intersystem crossing efficiency, k_{ph} is the rate of radiative decay from the excited dopant, k_{nr} is the rate of nonradiative decay, τ_{PL} is the intrinsic radiative decay lifetime of the donor, R is the distance between the donor and the acceptor, and R_0 is the Förster radius for concentration quenching at which the energy transfer between D-A falls to 50% efficient.

When this analogy extends to an inorganic system, such as UCNPs, the concentration quenching describes the phenomenon that the intensity of the luminescence decreases if the dopant concentration is higher than an appropriate value. Typically, the UCNPs contain two types of lanthanide dopants, i.e. the sensitizer (donor) and activator/emitter (acceptor)^{2,7}. Though some singly doped (e.g., Er^{3+}) particles can generate upconversion, researchers prefer to employ a sensitizer (e.g., Yb^{3+}) to enlarge the absorbance in NIR for enhancing the upconversion by 2-3 orders of magnitude. The process of the energy extraction from a sensitizer ion to an

acceptor ion usually takes place *via* nonradiative exchange (Dexter energy transfer) or multipolar interaction (FRET). The rate equations for the excited state populations of the Yb³⁺ and Ln³⁺ ions are as follows:³¹

$$\begin{aligned} \frac{dN_{Yb1}}{dt} &= AI_0 N_{Yb,0} - FN_{Ln,0} - C_{up} N_{Ln,1}; & \frac{dN_{Ln1}}{dt} &= k_1 c N_{Ln,2} - WN_{Ln,1} + FN_{Ln,0} - C_{up} N_{Ln,1}; \\ \frac{dN_{Ln2}}{dt} &= -k_1 c N_{Ln,2} - \frac{N_{Ln,2}}{t} + C_{up} N_{Ln,1}; & \frac{dN_{Ln0}}{dt} &= \frac{N_{Ln,2}}{t} + WN_{Ln,1} - FN_{Ln,0}; & \rho_p &= \frac{\lambda_p}{hc\pi w_p^2} P \end{aligned}$$

Here $F = N_{Yb} r_{FET}$ where r_{FET} is the forward energy transfer rate from Yb³⁺ to Ln³⁺, and $C_{up} = k_{C,up} N_{Yb,1}$ is related to the upconversion process involving excited Yb³⁺ and Ln³⁺ at the first excited states, c is the concentration of Ln ions which have their first excited state empty, and k_1 is the decay rate between the second and first excited states of the Ln ion. AI_0 is a product of the excitation power variable and absorption cross section, $AI_0 = \rho_p \sigma_0$. P is the incident pump power, λ_p and w_p are the pump wavelength and beam radius, respectively, h is Planck's constant and c is the speed of light.

Most of the lanthanides have plentiful excited states, which show high possibility of coupling with each other through multipolar interaction with matching energy gaps, which is known as cross relaxation (Figure 1b)⁷. But this kind of coupling effect only occurs when the doping concentration is above a certain threshold since this process depends on the interaction between two ions. Because the $4f-4f$ transitions are symmetry forbidden due to Laporte selection rule, the consequences are low intensity and long micro-to-milisecond decay lifetimes^{32,33}. This cross relaxation is primarily responsible for concentration quenching because neighbor ions, one in excited state and the other in ground state, non-radiatively exchange the energy which is often followed by non-radiative phonon relaxation of the latter excited states to lower states energy. Such cross-relaxation process is evidenced by shortening luminescence lifetimes and decreasing the luminescence intensity.

Considering the energy transfer between two identical ions (or a network of identical ions, e.g. Yb³⁺ ions with only a single long-lived excited state) in a concentrated system, the excited electron will 'hop' among a network of ions, i.e. the inter-dopant energy transfer can quickly bring the excitation energy far away from the one that sensitizes the excitation photon, known as "energy migration" (Figure 1b). Energy migration may be advantageous, which enables the upconversion process for Eu³⁺ or Tb³⁺ emitter ions³⁴ or for Nd³⁺ ion based sensitisation³⁵, but it also "short-circuits" the excitation energy to a quencher.

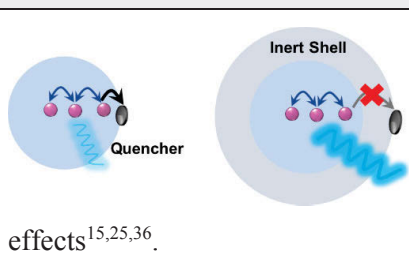
8.2.1 Emerging strategies to overcome concentration quenching

Recently, great efforts have been made to overcome concentration quenching in luminescent nanoparticles, in particular from the research community of upconversion nanomaterials. Approaches have been developed to alleviate the threshold of concentration quenching in both **homogeneously doped nanocrystals** and **heterogeneously doped core@shell nanocrystals**. **Box 2** summarizes the four

promising strategies. The commonly used strategy is via surface coating with inert shell (i.e. NaYF₄, NaGdF₄, NaLuF₄, or CaF₂) to effectively block the pathway of energy migration to the surface quenchers^{15,25,36}. The other strategy is to employ high irradiance of excitation power, which effectively excites almost all dopant ions and increase the distance between an excited ion and an ion in the ground state. This facilitates radiative transition to release the excited electrons while conquering the nonradiative consumptions³⁷. Another strategy is to tune the distance between activators by choosing an appropriate host lattice with a large unit cell^{24,38}. And the last strategy is to improve the doping uniformity in the host nanomaterials^{36,39}, which minimizes the segregation of ions and thus prevents ‘local’ concentration quenching.

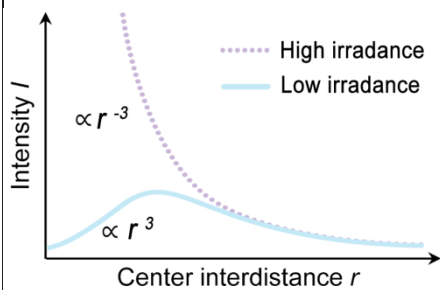
Wet-chemical synthesis has been advanced in nanomaterial sciences, and now it becomes possible to accurately control over both the number and the spatial location/distribution of the dopants. This paves the way for the formation of **heterogeneously doped core@shell nanocrystals**. Core@shell design not only enables many in-depth studies of concentration-dependent properties of doped nanomaterials, but also allows spatial selective isolation of high concentration of dopants with heavy chance of cross-relaxation. For example, Pilch et al. systematically studied a series of core@shell NaYF₄ UCNPs doped with Yb³⁺ and Ho³⁺ ions to understand the impact of the architecture on commonly used sensitizer and activator ions⁴⁰. Through core@shell nanostructure to separate sensitizers and emitters, the concentration quenching threshold of Er³⁺ has been lifted from 2% to 5%, in a design of NaYF₄:Yb³⁺,Er³⁺@NaYF₄:Yb³⁺@NaYF₄:Yb³⁺,Er³⁺@NaYF₄:Yb³⁺⁴¹.

Box 2. Strategies to overcome concentration quenching in homogeneously doped nanocrystals



Inert shell passivation is a common strategy to avoid the surface quenching by shielding the luminescent core from surface quencher, which prevents energy migration in bridging sensitized photon energy to reach the surface quenchers, as a primary way to overcome the detrimental quenching

effects^{15,25,36}.



Optically excited lanthanides suffer from concentration quenching due to a situation that the probability of nonradiative transition raises at high concentrations. **Supplying a high irradiance** to excite the dopants has been discovered highly effective in alleviating the thresholds of concentration quenching in UCNPs using Tm^{3+} or Er^{3+} as emitters^{17,18}. The fundamental of this can be illustrated as facilitating radiative transition to

release the excited electrons while conquering the nonradiative consumptions. This can be explained by using a rate equation model:³⁷

$$\frac{d}{dt} N_{exc} = p^{exc} \times N_{gr} - (p^{rad} + p^{non-rad}) \times N_{exc} \quad (1),$$

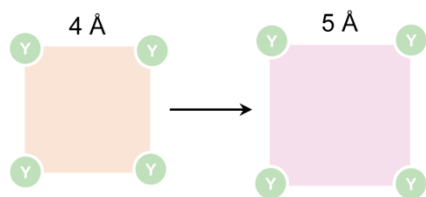
$$p^{rad} = A + B \times u(\omega_0) \quad (2),$$

$$p^{non-rad} = C + D \times p^{ET} \quad (3),$$

$$p^{ET} = \frac{1}{\tau_0} \times \left(\frac{R_0}{r}\right)^6 \propto N^2 \quad (4),$$

where N_{exc} and N_{gr} correspond to the number density of ions in the excited state and ground state; p^{exc} , p^{rad} , $p^{non-rad}$, and p^{ET} represent the probabilities for excitation, radiative transitions, nonradiative transitions, and concentration dependent energy transfer, respectively.

The overall density of ions N is a constant, composing of N_{exc} and N_{gr} , and obey the equation: $N = N_{exc} + N_{gr} \Leftrightarrow \frac{1}{r^3} \propto \frac{1}{r_{exc}^3} + \frac{1}{r_{gr}^3}$. Here r denotes the center inter-distance between excited and ground-state atoms. The



probability for concentration quenching depends on the distance, r_{gr} , between an excited ion and an ion in the ground state. The probability for stimulated emission depends on the distance, r_{exc} , between an excited ion and another excited ion.

Low irradiance means that almost all ions are confined in the ground state, thus $N \approx N_{gr}$. The luminescence

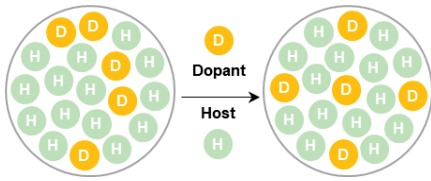
intensity, $I = \frac{A \times p^{exc} \times N}{p^{exc} + A + C + D \times p^{ET}} \propto \frac{1}{N} \propto r^3$. At a very high irradiance, almost all ions can be found in the excited

state, thus $N \approx N_{exc}$. The luminescence intensity is therefore defined as $I = \frac{[A + B \times u(\omega_0)] \times p^{exc} \times N}{p^{exc} + A + B \times u(\omega_0) + C} \propto N \propto r^{-3}$.

The distance between dopants can be enlarged via **choosing an appropriate host lattice** with a large unit cell^{24,38}.

The minimal distance between two dopants in a unit cell determines the concentration threshold, as a dopant either takes a place of element already in the crystal lattice of the host, or sometimes occupies an interstitial “hole”. Taking an example of the $\beta\text{-NaYF}_4$ crystalline structure, the average distance between a doping sensitizer

and an acceptor can be approximated using the following equation: $d_{\beta-NaYF_4} = \left(\frac{a^2 c \sqrt{3}/2}{1.5(x+y)}\right)^{1/3}$, which is evolved from the known lattice parameters when ignoring the lattice distortion caused by doping³¹. The x and y represent the doping concentrations of sensitizer and acceptor, while a and c are the lattice parameters of the hexagonal unit cells.



Material fabrication technique will largely determine the doping uniformity. **Homogenous distribution of dopants** is ideal to avoid ‘local’ concentration quenching. The layer-by-layer hot injection strategy has been found superior in yielding homogenous doping to the conventional heat-up procedures⁴². Precise control in Angstrom scale of the dopant distribution may be achieved through the management of precursor injection rate⁴².

8.2.2 Recent advances in breaking the limit of concentration quenching

Exceptional brightness of **highly doped homogenous UCNP** has been first reported by Zhao et al¹⁷. As shown in [Figure 2a](#), increasing the excitation irradiance from 1.6×10^4 to 2.5×10^6 W cm⁻² enhances the overall luminescence intensity by a factor of 5.6, 71 and 1105 for 0.5 %, 4 % and 8 % Tm³⁺, respectively¹⁷. A similar trend has been independently observed in highly Er³⁺-doped sub-10 nm NaYF₄ nanocrystals ([Figure 2b](#)). As the excitation power is raised, the conventional UCNPs (2% Er³⁺) saturate in brightness while the highly doped UCNPs (20% Er³⁺) become a lot of brighter than the conventional UCNPs¹⁸. The optimal concentration for Nd³⁺ (conventional c.a. 1%) has been increased to 20% with the sensitization of indocyanine green (ICG), resulting in ~10 times of the enhanced brightness ([Figure 2c](#))⁴³.

With inert shell coating, the conventional concentration of sensitizer Yb³⁺ (20%) has been maximized to the limit of 98% in α -NaYbF₄:2% Er³⁺@CaF₂, which design has shown 15-fold enhancement ([Figure 2d](#))⁴⁴. The β -NaYbF₄ nanocrystal has been approved as the better host matrix compared with β -NaYF₄ to improve the brightness of single UCNPs once coated with a NaYF₄ inert shell⁴⁵. Using an inert shell CaF₂, heavily doping Yb³⁺ ions in the ultra-small α -NaYF₄:Yb³⁺,Tm³⁺ and α -NaYbF₄:Tb nanoparticles has been found to dramatically enhance the upconversion emission for high-contrast bioimaging⁴⁶⁻⁴⁹. Encouragingly, the NIR emission from NaYF₄:x%Er³⁺@NaLuF₄ nanocrystals ([Figure 2e](#)) clearly displays high brightness at high dopants concentrations, and NaErF₄@NaLuF₄ (100% doping) shows the brightest luminescence²⁵.

With excellent optical properties being discovered, a range of **emerging applications** has become possible. A single, highly doped Tm^{3+} UCNP enables single nanoparticle sensitivity using a suspended-core microstructured optical-fiber dip sensor (Figure 2f)¹⁷. The diverging brightness trends, shown in Figure 2b, allow for the variation of excitation intensities for optical encoding applications¹⁸. More recently, Li et al. employed a living yeast or a human cell as a natural bio-microlens to concentrate the excitation light and to enhance the upconversion luminescence, which has realized the single-cell imaging and real-time detection of the labeled pathogenic bacteria in the dark fields⁵⁰. High efficiency of upconversion emission from NIR to UV has been achieved by high Yb^{3+} doping in $\text{NaGdF}_4:70\%\text{Yb}^{3+},1\%\text{Tm}^{3+}@NaGdF_4$ core@shell nanostructures, which has enabled the reversible dynamic NIR-light-driven red, green, and blue reflections of superstructure in a single thin film, controlled by varying the power density of the NIR light (Figure 2g)⁵¹. Through confined energy migration, an efficient five-photon upconversion emission of Tm^{3+} has been demonstrated in a NaYbF_4 host without concentration quenching. The large amount of spontaneous upconversion emissions has led to the stimulated lasing emissions in deep ultraviolet (around 311 nm) in a cavity (Figure 2h)⁵². Drees et al. has showed that the combination of elevated excitation power density and high doping concentration of Er^{3+} ions in a $\text{NaYF}_4:20\%\text{Yb}^{3+},20\%\text{Er}^{3+}@NaYF_4$ UCNP the resonance energy transfer has been enhanced by more than two orders of magnitude compared to that of standard $\text{NaYF}_4:20\%\text{Yb}^{3+},2\%\text{Er}^{3+}@NaYF_4$ particles operated at a low power density⁵³. After conjugation with anti-GFP nanobodies, the formed UCNPs nanoprobe has been used to target GFP fusion proteins inside living cells through resonance energy transfer of up-converted blue photons (Figure 2i)⁵³. More recently, Pliss et al. has reported that $\text{NaYbF}_4:\text{Tm}^{3+}@NaYF_4$ UCNPs showed 6 times higher blue emission compared with the typical $\text{NaYF}_4:30\%\text{Yb}^{3+},0.5\%\text{Tm}^{3+}@NaYF_4$ nanoparticles, and demonstrated for effective optogenetic activation with incident near-infrared light (Figure 2j)⁵⁴.

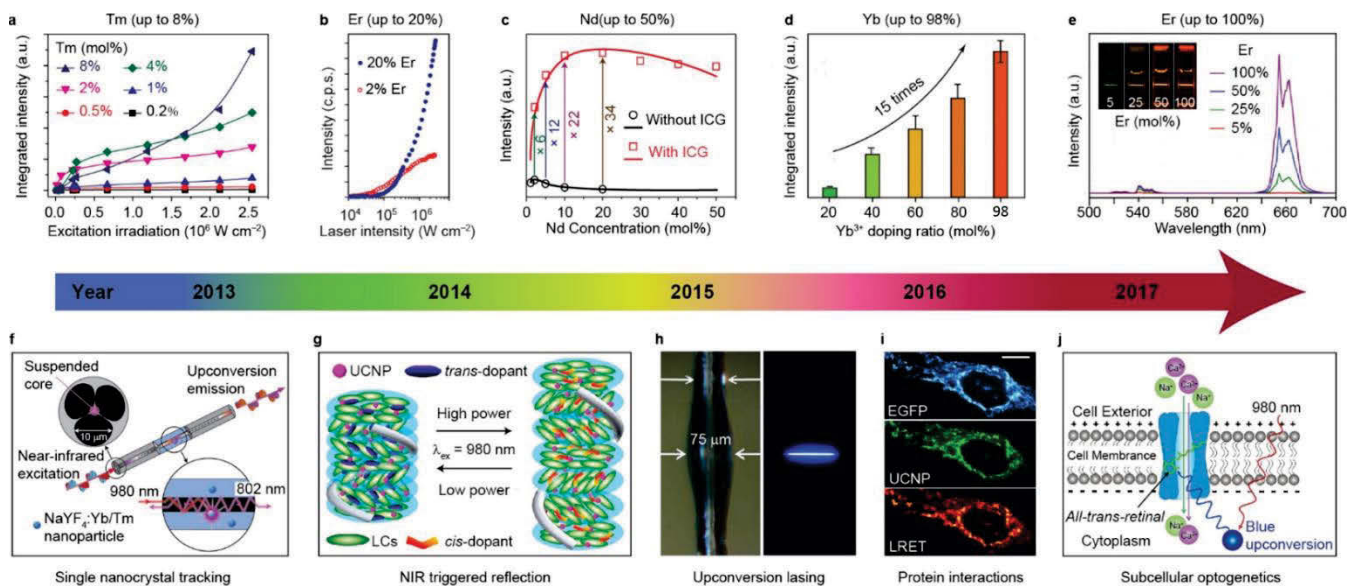


Figure 2 | Selected milestones overcoming concentration quenching in homogeneously doped upconversion nanocrystals.

a, Integrated upconversion luminescence intensity as a function of excitation irradiance for a series of Tm^{3+} -doped (0.2%-8%) nanocrystals. **b**, Upconversion luminescence intensity of single 8 nm UCNP with 20% and 2% Er^{3+} , each with 20% Yb^{3+} , plotted as a function of excitation intensity. **c**, Experimental results (black circle and red square) and theoretical modeling (black and red curves) of integrated upconversion luminescence intensities of a set of $\text{NaYF}_4:\text{Nd}^{3+}$ UCNP with and without indocyanine green (ICG) sensitization. **d**, Integrated upconversion luminescence intensity (from 400 to 750 nm) of $\alpha\text{-NaY}_{0.98-x}\text{Yb}_x\text{F}_4:2\%\text{Er}@CaF_2$ ($x = 0.2, 0.4, 0.6, 0.8, 0.98$). **e**, luminescence spectra of colloidal dispersion of $\text{NaYF}_4:x\%\text{Er}@NaLuF_4$ nanocrystals ($x=5, 25, 50, 100$) in the range of 500-700 nm; Inset: luminescence images of $\text{NaYF}_4:x\%\text{Er}@NaLuF_4$ in cyclohexane excited with a 980 nm laser. **f**, Schematic of the experimental configuration for capturing upconversion luminescence of $\text{NaYF}_4:\text{Yb}^{3+},\text{Tm}^{3+}$ nanocrystals using a suspended-core microstructured optical-fibre dip sensor. **g**, Upon irradiation by the NIR laser at the high power density, the reflection wavelength of the photonic superstructure red-shifted, whereas its reverse process occurs upon irradiation by the same laser but with the lower power density. **h**, Photographs of the microresonator with and without optical excitation, the diameters of the microcavity was 75 μm . **i**, Selective binding of UCNP-aGFP injected into HeLa cells stably expressing Tom20-EGFP HaloTag, which was labeled with TMR. Top: EGFP fluorescence upon excitation at 488 nm; middle: UCNP emission (500–570 nm) upon excitation at 978 nm; bottom: sensitized TMR emission (593–607 nm) upon excitation at 978 nm. **j**, Schematic of channelrhodopsin-2 activated in HeLa cells by strong blue upconversion luminescence from $\text{NaYbF}_4:\text{Tm}^{3+}@NaYF_4$ core@shell structure.

Figure reproduced with permission from: **a**, ref. ¹⁷, Nature Publishing Group; **b**, ref. ¹⁸, Nature Publishing Group; **c**, ref. ⁴³, American Chemical Society; **d**, ref. ⁴⁴, Royal Society of Chemistry; **e**, ref. ²⁵, American Chemical Society; **f**, ref. ⁵⁵, Nature Publishing Group; **g**, ref. ⁵¹, American Chemical Society; **h**, ref. ⁵², Nature Publishing Group; **i**, ref. ⁵³, Wiley; **j**, ref. ⁵⁴, American Chemical Society.

The precision in controlled growth has resulted in a library of intentional **heterogeneously doped core@shell UCNPs**^{56,57}. The doping concentrations in elaborated multilayer nanostructure can be tailored in a large range towards high performance of **energy migration** mediated energy transfer upconversion (**Figure 3**)¹⁶, by tuning either excitation^{16,35,58,59} and/or emission wavelengths^{34,60,61}. The fine tuning of upconversion emission colors through energy migration (**Figure 3a**) has been first demonstrated by us using Gd³⁺ sublattice structure to bridge efficient energy transfer across the core@shell interface. Upon 980 nm excitation of Yb³⁺ ions in the core, upconversion emission with tunable wavelengths and lifetimes has been realized (**Figure 3b**) via a prescribed Yb³⁺ → Tm³⁺ → Gd³⁺ → lanthanide activators (e.g. Tb³⁺, Eu³⁺, Dy³⁺, and Sm³⁺) energy cascade. Note that the energy migration mediated energy transfer upconversion emission of Tb³⁺, Eu³⁺ or Dy³⁺ at high-doping concentration is more than 2 orders of magnitude more efficient than that from Yb³⁺ sensitized cooperative energy transfer system³². Efficient photon upconversion has been demonstrated through the heterogeneous core@shell nanostructure of NaYbF₄:Gd³⁺,Tm³⁺@NaGdF₄@CaF₂:Ce³⁺ with high-doping concentration of Ce³⁺ in the shell layer⁶². CaF₂ host has been employed to reduce the *4f–5d* excitation frequency of Ce³⁺ to match the energy level of Gd³⁺. Zhang et al. has demonstrated the fabrication of NaGdF₄:Yb³⁺,Tm³⁺,Er³⁺@NaGdF₄:Eu³⁺@NaYF₄ incorporated with RGB-emitting lanthanide ions at high concentration, and showed an emission across the whole visible spectrum to generate high-brightness white light⁶³. Notably, apart from the lanthanide ions, organic dyes tethered on the surface of the nanocrystals have been demonstrated to accept the sensitized upconversion photon energy following the Gd³⁺ mediated energy transfer process, which can dramatically improve the sensitivity in FRET-limited measurement⁶⁴. Apart from Gd³⁺, Mn²⁺ and Tb³⁺ have showed a similar function for energy migration to shell layer with high concentration of activators, due to a large energy gap ($\Delta E > 5$ hv) between respective levels^{65,66}.

The energy migration approach has further shifted the excitation wavelength to ~800 nm for efficient delivery of light through deep tissue through the so-called transparent biological window³⁵. This has effectively addressed the issue of tissue damage induced by 980 nm laser heating, due to the strong water absorption of 980 nm excitation light. The solution is to use Nd³⁺ ions as 800 nm photon sensitizer with absorption cross section at 808 nm 25-fold higher than that of Yb³⁺ at 980 nm, resulting in brighter

upconversion emissions as well as negligible overheating effect⁶⁷. Since homogeneously co-doping high concentration of Nd³⁺ ions and activators will quench the upconversion emission, owing to the deleterious back energy transfer between activators and Nd³⁺, the concentration of Nd³⁺ has been limited to below 1%. To overcome this threshold, energy migration system has been employed to separate Nd³⁺ and activators (Figure 3c). Yan et al. has first demonstrated that the core@shell nanomaterials with high concentration of Nd³⁺ showed the significant upconversion luminescence enhancement compared with the homogeneous doped nanocrystals (Figure 3d). *In vivo* upconversion imaging studies confirm that highly Nd³⁺-sensitized upconversion nanoparticles give a better imaging performance (without overheating) than Yb³⁺-sensitized upconversion nanoparticles under the same excitation density condition (Figure 3d)³⁵. Xie et al. has further found that the NaYF₄:20%Yb³⁺,0.5%Tm³⁺,1%Nd³⁺@NaYF₄:20%Nd³⁺ core@active-shell nanoparticles with 20%Nd³⁺ in the shell were able to generate around 7 times stronger upconversion emission than that of NaYF₄:Nd³⁺,Yb³⁺,Tm³⁺@NaYF₄ core@inert-shell particles⁵⁸. To further reduce the cross-relaxation and back energy transfer from activators to Nd³⁺ sensitizers, Zhong et al. has designed NaYF₄:Yb³⁺,Er³⁺@NaYF₄:Yb³⁺@NaNdF₄:Yb³⁺ nanostructure, in which the intermediate NaYF₄:Yb³⁺ shell successfully separates Er³⁺ activators and Nd³⁺ primary upconversion sensitizers⁶⁸. The Nd³⁺ doping concentration has been increased to 90%, with 8 times more upconversion luminescence than the NaYF₄:Yb³⁺,Er³⁺@NaYF₄:Nd³⁺. Further coating with an inert NaYF₄ shell has been demonstrated with largely enhanced brightness and quantum yield⁶⁶. More encouragingly, control to generate a doping pattern of NaYF₄:2%Er³⁺,30%Yb³⁺@NaYF₄:20%Yb³⁺@NaNdF₄:10%Yb³⁺ has been found to facilitate more efficient energy transfer process of (Nd³⁺→Yb³⁺)→(Yb³⁺)→(Yb³⁺→Er³⁺) at higher Nd³⁺ doping concentration, which further lower the requirement in the excitation power, so that upconversion luminescence has been observed even under a 740 nm LED⁶⁹. The critical role of the Yb³⁺ ions in such a system is to bridge the sensitized energy from Nd³⁺ as the primary sensitizer and to activate the upconversion emissions. More detailed and systematic studies of the concentrations of both primary sensitizer and secondary sensitizers will improve the efficiency of energy cascade.

Combining strategies presented above (Figure 3a and 3c), the upconversion tuning with high-doping concentrations can be achieved by either Gd³⁺-mediated energy migration or Yb³⁺-mediated absorption/migration. For example, core@shell-shell structure of NaYbF₄:50%Nd³⁺@NaGdF₄:Yb³⁺,Tm³⁺@NaGdF₄:A (A: activator Eu³⁺, Tb³⁺, Dy³⁺) has been utilized to initiate the energy migration from Gd³⁺ to the activators with high concentration⁷⁰. In this system, the Nd³⁺ sensitized UCNPs display emissions spanning from UV to the visible region with high efficiency through

a single wavelength excitation at 808 nm. More recently, Liu et al. has designed a multilayer nanoparticle for simultaneously displaying short- and long-lived upconversion emissions with high concentration of different dopants at different layers, making a multilevel anti-counterfeiting possible at a single-particle level⁷¹.

In addition to the strategies in tuning excitation and emission properties, the control in doping location with a **blocking layer** (Figure 3e) has been demonstrated to emit the orthogonal emissions^{70,72,73}, spectral/lifetime multiplexing⁷⁴, up-converting/down-shifting⁵⁵, multimode imaging⁷⁵, and multi-optical functions (NIR-induced heat conversion, luminescence, and thermometry) in single particles⁷⁶. For example, reversible isomerization of spiropyran derivatives has been achieved by the orthogonal emissions of core@multishell UCNPs with high-doping concentration of Nd³⁺ under the irradiation of 800 nm and 980 nm NIR light (Figure 3f)⁷². Similar idea has been used to efficiently trigger reversible photocyclization of the chiral diarylethene molecular switch by the ultraviolet and visible luminescence from core@multishell UCNPs with dual wavelength NIR light transduction properties⁷⁷. The emission colors of these Ho³⁺, Tm³⁺ co-doped NaGdF₄:Yb³⁺ UCNPs can be tuned by changing the laser power or temperature, due to the different spectral responses⁷⁸. By design and synthesis of NaGdF₄:Nd³⁺@NaYF₄@NaGdF₄:Nd³⁺, Yb³⁺, Er³⁺@NaYF₄ nanoparticles, both upconversion and down-shifting luminescence, sensitized by highly doped Nd³⁺, can be achieved without cross interference⁵⁵. Moreover, excited Nd³⁺ can transfer energy to other lanthanide ions and result in tunable down-shifting emission. For instance, co-doping of Yb³⁺ with Nd³⁺ at high concentration would give intense NIR emission centered around 980 nm due to the efficient energy transfer from Nd³⁺ to Yb³⁺⁷⁹. The spectral and lifetime characters can correlate orthogonally with excitation by constructing noninterfering luminescent regions in a nanoparticle, which enable the multiplexed fingerprint and time-gated luminescent imaging in both spectral and lifetime dimensions⁷⁴. More recently, Marciniak et al. has demonstrated the heterogeneous doping of Nd³⁺ ions in different parts separated by an inert shell in NaNdF₄@NaYF₄@NaYF₄:1%Nd³⁺, to integrate three optical functions at different Nd³⁺ concentration, namely efficient ($\eta > 72\%$) light-to-heat conversion, bright NIR emission, and relatively sensitive ($S_R > 0.1\% K^{-1}$) localized temperature quantification⁷⁶.

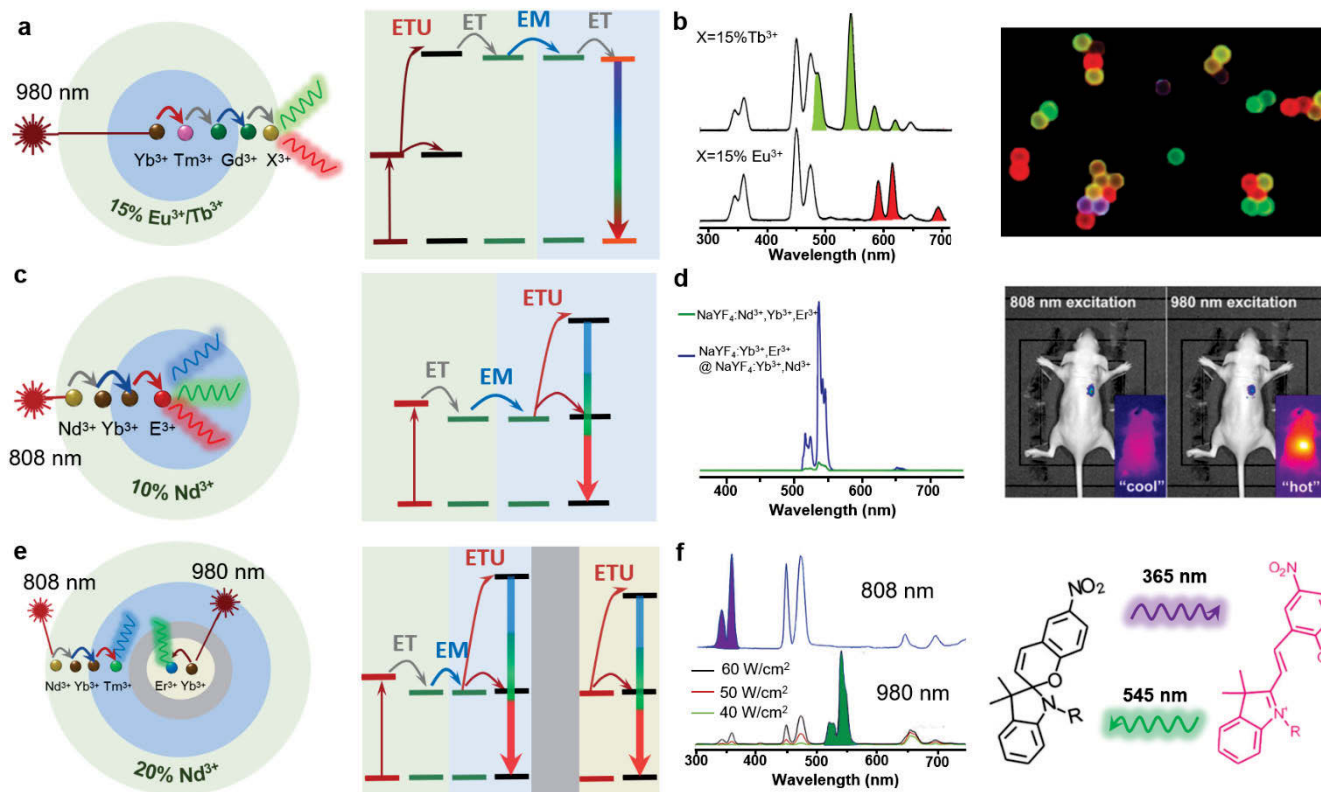


Figure 3 | Heterogeneously doped core@shell upconversion nanoparticles to overcome concentration quenching. **a**, The schematic of a core@shell design with energy migration at the emission part. **b**, Upconversion emission spectra with tunable wavelengths attributed to a prescribed $\text{Yb}^{3+} \rightarrow \text{Tm}^{3+} \rightarrow \text{Gd}^{3+} \rightarrow \text{Eu}^{3+}/\text{Tb}^{3+}$ energy cascade across the core@shell interface (left), and luminescence micrograph of polystyrene beads tagged with core@shell nanoparticles (right). **c**, The schematic of core@shell design with energy migration at the excitation part. **d**, Upconversion emission spectra of $\text{NaYF}_4:\text{Yb}^{3+},\text{Er}^{3+}@\text{NaYF}_4:\text{Yb}^{3+},\text{Nd}^{3+}$ core@shell and homogeneous doped nanoparticles (left), and the in vivo imaging of the core@shell nanoparticles under 808 nm and 980 nm excitation, respectively (right). **e**, The schematic of doping location control in core@shell design with energy transfer blocking layer. **f**, Core@multishell UCNPs ($\text{NaYF}_4:\text{Yb}^{3+}/\text{Nd}^{3+}/\text{Tm}^{3+}@\text{NaYF}_4@\text{NaYF}_4:\text{Yb}^{3+}/\text{Er}^{3+}$) with orthogonal emissions under the irradiation of 800 nm and 980 nm NIR light (left), and the orthogonal emissions was employed for reversible isomerization of spiropyran derivatives (right).

Figure reproduced with permission from: **b**, ref. ³⁴, Nature Publishing Group; **d**, ref. ³⁵, American Chemical Society; **f**, ref. ⁷², Wiley.

8.3 Emerging Applications Enabled by Cross-Relaxation Effect in Highly-Doped Nanoparticles

Cross-relaxation has often been perceived as being deleterious, but new research shows that cross relaxation can induce many unique properties, single-band emission^{80,81}, energy looping⁸², tunable color/lifetimes^{60,83}, enhanced down-shifting emissions⁸⁴, and photo-avalanche effect to establish population inversion and to enable amplified stimulated emissions^{1,85}.

High throughput molecular profiling requires optical multiplexing of single-band emission probes to target multiple analytes without crosstalk, but each lanthanide ion emitters in UCNPs has a set of multiple energy levels with multiple emission peaks⁸⁶. Cross relaxation by high-doping concentration has been used to quench the unwanted emission bands to yield single-band emissions^{87,88}. Chan et al. uses combinatorial screening of multiply doped NaYF₄ nanocrystals to identify a series of doubly and triply doped nanoparticles with pure emission spectra at various visible wavelengths⁸⁹. Approaching 100% red emission output has been reported by Wei et al. by using cross-relaxation effect relying solely on high activator interaction (Figure 4a)⁸¹. This strategy has been found successful in achieving pure red 696 or 660 nm upconversion emission as well as precisely tuning upconversion colors with new insight to study the upconversion mechanism.

More recently, Chen et al. has presented a new class of □-NaErF₄:0.5%Tm³⁺@NaYF₄ nanocrystals with bright red upconversion luminescence through high concentration Er³⁺-based host sensitization, in which Tm³⁺ ions are employed to trapping excitation energies and to minimize the luminescence quenching effects⁹⁰. Introducing high concentration of Ce³⁺ into NaYF₄:Yb³⁺/Ho³⁺ or NaYF₄:40%Gd³⁺ has greatly enhanced red-to-green upconversion emission ratio of Ho³⁺ through effective cross relaxation between Ce³⁺ and Ho³⁺ ^{91,92}. Similarly, in combination with the strategy shown in figure 3e, single-band red upconversion luminescence of Ho³⁺ could be achieved under 808 nm excitation by NaGdF₄:Yb³⁺,Ho³⁺,Ce³⁺@NaYF₄:Yb³⁺,Nd³⁺ core@shell nanoparticles with high concentration of Nd³⁺ (~10%) in the shell layer⁸⁰. Also, doping high concentration of Mn²⁺ into NaYF₄:Yb³⁺,Er³⁺ nanocrystals resulted in pure single-band red upconversion emission via efficient energy transfer between Mn²⁺ and Er³⁺ ⁸⁸. Levy et al. have used an energy-looping mechanism to nonresonantly excite upconversion in high concentration of Tm³⁺ doped NaYF₄:Tm³⁺ nanoparticles with 1064 nm light for deep tissue imaging⁸². In this work, one Tm³⁺ ion can cross-relax by donating energy partially to a second Tm³⁺ ion in its ground

state, resulting in two Tm^{3+} ions in their intermediate $^3\text{F}_4$ state (Figure 4b) from one 1064 nm photon, which further enables efficient excited state absorption and ~ 800 nm emission to occur⁸².

The energy transfer between the dopant ions in a core@shell nanostructure has also been found to be controllable by adjusting the pulse duration of the excitation laser (Figure 4c). Increasing pulse duration from 0.2 ms to 6 ms (at 980 nm), the intensity ratio of green to red emission from the shell of $\text{NaYF}_4:\text{Yb}^{3+},\text{Ho}^{3+},\text{Ce}^{3+}$ with high concentration of Ce^{3+} can be continuously modulated. The energy transfer from Ho^{3+} to Ce^{3+} by a cross-relaxation process: $^5\text{I}_6(\text{Ho}^{3+}) + ^2\text{F}_{5/2}(\text{Ce}^{3+}) \rightarrow ^5\text{I}_7(\text{Ho}^{3+}) + ^2\text{F}_{7/2}(\text{Ce}^{3+})$ is only allowed under a long pulse excitation, while the transition from $^5\text{I}_6(\text{Ho}^{3+})$ to higher levels of $^5\text{F}_4$, $^5\text{S}_2$ prevails over the above cross-relaxation process involving Ce^{3+} by a short-pulse excitation. This judicious design has further generated pure blue upconversion emission by pumping at 800 nm by $\text{Nd}^{3+} \rightarrow \text{Yb}^{3+} \rightarrow \text{Tm}^{3+}$ with high concentration of Nd^{3+} ⁶⁰. Cross-relaxation has been employed for enhancing the down-shifting emissions between 1500–1700 nm for high spatial resolution and deep-tissue penetration of photons for cerebral vascular image in the second NIR window⁸⁴. Facilitated by the high Ce^{3+} doping concentration, the Er^{3+} $^4\text{I}_{13/2}$ level is significantly populated through the accelerated nonradiative relaxation of Er^{3+} $^4\text{I}_{11/2} \rightarrow ^4\text{I}_{13/2}$ (Figure 4d), resulting in an 9-fold enhancement of the down-shifting 1550 nm luminescence of $\text{NaYbF}_4:2\%\text{Er}^{3+},2\%\text{Ce}^{3+}@\text{NaYF}_4$ nanoparticles.

Apart from color tuning, luminescence decay lifetimes are another set of optical signatures^{71,74,83,93}. By manipulating the degree of cross-relaxation, heavily Tm^{3+} doping can create a large dynamic range of lifetimes from 25.6 μs to 662.4 μs in the blue emission band, to produce a library of lifetime-tunable \square -dots for optical multiplexing (Figure 4e)⁸³. Time-resolved detection is essential in decoding the diverse time-domain optical barcodes to recognize the distinct patterns, printed by different invisible inks containing UCNPs with different emission lifetimes (Figure 4e). The ability to resolve superimposed lifetime-encoded images suggests a new way for optical data storage with high densities and fast data readout rates.

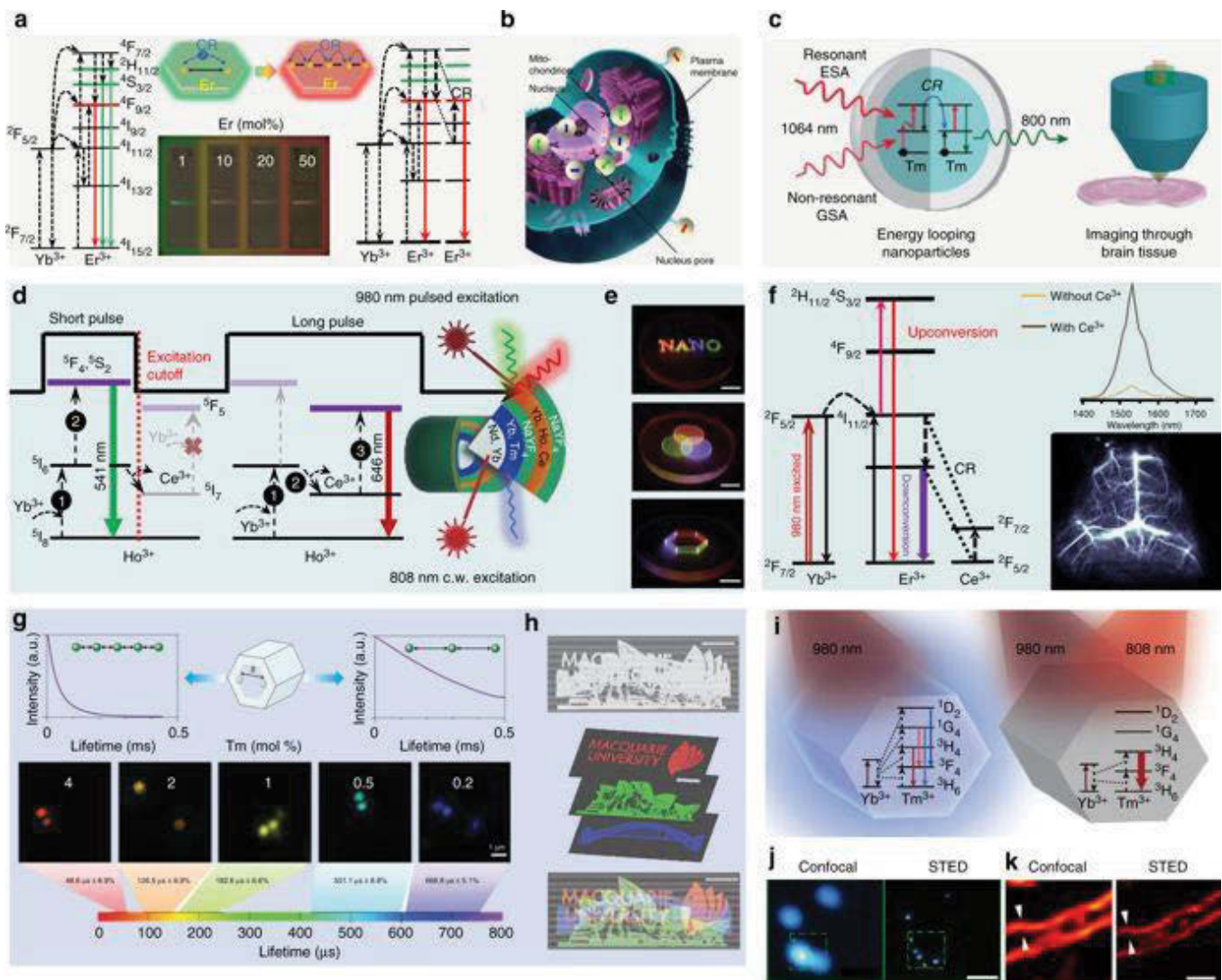


Figure 4 | cross-relaxation enabled nanotechnology using highly doped upconversion nanocrystals. **a**, upconversion mechanisms of Er^{3+} at low and high concentration doping levels and the fluorescence photographs of $\text{NaYbF}_4:\text{Er}^{3+}$ UCNPs with the different concentration of the activator. Cross-relaxation effect induces pure red emission when increasing Er^{3+} concentration (left). Application of single-band upconversion nanoprobes for multiplexed in situ molecular mapping of cancer biomarkers (right). **b**, Core@shell design and looping mechanism in highly Tm^{3+} -doped NaYF_4 (left), and their application for deep-tissue brain imaging (right). **c**, Design and mechanism of NaYF_4 -based core@shell nanocrystals capable of emitting tunable colors through combined use of continuous wave 808 nm laser and 980 nm laser with short or long pulse (left), and its application in 3-dimensional and full-color display systems with high spatial resolution and locally addressable color gamut (right). **d**, Simplified energy-level diagrams depicting the energy transfer between Yb^{3+} , Er^{3+} , and Ce^{3+} ions (left), down-shifting luminescence spectra of the $\text{NaYF}_4:\text{Yb}^{3+},\text{Er}^{3+}$ UCNPs with and without Ce^{3+} doping and their application for cerebral

vascular image through the second NIR window (right). **e**, Lifetime tuning scheme and time-resolved confocal images of NaYF₄:Yb³⁺,Tm³⁺ UCNPs with increasing doping concentration of Tm³⁺ (left), and their application in lifetime-encoded document security (right). **f**, Energy level diagrams of highly Tm³⁺ doped UCNPs under 980 nm or/and 808 nm illumination (top), confocal vs. super-resolution images of the 40 nm 8% Tm-doped UCNPs (down; left), and confocal vs. super-resolution images of cellular cytoskeleton labeled with antibody-conjugated 11.8 nm NaGdF₄:18%Yb³⁺,10%Tm³⁺ (down; right).

Figure reproduced with permission from: **a**, ref.⁸¹, American Chemical Society and ref.⁸⁶, Nature Publishing Group; **b**, ref.⁸², American Chemical Society; **c**, ref.⁶⁰, Nature Publishing Group; **d**, ref. ⁸⁴, Nature Publishing Group; **e**,ref.^{83,98}, Nature Publishing Group; **f**, ref.^{1,85}, Nature Publishing Group.

Another intriguing example is the new way for nanoscopic imaging using the highly Tm³⁺-doped UCNP as an effective STED probe. The advent of super resolution microscopy, such as stimulated emission depletion (STED) fluorescence microscopy, has revolutionized biological fluorescence microscopy and the field at large^{94,95}. However, STED beams with extremely high-power densities are indispensable for achieving super resolution imaging. Employing the cross-relaxation effect, we found highly Tm³⁺-doped UCNPs has a photon avalanche effect that facilitates the establishment of population inversion within a single UCNP. This enables a sub 30 nm optical super resolution with a STED beam density two orders of magnitude lower than that used on fluorescent dyes (Figure 4f)¹. This effect has only been found in highly doped UCNPs. This is because the dominating cross relaxation process, at a high Tm³⁺ doping concentration, can trigger a photon avalanche to establish a population inversion between metastable and ground levels. In that respect, upon 808 nm beam depletion, amplified stimulated emission is possible, resulting in a higher depletion efficiency and thus a reduced saturation intensity (Figure 4f). Independently, using this new mode of upconversion nanoscopy, Zhan et al. has reported super resolution imaging of cell cytoskeleton with 12 nm NaGdF₄:18%Yb³⁺,10%Tm³⁺ UCNPs⁸⁵. Other schemes, based on Pr³⁺ or Er³⁺ UCNPs, have been explored for super resolution nanoscopy applications^{96,97}.

8.4 Perspective

One of the major challenges to transform upconversion nanotechnology into real world applications is to enhance the brightness and efficiency of UCNPs⁴. This review summarizes the advanced optical properties of highly doped UCNPs by overcoming concentration quenching effect, towards a range of emerging applications. Notably, the unique optical properties creating layer-by-layer heterogeneous

nanoparticles has been attracting immense scientific and technological interests. Intentional doping high concentration of lanthanide ions into different sections of a single UCNP can enhance the desirable optical properties and introduce multi-functionalities. Thus far, only the spherical core@shell structure has been employed to modulate the energy transfer, while the studies on heterogeneous one-dimension structures, such as rods, plates and dumbbells, are still few^{57,99,100}. The controlled growth towards atomic precision is still needed for fully understanding of the sophisticated energy transfer process and to fine tune the upconversion properties. For example, arranging high concentration dopants into a host nanocrystal along one direction could confine the directional energy transfer, which may create new properties and open new applications beyond 3-dimensional transfer process in current heterogeneously doped core@shell nanomaterials.

The unique optical properties of highly doped UCNPs discussed above have largely impacted on emerging applications especially in biological and biomedical fields, such as single molecule sensing¹⁸, high throughput multiplexing detection^{71,74,83}, and super resolution nanoscopy^{1,85}. It is noteworthy that small and bright UCNPs are the key. Majority of currently developed UCNPs are relatively large (around 20-50 nm). It is challenging to design and fabricate highly doped smaller (sub-10 nm) UCNPs with brighter luminescence, comparable with that of quantum dots and organic dyes. Recently, fine tuning of the size below 10 nm has been demonstrated in many homogeneously doped UCNPs¹⁰¹, and with high doping concentration¹⁰². Fabrication of sub-10 nm heterogeneously doped core@shell UCNPs remains challenging and in high demand. Surface engineering is another key to producing smaller and brighter nanocrystals, which is challenged by their large surface-to-volume ratio and surface quenchers.

The surface molecules not only play an essential role in controlled synthesis of nanomaterials, but also can significantly alter their luminescence properties with even new effects¹⁰³. Examples include the recent developments of dye-sensitized UCNPs^{16,59,104,105}. Normally, lanthanide-doped inorganic nanocrystals exhibit narrowband (FWHM around 20 nm) and low (10^{-20} cm⁻²) absorption coefficients. It is notable that organic dyes have >10 times broader absorption spectra and 10^3 - 10^4 -fold higher absorption cross sections than Yb³⁺ sensitizer ions commonly used in UCNPs^{16,59,104,105}. Therefore, the organic-inorganic hybrid nanomaterials (i.e. dye-sensitized upconversion nanosystem) bridge the gap by combining their advantages¹⁶. Utilizing the efficient energy transfer of modified cyanine derivatives anchored on the surface of NaYbF₄:Tm³⁺@NaYF₄:Nd³⁺ core@active-shell nanoparticles, Chen et al. demonstrated dye sensitized upconversion¹⁶. Upon 800 nm excitation, a sequential energy transfer, i.e. dye+hv → Nd³⁺ →

Yb³⁺ → activators, has enabled the dye-sensitized nanoparticles to emit around 25 times higher upconversion emissions than canonical NaYF₄:Yb³⁺,Tm³⁺@NaYF₄ nanoparticles excited by 980 nm excitation. Similarly, the common triplet energy transfer could happen between inorganic nanocrystals and the surface dyes¹⁰⁶⁻¹⁰⁹. This has been found to facilitate excitonic energy transfer from ‘dark’ triplets in the organic semiconductor tetracene to colloidal PbS nanocrystals, thereby successfully harnessing molecular triplet excitons in the near infrared¹⁰⁸. We believe that hybrid and heterogeneous nanomaterials have the potential in pushing the performance of UCNPs into a new level, and broadly impacting on synergetic multi-facet photonics applications.

8.5 References

- 1 Liu, Y. *et al.* Amplified stimulated emission in upconversion nanoparticles for super-resolution nanoscopy. *Nature* **543**, 229-233, doi:10.1038/nature21366 (2017).
- 2 Zhou, B., Shi, B., Jin, D. & Liu, X. Controlling upconversion nanocrystals for emerging applications. *Nat Nano* **10**, 924-936, doi:10.1038/nnano.2015.251 (2015).
- 3 Wang, F. *et al.* Simultaneous phase and size control of upconversion nanocrystals through lanthanide doping. *Nature* **463**, 1061-1065, doi:10.1038/nature08777 (2010).
- 4 Wilhelm, S. Perspectives for Upconverting Nanoparticles. *ACS Nano*, doi:10.1021/acsnano.7b07120 (2017).
- 5 Chan, E. M. Combinatorial approaches for developing upconverting nanomaterials: high-throughput screening, modeling, and applications. *Chemical Society Reviews* **44**, 1653-1679, doi:10.1039/C4CS00205A (2015).
- 6 Liu, X., Yan, C.-H. & Capobianco, J. A. Photon upconversion nanomaterials. *Chemical Society Reviews* **44**, 1299-1301, doi:10.1039/C5CS90009C (2015).
- 7 Tu, L., Liu, X., Wu, F. & Zhang, H. Excitation energy migration dynamics in upconversion nanomaterials. *Chem Soc Rev* **44**, 1331-1345, doi:10.1039/C4CS00168K (2015).
- 8 Chen, X., Peng, D., Ju, Q. & Wang, F. Photon upconversion in core-shell nanoparticles. *Chemical Society Reviews* **44**, 1318-1330, doi:10.1039/C4CS00151F (2015).
- 9 Yang, P., Deng, P. & Yin, Z. Concentration quenching in Yb:YAG. *Journal of Luminescence* **97**, 51-54, doi:10.1016/S0022-2313(01)00426-4 (2002).
- 10 Viger, M. L., Live, L. S., Therrien, O. D. & Boudreau, D. Reduction of Self-Quenching in Fluorescent Silica-Coated Silver Nanoparticles. *Plasmonics* **3**, 33-40, doi:10.1007/s11468-007-9051-x (2008).
- 11 Tavernaro, I., Cavalius, C., Peuschel, H. & Kraegeloh, A. Bright fluorescent silica-nanoparticle probes for high-resolution STED and confocal microscopy. *Beilstein Journal of Nanotechnology* **8**, 1283-1296, doi:10.3762/bjnano.8.130 (2017).

- 12 Danielmeyer, H. G., Blätte, M. & Balmer, P. Fluorescence quenching in Nd:YAG. *Applied physics* **1**, 269-274, doi:10.1007/bf00889774 (1973).
- 13 Haase, M. & Schäfer, H. Upconverting Nanoparticles. *Angewandte Chemie International Edition* **50**, 5808-5829, doi:10.1002/anie.201005159 (2011).
- 14 Boyer, J.-C. & van Veggel, F. C. J. M. Absolute quantum yield measurements of colloidal NaYF₄:Er³⁺, Yb³⁺ upconverting nanoparticles. *Nanoscale* **2**, 1417-1419, doi:10.1039/C0NR00253D (2010).
- 15 Wang, F., Wang, J. & Liu, X. Direct Evidence of a Surface Quenching Effect on Size-Dependent Luminescence of Upconversion Nanoparticles. *Angewandte Chemie* **122**, 7618-7622, doi:10.1002/ange.201003959 (2010).
- 16 Chen, G. *et al.* Energy-Cascaded Upconversion in an Organic Dye-Sensitized Core/Shell Fluoride Nanocrystal. *Nano Letters* **15**, 7400-7407, doi:10.1021/acs.nanolett.5b02830 (2015).
- 17 Zhao, J. *et al.* Single-nanocrystal sensitivity achieved by enhanced upconversion luminescence. *Nat Nano* **8**, 729-734, doi:10.1038/nnano.2013.171 (2013).
- 18 Gargas, D. J. *et al.* Engineering bright sub-10-nm upconverting nanocrystals for single-molecule imaging. *Nat Nano* **9**, 300-305, doi:10.1038/nnano.2014.29 (2014).
- 19 Dexter, D. L. & Schulman, J. H. Theory of Concentration Quenching in Inorganic Phosphors. *The Journal of Chemical Physics* **22**, 1063-1070, doi:10.1063/1.1740265 (1954).
- 20 Chen, R. F. & Knutson, J. R. Mechanism of fluorescence concentration quenching of carboxyfluorescein in liposomes: Energy transfer to nonfluorescent dimers. *Analytical Biochemistry* **172**, 61-77, doi:10.1016/0003-2697(88)90412-5 (1988).
- 21 Arbeloa, I. L. Dimeric and trimeric states of the fluorescein dianion. Part 2.-Effects on fluorescence characteristics. *Journal of the Chemical Society, Faraday Transactions 2: Molecular and Chemical Physics* **77**, 1735-1742, doi:10.1039/F29817701735 (1981).
- 22 Zhao, G.-J., Liu, J.-Y., Zhou, L.-C. & Han, K.-L. Site-Selective Photoinduced Electron Transfer from Alcoholic Solvents to the Chromophore Facilitated by Hydrogen Bonding: A New Fluorescence Quenching Mechanism. *The Journal of Physical Chemistry B* **111**, 8940-8945, doi:10.1021/jp0734530 (2007).
- 23 Imhof, A. *et al.* Spectroscopy of Fluorescein (FITC) Dyed Colloidal Silica Spheres. *The Journal of Physical Chemistry B* **103**, 1408-1415, doi:10.1021/jp983241q (1999).
- 24 Wang, J. *et al.* Enhancing multiphoton upconversion through energy clustering at sublattice level. *Nat Mater* **13**, 157-162, doi:10.1038/nmat3804 (2014).
- 25 Johnson, N. J. J. *et al.* Direct Evidence for Coupled Surface and Concentration Quenching Dynamics in Lanthanide-Doped Nanocrystals. *J Am Chem Soc* **139**, 3275-3282, doi:10.1021/jacs.7b00223 (2017).
- 26 Jares-Erijman, E. A. & Jovin, T. M. FRET imaging. *Nat Biotech* **21**, 1387-1395 (2003).
- 27 Sun, T., Ma, R., Qiao, X., Fan, X. & Wang, F. Shielding Upconversion by Surface Coating: A Study of the Emission Enhancement Factor. *ChemPhysChem* **17**, 766-770, doi:10.1002/cphc.201500724 (2016).

- 28 Wang, F. & Liu, X. Upconversion Multicolor Fine-Tuning: Visible to Near-Infrared Emission from Lanthanide-Doped NaYF₄ Nanoparticles. *Journal of the American Chemical Society* **130**, 5642-5643, doi:10.1021/ja800868a (2008).
- 29 Heer, S., Kömpe, K., Güdel, H. U. & Haase, M. Highly Efficient Multicolour Upconversion Emission in Transparent Colloids of Lanthanide-Doped NaYF₄ Nanocrystals. *Advanced Materials* **16**, 2102-2105, doi:10.1002/adma.200400772 (2004).
- 30 Kawamura, Y., Brooks, J., Brown, J. J., Sasabe, H. & Adachi, C. Intermolecular Interaction and a Concentration-Quenching Mechanism of Phosphorescent Ir(III) Complexes in a Solid Film. *Physical Review Letters* **96**, 017404 (2006).
- 31 Nadort, A., Zhao, J. & Goldys, E. M. Lanthanide upconversion luminescence at the nanoscale: fundamentals and optical properties. *Nanoscale* **8**, 13099-13130, doi:10.1039/C5NR08477F (2016).
- 32 Auzel, F. Upconversion and Anti-Stokes Processes with f and d Ions in Solids. *Chemical Reviews* **104**, 139-174, doi:10.1021/cr020357g (2004).
- 33 Qin, X., Liu, X., Huang, W., Bettinelli, M. & Liu, X. Lanthanide-Activated Phosphors Based on 4f-5d Optical Transitions: Theoretical and Experimental Aspects. *Chemical Reviews* **117**, 4488-4527, doi:10.1021/acs.chemrev.6b00691 (2017).
- 34 Wang, F. *et al.* Tuning upconversion through energy migration in core-shell nanoparticles. *Nat Mater* **10**, 968-973, doi:10.1038/nmat3149 (2011).
- 35 Wang, Y.-F. *et al.* Nd³⁺-Sensitized Upconversion Nanophosphors: Efficient In Vivo Bioimaging Probes with Minimized Heating Effect. *ACS Nano* **7**, 7200-7206, doi:10.1021/nn402601d (2013).
- 36 Zuo, J. *et al.* Employing shells to eliminate concentration quenching in photonic upconversion nanostructure. *Nanoscale*, doi:10.1039/C7NR01403A (2017).
- 37 Benz, F. & Strunk, H. P. Rare earth luminescence: A way to overcome concentration quenching. *AIP Advances* **2**, 042115, doi:10.1063/1.4760248 (2012).
- 38 Marciniak, L., Streck, W., Bednarkiewicz, A., Lukowiak, A. & Hreniak, D. Bright upconversion emission of Nd³⁺ in LiLa_{1-x}Nd_xP₄O₁₂ nanocrystalline powders. *Optical Materials* **33**, 1492-1494, doi:10.1016/j.optmat.2011.03.005 (2011).
- 39 Xu, X. *et al.* Depth-profiling of Yb³⁺ sensitizer ions in NaYF₄ upconversion nanoparticles. *Nanoscale* **9**, 7719-7726, doi:10.1039/C7NR01456B (2017).
- 40 Pilch, A. *et al.* Shaping Luminescent Properties of Yb³⁺ and Ho³⁺ Co-Doped Upconverting Core-Shell β-NaYF₄ Nanoparticles by Dopant Distribution and Spacing. *Small*, DOI: 10.1002/smll.201701635, doi:10.1002/smll.201701635 (2017).
- 41 Liu, X. *et al.* Breakthrough in concentration quenching threshold of upconversion luminescence via spatial separation of the emitter doping area for bio-applications. *Chemical Communications* **47**, 11957-11959, doi:10.1039/C1CC14774A (2011).
- 42 Li, X., Wang, R., Zhang, F. & Zhao, D. Engineering Homogeneous Doping in Single Nanoparticle To Enhance Upconversion Efficiency. *Nano Lett* **14**, 3634-3639, doi:10.1021/nl501366x (2014).

- 43 Wei, W. *et al.* Alleviating Luminescence Concentration Quenching in Upconversion Nanoparticles through Organic Dye Sensitization. *Journal of the American Chemical Society* **138**, 15130-15133, doi:10.1021/jacs.6b09474 (2016).
- 44 Shen, B. *et al.* Revisiting the optimized doping ratio in core/shell nanostructured upconversion particles. *Nanoscale* **9**, 1964-1971, doi:10.1039/C6NR07687D (2017).
- 45 Ma, C. *et al.* Optimal Sensitizer Concentration in Single Upconversion Nanocrystals. *Nano Lett* **17**, 2858-2864, doi:10.1021/acs.nanolett.6b05331 (2017).
- 46 Chen, G. *et al.* (α -NaYbF₄:Tm³⁺)/CaF₂ Core/Shell Nanoparticles with Efficient Near-Infrared to Near-Infrared Upconversion for High-Contrast Deep Tissue Bioimaging. *ACS Nano* **6**, 8280-8287, doi:10.1021/nn302972r (2012).
- 47 Punjabi, A. *et al.* Amplifying the Red-Emission of Upconverting Nanoparticles for Biocompatible Clinically Used Prodrug-Induced Photodynamic Therapy. *ACS Nano* **8**, 10621-10630, doi:10.1021/nn505051d (2014).
- 48 Shen, J. *et al.* Tunable Near Infrared to Ultraviolet Upconversion Luminescence Enhancement in (α -NaYF₄:Yb,Tm)/CaF₂ Core/Shell Nanoparticles for In situ Real-time Recorded Biocompatible Photoactivation. *Small* **9**, 3213-3217, doi:10.1002/sml.201300234 (2013).
- 49 Xue, M. *et al.* Highly Enhanced Cooperative Upconversion Luminescence through Energy Transfer Optimization and Quenching Protection. *ACS Applied Materials & Interfaces* **8**, 17894-17901, doi:10.1021/acsami.6b05609 (2016).
- 50 Li, Y. *et al.* Enhancing Upconversion Fluorescence with a Natural Bio-microlens. *ACS Nano*, DOI: 10.1021/acsnano.1027b04420, doi:10.1021/acsnano.7b04420 (2017).
- 51 Wang, L. *et al.* Reversible Near-Infrared Light Directed Reflection in a Self-Organized Helical Superstructure Loaded with Upconversion Nanoparticles. *Journal of the American Chemical Society* **136**, 4480-4483, doi:10.1021/ja500933h (2014).
- 52 Chen, X. *et al.* Confining energy migration in upconversion nanoparticles towards deep ultraviolet lasing. *Nature Communications* **7**, 10304, doi:10.1038/ncomms10304 (2016).
- 53 Drees, C. *et al.* Engineered Upconversion Nanoparticles for Resolving Protein Interactions inside Living Cells. *Angewandte Chemie International Edition* **55**, 11668-11672, doi:10.1002/anie.201603028 (2016).
- 54 Pliss, A. *et al.* Subcellular Optogenetics Enacted by Targeted Nanotransformers of Near-Infrared Light. *ACS Photonics* **4**, 806-814, doi:10.1021/acsp Photonics.6b00475 (2017).
- 55 Zhang, Y. & Liu, X. Nanocrystals: Shining a light on upconversion. *Nat Nano* **8**, 702-703, doi:10.1038/nnano.2013.199 (2013).
- 56 Kovalenko, M. V. *et al.* Prospects of Nanoscience with Nanocrystals. *ACS Nano* **9**, 1012-1057, doi:10.1021/nn506223h (2015).
- 57 Liu, D. *et al.* Three-dimensional controlled growth of monodisperse sub-50 nm heterogeneous nanocrystals. *Nature Communications* **7**, 10254, doi:10.1038/ncomms10254 (2016).

- 58 Xie, X. *et al.* Mechanistic Investigation of Photon Upconversion in Nd³⁺-Sensitized Core–Shell Nanoparticles. *Journal of the American Chemical Society* **135**, 12608-12611, doi:10.1021/ja4075002 (2013).
- 59 Chen, G. *et al.* Efficient Broadband Upconversion of Near-Infrared Light in Dye-Sensitized Core/Shell Nanocrystals. *Advanced Optical Materials* **4**, 1760-1766, doi:10.1002/adom.201600556 (2016).
- 60 Deng, R. *et al.* Temporal full-colour tuning through non-steady-state upconversion. *Nat Nano* **10**, 237-242, doi:10.1038/nnano.2014.317 (2015).
- 61 Hao, S. *et al.* Nd³⁺-Sensitized multicolor upconversion luminescence from a sandwiched core/shell/shell nanostructure. *Nanoscale* **9**, 10633-10638, doi:10.1039/C7NR02594G (2017).
- 62 Chen, X. *et al.* Energy Migration Upconversion in Ce(III)-Doped Heterogeneous Core–Shell–Shell Nanoparticles. *Small* **13**, 1701479-n/a, doi:10.1002/smll.201701479 (2017).
- 63 Zhang, C. *et al.* White-Light Emission from an Integrated Upconversion Nanostructure: Toward Multicolor Displays Modulated by Laser Power. *Angewandte Chemie International Edition* **54**, 11531-11535, doi:10.1002/anie.201504518 (2015).
- 64 Deng, R., Wang, J., Chen, R., Huang, W. & Liu, X. Enabling Förster Resonance Energy Transfer from Large Nanocrystals through Energy Migration. *Journal of the American Chemical Society* **138**, 15972-15979, doi:10.1021/jacs.6b09349 (2016).
- 65 Li, X. *et al.* Energy Migration Upconversion in Manganese(II)-Doped Nanoparticles. *Angewandte Chemie* **127**, 13510-13515, doi:10.1002/ange.201507176 (2015).
- 66 Zhou, B., Yang, W., Han, S., Sun, Q. & Liu, X. Photon Upconversion Through Tb³⁺-Mediated Interfacial Energy Transfer. *Advanced Materials* **27**, 6208-6212, doi:10.1002/adma.201503482 (2015).
- 67 Xie, X. *et al.* Emerging \approx 800 nm Excited Lanthanide-Doped Upconversion Nanoparticles. *Small* **13**, 1602843-n/a, doi:10.1002/smll.201602843 (2017).
- 68 Zhong, Y. *et al.* Elimination of Photon Quenching by a Transition Layer to Fabricate a Quenching-Shield Sandwich Structure for 800 nm Excited Upconversion Luminescence of Nd³⁺-Sensitized Nanoparticles. *Advanced Materials* **26**, 2831-2837, doi:10.1002/adma.201304903 (2014).
- 69 Zhong, Y., Rostami, I., Wang, Z., Dai, H. & Hu, Z. Energy Migration Engineering of Bright Rare-Earth Upconversion Nanoparticles for Excitation by Light-Emitting Diodes. *Advanced Materials* **27**, 6418-6422, doi:10.1002/adma.201502272 (2015).
- 70 Wen, H. *et al.* Upconverting Near-Infrared Light through Energy Management in Core–Shell–Shell Nanoparticles. *Angewandte Chemie International Edition* **52**, 13419-13423, doi:10.1002/anie.201306811 (2013).
- 71 Liu, X. *et al.* Binary temporal upconversion codes of Mn²⁺-activated nanoparticles for multilevel anti-counterfeiting. *Nature Communications* **8**, 899, doi:10.1038/s41467-017-00916-7 (2017).
- 72 Lai, J., Zhang, Y., Pasquale, N. & Lee, K.-B. An Upconversion Nanoparticle with Orthogonal Emissions Using Dual NIR Excitations for Controlled Two-Way Photoswitching. *Angewandte Chemie International Edition* **53**, 14419-14423, doi:10.1002/anie.201408219 (2014).

- 73 Li, X. *et al.* Filtration Shell Mediated Power Density Independent Orthogonal Excitations–Emissions Upconversion Luminescence. *Angewandte Chemie International Edition* **55**, 2464-2469, doi:10.1002/anie.201510609 (2016).
- 74 Dong, H. *et al.* Versatile Spectral and Lifetime Multiplexing Nanoplatform with Excitation Orthogonalized Upconversion Luminescence. *ACS Nano* **11**, 3289-3297, doi:10.1021/acsnano.7b00559 (2017).
- 75 He, S. *et al.* Simultaneous Enhancement of Photoluminescence, MRI Relaxivity, and CT Contrast by Tuning the Interfacial Layer of Lanthanide Heteroepitaxial Nanoparticles. *Nano Lett* **17**, 4873-4880, doi:10.1021/acs.nanolett.7b01753 (2017).
- 76 Marciniak, L., Pilch, A., Arabasz, S., Jin, D. & Bednarkiewicz, A. Heterogeneously Nd³⁺ doped single nanoparticles for NIR-induced heat conversion, luminescence, and thermometry. *Nanoscale* **9**, 8288-8297, doi:10.1039/C7NR02630G (2017).
- 77 Wang, L. *et al.* Luminescence-Driven Reversible Handedness Inversion of Self-Organized Helical Superstructures Enabled by a Novel Near-Infrared Light Nanotransducer. *Advanced Materials* **27**, 2065-2069, doi:10.1002/adma.201405690 (2015).
- 78 Shao, Q. *et al.* Emission color tuning of core/shell upconversion nanoparticles through modulation of laser power or temperature. *Nanoscale* **9**, 12132-12141, doi:10.1039/C7NR03682E (2017).
- 79 Li, Y. *et al.* A Versatile Imaging and Therapeutic Platform Based on Dual-Band Luminescent Lanthanide Nanoparticles toward Tumor Metastasis Inhibition. *ACS Nano* **10**, 2766-2773, doi:10.1021/acsnano.5b07873 (2016).
- 80 Chen, D. *et al.* Nd³⁺-Sensitized Ho³⁺ Single-Band Red Upconversion Luminescence in Core–Shell Nanoarchitecture. *The Journal of Physical Chemistry Letters* **6**, 2833-2840, doi:10.1021/acs.jpcclett.5b01180 (2015).
- 81 Wei, W. *et al.* Cross Relaxation Induced Pure Red Upconversion in Activator- and Sensitizer-Rich Lanthanide Nanoparticles. *Chemistry of Materials* **26**, 5183-5186, doi:10.1021/cm5022382 (2014).
- 82 Levy, E. S. *et al.* Energy-Looping Nanoparticles: Harnessing Excited-State Absorption for Deep-Tissue Imaging. *ACS Nano* **10**, 8423-8433, doi:10.1021/acsnano.6b03288 (2016).
- 83 Lu, Y. *et al.* Tunable lifetime multiplexing using luminescent nanocrystals. *Nat Photon* **8**, 32-36, doi:10.1038/nphoton.2013.322 (2014).
- 84 Zhong, Y. *et al.* Boosting the down-shifting luminescence of rare-earth nanocrystals for biological imaging beyond 1500 nm. *Nature Communications* **8**, 737, doi:10.1038/s41467-017-00917-6 (2017).
- 85 Zhan, Q. *et al.* Achieving high-efficiency emission depletion nanoscopy by employing cross relaxation in upconversion nanoparticles. *Nature Communications* **8**, 1058, doi:10.1038/s41467-017-01141-y (2017).
- 86 Zhou, L. *et al.* Single-band upconversion nanoprobe for multiplexed simultaneous in situ molecular mapping of cancer biomarkers. *Nature Communications* **6**, 6938, doi:10.1038/ncomms7938 (2015).

- 87 Wang, J., Wang, F., Wang, C., Liu, Z. & Liu, X. Single-Band Upconversion Emission in Lanthanide-Doped KMnF₃ Nanocrystals. *Angewandte Chemie International Edition* **50**, 10369-10372, doi:10.1002/anie.201104192 (2011).
- 88 Tian, G. *et al.* Mn²⁺ Dopant-Controlled Synthesis of NaYF₄:Yb/Er Upconversion Nanoparticles for in vivo Imaging and Drug Delivery. *Advanced Materials* **24**, 1226-1231, doi:10.1002/adma.201104741 (2012).
- 89 Chan, E. M. *et al.* Combinatorial Discovery of Lanthanide-Doped Nanocrystals with Spectrally Pure Upconverted Emission. *Nano Letters* **12**, 3839-3845, doi:10.1021/nl3017994 (2012).
- 90 Chen, Q. *et al.* Confining Excitation Energy in Er³⁺-Sensitized Upconversion Nanocrystals through Tm³⁺-Mediated Transient Energy Trapping. *Angewandte Chemie International Edition* **56**, 7605-7609, doi:10.1002/anie.201703012 (2017).
- 91 Guanying, C., Haichun, L., Gabriel, S., Huijuan, L. & Zhiguo, Z. Upconversion emission tuning from green to red in Yb³⁺/Ho³⁺-codoped NaYF₄ nanocrystals by tridoping with Ce³⁺ ions. *Nanotechnology* **20**, 385704 (2009).
- 92 Gao, W. *et al.* Enhanced red upconversion luminescence by codoping Ce³⁺ in [small beta]-NaY(Gd_{0.4})F₄:Yb³⁺/Ho³⁺ nanocrystals. *Journal of Materials Chemistry C* **2**, 5327-5334, doi:10.1039/C4TC00585F (2014).
- 93 Zhao, J. *et al.* Upconversion luminescence with tunable lifetime in NaYF₄:Yb,Er nanocrystals: role of nanocrystal size. *Nanoscale* **5**, 944-952, doi:10.1039/C2NR32482B (2013).
- 94 Balzarotti, F. *et al.* Nanometer resolution imaging and tracking of fluorescent molecules with minimal photon fluxes. *Science*, doi:10.1126/science.aak9913 (2016).
- 95 Hanne, J. *et al.* STED nanoscopy with fluorescent quantum dots. *Nature Communications* **6**, 7127, doi:10.1038/ncomms8127 (2015).
- 96 Shin, K. *et al.* Distinct mechanisms for the upconversion of NaYF₄:Yb³⁺,Er³⁺ nanoparticles revealed by stimulated emission depletion. *Physical Chemistry Chemical Physics* **19**, 9739-9744, doi:10.1039/C7CP00918F (2017).
- 97 Kolesov, R. *et al.* Super-resolution upconversion microscopy of praseodymium-doped yttrium aluminum garnet nanoparticles. *Physical Review B* **84**, 153413 (2011).
- 98 Deng, R. & Liu, X. Tunable lifetime nanocrystals. *Nature Photonics* **8**, 10, doi:10.1038/nphoton.2013.353 (2013).
- 99 Zhuo, Z. *et al.* Manipulating energy transfer in lanthanide-doped single nanoparticles for highly enhanced upconverting luminescence. *Chemical Science*, doi:10.1039/C7SC01393K (2017).
- 100 Wen, H.-Q. *et al.* Sequential Growth of NaYF₄:Yb/Er@NaGdF₄ Nanodumbbells for Dual-Modality Fluorescence and Magnetic Resonance Imaging. *ACS Applied Materials & Interfaces* **9**, 9226-9232, doi:10.1021/acsami.6b16842 (2017).
- 101 Rinkel, T., Raj, A. N., Dühnen, S. & Haase, M. Synthesis of 10 nm β-NaYF₄:Yb,Er/NaYF₄ Core/Shell Upconversion Nanocrystals with 5 nm Particle Cores. *Angew. Chem. Int. Ed.* **55**, 1164-1167, doi:10.1002/anie.201508838 (2016).

- 102 Shi, R. *et al.* Tuning hexagonal NaYbF₄ nanocrystals down to sub-10 nm for enhanced photon upconversion. *Nanoscale*, doi:10.1039/C7NR04877G (2017).
- 103 Boles, M. A., Ling, D., Hyeon, T. & Talapin, D. V. The surface science of nanocrystals. *Nat Mater* **15**, 141-153, doi:10.1038/nmat4526 (2016).
- 104 Wu, X. *et al.* Tailoring dye-sensitized upconversion nanoparticle excitation bands towards excitation wavelength selective imaging. *Nanoscale* **7**, 18424-18428, doi:10.1039/C5NR05437K (2015).
- 105 Wu, X. *et al.* Dye-Sensitized Core/Active Shell Upconversion Nanoparticles for Optogenetics and Bioimaging Applications. *ACS Nano* **10**, 1060-1066, doi:10.1021/acsnano.5b06383 (2016).
- 106 Mongin, C., Garakyaraghi, S., Razgoniaeva, N., Zamkov, M. & Castellano, F. N. Direct observation of triplet energy transfer from semiconductor nanocrystals. *Science* **351**, 369-372, doi:10.1126/science.aad6378 (2016).
- 107 Wu, M. *et al.* Solid-state infrared-to-visible upconversion sensitized by colloidal nanocrystals. *Nat Photon* **10**, 31-34, doi:10.1038/nphoton.2015.226 (2016).
- 108 Tabachnyk, M. *et al.* Resonant energy transfer of triplet excitons from pentacene to PbSe nanocrystals. *Nat Mater* **13**, 1033-1038, doi:10.1038/nmat4093 (2014).
- 109 Huang, Z. *et al.* Hybrid Molecule–Nanocrystal Photon Upconversion Across the Visible and Near-Infrared. *Nano Letters* **15**, 5552-5557, doi:10.1021/acs.nanolett.5b02130 (2015).